University of Glasgow

Rodger, Andrew (2019) *Millimetre-continuum diagnostics and non-LTE radiative transfer modelling of solar prominences.* PhD thesis.

https://theses.gla.ac.uk/76747/

Copyright and moral rights for this work are retained by the author

A copy can be downloaded for personal non-commercial research or study, without prior permission or charge

This work cannot be reproduced or quoted extensively from without first obtaining permission in writing from the author

The content must not be changed in any way or sold commercially in any format or medium without the formal permission of the author

When referring to this work, full bibliographic details including the author, title, awarding institution and date of the thesis must be given

Enlighten: Theses
https://theses.gla.ac.uk/
research-enlighten@glasgow.ac.uk

Millimetre-Continuum Diagnostics and non-LTE Radiative Transfer Modelling of Solar Prominences

Andrew Rodger

Astronomy and Astrophysics Group
School of Physics and Astronomy
Kelvin Building
University of Glasgow
Glasgow, G12 8QQ
Scotland, U.K.

Presented for the degree of
Doctor of Philosophy
The University of Glasgow
November 2019

This thesis is my own composition except where indicated in the text. No part of this thesis has been submitted elsewhere for any other degree or qualification.

Copyright © November 2019 by Andrew Rodger

23 November 2019

Acknowledgements

Getting through a PhD can be difficult, but it can be made significantly easier by the people you have around you. I for one am immeasurably grateful for the help and support that so many people have shown me over the last few years. Although I expect that I will not be able to thank every person for the impact they have had on me during my PhD, I shall do my best to acknowledge those who helped me the most.

Firstly, I would like to thank my girlfriend, Shona, without whom I am sure I would not have reached this point. Thank you for picking me up when I was down and for reminding me that it is better to face forward than to look back. Thank you also to my family; Mum, Dad, Jamie and Granny, for supporting me throughout my whole time at university, and for believing that I could do this, even if I was not always so certain.

I would like to thank my supervisor, Dr Nicolas Labrosse, who's guidance was invaluable and who was always happy to patiently chat, discuss and explain whatever problem I brought to him on any given day.

An important aspect I found in living as a PhD student was making sure I was able to distract myself when I was worrying over work too much. For help in this I would like to thank each and every one of my friends for the various boardgame nights, pub trips, rugby matches and countless other distractions which allowed me to continue working on my thesis. I would, however, give a special thanks to Daniel for spending so many lunches listening to me complain and yet still nagging me to do things outside work.

I would then like to thank everyone from the sixth floor of the Kelvin building who made it a pleasure to work there for the last few years. A large contribution to this was the group's willingness to help in anything from guidance with using python to solar physics discussions. But perhaps most of all I am thankful for the chats in the common area during the afternoon coffee break.

I am also very grateful to Dr Sven Wedemeyer and everyone else in the Institute of

Theoretical Astrophysics in Oslo for teaching me about ALMA and making me feel welcome during my time working in Norway.

I would finally like to acknowledge the Astronomical Institute of the University of Wrocław for the use of Hα spectral imaging data taken with the Multi-Chanel Subtractive Double Pass Spectrograph (MSDP) in Białkow, Poland on the 19th of April 2018. This observation was taken by Dr K. Radziszewski, whilst the calibration of the intensities was conducted by Prof P. Rudawy.

This thesis makes use of the following ALMA data:ADS/JAO.ALMA#2011.0.00020.SV and ADS/JAO.ALMA#2017.1.01138.S. ALMA is a partnership of ESO (representing its member states), NSF (USA) and NINS (Japan), together with NRC (Canada), NSC and ASIAA (Taiwan), and KASI (Republic of Korea), in cooperation with the Republic of Chile. The Joint ALMA Observatory is operated by ESO, AUI/NRAO and NAOJ.

Abstract

With the advent of solar observing capability the *Atacama Large Millimeter/sub-millimeter Array* (ALMA), solar physicists now have access to high spatial resolution imaging of the millimetre-continuum emission from the solar atmosphere for the first time. The radiation in the wavelength range of ALMA is formed primarily through collisional processes, which, along with lying within the Rayleigh-Jeans Limit, results in a linear relationship between the brightness temperature and the electron temperature of the emitting plasma. Therefore, it is expected that millimetre observations have the potential for strong temperature diagnostics as well as other internal plasma parameters such as the emission measure. However, until ALMA the usefulness of millimetre-continuum observations has been hampered by low spatial resolutions.

In this thesis I address the potential for the plasma diagnostics of solar prominences using ALMA. Solar prominences are an extreme example of natural magnetic confinement, where relatively high density, low temperature plasma is suspended within the sparse, extremely high temperature energetic solar corona. The term solar prominence generally refers to these structures when viewed off the solar limb, however, they are also observable, often as dark absorption features known as filaments, against the disk. These structures are maintained for long periods of time ranging from days to weeks through detailed energy balance. However, once this balance is broken solar prominences can erupt violently leading to dramatic events, often including *Coronal Mass Ejections* (CMEs). Understanding the formation, structure and energy balance of solar prominences is therefore an integral part in understanding solar atmospheric activity as a whole.

To understand the formation of the millimetre-continuum from solar prominences I used the 2D non-Local Thermodynamic Equilibrium (non-LTE) cylindrical prominence code C2D2E of Gouttebroze & Labrosse (2009). This code considers a plasma consisting of both hydrogen and helium, with their ionization equilibrium. The use of a non-LTE model is

important because, although the millimetre-continuum is formed from LTE processes, the ionization populations of the hydrogen and helium will be determined by non-LTE processes caused by incident ionizing and energising UV radiation. Considering sets of both isothermal–isobaric and multi-thermal prominence models including an ad-hoc *prominence-to-corona transition region* (PCTR) I calculated the emergent brightness temperature expected from solar prominences using the output from the C2D2E models. The results from the isothermal–isobaric models found that, whilst the optical thickness of a given millimetre wavelength is $\gtrapprox 4-5$, the brightness temperature from the prominence at said wavelength equaled the constant electron temperature of the particular model. For the multi-thermal models it was found that the brightness temperature, whilst the plasma was optically thick, was representative of the electron temperature of a given formation layer within the particular line of sight (LOS). The formation layer was defined as the region/regions of each LOS with 70% the maximum contribution function for that LOS. When the material is optically thin the emergent brightness temperature is not representative of any unique layer within the prominence structure, but rather an integration across the entire temperature distribution within the LOS, with this integration also being affected by the optical thickness of the particular LOS. Therefore, in order to make assertions into the temperature structure from a solar prominence using millimetre-continuum diagnostics it is important to first have some understanding of the optical thickness regime of the emitting plasma. From the multi-thermal prominence models, of radius 1Mm, it was found that ALMA Band 3 produced a maximum optical thickness greater than 1 for pressures ≥ 0.1 dyn cm^{-2}, whilst Band 6 required pressures $\gtrsim 0.5$ dyn cm^{-2}

The millimetre-continuum prominence code was then altered to simulate the emergent brightness temperature from an on-disk filament observation. Again both isothermal–isobaric and multi-thermal PCTR filament models were considered, however, with the inclusion of various different background brightness temperatures from the solar disk. Using these models the visibility of filaments at ALMA Bands 3 and 6 is investigated by analysing their contrast against the background brightness temperature, with the inclusion of a discussion into how this may change with the inclusion of a "coronal cavity" above the overlying filament structure.

A possible method to estimate the optical thickness of a plasma is by using coordinated observation of the same structure but in a different wavelength regime. I investigate correlations between the millimetre-continuum optical thickness and the integrated intensity

from the important Lyman and Balmer lines of neutral hydrogen as well as the He I D3 line of neutral helium. The most important factor in determining the optical thickness of the millimetre-continuum is the charge squared weighted electron–ion emission measure. In this work a clear power-law relationship is found between the electron–proton emission measure and the integrated intensity of the Balmer lines, and between the electron–first ionized helium emission measure for the integrated intensity of the He I D3 line for isothermal–isobaric models. The brightness temperature of the millimetre–continuum is also found to produce a similar result to the colour temperature of the Lyman continuum when both are formed in near to overlapping formation regions.

Other methods to determine the optical thickness of the millimetre-continuum investigated in this thesis include using analysis of the millimetre-continuum spectra. A relationship between the gradient of the logarithmic brightness temperature spectrum and the optical thickness of the millimetre-continuum at band-centre is derived. This relationship is then tested using sets of isothermal and multi-thermal 2D prominence models. A case study into using the gradient of the brightness temperature enhancement observed in a sub-band, science verification ALMA observation of an on-disk plasmoid eruption is presented. The method proves to be a strong candidate for estimating the optical thickness of the millimetre-continuum. However, it relies on a good understanding of the uncertainty into the brightness temperature measurement as well as the gradient of the background brightness temperature spectrum, which, due to the current state of understanding into the uncertainty of absolute brightness temperature measurements with ALMA, needed to be estimated in this study.

In the final chapter of my thesis I present some preliminary results from the first high-resolution interferometric observation of a solar prominence with ALMA. Coordinated observation with Hα spectral imaging from the MSDP telescope in Białkow is used to estimate the optical thickness regime of prominence in the millimetre-continuum. A discussion into the morphology of the brightness temperature images of the prominence is provided as well as the correlations found between the brightness temperature distribution and the intensities from co-aligned images in each AIA band.

Contents

List of Figures

List of Tables

Chapter 1

Introduction

1.1 Solar Prominences

Solar prominences are one of the most extreme displays of magnetic confinement found in the solar system. Often appearing as cloud-like structures suspended in the outer solar atmosphere, prominences largely consist of denser, cooler and less ionized material than the surrounding extremely sparse, energetic solar corona. In visible light prominences appear as bright protrusions off the solar limb, and as dark structures when viewed against the solar disk. When they are viewed on the solar disk, prominences are referred to as filaments. Figure 1.1 shows an image of a prominence in the Hα line.

The environment where the plasma is contained is known as a filament channel, where the magnetic field is configured in such a way that the plasma is both held up against gravity, and sheltered from the coronal plasma. Filament channels are found in regions of neutral magnetic polarisation between regions of opposite polarity, frequently called the *polarity inversion line* (PIL) (Engvold 2015).

The plasma in solar prominences is considered to have typical densities between $\sim 10^{10}$, and $10^{11}\,\mathrm{cm}^{-3}$, with temperatures $\gtrapprox 10^4\,\mathrm{K}$ (Labrosse et al. 2010; Engvold 2015). This makes them approximately a factor of 10^2 cooler, and more dense than the surrounding corona. The magnetic field strength is expected to range between 3 and 30 G, with a *plasma-β* of less than 1 meaning that the magnetic pressure dominates over the gas pressure. The predominant magnetic field orientation in filament channels where the prominence is not erupting is horizontal (Engvold 2015; Levens et al. 2016), and the direction of this horizontal field defines the chirality of the prominence (Martin et al. 1992), i.e. whether it is dextral or

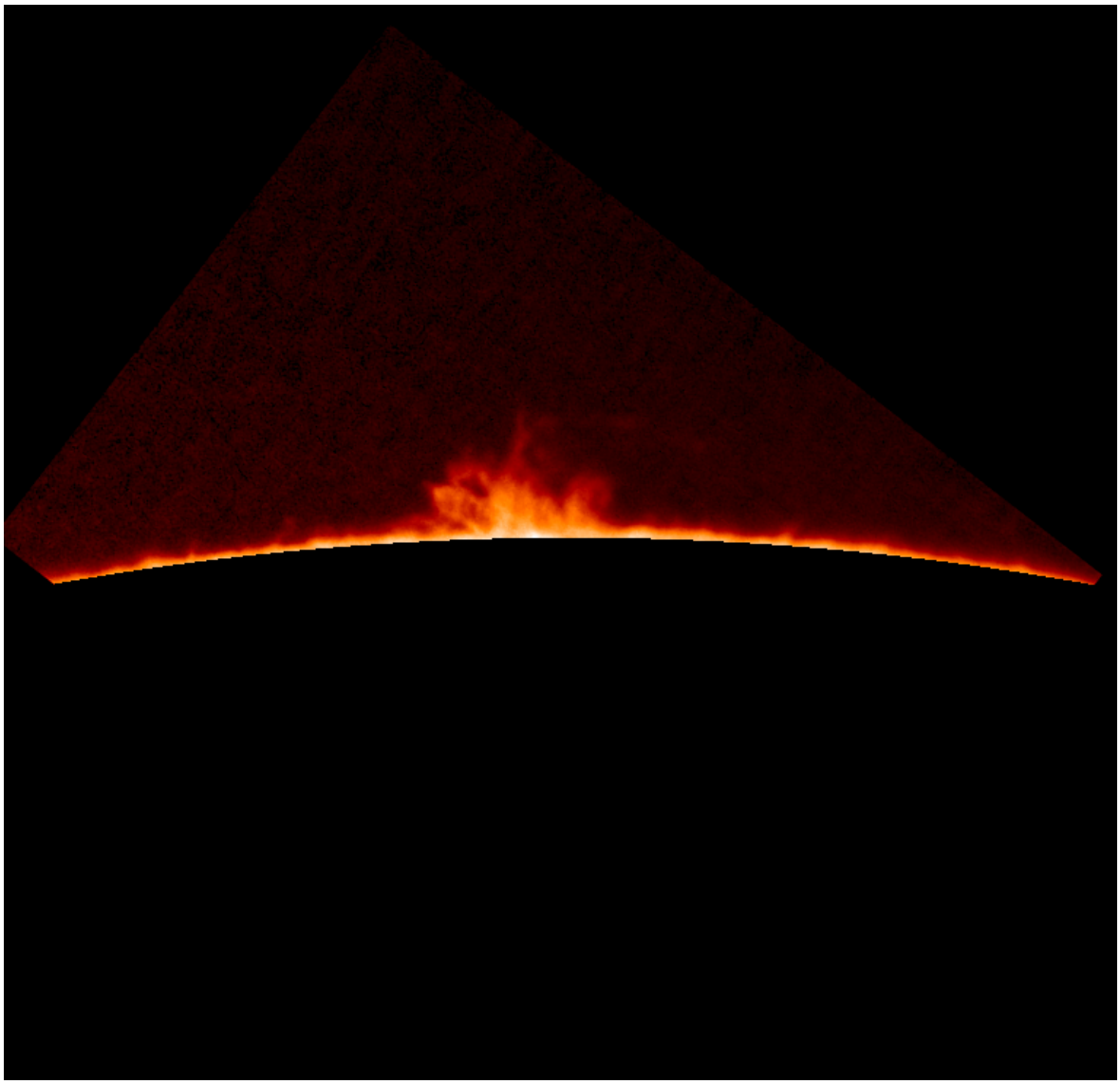

Figure 1.1: Example image of a prominence in Hα taken on the 19th of April 2018 using the MSDP instrument in Białków, Poland.

sinistral depends on whether the axial field moves to the right or left respectively in a helical pattern when viewed from the positive polarity side of the PIL. In Martin et al. (1994) it was found that the chirality of the channel of quiescent prominences is strongly linked to the hemisphere the channel is found in; with most dextral channels observed in the Northern Solar Hemisphere, and most sinistral channels found in the Southern Hemisphere.

The size and shape of prominences can vary wildly. This has led to a plethora of differing naming criteria, termed as a "zoo" in Engvold (2015), to describe the various morphologies. However, contemporary prominence observations are split into three broad categories: active

region, intermediate, and quiescent. Each of these names describes the nature of activity of the solar atmosphere surrounding the prominence, the dynamism of its material flows, its lifespan and the general extent of the prominence itself. There are also more complex prominence categorisations based on the orientation of the PIL where the filament channel is formed, defined in Mackay et al. (2008).

Active region prominences are formed in locations near to sunspots where events of magnetic activity occur at a higher frequency. Prominence bodies are generally composed of a long, thin *spine* with off shoots known as *barbs*. The spines of active region prominences are generally thin and straight when compared to other types of prominences. Active region prominences are also more likely to have small, or an absense of, barbs. Typical lengths of active region prominences are around 5–30 Mm, with widths of 0.35–0.65 Mm. Active region prominences are formed at significantly lower solar altitudes than intermediate, or quiescent prominences. They display an increased frequency of solar active events, including eruptions. The time scales between events is measured in hours, rather than the days/weeks between events for more stable prominences (Berger 2014; Engvold 2015).

In contrast, quiescent prominences are observed to be larger, long-lived stable structures. They are frequently formed at high solar latitudes ($\geq 50°$), which has sometimes led to the term *polar crown* prominences. They are the tallest form of prominence with altitudes reaching up to 50 Mm (Berger 2014). The lengths and widths of quiescent prominences range from 10–100 Mm, and 1–10 Mm respectively (Labrosse et al. 2010). Prominences observed at lower latitudes have a higher likelihood of occuring near to active regions, and thus being destabilised.

Intermediate prominences consist of the cases which exist between the other two groupings. They often occur near decaying active regions, and different parts of their morphology may resemble each of the other two prominence categories. The difference between the three types of prominences is more likely to be a difference in scaling and location with regards to solar activity, rather than any intrinsic difference in formation mechanism (Engvold 2015).

High resolution imaging of solar prominences shows that the large prominence structures are made up of collections of smaller fine structure elements (Lin et al. 2008). Using high resolution Hα observations from the *Swedish Solar Telescope* (SST), Lin et al. (2008) observed that the fine structures in the prominence barbs emerge from fine structure threads in the main prominence spine. The thickness of fine structure threads is observed to vary from a few arc seconds down to, and potentially below, the resolution limitations of current imaging

instruments ($\sim$ 0.15 arc seconds)(Engvold 2015).

The arrangement of the fine structures has deep implications on the interface region between the prominence and the surrounding corona. This interface region between the two drastically different plasma environments is referred to as the *prominence-to-corona transition region* (PCTR). The PCTR must cover the temperature and density gradients from the cool, dense prominence core to the extremely hot, sparse corona. Because of the difference in thermal conduction between gradients across and parallel to the magnetic field direction it is expected that the PCTR should have significantly less thickness perpendicular to the prominence axis (magnetic field), than along the prominence axis (Chiuderi & Chiuderi Drago 1991; Heinzel & Anzer 2001). The potential form for the structure of the PCTR was discussed in Pojoga (1994) who considered three different models commonly discussed in the literature. In these models the prominence and PCTR could either be formed of: individual cool cylindrical cores surrounded by hot sheaths of plasma; individual threads with their own, possibly constant, temperature structure; or individual cool cylindrical cores surrounded by warmer sheaths, with a globally hot surrounding envelope.

The prevailing theory for prominence formation and maintenance is that the cool plasma is contained in, and supported by, dipped nonpotential magnetic fields (Kippenhahn & Schlüter 1957), although there are competing theories for whether these are, or are not due to the weight of the prominence plasma (Mackay et al. 2010). Non-potential fields occur when there is a non-zero component of magnetic helicity, which is a measure of the twist in the magnetic field lines. Accepting the necessity for dipped magnetic fields, however, leaves two remaining questions; how the dipped magnetic fields are formed, and how the cool plasma is transported into them.

Mackay et al. (2010) gives a review of the many different models used to explain observations of, and simulate, the formation of the dipped magnetic field structure. In this review the authors categorise observational models of the configuration of the prominence magnetic field into groupings of surface motions which reconfigure existing coronal magnetic fields, and flux rope emergence. The authors summarise that both these mechanisms may be capable of forming prominences in different magnetic environments on the Sun. Theoretical models, however, are shown to have even more variety, and are broadly categorised into surface, and sub-surface models for filament formation. These models use different combinations of surface/sub-surface flows, magnetic reconnection, flux emergence, and flux cancellation/diffusion to yield the desired magnetic field for prominence formation (Mackay

2015).

With the prominence magnetic field formed, the remaining question is: where does the cool plasma come from? Because there is not enough plasma in the surrounding corona, it is understood that the plasma must be transported into the prominence from the lower atmosphere, i.e. the photosphere or chromosphere (Zirker et al. 1994). The three types of mechanism generally considered for the transport of plasma from the chromosphere into the corona are injection, levitation, and evaporation–condensation. Plasma injection models consider the possibility of cool plasma being forced upwards through flux tubes, usually through magnetic reconnection (Wang 1999). Levitation models, on the other hand, consider that the cool plasma is raised through the solar atmosphere by emerging and rising magnetic field lines (van Ballegooijen & Martens 1989; Rust & Kumar 1994). Finally, evaporation–condensation models consider a process of heating at the coronal loop foot points. This localized act causes an increase in density throughout the loop due to evaporation, and the need to maintain pressure balance. This density increase, however, will increase optically thin radiative losses. Thus by increasing the heating at the loop foot points it is possible to increase the radiative cooling at the midpoint (top) of the loop. This will lead to the dense, chromospheric temperature plasma observed in solar prominences (Antiochos & Klimchuk 1991). A review discussing the candidate mechanisms for prominence formation is given in Karpen (2015).

Quiescent prominences are observed to survive within the corona for long lifetimes whilst also displaying only modest flows of plasma. Thus, for the prominence to survive there is a necessity for a form of mechanical equilibrium. There is also a necessity for energy balance such that any cooling caused by radiative losses is balanced by various heating mechanisms (Gilbert 2015). Radiative losses here describe the difference between the energy of radiation emitted to absorbed.

There have been numerous publications where mechanical equilibrium and energy balance in solar prominences have been studied. However, these studies have frequently had issues maintaining both equilibria over all prominence scales, from the cool interior to the hotter PCTR. Poland & Anzer (1971) conducted an early attempt at modelling the energy balance in solar prominences. By considering isothermal slab prominence models these authors calculated radiative losses from hydrogen, whilst approximating them for Ca II. From these models they found that the thermal conduction was sufficient to balance their calculated and estimated radiative losses. These models, however, had drawbacks including

the requirement of a high density such that a strong 20 G magnetic field would be required to hold the prominence up against gravity, as well as not considering a PCTR or forms of heating mechanism other than thermal conduction.

In Heasley & Mihalas (1976), the authors achieved energy balance in a set of prominence models through the assumption of a radiative equilibrium; i.e. assuming that the radiative losses, and gains are balanced. This assumption, however, results in models with low central temperatures, and a lack of a PCTR (Anzer & Heinzel 1999). As radiative equilibrium means that there are no net radiative losses, if the temperature of the prominence is too low or high, there will be a requirement for either additional heating or cooling mechanisms.

In Chiuderi & Chiuderi Drago (1991) the importance of the direction of the thermal gradient of the PCTR with respect to the magnetic field vector is presented. It was found that increasing the angle between the magnetic field vector and the direction of the temperature gradient decreased the thickness of the PCTR. Fontenla et al. (1996) considered an energy balance between radiative losses and thermal conduction for isobaric, multi-thread prominence models with the inclusion of ambipolar diffusion. These models suggested the PCTR to be narrow to very narrow. However they did not consider either mechanical equilibrium or any potential heating mechanisms other than thermal conduction.

Anzer & Heinzel (1999) considered the energy balance in prominences using a set of 1D slab magneto-hydrostatic equilibrium models. Rather than prescribing any specific mechanism for the heating of their prominence models the authors used a generic heating function alongside the calculated heating from thermal conduction. Because of the low temperature gradients within the prominence core, the authors state that thermal conduction is negligible there, however, it plays a large role in the PCTR. The authors found that extra heating is required differently across the prominence to balance the local radiative losses minus the variations in thermal conduction. They postulated that if local energy balance is not achieved in parts of the prominence structure this could result in small scale plasma motions. In Anzer & Heinzel (2000) the authors tested whether mass inflows (as discussed in Poland & Mariska (1986)) could provide the local heating required by their models of Anzer & Heinzel (1999). In doing this they only considered the effect on the local energy balance of the cool prominence core as the PCTR was previously found to be fairly self-sustaining through thermal conduction (Anzer & Heinzel 1999). They found that their models with lower column masses could be sustained in energy equilibrium at a temperature of 8000K through heating from enthalpy inflow, whilst larger prominences would require significantly

lower central temperatures. An issue with this heating mechanism, however, is that these models would result in a continuous increase in prominence mass due to material building up in the centre of the prominence as there was no movement across the magnetic field lines. The authors postulated that to counter this, some form of diffusive flow across the magnetic field lines within the centre of the prominence must be present.

In Heinzel & Anzer (2012) energy balance was again considered from a radiative equilibrium standpoint to determine the radiative losses from Ca II in prominences. They found that in thick, dense prominence models, Ca II had a large effect on radiative losses. However, in thin or sparse models the effect is negligible. The radiative losses associated with the Mg II ion were addressed in Heinzel et al. (2014) for the first time. It was found that the effect on the central temperature was only important for low pressure models, with higher temperature models displaying less change.

Lingering questions in determining the energy balance in prominences are the temporal and spatial scales involved in prominence heating. Solar prominences can be heated through a myriad of different mechanisms including: thermal conduction; radiative heating; the dissipation of Alfvén and sound waves (Parenti & Vial 2007); enthalpy flux, describing convective heating from plasma inflows (Poland & Mariska 1986); and magnetic reconnection. It is likely that not any one of these mechanisms is solely responsible for maintaining the energy budget of solar prominences. The role that each mechanism plays may effect or be effected by the thermal structure of the PCTR. Better measurements of the fine temperature structure of prominences will therefore help to improve understanding into how equilibrium is successfully sustained for the long lifetimes of solar prominences (Gilbert 2015).

Despite the overall stability of quiescent prominences they can display dynamic plasma motions such as oscillations. Generally there are two types of prominence oscillations which are respectively defined as large, and small amplitude oscillations. Large amplitude oscillations are caused when the whole prominence is shaken, and can have amplitudes reaching $20\,\mathrm{km\,s^{-1}}$ or higher. These disturbances may be damped oscillations from the prominence equilibrium position caused by vibrations from solar flares. Moreton & Ramsey (1960) observed optically the propagating disturbance caused by a solar flare through the "activation" of distant filaments. If large amplitude oscillations cause significant doppler shift in a spectral line observation, this can cause a phenomena known as a "winking filament", where the filament will appear to disappear and reappear from view (Oliver & Ballester 2002; Ballester 2015).

Small amplitude observations conversely are generally local to discrete parts of the prominence, with amplitudes ranging from the background noise up to ~ 2–$3\,\mathrm{km\,s^{-1}}$. Individual groups of fine structure threads have been observed using high resolution Hα observations to oscillate independently from the rest of the prominence by Thompson & Schmieder (1991) using the MDSP in Meudon, and by Lin et al. (2007) using the SST. Lin et al. (2007) presented evidence for travelling waves along fine structure threads.

The life of a prominence will usually end with an eruption followed by its disappearance, or through the draining of the material back into the chromosphere. Prominence eruptions occur when the quasi-equilibrium maintaining the prominence structure breaks. During a prominence eruption, part or all of the prominence material leaves the Sun's atmosphere (Gopalswamy 2015). In Munro et al. (1979) the correlation between *coronal mass ejections* (CMEs) and prominence eruptions was considered using Skylab Hα observations. CMEs are highly energetic stellar phenomena consisting of large scale expulsions of plasma from the Sun into the solar wind where they are carried further out through the Heliosphere. In this study it was discovered that more than 70% of CMEs were associated with prominence eruptions, or filament disappearances. Gopalswamy et al. (2003) conducted a statistical study of prominence eruptions using an automatic detection mechanism for microwave data from the Nobeyama Radioheliograph (Shimojo et al. 2006). In this study they found that 72% of prominence eruptions had associated CMEs, with this number rising to 83% when considering only prominences where the dominant direction of the eruption was radially away from the solar surface. Prominences, and their need for delicate equilibria, therefore, play an important role in space weather, and in the cycle of solar activity as a whole.

1.2 Radiative Transfer

The theory of radiative transfer describes the interaction between light and the medium in which it travels through. This medium can add or subtract to the light at a given frequency through various processes of absorption, emission, and scattering of photons. When an observer measures the emergent intensity from an astrophysical object it is thus important to understand the internal radiative transfer processes within the emitting plasma to infer the conditions of the plasma. In this Section I shall cover the basic processes involved in radiative transfer with particular emphasis on those which will be important in later chapters. The content for this section has been predominantly sourced from Rutten (2003) and Labrosse

et al. (2010).

1.2.1 Radiative Processes

Atomic radiative processes are often grouped into three categories; bound–bound (bb) , bound–free (bf), and free–free (ff) processes. The name of each of these categories describes the state of the electron in the emission process. Atomic emission and absorption lines are both examples of bound–bound processes where the electron involved in the interaction is bound to an atom/ion before and after the interaction in question. Whilst free–free processes involve interactions where the electron is never bound to a specific atom/ion, and moves as a free electron in the plasma. Thus, bound–free interactions involve the cases when a bound electron becomes free from an atom/ion (ionization), or where a free electron is captured by an atom/ion (recombination).

Spectral lines are examples of discrete emission, as they occur at specific frequencies within the atomic spectrum corresponding to the energy between the atomic levels which the electron transitions. The width of each spectral line is defined by quantum mechanics, doppler effects, collisions, optical thickness effects, and others such as non-thermal broadening. Bound-free and free-free mechanisms are called continuum processes as they can produce a smoothly varying contribution across the whole spectrum. Unlike free-free processes, bound-free absorption has a frequency threshold. This threshold is defined by the energy of the incoming photon required to free the electron from its bound state. In the spectrum this is observed as a straight vertical edge to the smoothly varying continuum.

The emission from the Sun at millimetre wavelengths is dominated by free-free continuum processes, however, much of the energetic state of solar prominences, and other parts of the solar atmosphere, is driven by important interactions from spectral lines and ionization/recombination processes.

1.2.2 The Radiative Transfer Equation

When light travels along a given path through a medium its intensity can by enhanced by the medium (emission), or reduced by the medium (absorption). Emission and absorption can be caused by several different mechanisms. In bound–bound transitions these include: radiative excitation; spontaneous radiative de-excitation; induced radiative de-excitation; collisional excitation; and collisional de-excitation. Bound-free transitions include: collisional and

radiative recombination and ionization. Free-free transitions include: bremsstrahlung; and Rayleigh and Thompson scattering. Each of these processes within a plasma can be described by an emission and absorption coefficient. The emission and absorption coefficients can be defined: per particle; per path length; per gram; or per volume. Throughout my work I have consistently considered the linear absorption coefficient defined as the number of absorptions at a given frequency per unit path length in units of cm^{-1}. The units of the emission coefficient are: $\mathrm{erg\,cm^{-3}\,s^{-1}\,Hz^{-1}sr^{-1}}$. The monochromatic source function, S_ν^i, for a given process, i, is defined as the ratio of emission in a medium to absorption:

$$S_\nu^i = \frac{j_\nu^i}{\kappa_\nu^i}, \tag{1.1}$$

where j_ν^i, and κ_ν^i are the monochromatic emission and absorption coefficients respectively. The units for the source function are thus the same as those for intensity in cgs units as: $\mathrm{erg\,cm^{-2}\,s^{-1}\,Hz^{-1}sr^{-1}}$. When multiple processes are emitting/absorbing photons, the total source function is defined by the sums of the emission and absorption coefficients:

$$S_\nu^{\mathrm{TOT}} = \frac{\sum_i j_\nu^i}{\sum_i \kappa_\nu^i}. \tag{1.2}$$

The source function for emission from a given atomic line transition of level j to i is dependent on the energy level populations, and the transition rates between them as follows:

$$S_{\nu,i} = \frac{n_j A_{ji} \psi(\nu - \nu_0)}{n_i B_{ij} \phi(\nu - \nu_0) - n_j B_{ji} \chi(\nu - \nu_0)}, \tag{1.3}$$

where n is the population density of each energy level; A_{ji} is the transition rate for spontaneous emission; whilst B_{ji} and B_{ij} are the transition rates from stimulated emission and absorption respectively. ψ, ϕ, and χ are the profiles for each process. When considering *complete redistribution* in frequency (CRD) these profiles are said to be equal to one another such that in the scattering process the scattered photon can be redistributed to any given frequency within the line, irrespective of the frequency of the incident photon. Whilst if the absorbed radiation is re-emitted at exactly the same frequency this process is known as *coherent scattering*. When neither CRD or coherent scattering are applicable for a given spectral line an intermediate process known as *partial redistribution* in frequency (PRD) must be considered. In PRD there will be a range of different frequencies that the scattered photon can have, however, unlike CRD the frequency of the incoming photon will effect this process. It has been found for some important lines in prominences, e.g. for Lyman α (Paletou et al. 1993) and Mg II h, and k (Heinzel et al. 2014), that PRD effects are important, and that PRD must then be considered in forward modelling of these lines.

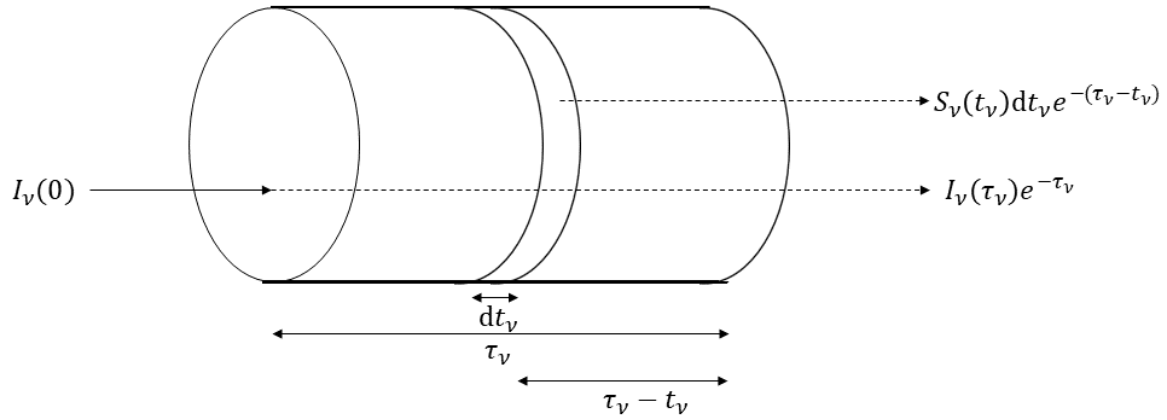

Figure 1.2: Diagram depicting how the radiative transfer equation (Equation 1.8) affects the intensity of radiation travelling through a medium of optical thickness, τ_ν, and source function, S_ν.

With these definitions made, the radiative transfer equation describes the change of the intensity of light at a given frequency along a path, s, as:

$$\frac{\mathrm{d}I_\nu}{\mathrm{d}s} = j_\nu - \kappa_\nu I_\nu, \tag{1.4}$$

which roughly states that the change in intensity is equal to the amount of emission minus the incident intensity, I_ν, multiplied by the absorption coefficient. Rearranging this equation gives the change in intensity in terms of the source function:

$$\frac{\mathrm{d}I_\nu}{\mathrm{d}\tau_\nu} = S_\nu - I_\nu, \tag{1.5}$$

where $\mathrm{d}\tau_\nu$ is the incremental optical path length, defined as:

$$\mathrm{d}\tau_\nu = \kappa_\nu \mathrm{d}s. \tag{1.6}$$

The optical thickness is defined as the integral of this quantity over the entire line of sight (LOS) of total length, L, e.g.:

$$\tau_\nu = \int_0^L \kappa_\nu \mathrm{d}s. \tag{1.7}$$

Multiplying the radiative transfer equation (Equation 1.5) by a factor of e^{τ_ν}, and integrating over optical thickness leads to the formal solution of the radiative transfer equation:

$$I_\nu(L) = I_\nu(0)e^{-(\tau_\nu(L) - \tau_\nu(0))} + \int_{\tau_\nu(0)}^{\tau_\nu(L)} S_\nu(t_\nu)e^{-(\tau_\nu(L) - t_\nu)}\mathrm{d}t_\nu. \tag{1.8}$$

For a homogeneous LOS, i.e. such that S_ν is constant across it, this equation simplifies to:

$$I_\nu(L) = I_\nu(0)e^{-\tau_\nu} + S_\nu(1 - e^{-\tau_\nu}), \tag{1.9}$$

where τ_ν is used as the total optical thickness of the LOS (i.e. $\tau_\nu(L)$), whilst the optical thickness at the start of the LOS is set to 0. A diagram displaying how the radiative transfer equation, Equation 1.8, describes the change in the emitted intensity from light travelling through a medium of optical thickness τ_ν is given in Figure 1.2.

1.2.2.1 The Eddington-Barbier Approximation

The Eddington-Barbier approximation states that: when considering a path normal to a given surface, the emergent intensity is approximately equal to the source function where the optical depth equals 1. The optical depth here is defined as the optical thickness when considered zero at the surface where the emission emerges from. When the optical thickness is < 1 the material is said to be optically thin, and thus mostly transparent to the radiation travelling through it. For plasma to be optically thick requires $\tau > 1$, such that it is mostly opaque to the radiation travelling through it. $\tau = 1$ is thus the transition between optically thin, and optically thick material. The Eddington-Barbier approximation can be found by considering a stellar atmosphere, whilst considering a plausible expansion for the source function in terms of the optical thickness. The emergent intensity from a stellar atmosphere can be expressed as follows:

$$I_\nu(\tau_\nu = 0) = \int_0^\infty S_\nu(t_\nu)e^{-t_\nu}\mathrm{d}t_\nu.$$

If an expansion for the source function in terms of the optical thickness is used, in the form:

$$S_\nu(t_\nu) = \sum_0^\infty a_n\tau_\nu^n = a_0 + a_1\tau_\nu + \cdots + a_n\tau_\nu^n,$$

the standard integral $\int_0^\infty x^n e^{-x}\mathrm{d}x = n!$ may be utilised. When doing this the emergent intensity is described by the expression:

$$I_\nu(\tau_\nu = 0) = a_0 + a_1 + \cdots + n!a_n.$$

The Eddington-Barbier approximation is then found by considering the first two terms of each expansion, solely. Comparing these two expressions results in the following expression:

$$I_\nu(\tau_\nu = 0) \approx S_\nu(\tau = 1), \tag{1.10}$$

as expected.

1.2.3 Local Thermodynamic Equilibrium Radiative Transfer

A plasma in local thermodynamic equilibrium (LTE) is such that the energy partitioning of the ionization degree and atomic energy levels are defined by Saha-Boltzmann statistics using the local plasma temperature. The Boltzmann equation describing the energy level partitioning in LTE is defined by:

$$\left[\frac{n_{m,j}}{n_{m,i}}\right]_{\mathrm{LTE}} = \frac{g_{m,j}}{g_{m,i}} e^{-(\chi_{m,j}-\chi_{m,i})/k_B T}, \tag{1.11}$$

where n is the number density in the energy level i or j of ionization stage m. Whilst similarly g is the statistical weight of each level, and χ is the excitation energy of each level relative to the respective ground state for the ionization stage. The difference in excitation energy, $\chi_{m,j} - \chi_{m,i}$, is the energy of a photon, $h\nu$, emitted from atomic transition from stage j to i. k_B is the Boltzmann constant, as usual.

The Saha-Boltzmann distribution similarly describes the partitioning between a given energy state relative to an upper ionization stage as follows:

$$\left[\frac{n_{m+1,1}}{n_{m,i}}\right]_{\mathrm{LTE}} = \frac{1}{n_e} \frac{2g_{m+1,1}}{g_{m,i}} \left(\frac{2\pi m_e k_B T}{h^2}\right)^{3/2} e^{-\chi_{ionization}/k_B T}, \tag{1.12}$$

where n_e and m_e are the electron density and mass, respectively. $\chi_{ionization}$ is the ionization energy from energy level i in ionization stage m to the ground level of ionization stage $m+1$.

When Saha-Boltzmann statistics are applicable, the source function for the plasma may be described by the Planck function, B_ν:

$$S_{\nu,\mathrm{LTE}} = B_\nu \equiv \frac{2h\nu^3}{c^2} \frac{1}{e^{h\nu/k_\mathrm{B}T} - 1}, \tag{1.13}$$

where h and c are the Planck and speed of light in vacuum constants, respectively.

1.2.3.1 Radiative Transfer in the Millimetre/sub-millimetre Regime

At millimetre/sub-millimetre wavelengths the Sun's radiation is dominated by the free-free thermal continuum (Wedemeyer et al. 2016). Free-free processes are fully collisional so the continuum radiation is thus formed under the local thermodynamic equilibrium (LTE) conditions described in the previous section. The corresponding source function is therefore given by the Planck function. Using the Rayleigh-Jeans Law the millimetre-continuum source function S_ν^{RJ} is thus:

$$S_\nu^{\mathrm{RJ}} = \frac{2\nu^2 k_\mathrm{B} T}{c^2}\,. \tag{1.14}$$

The continuum specific intensity, I_ν, emitted in LTE over a given optical path length at frequency ν is described by:

$$I_\nu = \int S_\nu e^{-\tau_\nu} d\tau_\nu = \int \kappa_\nu S_\nu e^{-\tau_\nu} ds \,, \tag{1.15}$$

which in the Rayleigh-Jeans limit simplifies to:

$$I_\nu^{\mathrm{RJ}} = \frac{2\nu^2 k_\mathrm{B} T_\mathrm{B}}{c^2} \,. \tag{1.16}$$

Here T_B is the brightness temperature, *i.e.* the temperature a black body would have if it were to emit with the intensity, I_ν^{RJ}. Through simple comparison between Equations 1.14, 1.15 and 1.16 an expression for the observable brightness temperature in terms of the kinetic temperature (usually taken as the electron temperature), the local absorption coefficient, and the optical thickness can be derived as:

$$T_\mathrm{B}(\nu) = \int \kappa_\nu T e^{-\tau_\nu} ds \,. \tag{1.17}$$

From a known kinetic temperature, and by calculating the position- and wavelength-dependent absorption coefficient across a LOS, it is possible to model what the emergent brightness temperature distribution should look like. In the case where T is constant across the LOS, Equation 1.17 simplifies to;

$$T_\mathrm{B} = T(1 - e^{-\tau_\nu}). \tag{1.18}$$

It can be found that for a very optically thick plasma, $\tau \gg 1$, this equation reduces to $T_\mathrm{B} = T$, and $T_\mathrm{B} = T\tau$ for a very optically thin plasma, $\tau \ll 1$.

1.2.4 Non-Local Thermodynamic Radiative Transfer and Statistical Equilibrium

Much of the plasmas in the solar atmosphere, including those under conditions found in solar prominences, have atomic populations which differ from the simple case described by LTE. LTE holds when the source function is dominated by collisions and the frequency- and angle-averaged radiation field, which is an important factor in the statistical equilibrium equations, is Planckian. In prominences, the radiation field will be strongly effected by the presence of high intensity, energetic incident radiation from the solar disk. The radiation field will thus dominate the global energy budget of prominences through radiative losses/gains, whilst it will also dominate over collisional ionization in the determination of the ionization state of the plasma as prominences have generally sufficiently low densities. Any change

in the ionization will modify the interaction between pressure, density and temperature through the equation of state.

In these cases, Equations 1.11, and 1.12 no longer hold. This results in the necessity for the atomic energy level populations and ionization degree to be calculated using the equations of statistical equilibrium. Therefore, even though the source function for the millimetre-continuum is Planckian, due to being formed from collisional processes, the ionization degree, and energy level partitioning may be defined by non-LTE processes in the prominence plasma.

The implied assumption in statistical equilibrium is that the level populations, and radiation field do not vary with time, such that the rate of change of any given energy level, n_i, may be described as:

$$\frac{\mathrm{d}n_i}{\mathrm{d}t} = \sum_{j \neq i}^{N} n_j P_{ji} - n_i \sum_{j \neq i}^{N} P_{ij} = 0, \tag{1.19}$$

where P_{ij} and P_{ji} are the rates of transitions from energy level i to another j; and from j to i, respectively. N is the total number of energy levels with important transitions to level i. Equation 1.19 states that the population of state i is constant with the transitions out of it balanced with transitions into it. Inflow or outflow of material can cause statistical equilibrium to not be met. In these cases, the populations become time-dependent and particle conservation must then be met rather than population conservation.

The rates of each transition will have both radiative and collisional components, such that:

$$P_{ij} = R_{ij} + C_{ij} \tag{1.20}$$

where R_{ij} is the radiative transition rate from state i to j, and C_{ij} is the collisional transition rate, similarly. Each radiative transition rate, R_{ij}, will be dependent on the radiation field. The radiation field, however, will vary with the radiative transfer equation through Equation 1.4, and as the radiative transfer requires knowledge of the energy level populations, through the source function (Equation 1.3), there is thus no simple solution to this set of equations, as many different transitions can effect the overall radiative transfer. Therefore, to find any solution these equations need to be solved iteratively using complex numerical codes. A background of non-LTE radiative transfer modelling in solar prominences is given in Section 1.2.5, whilst a description of the particular C2D2E code used throughout my PhD work is given in Section 2.2 of Chapter 2.

1.2.5 Numerical Models for Radiative Transfer in Solar Prominences

Severe complications are presented when trying to directly invert physical properties from spectral observations of solar prominences. For some plasmas it is possible to infer parameters such as the temperature directly from measuring spectral properties such as line widths, or ratios of intensities from optically thin plasmas. These relationships are less clear in plasmas like solar prominences due to the lack of local thermodynamic equilibrium (non-LTE) causing the atomic level populations of the plasma species within the prominence to become non-linearly coupled to the background radiation field. A discussion into non-LTE radiative transfer is given in Section 1.2.4. A spectroscopic analysis of the physical parameters within a prominence requires non-LTE forward modelling simulations. These simulations, when used in conjunction with spectral measurements, can improve our understanding of the structures being observed (Labrosse et al. 2010). This section gives an account of the history and advances made into non-LTE forward modelling of solar prominences.

Early prominence observations were restricted by low spatial and temporal resolutions. Therefore, when modelling attempts were made simple 1D models more than sufficed (Heasley & Mihalas 1976). 1D models obviously have limitations when used in comparison with fully resolved 3D objects, however despite their limitations, 1D models have provided great insights and improvements into the physics and modelling of radiation transfer. An example of the insight gleaned from 1D modelling is the understanding of the influence of *partial frequency redistribution* (PRD), when compared with *complete frequency redistribution* (CRD), on the hydrogen Lyman spectral lines (Heinzel & Vial 1983). The differences between these two situations is discussed in Section 1.2.2. Comparisons with observations showed that 1D PRD models were more successful at reproducing the observed line profiles (Heinzel et al. 1987).

A large modelling effort was conducted by Gouttebroze et al. (1993) (GHV) who used an extensive set of plane-parallel, static, isothermal and isobaric 1D models to create a catalog of various prominence spectral parameters. This was the first study to use incident intensity profiles for the spectral lines, with previous works considering uniform incident intensities only. The simulated line profiles and parameters were extremely useful in comparison with prominence observations, as well as for the derivation of correlations between parameters (e.g. the relation between Hα line intensity with the emission measure (Heinzel et al. 1994), which is discussed further in Section 3.3). Although the results from this study were unlikely to correspond to a realistic representation of the far more complex prominence, GHV

succeeded in calculating general and approximate relations between physical conditions and observables.

Isobaric-isothermal models, however useful, did possess some drawbacks. For example they could not replicate the observed intensity relations between Lyα and Lyβ intensities, with simulated Lyβ intensity being systematically lower than the observations (Heinzel et al. 1987). Suggested explanations to solve this inconsistency between simulations and observations included the presence of prominence *fine structure*, i.e. an underlying structure usually considered as thin threads, and the existence of a *prominence-to-corona transition region* (PCTR). The structure of the PCTR is described by the pressure, temperature and density distributions between the prominence core, and the surrounding corona. Both these concepts are widely accepted and are backed with substantial evidence. For example recent high spatial resolution observations of prominences repeatedly show the presence of fine-structure threads (Lin et al. 2008; Berger 2014). The concept of a PCTR successfully explains the observations of two different classes of observed line profiles as the effects caused by the orientation of the line of sight with respect to the axis of the observed thread, and the magnetic field (Chiuderi & Chiuderi Drago 1991; Heinzel et al. 2001b; Heinzel & Anzer 2001).

Observations show prominences as complex structures with varying internal features such as differing temperature and pressure gradients depending on the line of sight. To understand fully how these effects alter the observations seen there came a requirement to consider how each part of the prominence as a whole effected the overall radiative transfer, i.e. the requirement for 2D or 3D models. 2D prominence modelling is conducted by fully considering two of the three directions whilst assuming the third to be infinite; e.g. considering (x,y) in Cartesian space, or (r,ψ) in cylindrical space whilst both assuming an infinite z direction. An early attempt at modelling non-LTE radiative transfer in 2D was undertaken by Mihalas et al. (1978). These models were, however, limited as they were designed only to consider CRD and the two-level atom approximation. Auer & Paletou (1994) developed codes that could calculate non-LTE radiative transfer including PRD using the *accelerated lambda iteration* (ALI) method. Auer et al. (1994) produced a 2D multi-level non-LTE radiative transfer code, rather than the simplified 2-level atom case, using a method based on the Multilevel Accelerated Lambda Iteration (MALI) presented in 1D by Rybicki & Hummer (1991) and Rybicki & Hummer (1992).

All the 2D models described so far consider a rectangular plane-parallel prominence

slab orientated either horizontally or vertically in the solar atmosphere. In these cases the radiation from the solar disk is incident on the lower boundary and sides of the rectangular slab; with no external incident radiation illuminating the top boundary. To attempt to improve this by simulating a prominence with a non-homogeneous incident radiation, Gouttebroze (2004) modelled a 2D cylindrical prominence orientated vertically in the solar atmosphere. This model was expanded in a series of papers (Gouttebroze 2005, 2006, 2007, 2008; Gouttebroze & Labrosse 2009; Labrosse & Rodger 2016) to consider: higher level hydrogen and helium atoms; 3D velocity fields; and multi-thread models, amongst other aspects of radiative transfer. Cylindrical models have successfully investigated the effects of various prominence parameters such as temperature, pressure and helium abundance ratio in both isothermal and non-isothermal cases. These computer codes are the basis of the forward modelling presented in this thesis, and as such they are discussed in more detail in Section 2.2.

As mentioned previously, observations of prominences with high spatial resolution show large numbers of fine thread-like structures. This leads to the idea that it may be more prudent to model prominences, not as a singular large rectangular slab or cylinder, but as a collection of fine-threads. There have been several different attempts at such multi-thread modelling. Gunár et al. (2007) investigated the hydrogen Lyman emission from an arbitrary number of threads using a set of 2D Cartesian slab models configured to represent a series of threads in the LOS, each of their threads considered had a separate PCTR. The authors compared their synthetic spectra with observations from the SUMER instrument aboard SOHO to find that prominence fine structures are better simulated by a multiple thread model, than a singular thread case. In Gunár et al. (2008) the authors expand on their previous work to include randomly generated motions between threads in the LOS. These results were again compared with hydrogen Lyman observations from SUMER to conclude that asymmetric line profiles, as observed, can be reproduced using LOS velocities between threads in the LOS, in a multi-thread model. A multi-thread system of 2D cylindrical threads considering both hydrogen and helium was successfully simulated by Labrosse & Rodger (2016). In doing this the importance of multi-thread modelling was again verified not only in the effects present in asymmetric line profiles, but also in the effects on spatial intensity variation across the field of view.

Advancements in instrumentation lead to continuing improvements in the spatial, temporal and spectral resolution of solar prominence observations in various regions of the solar

spectrum. The new opportunities presented by these instruments create the necessity for further modelling efforts. IRIS, or the *Interface Region Imaging Spectrograph*, is a space-based mission which provides simultaneous spectra and imaging throughout the solar atmosphere (De Pontieu et al. 2014). Some important spectral lines in which IRIS can observe are the chromospheric Mg II h and k lines as well as the transition region C II 1334/1335 Å and Si IV 1394/1403 Å lines. These lines have complex formation mechanisms and contain a lot of information about the surrounding plasma. To be able to analyse well the information from spectral lines it is desirable to have numerical models that help to understand the formation of the lines and how this affects the line's profiles and intensities.

Most of the research undertaken so far has looked into the Mg II h & k lines, which have been successfully forward modelled for the chromosphere in a series of papers (Leenaarts et al. 2013a,b; Pereira et al. 2013); considering the diagnostic potential of the line whilst also taking into account the finite instrumental limitations of IRIS. These models compromise by using 1D PRD computations to model the line profile up to and including the emission peaks; whilst using 3D transfer with CRD to model the central depression. Work into modelling 1D atmospheres considering C II and Si IV as well as Mg II h & k lines has been conducted by Avrett et al. (2013).

Mg II h & k lines have been modelled in the specific case of solar prominences by Heinzel et al. (2014). This was done using a 1D isobaric slab model considering various temperature structures: isothermal, PCTR models, and models that are consistent with radiative equilibrium. The study provided early results that can be used for diagnostic tools in IRIS observations. However, due to the 1D simplification many effects, such as are caused by fine structure, remain unknown. Levens & Labrosse (2019) presented a further use of 1D models for modelling the Mg II h & k lines over a large grid of parameters considering both isothermal–isobaric models, as well as multi-thermal PCTR models.

1.3 Centimetre–Millimetre Observations of Solar Prominences

In the previous sections of this introduction I have discussed how the physical parameters of the prominence plasma have been evaluated through spectral line analysis (Labrosse et al. 2010; Parenti 2014; Labrosse 2015). Analyzing the shape and intensity of spectral lines can, however, be difficult due to the complex mechanisms in which the lines and continua are formed, especially at optical or UV wavelengths. As discussed in Section 1.2.4, non-LTE

plasmas do not have a straight-forward relationships between the observed emission and the parameters of the plasma itself, and thus require large numerical codes for a solution to the radiative transfer to be found. Lines from an optically thick plasma may also be subject to further complications, such as non-Gaussian broadening making it difficult to discern the temperature, as the underlying thermal broadening profile could be masked. Line of sight (LOS) effects may also play significant effects on the shape of line profiles as emission at any wavelength where the plasma is optically thin will be the product of an integration across all material in the LOS; thus any information on the temperature etc of a specific region of the structure will be lost (Gunár et al. 2008; Labrosse & Rodger 2016). This is particularly problematic for fine-structure observations due to their limited physical extent, such that multiple fine structure threads could contribute to the observed line profile. Complex line profiles can also occur due to multiple structures within the LOS moving with respect to each other (Gunár et al. 2008; Labrosse & Rodger 2016). Much of these issues may be addressed by observations of the millimetre-continuum, as they should be able to provide a more direct measurement of the plasma's internal parameters (see Section 1.2.3.1).

The quiet solar chromosphere emits millimeter/sub-millimeter radiation in the Rayleigh-Jeans limit predominantly through thermal bremsstrahlung, which is a local thermodynamic equilibrium (LTE) emission mechanism. This will cause the measured brightness temperature to be dependent on the temperature where the radiation is formed, with optically thick material emitting at a brightness temperature representative of the electron temperature of the plasma (Wedemeyer et al. 2016; Rodger & Labrosse 2017). In the chromosphere this will mean that the contribution function will peak at a specific temperature/height within the solar atmosphere. In Loukitcheva et al. (2015) the authors conclude, for chromospheric radiation, that millimetre brightness provides a reasonable measure of the thermal structure, up to resolutions of 1″. In the context of solar flare models, Heinzel & Avrett (2012) synthesized the thermal continua from the optical to the millimeter, demonstrating how these continua are formed, and again showing the close correspondence between brightness temperature and the kinetic temperature. Despite these advantages, however, observations of solar prominences using the millimetre-continuum have so far been hampered by low spatial resolutions.

Vrsnak et al. (1992) presented an analysis of a large number of observations of the solar disk using wavelengths between 4 and 26 mm. The resolution of these maps was limited, with a beam size of 2.4′ reported for observations at 8 mm. The authors looked at the correlation

between so called "low temperature regions" (LTRs) observed in the millimetre-continuum maps with the various structures observed on the solar disk, including solar filaments. However, they did not find an obvious relationship between LTRs and solar filaments. While 60% of LTRs were associated with filaments many filaments did not present a discernible temperature reduction in the millimetre-continuum maps.

A study of prominences at 1mm was conducted by Bastian et al. (1993) using the Caltech submillimeter observatory. The resolution of the maps they used was 20″.6, and 30″ for observations at 0.85mm, and 1.25mm respectively. They found that Hα filaments when observed at 0.85mm presented a low contrast to the background solar atmosphere, with brightnesses comparable to, or below that of the disk centre. This led to them suggesting that the filaments were optically thin at 0.85mm. They supported this argument using an off-limb observation of a prominence which they estimated the optical thickness for as $\tau \approx 0.12$.

Harrison et al. (1993) presented the observation of a prominence using the James Clerk Maxwell Telescope at a wavelength of 1.3mm. This observation caught an exceptionally large prominence which exceeded 75Mm in height above the solar limb, however Hα images on the next day displayed no prominence suggesting that it had erupted. The large size of this prominence allowed for a good observation despite the diffraction limited resolution of the JCMT at 21″.

Simultaneous measurements of an eruptive prominence at multiple millimetre wavelengths have been presented for the first time in Irimajiri et al. (1995). The observing wavelengths were 2.7mm (110GHz), 3.4mm (89GHz), and 8.3mm (36GHz), with spatial resolutions of 46″, 19″, and 15″ respectively. Using the multiple frequency observations, the authors measured the spectral index for the prominence, and thus its optical thickness in each observing band. It was found that the prominence was neither truly optically thick or thin across the observing range. The largest opacity observed was estimated to be 5.8 for the 8.3mm emission.

There has also been a long history of prominences being observed at centimetre wavelengths. A review of observations of erupting filaments using radio, and X-ray observations is given by Gopalswamy et al. (1998). Chiuderi Drago et al. (2001) presented a joint observation of a solar filament with both EUV from CDS, and SUMER on board the spacecraft SOHO, as well as microwave observations from the VLA, and the Nobeyama Radioheliograph. The authors found that these observations supported a prominence model which is composed of cool threads, each with a "sheath-like" PCTR around them, embedded in a hot coronal

plasma envelope.

A common factor in each of these studies is the low resolution available to the millimetre continuum observations, with the smallest in this set being measured at 15″ being measured for 2.7mm emission by Irimajiri et al. (1995). Finer resolution imaging of the solar filaments at centimetre wavelengths has been performed using aperture synthesis with instruments such as the Very Large Array (VLA). Filament observations using the VLA include Kundu et al. (1986) at 1.5 and 5 GHz and Gary et al. (1990) at near 8.5 GHz. Both these observations found brightness temperature depressions around filament cavities which were wider than any corresponding Hα filament counterpart, attributing this difference to the presence of a coronal cavity. These aperture synthesis observations, however, still did not produce resolutions capable of observing prominence fine structures, which are known to be found down to sub-arcsecond resolution (Engvold 2015). A potential answer to this problem is the advent of the *Atacama Large Millimeter / Submillimeter Array* (ALMA) (Wootten & Thompson 2009; Hills et al. 2010; Karlický et al. 2011), which has begun offering solar observations with unprecedented high spatial resolution of the millimetre-continuum. Using science verification data, Shimojo et al. (2017a) quote the resolution of a 3mm map at $4.9'' \times 2.2''$ which is significantly better than those quoted above, despite the observation being carried out in a reduced array configuration than would be typically available during a full observing cycle. Wedemeyer et al. (2016) presents a view of the potential for solar science using ALMA.

A study was conducted by Heinzel et al. (2015a) in which the appearance of a prominence, as if viewed through ALMA was simulated. This was done by taking an Hα coronagraphic image and, using the empirical relation between Hα intensity and emission measure, estimating the brightness temperature for such a plasma. These brightness temperatures were used with the *Common Astronomy Software Applications* (CASA) package to simulate ALMA observations. However, assumptions were required including the use of a simple temperature structure for the prominence, whilst the simulated ALMA observations were restricted by the resolution of the instrument used to create the original Hα observation.

The emission from solar prominences in the millimetre regime has been presented by Gunár et al. (2016),Gunár et al. (2018) and Rodger & Labrosse (2017). Gunár et al. (2016) and Gunár et al. (2018) use a 3D fine-structure model constructed from a dipped magnetic field configuration created by a non-linear force-free field simulation. Rodger & Labrosse (2017) on the other hand consider a 2D cylindrical model consisting of both hydrogen and helium. The results from Gunár et al. (2016) and Gunár et al. (2018) are discussed in detail in

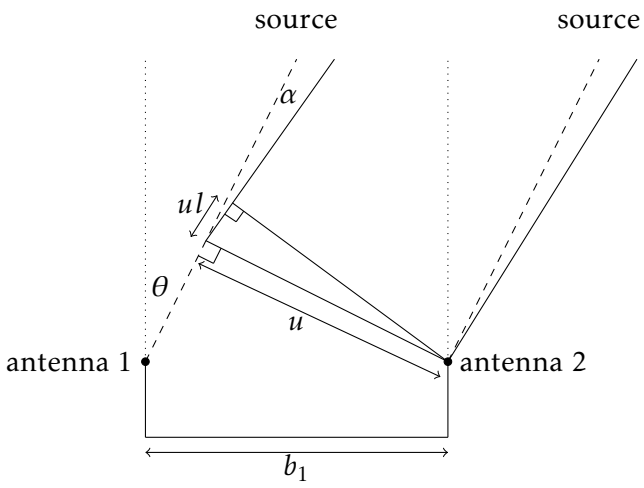

Figure 1.3: Schematic diagram of a 1D interferometer. Adapted from a similar schematic in Warmels et al. (2018).

Section 2.1; whilst I cover the details and results from Rodger & Labrosse (2017) throughout Chapter 2.

The first observation of a prominence using high resolution interferometric ALMA imaging was obtained on the 19th of April 2018 which I cover in Chapter 5.

1.4 Basics of Radio Interferometry

The fundamental theory behind interferometry is that, through combining signal from multiple physically separated apertures it is possible to produce measurements with higher spatial resolution than is possible using any given aperture on their own. The first forays into optical interferometry were conducted by Michelson (1920), and later Michelson & Pease (1921), who managed to manufacture a suitable angular resolution to measure the diameter of large stars such as Betelgeuse. It was not long, however, until these tenets were transferred to the field of radio astronomy with Ryle & Vonberg (1946) constructing the first two-element radio interferometer to observe cosmic radio emission. In this section the sources which I have used are predominantly Cornwell (2008), Thompson et al. (2017) and Warmels et al. (2018).

Radio astronomy using single dish antennas suffers from diffraction limited spatial resolution, as the finest resolvable angular resolution is $\sim \lambda/D$, where D is the diameter of

the aperture; such that at long wavelengths, very large diameter dishes are required, yet still cannot match the same resolution as achievable with optical telescopes. A method commonly used to avoid this issue is radio interferometry, commonly known as *aperture synthesis*. Through the use of multiple, spatially separated antenna, this method can achieve an angular resolution which would otherwise need a much larger diameter aperture. Aperture synthesis is based on the fact that the voltage, and thus power and intensity observed using a radio antenna with a filled aperture can be expressed as the sum of N pairs of voltage elements across the dish. Because of this, as long as each element is in phase with each other, there is no necessity for the elements to be located next to one another, and thus the correlated voltages from two physically separated antennas may be used to simulate a measurement of a larger aperture single antenna.

In a radio interferometer the physical separation between two antennas is referred to as their baseline, b, which is usually defined in units of the observing wavelength λ. If both antennas observe the same source with an angle θ from the normal, the separation of the two antennas in the frame of the source is defined as:

$$u = b_1 \cos\theta, \tag{1.21}$$

where b_1 is the component of the baseline vector in the same direction as u. If the antenna moves slightly off this axis by an angle of α, the change in the path length would then be equal to $u\sin\alpha$; or ul, where $l = \sin\alpha$. The u projection is generally defined in the East–West direction. A schematic of the 1D case is shown in Figure 1.3. When adding in the second dimension, another projection v is thus defined similarly as:

$$v = b_2 \cos\psi, \tag{1.22}$$

where the ψ angle is oriented orthogonally to θ. Similarly any small change in angle, β, will result in a change to the path length of $v\sin\beta$; or vm, where $m = \sin\beta$. The v projection is defined in the North–South Direction. With these definitions, the voltage from one antenna, V_2, can be given in terms of the other, V_1, with a complex delay factor as follows:

$$V_2 = V_1 e^{2\pi i(ul+vm)}. \tag{1.23}$$

The interferometer's correlator is a device which multiplies and time-averages the signals from the array's antennas. With the assumption that the signal from different parts of the sky is incoherent, i.e. there is no intrinsic similarity in phase such that the time average of

the correlations of the signals should equal zero, the output of the correlator will vary as:

$$\langle V_1 V_2^* \rangle = \int \int \langle V_1(l,m) V_2(l,m) \rangle \mathrm{d}l \mathrm{d}m. \tag{1.24}$$

Substituting using Equation 1.23, and remembering that $I \propto P \propto V^2$, the output of the correlator describes:

$$\langle V_1 V_2^* \rangle \propto \int \int I(l,m) e^{2\pi i(ul+vm)} \mathrm{d}l \mathrm{d}m = \mathcal{V}(u,v), \tag{1.25}$$

where $\mathcal{V}(u,v)$ is called the *complex visibility*, and is the Fourier-transform of the intensity distribution across the sky. Interferometric images are thus produced by measuring complex visibilities, and performing inverse Fourier-transforms to return a synthesised intensity image of the sky.

This is, however, an idealised case and in a real interferometer it is impossible to perfectly sample the complex visibility function, as the measurements can be noisy and are found at discrete locations within the u-v plane (Cornwell 2008). The measured visibilities will therefore be the product of the true complex visibility and some sampling function, $S(u,v)$. Taking a simple inverse fourier transform of the measured complex visibility from a real interferometer produces what is known as a "Dirty Image", I^D, i.e.:

$$I^D = \mathcal{F}^{-1}\{S\mathcal{V}\}. \tag{1.26}$$

The convolution theorem states that for two functions, f and g:

$$f * g = \mathcal{F}^{-1}\{\mathcal{F}\{f\} \cdot \mathcal{F}\{g\}\}, \tag{1.27}$$

such that the Dirty image can be described as:

$$I^D = B * I, \tag{1.28}$$

where B is known as the "Dirty Beam" or the Point Spread Function and is defined as:

$$B = \mathcal{F}^{-1}\{S\}. \tag{1.29}$$

Therefore to estimate the true image from a real set of measured visibilities requires deconvolution algorithms which solve for I using the known Dirty image and the point spread function. The most basic and widely used algorithm is known as the CLEAN algorithm of Högbom (1974).

Band	Wavelength (mm)	Frequency (GHz)
1	8.6–6.0	35–50
2	4.6–3.3	65–90
3	3.6–2.6	84–116
4	2.4–1.8	125–163
5	1.8–1.4	163–211
6	1.4–1.1	211–275
7	1.1–0.8	275–373
8	0.8–0.6	385–500
9	0.5–0.4	602–720
10	0.4–0.3	787–950

Table 1.1: Table of ALMA Observing Bands (Warmels et al. 2018).

1.4.1 The Atacama Large Millimeter/sub-millimeter Array (ALMA)

The *Atacama Large Millimeter/sub-millimeter Array* (ALMA) (Wootten & Thompson 2009; Hills et al. 2010) is an interferometer array situated in the Atacama Desert in Chile. The site of the array is at an altitude of 5000km above sea level, allowing for excellent transmission of electromagnetic radiation in the atmosphere within the range of observing wavelengths from 0.3 – 10 mm. The wavelength and frequency ranges of ALMA's observing bands are shown in Table 1.1. ALMA consists of 66 antennas making up two separate interferometric arrays: the 12 m array which is composed of 50×12 m antennas; and the Atacama Compact Array (ACA) composed of 12×7 m antennas. Whilst the 12 m array was designed to allow high resolution, sensitive imaging; the purpose of the ACA is to allow sampling of the baseline distributions at distances shorter than possible with the larger 12 m dishes. This allows for improved imaging of large-scale, extended structures. The two interferometric arrays are also complemented by 4×12 m antennas for the single dish, or "total power" (TP) observations (Warmels et al. 2018). Due to the physical limitation in the length of the shortest baseline it is not possible to produce absolute brightness temperature measurements with just the interferometric arrays alone, as the resulting values show the change in the brightness temperature relative to some background value defined by the largest spatial scales. In some astrophysical observations this background value can be estimated through knowledge of where there should be areas of no emission. However, in instances where

this is not possible, such as solar observations, measurements of the absolute brightness temperature can be found using the lower resolution single dish (total power) dishes. ALMA has been imaging astrophysical objects since Cycle 0 in 2011, however only recently has its capability for solar observation been achieved, with the first full science solar observations taking place in Cycle 4 in 2016. A review of the scientific potential for solar observations using ALMA is given in Wedemeyer et al. (2016).

The Sun is an extremely bright and intense source of millimetre/sub-millimetre radiation; far too bright to be directly measured by receivers in ALMA's antennas directly. For the receivers to work as designed, i.e. with a linear response, the signal needs to be attenuated significantly for correct measurements to be taken. In the development of the solar observing capacity of ALMA, two solutions to this problem were considered (Shimojo et al. 2017a): solar filters in the optical path, and the reduction of the receiver gain through detuning of the mixer. The solar filters fitted in ALMA's antennas were found to have a significant number of drawbacks. These drawbacks included: a lower SNR for calibration sources; blocking of the *Water Vapor Radiometers* (WVR), such that it would not be possible to actively correct for water vapor in the Earth's atmosphere; amongst others. Yagoubov (2013) suggested a solution to this where ALMA's antenna's mixers were to be detuned such as to reduce the receiver gain. Reducing the gain in this way allowed ALMA to observe over a wider dynamic range of signals, thus negating the need for the solar filters in observing the Sun. After testing, this method was adopted in the Solar Verification campaigns, and in the full scientific campaigns starting in Cycle 4 in 2016. The solar filters may, however, be used in the future for observations of high solar activity, such as solar flares.

Interferometers are incapable of resolving spatial scales larger than the fringe spacing defined by the shortest baseline in the array. Because of this, the field of the interferometer of ALMA is fairly small, whilst it is unable to measure the absolute temperature of the solar atmosphere. The way ALMA works around this is to use single dish measurements with the TP array to fill in the large spatial scale information. For this to be possible, however, a technique was needed to be developed so that the TP array antennas could quickly, and accurately map the entire solar disk, and some of the surrounding coronal material. The pattern utilised is referred to as a *double—circle* scanning pattern (see Figure 1 in White et al. (2017)). This method provides a 1200″ radius map of the solar disk, including 200″ from the solar limb.

In the next section I shall give an account of the published work using the solar capability

of ALMA.

1.5 Solar Observations with ALMA

Solar science was always planned to be part of the observing program for ALMA, however, because of the unique circumstances involved with solar observation, ALMA cannot operate in the same mode when directed towards the Sun as it can use for non-solar cases. The first full observing cycle where solar observation proposals were considered was Cycle 4 beginning in 2016. Before this, however, the solar observing modes were developed by the Joint ALMA Observatory and ALMA Regional Centres (ARC)s in a series of science verification (SV) campaigns conducted between 2011 and 2015. The details of these observing campaigns, and the methods for solar observation using ALMA have been reviewed in Shimojo et al. (2017a). In Shimojo et al. (2017a) the authors discuss the parameters used in the image synthesis from the visibility data, as well as presenting a method for attributing a value to the noise level in the interferometric images using the difference between the XX and YY cross-correlated polarisations. The estimation of the noise level in interferometric images is addressed in more detail in Section 4.3.1.1.

As stated in the previous section, interferometric observation alone cannot provide absolute brightness temperature values due to the so-called "zero-basing" problem. Absolute brightness temperature measurements thus require the combination of the interferometric data with that observed using single-dish measurements. In ALMA the single-dish measurements are taken using the 12 m total power (TP) array using the fast-scanning method to produce full disk maps of the solar brightness temperature. An account of the single-dish fast-scanning for solar full-disk mapping is given by White et al. (2017). In an attempt to characterise the typical millimetre brightness temperature distribution White et al. (2017) considered a large number of datasets within the 2015 and 2016 solar SV campaigns. In doing so they found that it was not uncommon for the TP antennas to yield systematically differing values between polarizations for a given antenna and observation. To test these results they analysed the distributions at disk centre where they expected quiet Sun conditions, and averaged over areas larger than the spatial scales of network structures, where they expected the brightness temperature value to be approximately consistent across all datasets for a given band. Fitting gaussian curves to the brightness temperature distributions from both 2015 and 2016 separately whilst excluding bad datasets, White et al. (2017) found

recommended values for the typical quiet Sun brightness temperature at disk centre of 7300 ± 100 K for Band 3, and 5900 ± 100 K for Band 6. These values are used to rescale currently observed brightness temperature single-dish solar data to account for the variation between antennas. The authors also compare these values to previously observed values for the millimetre brightness temperature spectrum collated in Loukitcheva et al. (2004) and Loukitcheva et al. (2015), where they find their recommended values to be consistent with previous observations. The authors also report that the observed millimetre brightness temperatures observed with ALMA TP maps are significantly higher than that expected by the atmospheric models of Wedemeyer-Böhm et al. (2007) and Loukitcheva et al. (2017a), although emphasise that for in-depth comparisons, models with resolution of the ALMA TP maps would be required.

The data used in the science verification campaigns was released to the public in January 2017, and since then several publications have been made using results from these data sets. The rest of this section focusses on some of the results found through the analysis of the ALMA SV and full-science observations.

A key area of interest for ALMA observations has been the analysis of limb brightening of millimetre wavelength emission. Through the observation of the centre-to-limb variation at a given wavelength it is possible to constrain the possible solutions for the radiative transfer equation through the solar atmosphere, thus constraining empirical atmospheric models. The millimetre regime should be particularly suited for this type of study due to its LTE emission mechanism. The centre-to-limb variation as observed with ALMA SV data was analysed by Alissandrakis et al. (2017) using full-disk total power maps, whilst also comparing the resulting centre-to-limb variation curves to a companion high resolution interferometric observation. Through the inversion of their measured centre-to-limb variation the authors calculated the expected relationship between the electron temperature and optical thickness at 100 GHz within the solar atmosphere. Comparing their results to a few empirical atmospheric models they found that their inversion most closely matched the atmospheric structure as predicted by the FAL-C model (Fontenla et al. 1993). Nindos et al. (2018) then followed this work by analysing a set of high-resolution ALMA Band 3 interferometric datasets with FOVs orientated at different positions ranging from the solar disk centre to the limb taken in March 2017. They found the chromospheric structure displayed in the images had scales lying between those observed in AIA 1600 and 304 Å images, suggesting the location of the forming region. They also found that the observed

centre-to-limb variation was similar to that observed using the SV data in Alissandrakis et al. (2017), and that spicule-like structures were observable off-limb. The authors also reported observation of brightness temperatures above the solar limb of up to 1000 K which may be caused by imaging artifacts as discussed in Shimojo et al. (2017a). In Selhorst et al. (2019) the authors investigated the solar polar brightening of millimetre emission using the full-disk total power maps for both Band 3 (100 GHz) and Band 6 (230 GHz). To do this they degraded the higher resolution maps of Band 6 to the lower resolution for Band 3 using a gaussian beam correlation. They found the polar intensity to be higher than the respective disk intensities for both bands, and in 8 out of 9 maps the south pole presented a higher polar brightening than the north pole. They suggest that the difference between the two polar brightenings may be caused by the presence of a coronal hole with small bright structures, although the difference between the two still lies within the value for the standard deviation. The authors report that the polar brightening intensities observed using ALMA were smaller than those predicted by the atmospheric models FAL-C (Fontenla et al. 1993) and SSC (Selhorst et al. 2005), with both models being in better agreement with Band 6 than Band 3.

A couple of ALMA SV datasets which have been analysed quite thoroughly are the observations of a sunspot observed on the 16th of December 2015 in ALMA Band 3, and on the 18th of the same month in Band 6. These observations were analysed in Iwai et al. (2017) and Loukitcheva et al. (2017b). In Iwai et al. (2017) the authors discuss the implication of a brightness temperature enhancement which is observed in the Band 3 emission within the sunspot's umbra. Prior to this observation, sub-millimetre and millimetre observations of sunspots had presented umbra which appeared darker or neutral compared to the surrounding area. The authors, however, attribute this lack of consistency to the previously low spatial resolution of sub-millimetre/millimetre observations, such that it would have been difficult to distinguish penumbral from umbral material. Loukitcheva et al. (2017b) expanded on the work of Iwai et al. (2017) by analysing the brightness temperature distribution found in both observing bands, and by comparing these results to those expected from contemporary umbral and penumbral models. These authors found that the sunspot umbra presented a thoroughly different appearance in Band 3 when compared to Band 6, whilst the penumbral structure was similar in both observations. The umbral material was found to be brighter than the surrounding quiet Sun material in Band 3, whilst it appeared as a dark feature in Band 6. Although some umbral atmospheric models were found to come close to predicting the brightness temperature distributions observed with ALMA, the authors did not find any

penumbral models which they considered a satisfactory fit to the data.

The first analysis of a small solar eruptive event observed with ALMA was presented in Shimojo et al. (2017b). By analysing the enhancement in brightness temperature observed in ALMA Band 3, and comparing the corresponding enhancements observed in selected AIA bands, the authors estimate ranges for the plausible electron density and temperature for the enhancing plasma. In Section 4.3 I also present work using this dataset which has been published in Rodger et al. (2019). In this study I consider the logarithmic-scale spectral gradient observed in the ALMA sub-band 3 spectrum, using this measurement to estimate the plausible range in optical thickness for the emitting plasma. With bounds on the plasma optical thickness the estimates on the electron temperature and electron density of the plasma are constrained further.

Bastian et al. (2017) investigated the relationship between the brightness temperature distribution observed using ALMA Band 6, and the emission observed in the UV line of Mg II h. This study found that the brightness temperature of Band 6 was linearly correlated to the radiation temperature of the Mg II h line, although with a slope of less than 1. They also found that the correlation is feature-dependent with sunspots, plage, and quiet Sun presenting clearly different relationships. The authors postulate that this could be caused by the difference in formation region for the two types of emission within the different solar features, i.e. in different features the Mg II h source function may experience different degrees of decoupling from the electron temperature of the emitting plasma. Jafarzadeh et al. (2019) revisited this topic with the extension that they measured the brightness temperature at each of the constituent sub-bands of ALMA band 6, and compared the resulting distributions to those observed in the IRIS Mg II h & k lines, as well as C II 1344 Å, O I 1356 Å, and Si IV 1394 Å UV lines. For this analysis the authors used again the sunspot observation from the ALMA SV campaign of December 2015. By splitting the Band 6 data into the constituent sub-bands the authors report a small improvement in the spatial resolution of the synthesised images. They attribute this primarily to the difference in formation heights for each wavelength, and as such averaging over the full band would result in smearing of the different height scales, although they state that differences in the relative beam sizes could also play a role in the difference in spatial resolutions. In comparison between the band 6 brightness temperature and the radiation temperature of the various UV lines, the authors found relatively good correlations. The C II 1344 Å line was found to generally present the closest match in temperature to the millimetre value, however not within the sunspot umbra

where C II was significantly higher. The authors attribute the offsets from $y = x$ found in the plotted correlations to the departure from LTE formation found in the UV lines.

Brajša et al. (2018) presented a study of an ALMA Band 6 (1.21mm) full-disk, total-power image, comparing it to similar maps in Hα, He I 10830Å, various AIA bands, as well as an HMI magnetogram. The purpose of this study was to identify typical solar features observed on the disk in the Band 3 total-power image, whilst measuring their brightness temperature. The authors found that sunspots appeared as dark structures, whilst ambient active regions appeared bright compared to the background quiet Sun. Filaments, on the other hand, are found to have a very low contrast against the Quiet Sun in Band 6. In Loukitcheva et al. (2019) the authors present the detection of a dark chromospheric feature observed which they termed as a "Chromospheric ALMA Hole". This feature appeared significantly darker than the surrounding chromospheric internetwork structure in ALMA Band 6, however, was unidentifiable in the IRIS Mg II k line or in chromospheric AIA bands. The same structure appeared bright in Hα which the authors use to imply that Band 3 and Hα probe differing heights in the atmosphere.

Most of the published solar ALMA observations have focussed on on-disk observations. A reason for this could be that off-limb observations with ALMA may be subject to interferometric artifacts caused by incomplete sampling of the "step-function like" nature of the solar limb in the u–v plane (Shimojo et al. 2017a). Despite this, however, Yokoyama et al. (2018) conducted a study into structures on the solar chromospheric limb using an ALMA Band 3 observation from the 29th of April 2017. The structure of the solar limb in these observations appears to show a saw-tooth like pattern, similar to that observed in the AIA 171 Å band. The authors also observed structures extending from the saw-tooth like patterns which they attribute to jet-like activity in the millimetre emission, as well as the ejection of plasma blobs which appear to follow the trajectory of spicules as observed in the Mg II Slit-Jaw images of IRIS. A prominence was observed off-limb using the full ALMA array for the first time on the 19th of April 2018. Preliminary results from this observation are covered in Chapter 5.

The purpose of the work presented in this thesis is thus to investigate and prepare for high resolution millimetre wavelength observations of solar prominences using ALMA. In the first chapter (Chapter 2) I present the development and results from numerical non-LTE forward models for the expected brightness temperature from solar prominences as observed with ALMA. Chapter 3 then describes further application of these forward models by discussing the expected visibility of solar filaments with ALMA and investigating the

relationships between the intensities observed from hydrogen and helium transitions with the millimetre-continuum. Spectral diagnostics from multiple wavelength observations of the millimetre-continuum are then investigated in Chapter 4. Finally, Chapter 5 presents preliminary results from the first observation of a solar prominence using high resolution ALMA imaging. The conclusions from across my entire thesis are summarised in Chapter 6.

Chapter 2

Solar Prominence Modelling at Millimetre Wavelengths

This chapter includes work previously published in Rodger & Labrosse (2017). For this publication I contributed by constructing and running the code to numerically model the millimetre-continuum from the output of the previously existing C2D2E code. This included the production of all of the figures. The analysis was then made through discussions between myself and my co-author Dr N. Labrosse. Because of this, much of the content of this chapter follows directly from what is stated in Rodger & Labrosse (2017). Figures which come from this publication are explicitly labelled in their captions.

2.1 Introduction

In this chapter I will describe my work into the creation of a 2D cylindrical non-LTE radiative transfer model for the simulation of millimeter/sub-millimetre emission from solar prominences. The *Atacama Large Millimeter/sub-millimeter Array* (ALMA) presents a new window in which to observe the Sun.

The temperature structure of solar prominences remains an important question in solar physics. Prominences are cool, dense structures suspended in the hot sparse corona, and it is generally accepted that there is a Prominence-to-Corona Transition Region (PCTR) between the two regimes. The importance of the PCTR in prominence modelling has been discussed by Anzer & Heinzel (1999), and its effect on various spectral lines demonstrated by *e.g.* Heinzel et al. (2001b); Labrosse & Gouttebroze (2004); Labrosse et al. (2010); Heinzel

et al. (2015c). However, the nature of the PCTR and its relationship to the prominence and prominence fine-structure is not fully understood. To address this, an accurate and reliable temperature diagnostic, capable of resolving fine-structures is required.

A wavelength domain with the capability for reliable temperature diagnostics is the millimetre/sub-millimetre continuum (Loukitcheva et al. 2004; Heinzel et al. 2015a; Wedemeyer et al. 2016). Until the advent of solar observations with ALMA, millimetre/sub-millimetre wavelength observations were hindered by low spatial resolutions, such that fine-structure observations in this domain are only recently possible. In the solar millimetre/submillimetre domain the dominant emission mechanism is free-free collisional processes. The source function hence results from local thermodynamic equilibrium (LTE) conditions and is thus Planckian. In the Rayleigh-Jeans domain this means the source function varies linearly with kinetic temperature. This can cause the contribution function of the continuum radiation to peak at a specific local temperature, leading to the often used term "linear thermometer". In Loukitcheva et al. (2015), the authors conclude that, for chromospheric radiation, brightness temperatures at millimetre wavelengths provide a reasonable measure of the thermal structure, up to resolutions of 1″. In the context of solar flare models, Heinzel & Avrett (2012) synthesized the thermal continua from the optical to the mm radio, demonstrating how these continua are formed and again showing the close correspondence between brightness temperature and the kinetic temperature.

ALMA offers the opportunity of a new approach to the observation and study of the Sun and thus solar prominences. Because of this it is therefore important to build an understanding of how we may expect solar prominences and their associate fine-structure to appear in brightness temperature when observed in ALMA's wavelength range. When a prominence observation is then obtained it will be equally important to know how to use such measurements to infer the desired information on the temperature and other plasma properties.

A study into how prominences may appear as viewed through ALMA was conducted by Heinzel et al. (2015a). This was done by taking an Hα coronagraph image and, using the empirical relation between Hα intensity and emission measure, estimating the brightness temperature for such a plasma. These brightness temperatures were tested using the *Common Astronomy Software Applications* (CASA) package, to simulate ALMA observations. Assumptions were however required including the use of a simple temperature structure for the prominence, whilst the simulated ALMA observations were restricted by the resolution

of the instrument used to create the original Hα observation.

Simulated observations of whole prominences in the mm domain have been created by Gunár et al. (2016) using a 3D whole-prominence fine-structure model. The prominence fine-structures are formed within dips in a synthetic prominence magnetic field. From the material within the fine-structure the hydrogen free-free extinction coefficient and thus the brightness temperature are calculated. This model is used to visualize the brightness temperature and optical thicknesses of prominences on the limb and on-disk filaments at a range of ALMA wavelengths. The authors underline the requirement for mm observations in both optically thin and optically thick wavelengths for observations of filaments in order to distinguish between sparse, low-emitting material and dense high-absorbing material.

In Rodger & Labrosse (2017) we presented a 2D non-local thermodynamic (non-LTE) prominence model for the millimetre continuum to test the potential for solar prominence plasma diagnostics using ALMA. The model was based on the non-LTE radiative transfer, 2D cylindrical cross-section prominence model of Gouttebroze & Labrosse (2009) which considers both hydrogen and helium. From the output of this code we calculated the expected brightness temperature produced across all potential ALMA observing bands for two distinct prominence models: isothermal-isobaric fine-structure and multi-thermal large-scale prominence models. For each case we discussed the potential for ALMA wavelength measurements as a kinetic temperature diagnostic. The content of this study is presented at length throughout the remainder of this chapter.

The 3D whole-prominence fine-structure model was employed again in Gunár et al. (2018) where the authors use two simulated ALMA observations, one at a wavelength where the plasma is optically thin and the other where a significant amount of the plasma is optically thick. From these two contrasting measurements they attempt to develop a technique for the analysis of the prominence's thermal structure. The method described produces a derived kinetic temperature for the prominence. Through comparison between the derived kinetic temperature of the prominence plasma and the known thermal structure of the model prominence the authors assess the quality of the diagnostic technique. In doing so they find that to produce a derived kinetic temperature value representative of the known temperature distribution the optical thickness for the optically thick measurement has to be of a sufficiently large value. They state that for the derived value to be within 1000 K of the mean kinetic temperature of the known distribution the optical thickness of the plasma should be greater than 2. For a means to determine whether a given pixel holds

information from a sufficiently optically thick plasma Gunár et al. (2018) determine from their simulations a minimum brightness temperature in the optically thin measurement for a given optical thickness in the optically thick measurement, i.e. they state $T_{B\,\mathrm{min}}^{0.45\mathrm{mm}} \sim 32$ K for $\tau^{9\mathrm{mm}} > 1$. The 3D Whole-prominence model is, by its definition, multi-thread in nature, and as such the authors are able to comment on the ability for ALMA observations to determine the temperature "tomography" of a prominence where the structure is formed of a collection of smaller individual structures. In their model each fine-structure magnetic "dip" has an individual temperature structure. As they find that the contribution function of millimetre/sub-millimetre radiation covers multiple fine-structures, there is thus multiple similarly sized contribution function maxima rather than a single clear global maximum. They therefore conclude that it would not be possible, for a prominence of similar temperature structure to their model, to have its temperature distribution mapped by varying the wavelength of the observed millimetre/sub-millimetre radiation, as is described for the chromosphere in Loukitcheva et al. (2015).

In the rest of this chapter I cover in detail the development of the model presented in Rodger & Labrosse (2017) and the initial results found when testing the plasma diagnostic potential of the millimetre/sub-millimetre continuum. Firstly in section 2.2 I give an account of the background for the C2D2E model for which all subsequent modelling efforts are based on. Section 2.3 describes how the models are defined. This section includes subsections on the input parameters to the model (2.3.1), the formation of the millimetre/sub-millimetre continuum (2.3.2), and the geometry of the prominence threads (2.3.3). Section 2.4 covers the initial results found when testing the developed model, including discussion into two distinct prominence models; isothermal-isobaric fine-structure models (2.4.1) and multi-thermal large-scale structures (2.4.2). The content of this chapter of the thesis is summarised in Section 2.5.

2.2 Background of the C2D2E model

The C2D2E model was developed over a series of studies by P. Gouttebroze and later N. Labrosse. The series began with Gouttebroze (2004) presenting a method to solve the non-local thermodynamic equilibrium (non-LTE) radiative transfer equations in a cylindrical framework. Prior to this work most radiative transfer models of solar prominences had involved 1D or 2D plane-parallel, rectangular slab models of plasma. In plane-parallel slab

models incident radiation from the solar disc illuminates the bottom and side boundaries with no external illumination on the upper boundary. The introduction of a cylindrical prominence model thus allowed for the introduction of a non-homogeneous incident radiation on the modelled prominence plasma. The model was initially restricted to one-dimension, however later in the second paper in the series (Gouttebroze 2005) a 2D method is presented by the addition of an azimuth-dependent solution. This model was initially restricted to a 2-level atom, however in Gouttebroze (2006) the author expanded this to simulate a 10-level plus continuum hydrogen atom using complete redistribution (CRD) of the spectral lines. In Patsourakos et al. (2007) the 10-level plus continuum hydrogen C2D2E code of Gouttebroze (2006) was used to model cool, transition region temperature loops as observed using the *Very High Angular Resolution Ultraviolet Telescope* (VAULT).

Gouttebroze continued this series of papers producing other improvements to the 2D cylindrical prominence models. These improvements included both the introduction of a time-dependent solution to study thermal equilibrium (Gouttebroze 2007) and 3D radial, rotational and longitudinal velocity fields (Gouttebroze 2008) allowing for the study of doppler shifts and broadening on spectral lines from a singular prominence thread. Gouttebroze (2007) computed the radiative gains and losses from 1D cylindrical models and used the isobaric derivative of the temperature to measure the models' evolution towards radiative equilibrium. It was found that thick cylindrical models displayed slow temperature evolution near to the cylindrical axis, increasing the likelihood of having a departure from thermal equilibrium there. Gouttebroze & Labrosse (2009) then expanded the models of Gouttebroze (2006) to contain the addition of an He I, He II and He III system. With this addition they were able to produce an electron density defined by the ionization equilibrium of hydrogen and helium's ionized species. Cylindrical models have successfully investigated the effects of various prominence parameters such as temperature, pressure and helium abundance ratio in both isothermal and multi-thermal cases.

In Labrosse & Rodger (2016) the models of Gouttebroze & Labrosse (2009) were utilised to investigate the effects of a multi-thread system, where the prominence was described as a collection, or bundle, of individual thread models. This study allowed for the investigation of how multiple structures within the field of view (FOV) of an observation affected the resulting hydrogen and helium line emission. From considering multiple threads it was also possible for the authors to consider peculiar velocities between said threads, i.e. global velocities which describe how the threads as a whole move with respect to one another, and

not internal velocity distributions as had previously been analysed in Gouttebroze (2008). This study was able to display both how the structures present in the FOV of an observation are determined differently for optically thin and optically thick material, as well as show how peculiar velocities between multiple threads within a larger prominence structure can create complex, asymmetrical line profiles, e.g. as have been found in prominence observations in the Lyman lines by Heinzel et al. (2001b).

2.3 Description of the Model

2.3.1 Input Parameters

C2D2E can consider a range of intrinsic thread parameters as inputs. For geometric variables these include altitude above solar disc, inclination angle and thread diameter. A diagram showing the orientation of the prominence cylinder with respect to the solar disk, including incident radiation, is shown in Figure 2.1. In this work I consider model cylinders which are orientated horizontally to the solar disk ($\alpha = 90$ as shown in Figure 2.1), each with an altitude of 10000 km. As the inclination and altitude are held constant for all models the incident radiation on the cylindrical will be the same for each model. The C2D2E model calculates the incident radiation by assuming that it is emitted from a sphere representing the solar surface (see Figure 2.1) in a method described in Gouttebroze (2005). The brightness temperature for the full solar disk, including the Lyman lines, as used in C2D2E (Gouttebroze & Labrosse 2009) is shown in Figure 2.2.

The internal thread parameters are gas pressure (P_g), kinetic temperature (T) and helium abundance ratio (A_{He}). In Rodger & Labrosse (2017) these parameters were used to consider two different types of prominence model: fine-structure isothermal-isobaric prominence threads, and larger-scale threads with radially increasing temperature distributions.

High-resolution observations of solar prominences reveal increasing degrees of fine-structure (Lin et al. 2008). It is often theorised that the prominence structure as a whole is defined not by a singular structure, but by a collection (or bundle) of individual fine-structure threads. These fine-structure threads could have individually varying temperatures distributions, or an overlying PCTR temperature structure (Fontenla et al. 1996; Gunár et al. 2008; Labrosse & Rodger 2016). ALMA will have the potential, once wide baseline array configurations are available for solar observations, to observe with resolutions of up to 0.015″– 1.4″$\times\lambda_{mm}$ (Bastian 2002), and thus will have the capability to observe such fine-

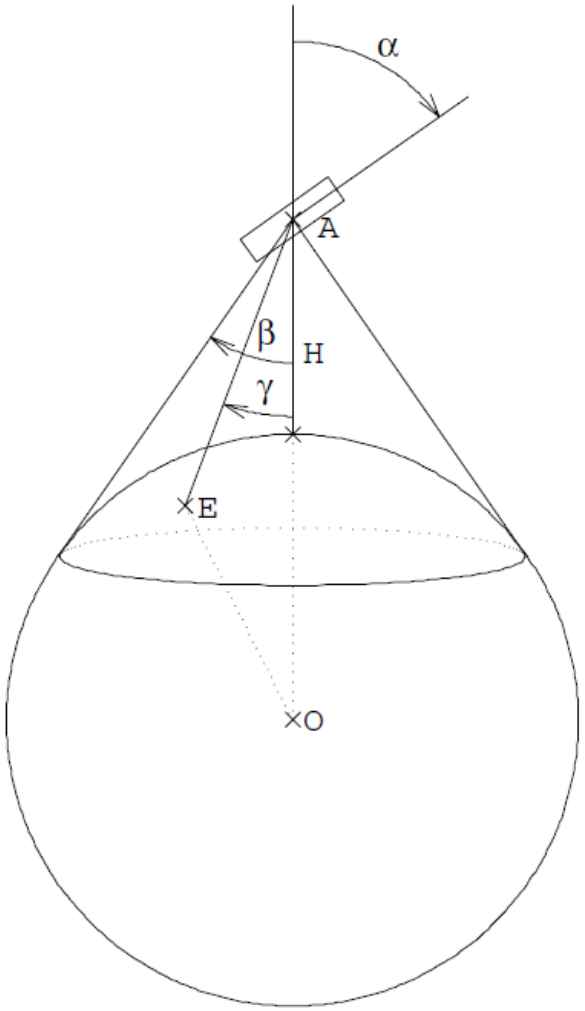

Figure 2.1: Diagram, taken from Gouttebroze (2005), showing the orientation of the C2D2E model cylinder with respect to the solar disk and the incident radiation. H and α define the altitude and inclination of the prominence, whilst β and γ are angles used in the incident radiation calculations.

structure threads individually, as a 500km wide fine-structure thread would have an angular size of $\approx 0.7''$.

To define the prominence fine-structure models I considered cylinders of plasma with constant temperature and pressure. This was believed to be a valid assumption because over comparatively small distances, such as are presented in fine-structure observations, temperature and pressure variations may be relatively small. To analyse these isothermal-isobaric fine-structures a grid of models was created using 6 values for the temperature and 5 for the pressure. The input parameters can be seen in Table 2.1. The helium abundance

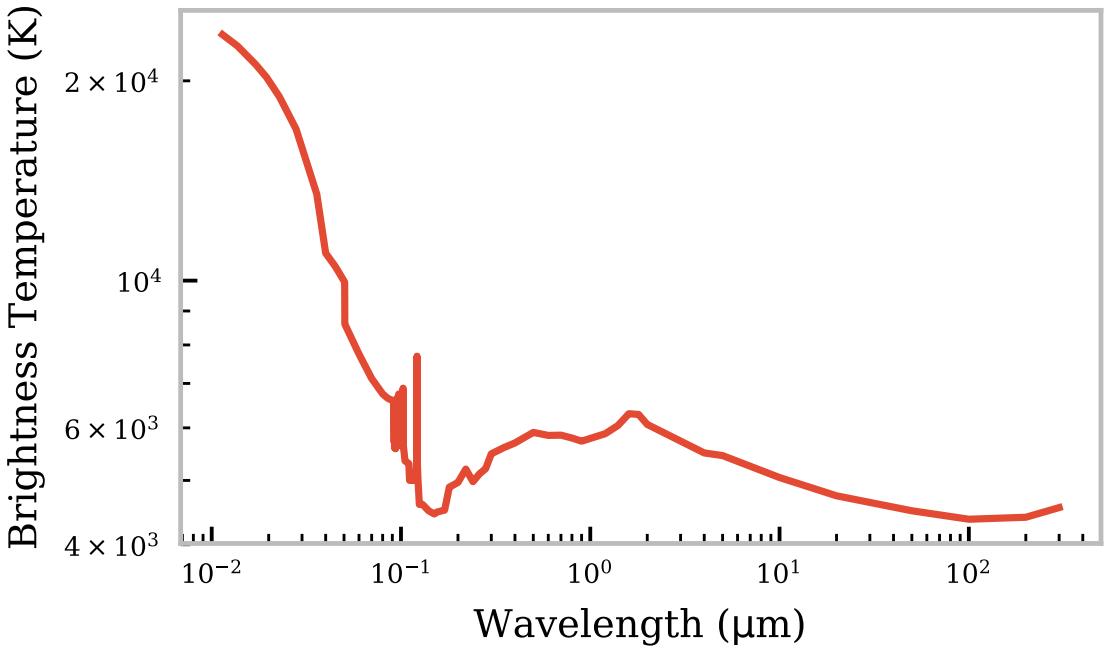

Figure 2.2: Brightness temperature of the full solar disk, including the Lyman Lines, with wavelength in microns used in the calculation of incident radiation for C2D2E (Gouttebroze & Labrosse 2009).

Table 2.1: Parameters for isothermal-isobaric fine-structure models used in Rodger & Labrosse (2017).

Parameter	Value
Temperature (K)	$\{5000, 6000, 7000, 8000, 9000, 10000\}$
Pressure (dyn cm^{-2})	$\{0.02, 0.05, 0.1, 0.3, 0.5\}$
Radius (km)	250

and microturbulent velocity are set to 0.1 and 5 km s^{-1}, respectively.

In observations of larger, or less resolved structures, it might not be prudent to assume an isothermal distribution. For these cases larger scale, full-prominence width threads are considered, including both distinct core and PCTR regions. In these models, the prominence core is defined by a uniform temperature distribution, whilst the PCTR is defined by a temperature distribution which increases radially with distance from the thread's axis. Across the cylinder a constant gas pressure is again assumed. These multi-thermal models

Table 2.2: Parameters for large-scale, multi-thermal models used in Rodger & Labrosse (2017)

Parameter	Value
Temperature (K)	$T_0 = 6 \times 10^3$, $T_1 = 1 \times 10^5$
Pressure (dyn cm^{-2})	$\{0.02, 0.03, 0.05, 0.1, 0.2, 0.3, 0.5\}$
Inner radius (km)	500
Outer radius (km)	1000

use an ad-hoc temperature gradient for the PCTR of the form (Gouttebroze 2006):

$$\log T(r) = \log T_0 + (\log T_1 - \log T_0)\frac{r - r_0}{r_1 - r_0}, \tag{2.1}$$

where T_0 and T_1 are the kinetic temperatures attributed to the thread core and surrounding corona, respectively. The inner radius of the transition region is defined by r_0 whilst the radius of the cylinder is r_1. Within the isothermal core ($r < r_0$), the temperature of the plasma is fixed at $T = T_0$. This temperature distribution is not generated from any theoretical model and simply serves the purpose of showing the effect of a radial temperature gradient. Table 2.2 gives the parameters used to define this set of models. The helium abundance and microturbulent velocity are again fixed at 0.1 and 5 km s^{-1}, respectively.

An example plot showing the variation of the electron density across a typical thread from a multi-thermal, large-scale prominence model with a pressure of 0.1 dyn cm^{-2} is shown in Figure 2.3. This figure shows the importance of both the radial temperature distribution and the ionizing incident radiation on the lower boundary of the thread. The higher temperatures in the thread PCTR create a ring-like enhancement in the electron density through an increased ionization fraction. The incident UV radiation on the lower boundary of the thread also increases ionization near where the radiation makes contact with the prominence plasma, thus creating the slightly increased electron density there.

2.3.2 Calculating the Millimeter/sub-millimeter Continuum Absorption Coefficient in Solar Prominences

When computing the radiation at a given wavelength an important question to consider is what the emission mechanisms are. ALMA will eventually have the capability to take observations at wavelengths ranging between 0.3 mm and 9.0 mm (Karlický et al. 2011). In initial solar observational campaigns, such as Cycle 4, 5 and 6, however, observations were

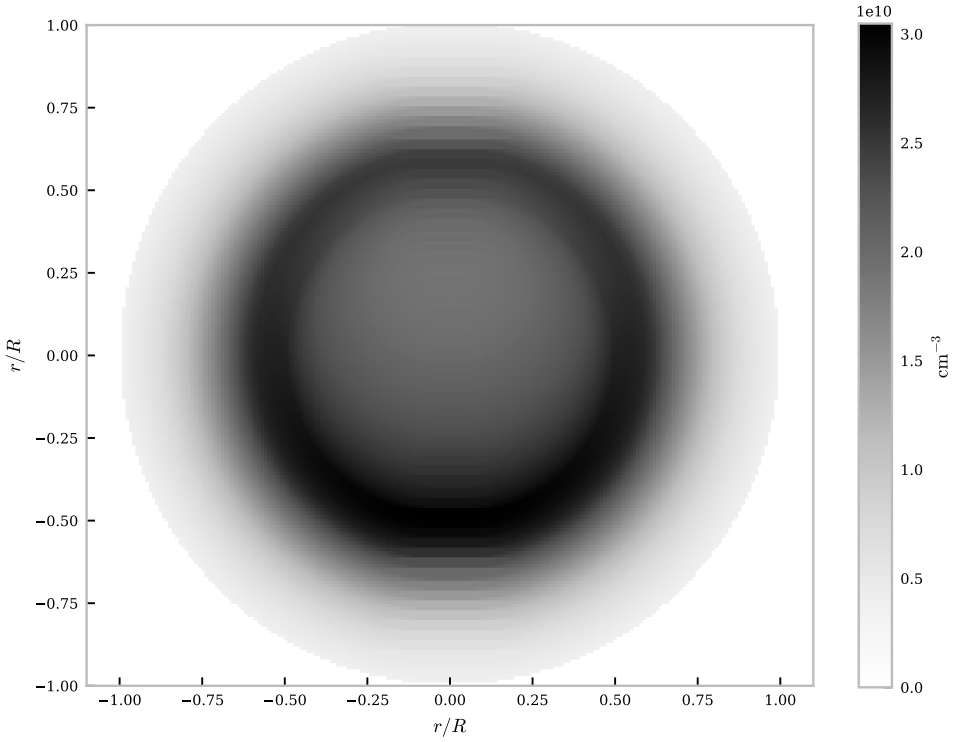

Figure 2.3: Electron density distribution for a multi-thermal large-scale prominence as described in Table 2.2 with a pressure of 0.1dyn cm^{-2}. Replication of a figure previously published in Rodger & Labrosse (2017)

limited to the wavelength bands 2.6 – 3.6 mm (Band 3) and 1.1 – 1.4 mm (Band 6). In the upcoming Cycle 7 Band 7 (0.8–1.1mm) is now available.

The largest contributions to absorption in the millimetre/submillimetre wavelength regime are free-free absorption due to inverse thermal bremsstrahlung from ionized hydrogen and helium, and to a lesser degree negative hydrogen (H^-) extinction. Inverse thermal bremsstrahlung describes the process where an electron, in the Coulomb field of an ion, becomes energised through the absorption of a photon from the radiation field. In cgs units of cm^{-1}, the absorption coefficient describing inverse thermal bremsstrahlung, including the stimulated emission term, is:

$$\kappa_{\text{ion}}^{\text{ff}} \approx 9.78 \times 10^{-3} \frac{n_{\text{e}}}{\nu^2 T^{\frac{3}{2}}} \sum_i Z_i^2 n_i \times (17.9 + \ln T^{\frac{3}{2}} - \ln \nu)\,, \tag{2.2}$$

where T is the kinetic temperature, ν is the frequency and n_e is the electron density, i

represents each ion species considered, *e.g.* hydrogen or helium ions, and n_i and Z_i are the ion density and ion charge respectively (Wedemeyer et al. 2016). The term in parentheses in Equation 2.2 is an approximation of the thermal Gaunt factor. This approximation was used throughout Rodger & Labrosse (2017), and thus the results presented in this chapter reflect that, however, in Section 3.1 of this thesis I reevaluate the use of this factor for use in later studies. Equation 2.2 is evaluated from the semi-classical inverse thermal bremsstrahlung absorption, in the absence of magnetic field, given in Dulk (1985). In the optically thin limit of an isothermal plasma, $\tau \ll 1$, Equation 1.18 would become $T_B(\nu) \approx T\tau_\nu$, and the optical thickness may be considered to be $\tau_\nu \approx \kappa_\nu L$. In this case, a purely inverse thermal bremsstrahlung emission mechanism would produce a brightness temperature, T_B proportional to $T^{-\frac{1}{2}}$.

Continuum H^- absorption occurs from two sources, photo-detachment and free-free transitions, described in Equations 2.3 and 2.4 respectively:

$$h\nu + H^- \rightarrow H + e^- \,, \tag{2.3}$$

$$h\nu + e^- + H \rightarrow H + e^{-*} \tag{2.4}$$

where e^{-*} symbolises an energised electron.

Photo-detachment, Equation 2.3, describes the mechanism where a photon interacts with the negative hydrogen ion resulting in the absorption of said photon and the release of a free electron. This process continues up to the ionization threshold of 1.6421 μm, and thus does not contribute to the millimetre range continuum as observed with ALMA. If these models were applied to the shorter wavelength infra-red regime, such as will be observed in the DL-NIRSP and Cryo-NIRSP instruments on DKIST, however, photo-detachment extinction would play a significant role. According to John (1988) the expression for the continuous absorption coefficient of bound-free photo-detachment from the negative hydrogen ion is given by:

$$\kappa^{\mathrm{bf}}_{H^-} = 0.75 T^{-5/2} e^{\alpha/(\lambda_0 T)} (1 - e^{-\alpha/(\lambda T)}) \sigma_\lambda n_{\mathrm{HI}} n_e k_B T, \tag{2.5}$$

where α is $1.439 \times 10^4 \mu\mathrm{mK}^{-1}$, λ_0 is the ionization threshold 1.6419μm, and σ_λ is the collisional cross-section for the photo-detachment. The units in this expression have been converted to cm^{-1} using the addition of the terms to the right of σ_λ. n_{HI} and n_e are the densities of neutral hydrogen and electrons, respectively. This expression takes into account Saha-Boltzmann weighting and stimulated emission. An analytical expression for σ_λ is given, along with a corresponding table of coefficients in John (1988).

Equation 2.4 shows the atomic process wherein an electron interacting with a neutral hydrogen atom absorbs a photon. This process can occur at any wavelength in the spectrum, however, it is the sole contribution to H^- absorption above the ionization threshold at 1.6412 μm. The analytical formula used to calculate the absorption coefficient for this process is defined in John (1988), and is given in Equation 2.6, where again a conversion to cm^{-1} has been applied.

$$\kappa^{\mathrm{ff}}_{\mathrm{H^-}} = 10^{-29} \sum_{n=1}^{6} \left(\frac{5040}{T}\right)^{(n+1)/2} \times \{\lambda^2 A_n + B_n + C_n/\lambda + D_n/\lambda^2 + E_n/\lambda^3 + F_n/\lambda^4\} n_{\mathrm{HI}} n_e k_B T, \quad (2.6)$$

where A_n to F_n are coefficients given in Tables 3a or 3b of John (1988) depending on whether the given wavelength is in the range $\lambda \geq 0.3645\,\mu$m or $0.1823\,\mu\mathrm{m} \leq \lambda \leq 0.3645\,\mu$m, respectively. The total absorption coefficient from H^- extinction is considerably lower than that for inverse thermal bremsstrahlung, however at high temperatures and low wavelengths its significance does increase.

Other absorption mechanisms that have been considered include Thomson and Rayleigh scattering, however these mechanisms proved to have minimal contribution within the wavelength ranges considered here. These mechanisms were thus included in the Rodger & Labrosse (2017) study, but subsequently ignored in any later modelling work. A comparison of the contribution provided by neutral hydrogen and thermal bremsstrahlung emission mechanisms across the radial profile of a sample prominence model is shown in Figure 2.4. This figure compares the azimuthally-averaged radial distributions of the two dominant absorption coefficients to the densities of electrons, neutral and ionized hydrogen and kinetic temperature for the typical multi-thermal prominence model with gas pressure of $0.1\,\mathrm{dyn\,cm^{-2}}$. Across the whole distribution thermal bremsstrahlung from ions is dominant over H^- absorption, however, the difference between the two mechanisms is smaller at the thread centre where more neutral hydrogen is found. In the PCTR, where the temperature increases, the density of the neutral hydrogen species decreases steeply, whilst the ionized hydrogen and electron densities at first increase slightly through hydrogen ionization but then also decrease, albeit less steeply. Due to this the gap between thermal bremsstrahlung and H^- absorption increases through the *PCTR*. Any difference between ionized hydrogen and electron density distributions is caused by the inclusion of ionized species of helium in the prominence model.

In Figure 2.5 I show the variation across frequency of the thermal bremsstrahlung and H^- absorption coefficients. The values used are averaged across the azimuth and radius grid for a

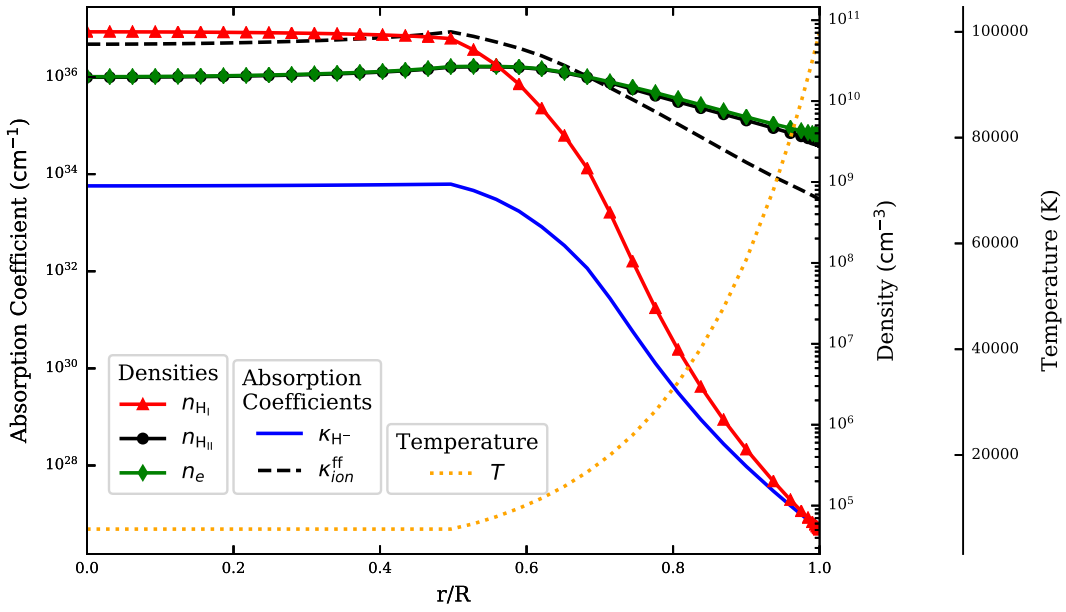

Figure 2.4: The azimuthally averaged radial distributions for H^- and thermal bremsstrahlung absorption coefficients are given on the *left* y-axis. The x-axis gives the fractional radial distance from the cylinder axis in terms of the total thread radius. The *inner right* y-axis shows the azimuthally averaged radial distributions of the densities for both neutral, and ionized hydrogen species, as well as the electron density. The *outer right* y-axis shows the radial temperature distribution.

typical multi-thermal prominence model, with a gas pressure of 0.1 dyn cm^{-2}. The figure also shows all 10 potential ALMA observing bands such that it can be seen that throughout the ALMA frequency range thermal bremsstrahlung should remain the dominant mechanism.

To calculate the combined total absorption coefficient, κ_{tot}, the expressions for the absorption coefficients from Equations 2.2, 2.5, 2.6, and other, smaller contributions to absorption are combined in the following manner:

$$\kappa_{tot} = \kappa^{ff}_{ion} + \kappa^{ff}_{H^-} + \kappa^{bf}_{H^-} + \kappa_{\text{Rayleigh}} + \kappa_{\text{Thompson}} \tag{2.7}$$

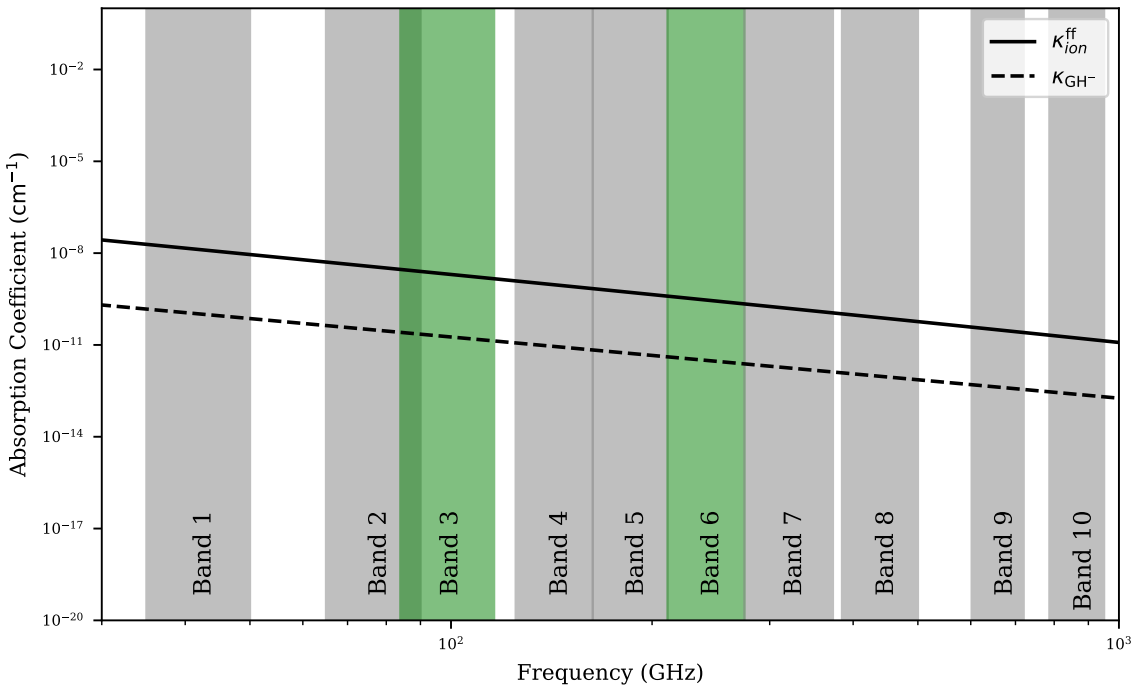

Figure 2.5: The distribution in frequency for absorption coefficients of thermal bremsstrahlung (solid line) and H^- (dashed line). The shaded areas show the 10 ALMA bands, with the two highlighted in green displaying the bands available in Cycle 4, 5 and 6 to solar physics observations, i.e. Bands 3 and 6. This figure was produced using a multi-thermal prominence model, as defined in Table 2.2, with a gas pressure of 0.1 dyn cm^{-2}.

2.3.3 Geometry and Integration Method

Whilst C2D2E can consider any range of line-of-sight directions or prominence inclinations, Rodger & Labrosse (2017) presented results from off-limb threads solely. I discuss using an alternative, on-disc, filament model in Section 3.2. For the off-limb prominence case the thread was orientated horizontally with respect to the solar surface, whilst the line of sight of the "observer" was directed to cross the cylindrical axis perpendicularly. A diagram showing the orientation of the prominence model with respect to the incident radiation from the solar disk is shown in Figure 2.1. A vertical field of view (FOV) is defined such that the centre of the FOV corresponds to the cylindrical axis of the thread. For each position in the FOV the maximum length for the path of a horizontal LOS through the thread is defined. Through interpolation the local temperature and absorption coefficient are determined at every point

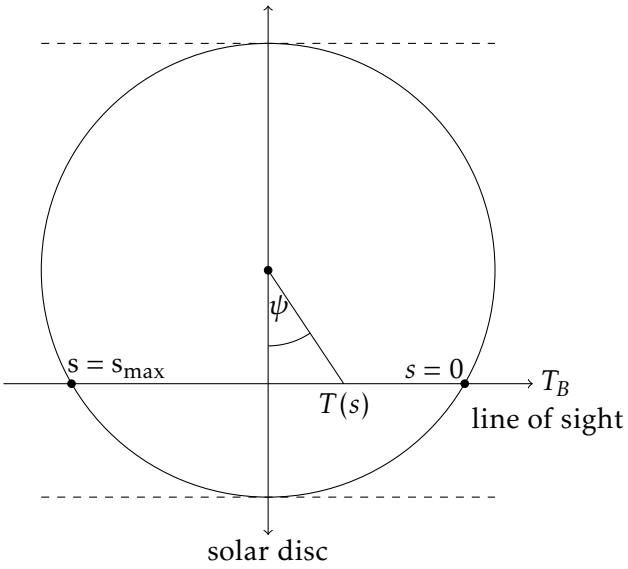

Figure 2.6: Schematic diagram showing the integration direction along a line-of-sight orthogonal to the cylindrical axis for an off-limb prominence model. Here $s = 0$ and $s = s_{\max}$ correspond to the start and the end of the light's path through the cylinder, respectively. The *dashed lines* correspond to the edges of the field of view. Adapted from a figure previously published in Rodger & Labrosse (2017).

on the path, and are then integrated in the manner described in Equation 1.17. The optical depth, τ_ν, is defined such that it is zero at the edge of the cylinder closest to the observer and maximal at the opposite end of the path. A schematic diagram of the geometry of these off-limb models is visualised in Figure 2.6.

The grid of radial and azimuthal positions defined for each thread quantity, *e.g.* electron temperature or absorption coefficient, is discrete and hence taking values at any given position along a path will require interpolation. The azimuthal grid has constant steps and is symmetric with respect to the ($\psi = 0$) plane, *i.e.* can be reduced to the range $[0,\pi]$. To interpolate across the azimuthal grid a Fourier method is utilised (Gouttebroze 2005). For a variable within the cylinder, F, an interpolated value for any given azimuth, ψ, is described by:

$$F(\psi) = \sum_{j=1}^{N_\psi} a_j \cos[(j-1)\psi] \,, \tag{2.8}$$

where N_ψ is the total number of positions in the azimuthal grid and a_j is a coefficient

calculated from the discretized variable, F_j. The coefficient, a_j is defined by:

$$a_j = \sum_{k=1}^{N_\psi} B_{jk} F_k \, . \tag{2.9}$$

The matrix, B, is defined solely by the azimuthal grid, as the inversion of the matrix $\|b\|$ (i.e. $\|B\| = \|b\|^{-1}$), where:

$$b_{jk} = \cos[(k-1)\psi_j]. \tag{2.10}$$

Fourier series interpolation has the advantages of smoothness and periodicity (Gouttebroze 2005).

2.4 Computed Brightness Temperatures

2.4.1 Isothermal-isobaric Fine-structures

Figure 2.7 shows the computed brightness temperature of 1.3 mm emission (ALMA band 6) across the synthetic field of view (FOV) for a set of isothermal-isobaric fine-structure models. The FOV is orientated such that the position axis increases with increasing distance from the solar surface. Figure 2.7a shows the brightness temperature across the field of view for models with differing isobaric pressures. From the equation of state, low pressures reduce the overall density of the prominence resulting in a lower brightness temperature, as lower densities yield lower optical thickness plasmas, i.e. see equation 2.2. Plasma which is optically thin, $\tau < 1$, in the EUV range allows ionizing incident radiation to penetrate throughout the thread, creating a symmetrical brightness temperature distribution. When considering increasingly high pressures the density will increase, and thus too the optical thickness and brightness temperature. Threads that are optically thick, $\tau > 1$, in the EUV range prevent incident radiation penetrating through the entire LOS. This causes a higher ionization towards the thread's lower boundary, which receives more radiation from the solar disk, relative to the upper boundary. The higher abundance of ionized material in turn increases inverse-thermal bremsstrahlung absorption in this area, leading to higher brightness temperatures, thus creating an asymmetric distribution, as can be seen in Figure 2.7. In all instances in Figure 2.7, the LOS through the prominence fine-structure model is optically thin for 1.3mm emission, so the respective brightness temperature is below the kinetic temperature of the plasma.

Figure 2.7b shows the brightness temperature across the field of view for models with the same constant pressure (0.1 dyn cm^{-2}) but with different temperatures. At low temperatures,

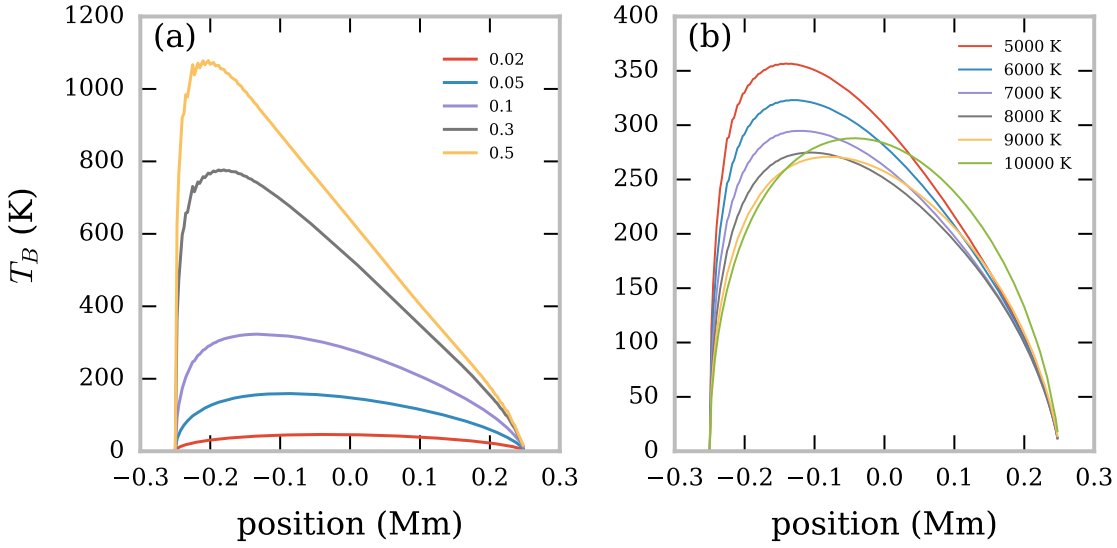

Figure 2.7: Computed brightness temperature across FOV for ALMA Band 6, $\lambda = 1.3$ mm. (a) shows the effect of increasing gas pressure (dyn cm^{-2}) on models with a temperature of 6000 K. (b) shows the effect of increasing temperature (K) on models with a gas pressure of 0.1 dyn cm^{-2}. Reproduction of a figure previously published in Rodger & Labrosse (2017).

an increase in the kinetic temperature causes a decrease in the brightness temperatures across the FOV. This will be partly due to the decreased density through the equation of state, but also partly due to being optically thin in the millimetre regime, as a predominantly thermal bremsstrahlung emission mechanism will yield a brightness temperature which is approximately $\propto T^{-\frac{1}{2}}$ (Equations 1.18 and 2.2). At high temperatures the increase in temperature leads to further ionization of the neutral material, increasing inverse-thermal bremsstrahlung opacity and thus the brightness temperature. When the material is ionized due to a temperature increase, the ionizing incident radiation has a less significant effect, creating a symmetrical brightness temperature distribution across the FOV.

In Figure 2.8 I show the wavelength, temperature and pressure dependence of the maximum (or peak) brightness temperature within the FOV for all isothermal-isobaric models considered in this study. This brightness temperature will also be dependent on the radius, *i.e.* length of the LOS, and the altitude of the prominence fine-structure. In Rodger & Labrosse (2017) we considered fixed values for both these quantities, whilst observationally these values could be fairly easily constrained.

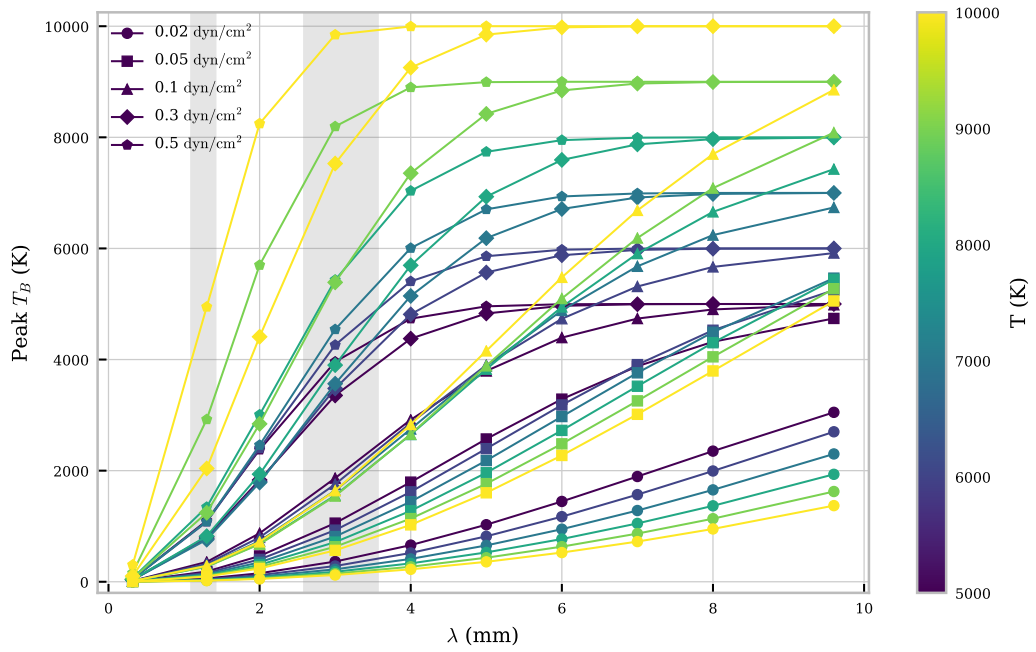

Figure 2.8: Relationship between peak brightness temperature and wavelength for a set of isothermal-isobaric fine structure models. Each colour corresponds to a constant temperature (K), as described in the colour bar to the right. Each symbol corresponds to a constant pressure (dyn cm^{-2}), as described in the legend. The two grey-shaded areas depict ALMA observing Bands 6 and 3. This is a reproduction of a figure previously published in Rodger & Labrosse (2017).

From Figure 2.8 it can be seen that the peak brightness temperature increases with wavelength, until the point at which it reaches the temperature of the plasma. From the Eddington-Barbier approximation the expected position where the brightness temperature first equals the temperature of the plasma should occur when the optical thickness at the observed wavelength reaches or exceeds unity. I discuss in more detail the required optical thickness such that the brightness temperature may be used as a direct analogue of the temperature of the emitting plasma in Section 2.4.1.1.

The brightness temperature generally increases with wavelength due to the enhanced absorption from inverse-thermal bremsstrahlung (Equation 2.2). The point at which the peak brightness temperature reaches saturation with the kinetic temperature is defined by the radiation's absorption coefficient, *i.e.* the higher the absorption coefficient, the lower the wavelength required to reach saturation with the kinetic temperature. The absorption

coefficient is not purely wavelength dependent, but also depends on electron and ion density and temperature: the higher the pressure, the higher the density, which leads to more absorption and thus higher brightness temperatures. Increasing temperature in high pressure models leads to more ionization and thus higher brightness temperatures. At low pressures, where the optical thickness is a lot less than 1, the brightness temperature is proportional to $T^{-\frac{1}{2}}$. Increasing the temperature can also decrease the overall density more than it increases the ionization, causing a decrease in absorption and brightness temperature.

Each individual isobaric-isothermal model produces a distinct peak brightness temperature versus wavelength curve. If geometrical variables such as altitude or LOS width can be constrained, a brightness temperature observation of an isobaric-isothermal fine-structure thread, at known wavelength, could be used in conjunction with our set of models to set constraints on the pressure and temperature of the structure in consideration. If multiple observations at different wavelength bands are available, the constraints on the isobaric-isothermal model should improve greatly.

2.4.1.1 Optical Thickness and the Direct Temperature Diagnostic

The observed brightness temperature from an optically thick plasma will be representative of primarily the temperature of the plasma at the transition where the optical depth reaches and exceeds unity through the Eddington-Barbier approximation, see Equation 1.10 in Section 1.2. For a perfectly isothermal, optically thick plasma a brightness temperature measurement would thus be an accurate representation of the kinetic temperature over the entire thread. Multiple wavelength observations from optically thick plasma would hence reproduce the same brightness temperature measurement, this is seen as the saturation features in Figure 2.8.

Although the Eddington-Barbier approximation suggests $T_B(\nu) \approx T(\tau(\nu) = 1)$ the exact optical depth required for this equality will be slightly larger. Figure 2.9 presents a combined scatter plot for output brightness temperature versus overall thread optical thickness in all isothermal-isobaric fine-structure models, across all LOS in each FOV, and at 10 wavelengths ranging from 0.32 to 9.60 mm. The temperature of each model is given by the colour as defined in the plot's colourbar and displayed on the plot as the faint, horizontal line with matching colour. It can be seen that for all models the minimum optical thickness required for the brightness temperature to equal the kinetic temperature of the given isothermal-isobaric model is approximately between $\tau \sim 4$–5.

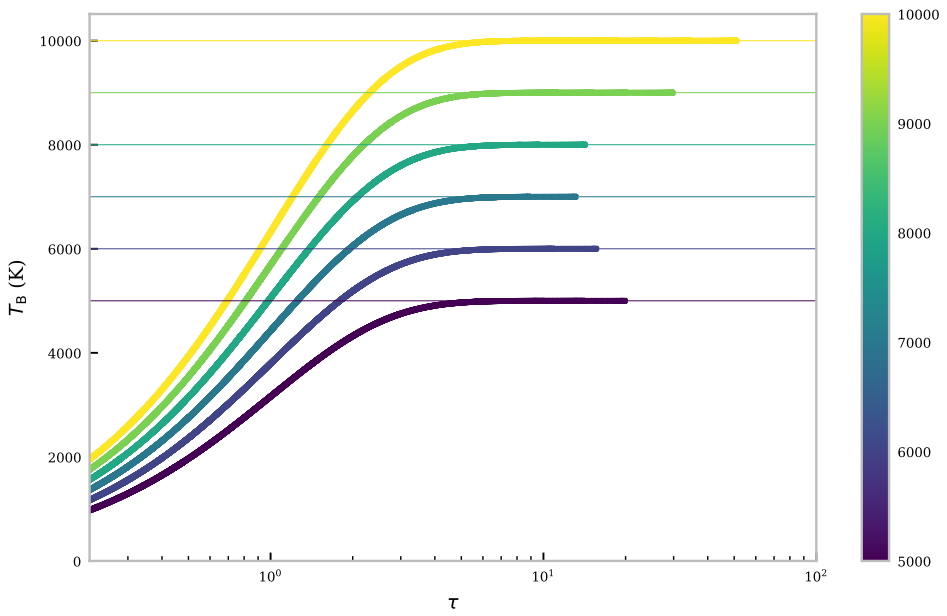

Figure 2.9: Scatter plot showing the brightness temperature versus optical thickness relationship for the full set of 30 isothermal-isobaric fine-structure prominence models. For each model the scatter plot consists of all LOSs in the FOV and 10 wavelengths spanning ALMA's potential observing range. The colour determines the temperature of the model as defined in K in the colour bar to the right of the main panel. The thin, horizontal lines of matching colour to the scatter plots show the isothermal temperature of the given models.

Due to their limited spatial extent, individual observed fine-structure threads will naturally tend towards being optically thin in the millimetre-continuum for all cases excluding the highest wavelengths and absorption. In this set of isobaric-isothermal models with radius of 250 km, the peak optical thickness of Band 6 radiation fails to reach $\tau = 1$ for all models, whilst the optical thickness of Band 3 radiation exceeds $\tau = 1$ for models at pressures of 0.3 or 0.5 dyn cm^{-2} (Table 2.1). The relationship between wavelength and peak optical thickness, which is defined here as the maximum optical thickness for any LOS within the FOV, for this set of isothermal-isobaric fine-structure models is shown in Figure 2.10. Increasing the length of the LOS will increase the optical thickness at the observed wavelength.

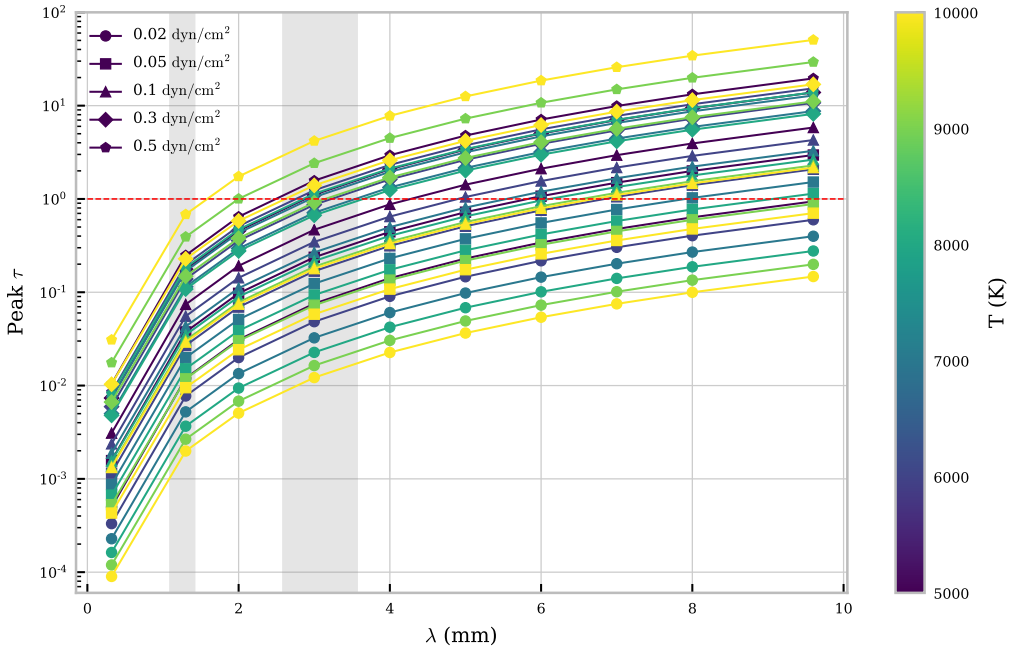

Figure 2.10: Relationship between peak optical thickness and wavelength for a set of isothermal-isobaric fine-structure models. Each colour corresponds to a temperature (K) as described in the colourbar to the right. Each symbol corresponds to a pressure (dyn cm^{-2}) as described in the legend. The red-dashed line shows the transition between optically thick and optically thin emission. The two grey-shaded areas depict ALMA observing Bands 6 and 3. Reproduction of a figure previously published in Rodger & Labrosse (2017).

2.4.2 Multi-thermal Large-scale Structures

In Figure 2.11 I show the variation of the brightness temperature across the FOV for a large-scale prominence structure model with a radially increasing temperature distribution and a constant pressure of 0.1 dyn cm^{-2} (Table 2.2) at several millimetre/sub-millimetre wavelengths. Immediately it can be seen that there are two regimes that can describe the brightness temperature variation. The emission at 0.45, 1.3 and 3.0 mm is emitted from optically thin ($\tau < 1$) plasma in this model, and thus displays a smooth, asymmetric variation across the FOV. Emission at 5.0, 7.0 and 9.0 mm is emitted from optically thick ($\tau \geq 1$) plasma and shows a nearly symmetric, dual-peaked variation. The formation of these two regimes is better understood through considering the contribution function and its constituent parts (see Figures 2.12 and 2.13).

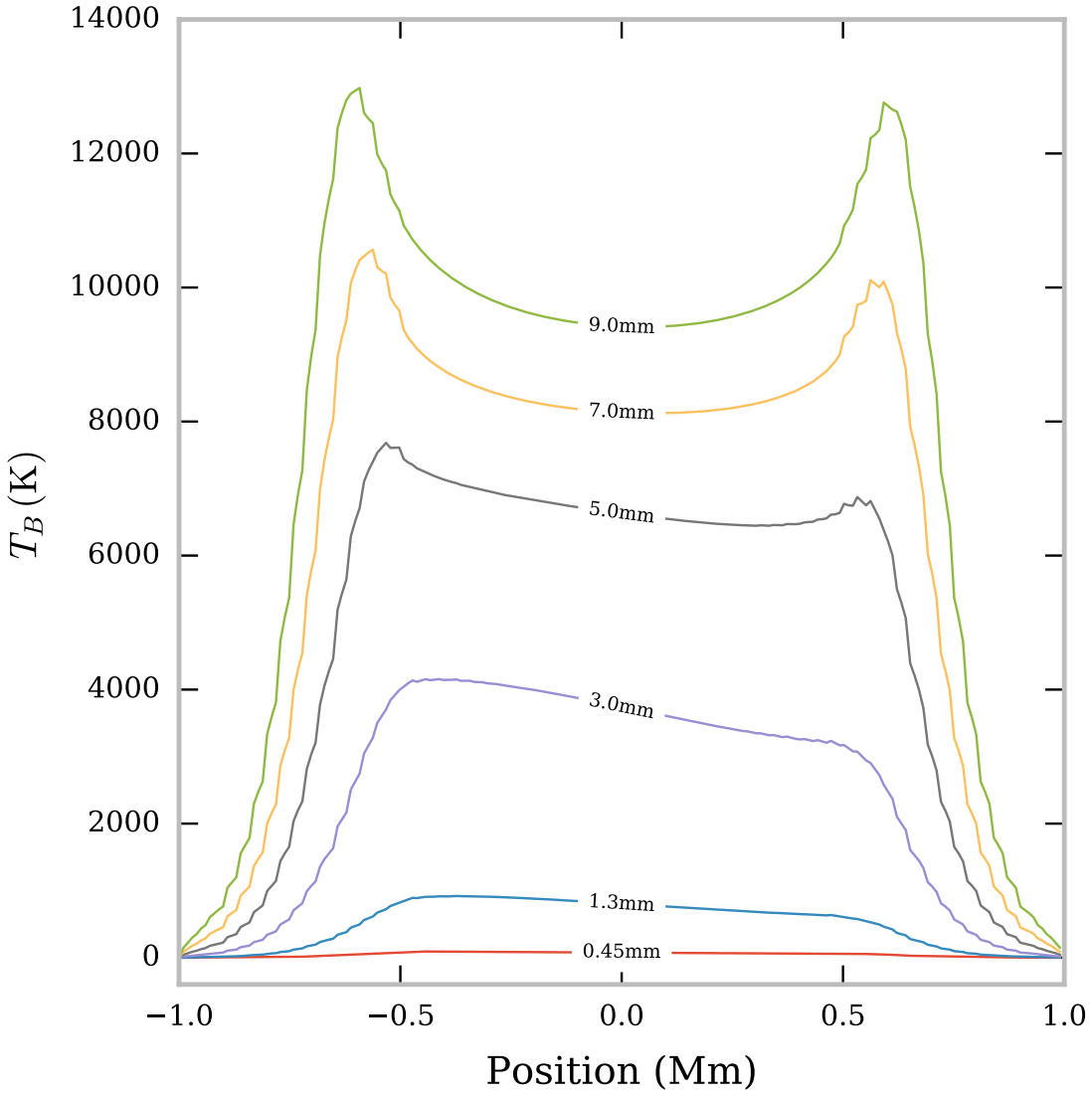

Figure 2.11: Variation of brightness temperatures across FOV in multi-thermal large-scale prominence models. The pressure is 0.1 dyn cm^{-2} and the FOV is orientated vertically in the solar atmosphere with the positive x-axis directed radially away from the Sun. Reproduction of a figure previously published in Rodger & Labrosse (2017).

The formation plots, Figures 2.12 and 2.13, show how the distributions of absorption coefficient, source function and optical thickness combine across the thread to produce the contribution function distribution seen in the bottom right panel of each figure. In this study the contribution function is defined to be the direct product of the absorption coefficient,

source function and the exponential optical thickness attenuation term, $e^{-\tau_\nu}$. Integrating the contribution function along a path will yield the observed brightness temperature for that given LOS. In Figure 2.12 the formation of the millimetre continuum from an optically thin plasma is shown. Here the attenuation term, $e^{-\tau_\nu}$, is close to 1 and nearly uniform across all LOSs in this cross-section. Photons with millimetre wavelengths will thus travel through the thread mostly unperturbed allowing the plasma at the far side of the LOS to have almost equal contribution when compared to the material near the surface closest to the observer. The prominence plasma is, however, non-transparent at UV wavelengths. This leads to an increase in ionizing radiation incident on the lower side of the thread, resulting in higher ionization, and therefore higher contribution function at the side of the thread closer to the solar disc. Choosing an integrating path orthogonal to the cylindrical axis results in a brightness temperature curve for the FOV as seen in the bottom right figure. The brightness temperature distribution is skewed towards the lower boundary of the prominence due to the increased ionization from incident radiation. The temperature variation is azimuthally symmetrical, hence, so too is the source function (Equation 1.14).

Figure 2.13 is an example of millimetre-continuum formation from a predominantly optically thick prominence plasma, where within the central part of the thread the optical thickness attenuation term has a large effect. The red-dashed line represents the $\tau = 1$ line, *i.e.* the point in which the thread becomes optically thick. The high attenuation within the central region leads to a crescent shaped contribution function map around the $\tau = 1$ line. This causes the core and far side of the thread to be under-represented in the integration over the LOS. The two peaks in the brightness temperature variation correspond to the extremal heights for which the plasma is optically thick. This is due to a longer LOS intersecting through more high temperature, PCTR material. Further out with respect to the cylindrical axis from the peaks, the LOSs are once again optically thin and the brightness temperature drops off steeply.

The incident radiation ionizing the optically thick plasma leads to an increase in absorption coefficient but also an increase in attenuation from the $e^{-\tau_\nu}$ term. This produces an almost symmetrical brightness temperature variation.

2.4.2.1 Thermal Diagnostic for Multi-thermal Structures

It is difficult to determine information on the structure of a temperature distribution from brightness temperature measurements of optically thin plasma. The resultant brightness

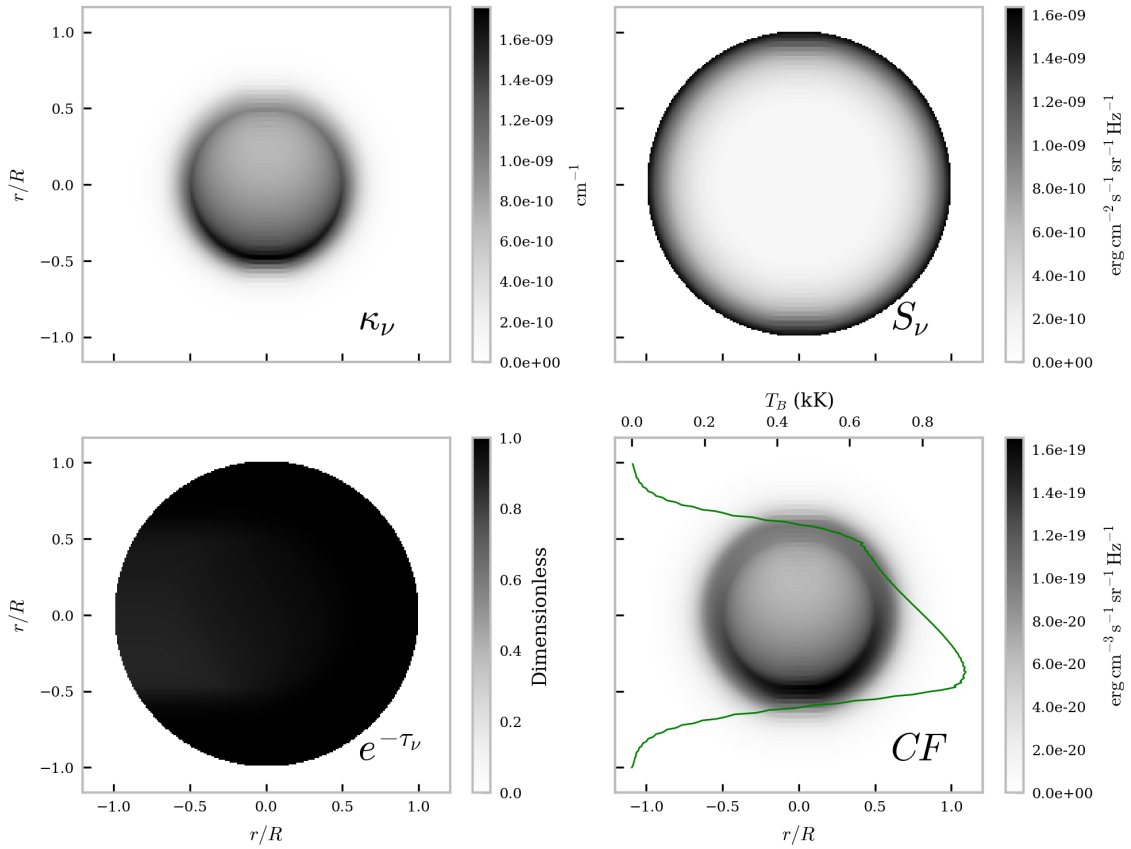

Figure 2.12: Formation plot for the millimetre-continuum from an optically thin prominence plasma. The model used is a multi-thermal large-scale prominence structure with gas pressure of 0.1 dyn cm^{-2}, evaluated at a wavelength of $\lambda = 1.3$ mm. The *top left* figure shows a map of the absorption coefficient, the *top right* shows the source function, and the *bottom left* shows the optical thickness attenuation term. The source function here is described by the Planck function. The contribution function map, *bottom right* hand panel, results from the product of the other three panels. Integrating the contribution function over each horizontal LOS results in the "observed" brightness temperature (K) curve for the FOV, *solid green line*. r/R defines the position in terms of the fractional radius of the cylinder, which is given in Table 2.2. Reproduction of a figure previously published in Rodger & Labrosse (2017).

temperature will be an integration over potentially large temperature variations, hence losing any discernible structure. Conversely, optically thick emission is representative of a specific formation region, *i.e.* the Eddington-Barbier approximation states $T_B(\nu) \approx T(\tau_\nu = 1)$ (Section 1.2.2.1). See Section 2.4.1.1 for a discussion on the optical thickness required for a

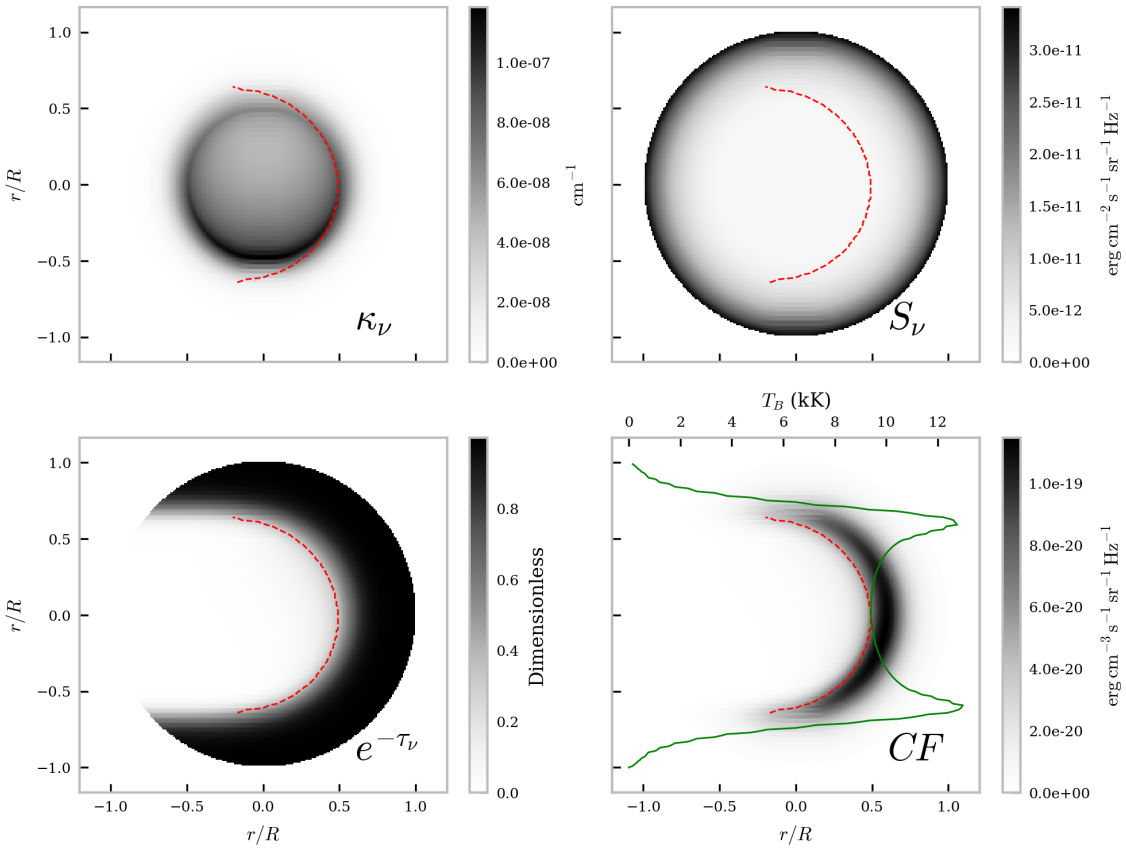

Figure 2.13: Formation plot for the millimetre-continuum from an optically thick prominence plasma. The model used is a multi-thermal large-scale prominence structure with gas pressure of 0.1 dyn cm^{-2}, evaluated at a wavelength of $\lambda = 9$ mm. The *top left* figure shows a map of the absorption coefficient, the *top right* shows the source function, and the *bottom left* shows the optical thickness attenuation term. The source function here is described by the Planck function. The contribution function map, *bottom right* hand panel, results from the product of the other three panels. Integrating the contribution function over each horizontal LOS results in the "observed" brightness temperature (K) curve for the FOV, *solid green line*. The *dashed red line* shows the $\tau = 1$ line. r/R defines the position in terms of the fractional radius of the cylinder, which is given in Table 2.2. Reproduction of a figure previously published in Rodger & Labrosse (2017).

direct temperature diagnostic with respect to isothermal models.

To investigate how a brightness temperature measurement relates to the prominence plasma in a given formation region an effective formation layer is defined as the parts of

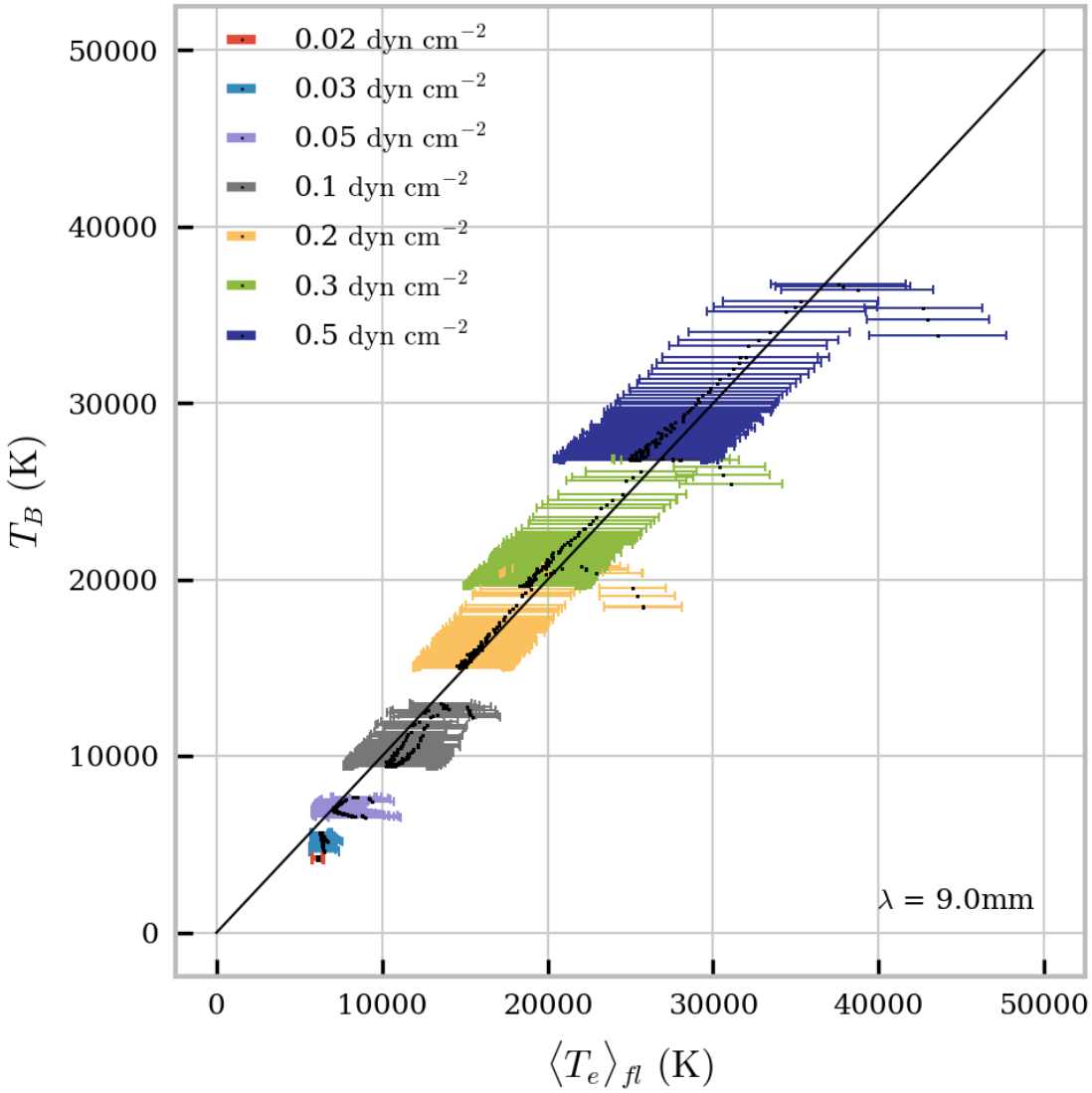

Figure 2.14: Relationship between brightness temperature and average kinetic temperature over the formation layer in the LOS. The formation layer is defined as the region or regions with ≥ 70% of the maximum contribution function for each LOS in which the plasma is optically thick. The error bars show a representation of the width of the kinetic temperature distribution within the formation layer. Each colour corresponds to a different pressure as defined in the legend. Reproduction of a figure previously published in Rodger & Labrosse (2017).

the prominence where the contribution is equal to or greater than 70% of the maximum contribution function for each LOS. The effective formation temperature ($\langle T \rangle_{\rm fl}$) is then found by taking the contribution function weighted mean of the temperature distribution across the effective formation layer.

Figure 2.14 shows the relationship between the computed brightness temperature and the mean temperature of the effective formation layer for $\lambda = 9.0$ mm, across a range of pressures. Each point on the graph represents an optically thick LOS. Optically thin LOSs are ignored as their contribution functions are very broad across the LOS, giving poor temperature diagnostics. At higher pressures more of the thread is optically thick, and hence more LOS points are shown on the graph. For the majority of LOSs the brightness temperature scales linearly with the mean temperature of the formation layer, with only some deviation at high temperatures in each model, and for low pressure models. At low pressures, the effect of lower boundary ionization from incident radiation can again be seen through the splitting of the trend into two separate lines. Observations of brightness temperatures at optically thick wavelengths, such as $\lambda = 9.0$ mm, are thus fairly good indicators of the mean electron temperature of specific areas of the prominence. Restricting the analysis to LOSs with optical thickness greater than 4, as discussed in Section 2.4.1.1, both sets of deviating points due to either low pressure or high temperature LOSs are removed. For a prominence of structure corresponding to this model, and with high resolution observations of multiple optically thick wavelength bands, it should be possible to build up an understanding of the temperature distribution within the prominence structure, as each wavelength band should be formed at a different formation layer. Although, as discussed in Gunár et al. (2018), it will be difficult to map the temperature structure of prominences made of multiple individual fine-structure threads without a clear global temperature structure, as the effective formation region will likely cover multiple different threads, unless the plasma is very optically thick.

In Cycles 4, 5 and 6 of ALMA the only two wavelength bands available to solar observations were Bands 3 and 6, with Band 7 becoming available in the upcoming Cycle 7. These bands are significantly less optically thick than radiation at $\lambda = 9.0$ mm, with τ for Bands 3 and 6 only exceeding unity at the centre of the thread for models with high pressures. The relationship between wavelength and peak optical thickness is shown in Figure 2.15 for the multi-thermal models described in Table 2.2. The two grey shaded areas represent ALMA Bands 3 and 6. As expected, the peak optical thickness (*i.e.* the maximum optical thickness found in each model as the line of sight is varied) increases with wavelength and

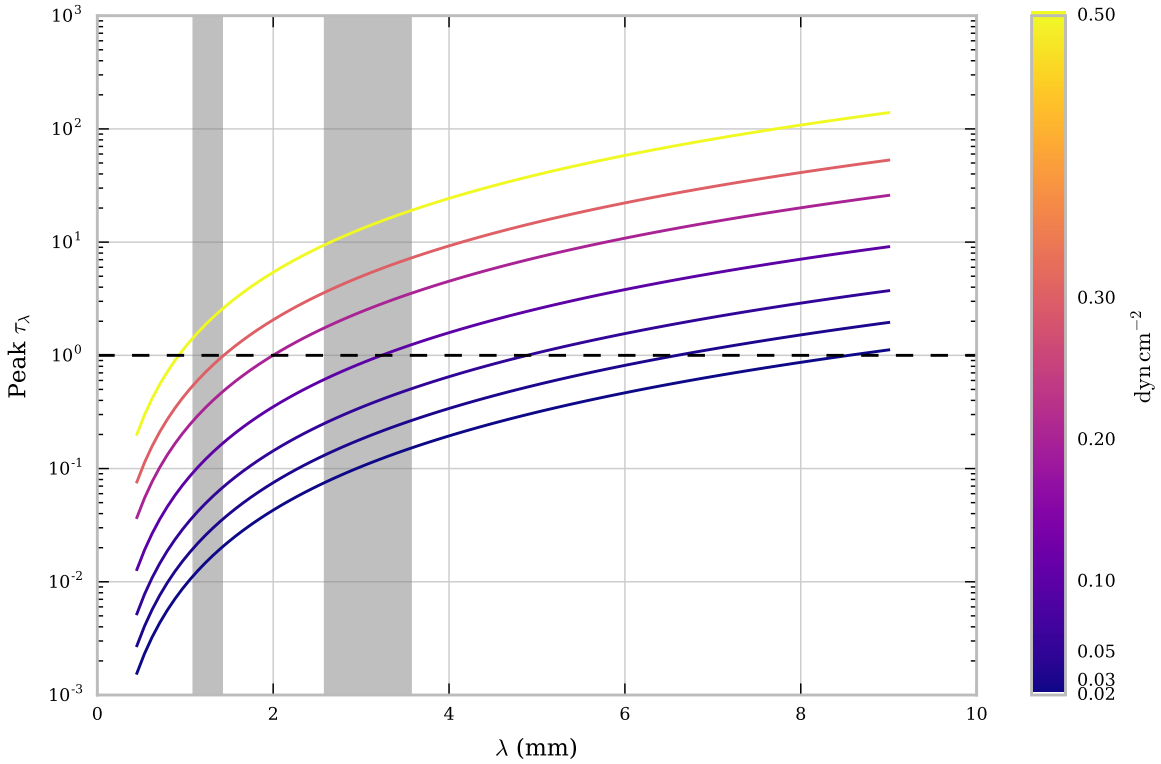

Figure 2.15: Relationship between peak optical thickness and wavelength for a set of multi-thermal large scale structures at various pressures. The dashed line represents the transition between optically thin and thick plasma. The two grey shaded areas cover ALMA Bands 3 and 6. Reproduction of a figure previously published in Rodger & Labrosse (2017).

with pressure. Figure 2.15 shows that a structure of a similar size to what is modelled here (radius ≈ 1000 km) observed with ALMA in Bands 3 and 6 can only be expected to be optically thick in both bands at high pressures, *i.e.* greater than 0.5 dyn cm^{-2}.

2.5 Conclusion

In conclusion, this chapter presents the development of a 2D cylindrical non-LTE radiative transfer model for the millimetre/sub-millimetre continuum. In doing so it predominantly covers work previously published in Rodger & Labrosse (2017). The development of the models involved defining suitable input parameters for two distinct types of prominence model (isothermal-isobaric fine-structure and multi-thermal large-scale prominence models), as well as the cylindrical geometry and relevant emission mechanisms.

The results from the isothermal-isobaric fine-structure models prove the strong potential for plasma diagnostics using millimetre/sub-millimetre wavelength measurements, i.e. such as are now available to solar physics at much higher spatial resolutions than previously with the advent of the *Atacama Large Millimeter/sub-millimeter Array* (ALMA). It is found that for plasmas with optical thicknesses greater than ~ 4–5 that the brightness temperature emitted should equal the constant temperature provided by the model. Whilst for optically thin plasma, multiple observations at varying millimetre/sub-millimetre wavelengths could be used to restrict the set of realistic prominence models using the brightness temperature spectrum, provided such physical parameters as thread width and altitude can be constrained also.

For multi-thermal models the temperature diagnostic becomes more complex as the brightness temperature of a sufficiently optically thick plasma will be representative of a given formation region, rather than the whole thread. As such it was found that a linear relationship exists between the brightness temperature observed from the thread and the contribution function weighted mean kinetic temperature for the LOS's formation region, which was defined as the region with $\geq 70\%$ the maximum contribution function for that LOS. The linear relation again improves, however, when restricted to LOSs with $\tau \geq 4$ only.

In all instances the importance of understanding the optical thickness of the continuum radiation is clear, and thus much of the following chapters investigate possible methods for estimation of the millimetre/sub-millimetre optical thickness.

Chapter 3

Applications of Modelling Work

In this chapter I shall cover the work I have conducted applying the modelling work described in the last chapter after the publication of Rodger & Labrosse (2017). This will also include, in Section 3.1, a discussion into an improved method for the estimation of the thermal Gaunt factor where an interpolated value of an exact calculation is used in place of the classical limit assumption. For the rest of the chapter I then cover two applications for the millimetre-prominence code presented in Chapter 2: modelling solar filament emission, and comparing the prominence millimetre-continuum emission to that from prominent hydrogen and helium lines. In Section 3.2 I discuss how the prominence model of Chapter 2 was successfully altered to simulate the millimetre-wavelength emission from solar on-disk structures, such as solar filaments. The results from this study are summarised and discussed in Section 3.2.3. Finally, in Section 3.3 I cover my efforts using the C2D2E model to understand the correlations found between millimetre-wavelength emission from solar prominences with corresponding hydrogen and helium line emission; with the results summarised in Section 3.3.4.

3.1 Improved Estimation of the Thermal Gaunt Factor

Thermal bremsstrahlung, or braking radiation, is the continuum process where an electron is decelerated through deflection within the Coulomb field of an ion such that it emits a photon. The inverse to this process is a form of free-free absorption wherein an electron will resonantly oscillate with an electromagnetic wave. The electron will gain kinetic energy through this process which will be subsequently dispersed through electron-ion collisions. In the expression for the absorption coefficient for inverse thermal bremsstrahlung, a variable called

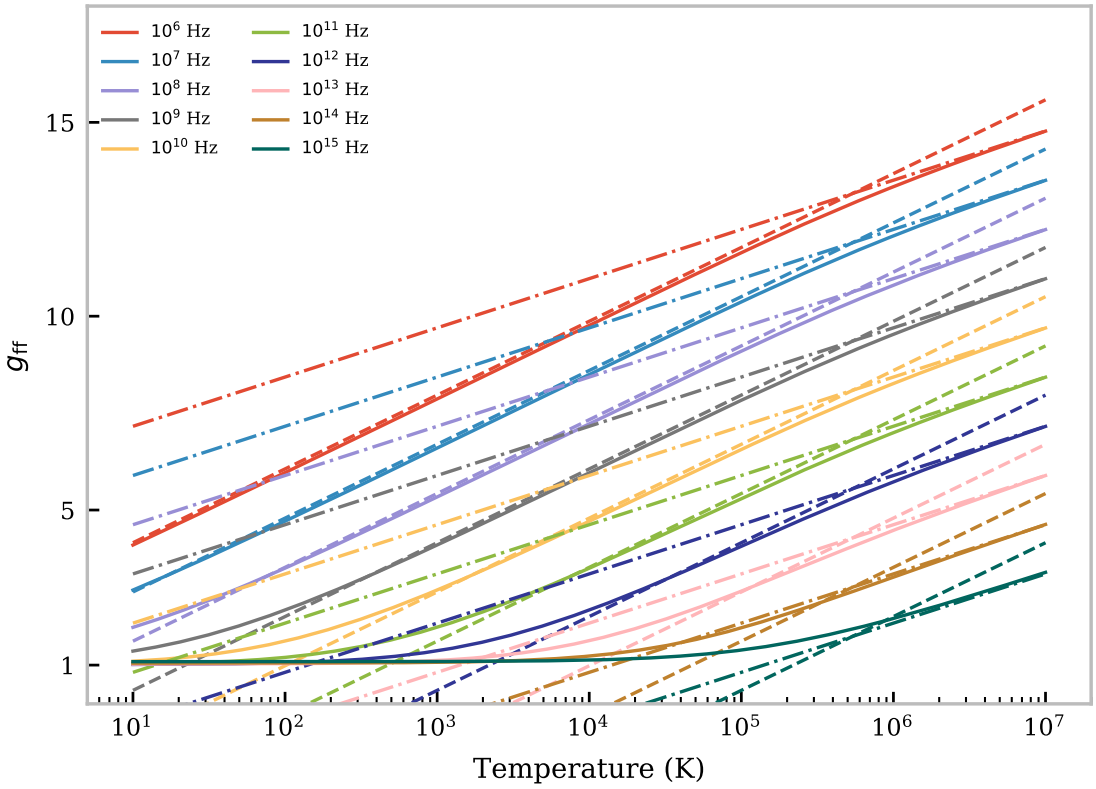

Figure 3.1: Replication of Gayet (1970) Figure 2 using Equations 3.2 (*dashed line*), 3.4 (*dot-dashed line*) and values interpolated from the table of calculated exact thermally averaged Gaunt Factors of van Hoof et al. (2014) (*solid line*). Each colour represents a frequency given in the legend.

the thermally-averaged Gaunt factor, $g_{\rm ff}$, often appears. It is proportional to the logarithm of the ratio between maximum and minimum impact parameters, and is averaged with respect to a Maxwellian distribution. When considering specific limits for the Gaunt factor this average yields manageable integrals, however, the exact formula cannot be described by simple functions in this way (Oster 1963; Dulk 1985). In Chapter 2 and Rodger & Labrosse (2017) I used the classical limit approximation for the thermally-averaged aunt factor to define the absorption coefficient in our models, see Equation 2.2. The classical limit approximation assumes a temperature less then 2×10^5 K, and is defined in Wedemeyer et al. (2016), as an adaption of work in Dulk (1985) as:

$$g_{\rm ff\,classical} = \frac{\sqrt{3}}{\pi} \ln\left(\frac{(2k_{\rm B}T)^{3/2}}{2\pi\Gamma\nu\sqrt{m_e}e^2} \right), \tag{3.1}$$

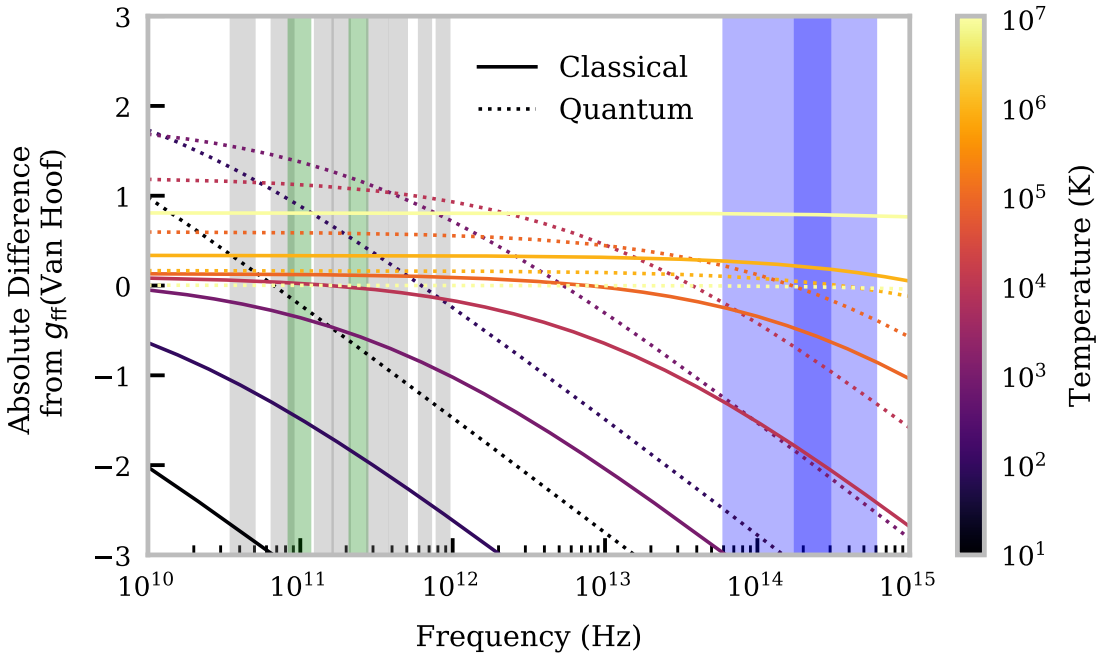

Figure 3.2: Absolute difference between the classical (3.2) and quantum (3.4) assumptions for the thermally-averaged Gaunt factor with the value as interpolated from the table of calculated values of van Hoof et al. (2014). Plot shows variation over frequency for a set of different temperatures given by the colour of each line using the colour bar to the right of the plot. The ALMA observing bands are shown on the plot as shaded regions in grey, with bands 3 and 6 highlighted in green. The blue shaded regions show the infra-red regime which will be observable by the DKIST Cryo-NIRSP, and DL-NIRSP instruments, respectively.

where m_e and e are the mass and charge of the electron, respectively, and Γ is Euler's constant which is ≈ 1.781. Numerically this approximates to:

$$g_{\mathrm{ff\,classical}} \approx \frac{\sqrt{3}}{\pi}(17.9 + \ln(T^{3/2}) - \ln(\nu)). \tag{3.2}$$

For temperatures greater than 2×10^5 K, there exists a quantum limit approximation, which is defined in Dulk (1985) as:

$$g_{\mathrm{ff\,quantum}} = \frac{\sqrt{3}}{\pi}\ln\left(\frac{2k_{\mathrm{B}}T}{h\nu}\right), \tag{3.3}$$

where h is the Planck constant. This equation approximates numerically to:

$$g_{\mathrm{ff\,quantum}} \approx \frac{\sqrt{3}}{\pi}(24.5 + \ln(T) - \ln(\nu)). \tag{3.4}$$

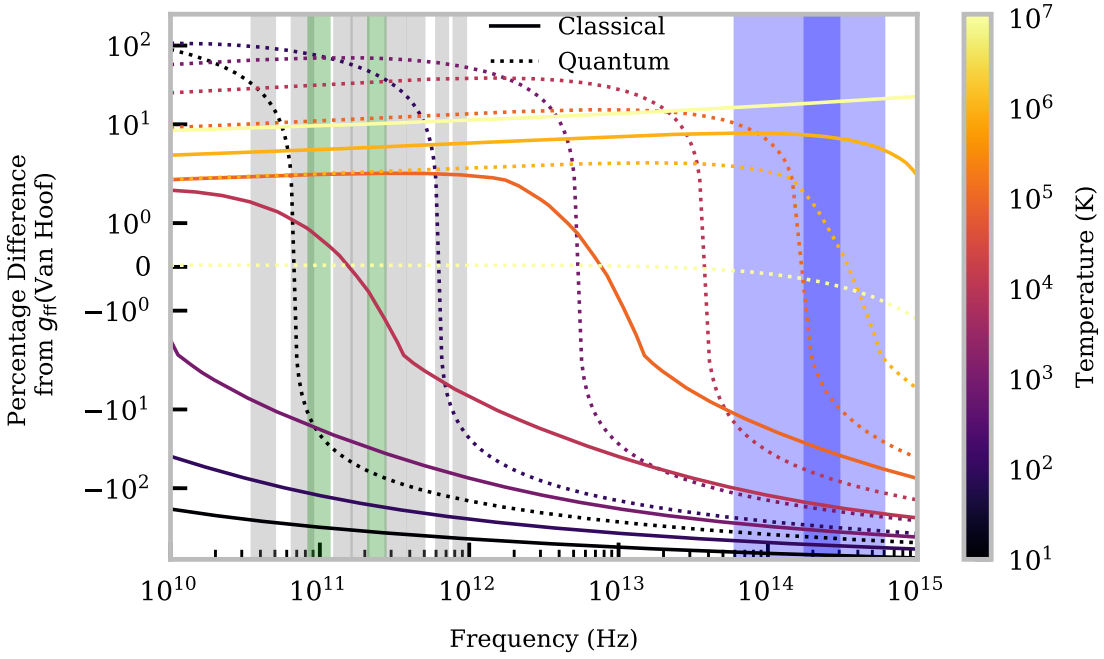

Figure 3.3: Relative difference between the classical (3.2) and quantum (3.4) assumptions for the thermally-averaged Gaunt factor with the value as interpolated from the table of calculated values of van Hoof et al. (2014) as a percentage of the van Hoof et al. (2014) value. Plot shows variation over frequency for a set of different temperatures given by the colour of each line using the colour bar to the right of the plot. The ALMA observing bands are shown on the plot as shaded regions in grey, with bands 3 and 6 highlighted in green. The blue shaded regions show the infra-red regime which will be observable by the DKIST Cryo-NIRSP, and DL-NIRSP instruments, respectively.

In Gayet (1970) a comparison is shown between the classical and quantum limit approximations, with the average over a maxwellian distribution of the exact quantum formula of Menzel & Pekeris (1935) and Sommerfeld (1951). The two separate exact formula for the Gaunt factor of Menzel & Pekeris (1935) and Sommerfeld (1951) were previously proven to be equivalent by Grant (1958). The exact quantum formula is beyond the scope of this study, and thus is not given here, although it can be found in e.g. Gayet (1970). In Gayet (1970) the author shows that a combination of the two approximations, Equations 3.1 and 3.3, are suitably equivalent to the exact formula for radio frequencies ($\nu \leq 10^{10}$ Hz) and for astrophysical temperatures. This is in agreement with Oster (1963). Whilst, at higher frequencies ($\nu > 10^{11}$ Hz), such as in the infra-red regime, Gayet (1970) finds that the exact

formula is necessary. With the frequency range of ALMA spanning from $\sim 10^{10}$–10^{12} Hz, the question of which method for aunt factor calculation is appropriate arises.

van Hoof et al. (2014) have produced a data set of calculated exact thermally-averaged, non-relativistic Gaunt factor values over a wider frequency and temperature range than has previously been published. Using interpolation of this data set, as was previously done in Simões et al. (2017), these values are compared to the classical and quantum limit approximations in a reproduction of Figure 2 of Gayet (1970), with an extended range of frequencies covering the infra-red observing range of the CRYO-NIRSP[1] (1000 – 5000 nm) and DL-NIRSP[2] (500 – 1700 nm) instruments at the upcoming DKIST telescope, in Figure 3.1.

Figure 3.1 successfully reproduces Figure 2 of Gayet (1970), thus showing firstly that this interpolation of the table of values presented by van Hoof et al. (2014) correctly and reliably gives estimates of the exact thermally-averaged Gaunt factor, and secondly that the trend-line for infra-red frequencies, up to those observable by DKIST, is poorly approximated by the classical limit, whilst the quantum limit assumption only holds for very high temperatures.

In Figures 3.2 and 3.3 I look more closely at the difference from the exact Gaunt factor value for both the classical and quantum limit approximations within the frequency range observable with ALMA and DKIST's CRYO-NIRSP and DL-NIRSP instrument, with Figure 3.2 showing the absolute difference and Figure 3.3 showing the relative difference as a percentage. For low temperatures (below 10^3 K), both the classical and quantum limit assumptions poorly reproduce the exact Gaunt factor calculations. At these temperatures the classical assumption underestimates the exact value in the frequency range of ALMA, whilst greatly underestimating it in DKIST's infra-red range. The quantum assumption, in this temperature range, varies from slightly overestimating to underestimating the Gaunt factor. The small overestimation in absolute difference does, however, translate to a large overestimation in the relative value.

For the temperatures in the middle of our set (i.e. 10^4 – 10^5 K), the classical assumption is a fairly good approximation for the ALMA frequencies (i.e. ~ 0.1–0.2 in absolute difference or $< 10\%$ in relative difference away from the interpolated van Hoof et al. (2014) value), but underestimates it in the infra-red regime. The quantum assumption overestimates the Gaunt factor for ALMA frequency emission at these temperatures, but underestimates it in the infra-red.

[1] https://dkist.nso.edu/inst/CryoNIRSP
[2] http://dlnirsp.ifa-instruments.org/DL-NIRSP/

At the highest temperatures considered (10^6 K and above), the classical assumption overestimates the aunt factor in the ALMA and DKIST frequency ranges, whilst the quantum assumption is a fairly good approximation.

Prominences could feasibly be expected to have core temperatures ranging from $\sim 4\times10^3$–1×10^5 K, and with PCTR reaching up to 10^6 K(Labrosse et al. 2010). Whilst the classical assumption, for the ALMA frequencies, is fairly good across most of this range, it does differ towards the extremal temperatures. DKIST infra-red frequencies on the other hand, are only represented well by the quantum limit, and only at very high temperatures. Therefore, in order to be able to consider a large range of potential prominence/PCTR temperatures at both ALMA and infra-red frequencies, the interpolated values for the exact thermally-averaged Gaunt factor calculated by van Hoof et al. (2014) are now used to estimate the absorption coefficient for thermal bremsstrahlung in all future modelling studies. Re-arranging Equation 2.2 to remove the classical limit approximation (Equation 3.2), an expression for the absorption coefficient is found as follows:

$$\kappa_{\text{ion}}^{\text{ff}} \approx 1.77\times10^{-2}\frac{n_e g_{\text{ff}}}{\nu^2 T^{\frac{3}{2}}}\sum_i Z_i^2 n_i. \tag{3.5}$$

3.2 Modelling the Visibility of Solar Filaments in the Millimetre-continuum

Millimetre to centimetre observations of solar filaments have been observed as "*temperature depressions*" on the solar disk (Kundu 1972). There have, however, been observations at longer decimetre wavelengths where filaments have been observed in emission e.g. Lang & Willson (1989) who attributed the increased emission to a hot plasma envelope around the cool Hα filament. In a more recent study, using the Nançay Radioheliograph, which is a T-shaped interferometer, and using Earth-rotation aperture synthesis, Marqué (2004) presented a set of filament observations at 73cm. Earth-rotation interferometry allows for an improved angular resolution through additional sampling of the u-v plane, with the caveat that it requires long time-scales such that dynamic motions cannot be resolved. Despite this, however, the finest resolution achieved in this study was 0′.4 which varied with observation date and direction. They found filaments to appear as so called "radio depressions", with the width of the depressions wider than the corresponding Hα filaments, and more similar to the filament channels observed in EUV observations. The author's suggested reason for these results is that

the radio depressions are not related to absorption by cool material (i.e. Hα filaments), but rather to the surrounding coronal or filament channel environment. It is highlighted that the literature on filament observations in millimetre–centimetre wavelengths has frequently been contradictory with some studies suggesting broadening of the radio depression compared to Hα filaments, and some not, e.g. Kundu (1972) and Kundu & McCullough (1972) found that filaments were larger than the optical counterparts, whilst Butz et al. (1975) found that they had a similar extent. Kundu et al. (1978) suggested that the broadening was due to an intrinsic difference in the surrounding environment of solar filaments compared to the quiet corona. These regions would be of a low density compared to the quiet corona, and are termed as cavities. The decreased optical thickness in the coronal cavity would cause the $\tau = 1$ line to lie lower within the solar atmosphere where the electron temperature is smaller, resulting in lower brightness temperatures. Marqué (2004) suggests that the contradictory evidence for filament broadening could be due to instrumental differences, or to intrinsic variability in the relationship between the filament cavity, and the filament itself. Bastian et al. (1993), on the other hand, suggest a different cause for the wider observed temperature depressions at radio wavelengths. Rather than a lower brightness temperature due to a cavity within the corona, they suggest that the depression may be caused by a significant reduction in chromospheric heating in filament channels, which they say is evidenced by a lack of spicules and network activity.

In Gunár et al. (2016) the authors simulated the visibility of a solar prominence/filament with ALMA using their 3D Whole Prominence Fine Structure (WPFS) model. The WPFS model produces a 3D prominence through the identification of dipped magnetic fields within a magnetic field model, and subsequently filling said dips with plasma. The model does not calculate the ionization degree through full non-LTE radiative transfer modelling, but rather the fast approximate radiative transfer method presented in Heinzel et al. (2015b). To calculate the background emission from the solar disk these authors calculated the emission produced using the C7 model of Avrett & Loeser (2008), and applied this result to each column within their 3D grid. The authors found that their filament could be observed in either emission or absorption against the solar disk, dependent on the particular LOS and its optical thickness. The central parts of their filament appeared dark for high wavelengths (e.g. 9mm), whilst the peripheral parts appeared bright.

In this project I aim to investigate the visibility of solar filaments using the 2D solar prominence models described in Chapter 2. Due to the geometry of the C2D2E model the

emission from the filament alone is considered in isolation without the capability to account for changes in the emission due to e.g. a filament cavity. This approach, however, in conjunction with millimetre observations of a solar filament could result in better understanding of any effect caused by the presence, or lack thereof, of the said cavity above the filament structure. In doing so I consider the effect of a variable background brightness temperature from the solar disk as is observed across the chromospheric network and internetwork. As was done in the previous chapter for solar prominences, both isothermal-isobaric models and multi-thermal models with a PCTR are considered in this study. I discuss the necessary changes to the prominence model required to simulate solar filaments in Section 3.2.1. The results which are found from isothermal-isobaric and multi-thermal models are presented in Section 3.2.2, whilst a brief summary and discussion are given in Section 3.2.3.

3.2.1 Defining the Filament Model

Despite being the same structures, prominences and filaments display significantly different features. Optical filaments appear like long elongated dark structures in absorption, whilst off-limb prominences appear bright in emission. Prominences also show significantly more faint, wispy fine structure compared to the less highly contrasted view of solar filaments. These changes are due to the differences in the background emission in the LOS, as well as the angle for which the observer's LOS views the prominence/filament. When modelling the emission from a solar prominence the incident radiation at the far end of the LOS, i.e. the background corona, is usually considered negligible. The difference caused by considering radiation from within the corona on any incident radiation within the solar atmosphere is, however, considered in Brown & Labrosse (2018). Conversely, the background incident radiation from the solar disk onto a solar filament is integral to the definition of the observable filamentary structure. Using the prominence models described in Chapter 2 to calculate the emission from an on-disk filament thus requires two changes to the code: an alteration to the LOS geometry, and the inclusion of incident radiation at the disk side of the LOS.

3.2.1.1 Geometry of the Model Filament

The geometry chosen for the filament model is a cylinder orientated parallel to the solar disk, with an observer viewing the structure from above (i.e. orthogonal to the solar disk/cylindrical axis). This geometry is shown as a schematic diagram in Figure 3.4. The

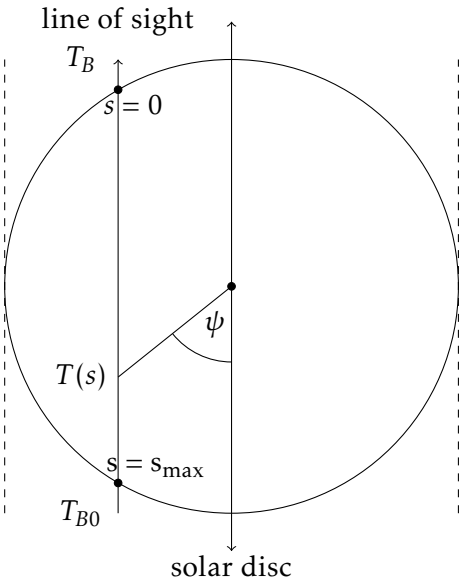

Figure 3.4: Schematic diagram showing the integration direction along a LOS orthogonal to the cylindrical axis, and parallel to the solar radial vector, for an on-disk filament model. Here $s = 0$ and $s = s_{max}$ correspond to the start and the end of the light's path through the cylinder, respectively. The *dashed lines* correspond to the edges of the FOV.

only change necessary in the calculation of the integration path, between this filament model and the prominence model discussed earlier, is how the azimuth angle, ψ, is calculated. The ψ angle is defined as the angle between each point in the integration path and the lower vertical axis (Figure 3.4). Once ψ is calculated for a given position on the path, the necessary parameters for integration, e.g. the absorption coefficient and temperature, may be interpolated using the method described in Section 2.3.3.

3.2.1.2 Background Emission from the Solar Disk

In this study, an important parameter that needed to be considered was the brightness temperature of the solar disk incident on the lower boundary of the model cylinder. The expression relating the incident brightness temperature from the solar disk, T_{B0} to the emergent brightness temperature of the filament, T_B, is given by:

$$T_B = T_{B0} e^{-\tau_\nu} + \int_0^{s_{MAX}} T \kappa_\nu e^{-\int_0^s \kappa_\nu ds'} ds, \tag{3.6}$$

where the integration is conducted over a path of length s_{max} through the filament with a path element of ds. κ_ν and τ_ν are the frequency-dependent absorption coefficient and optical

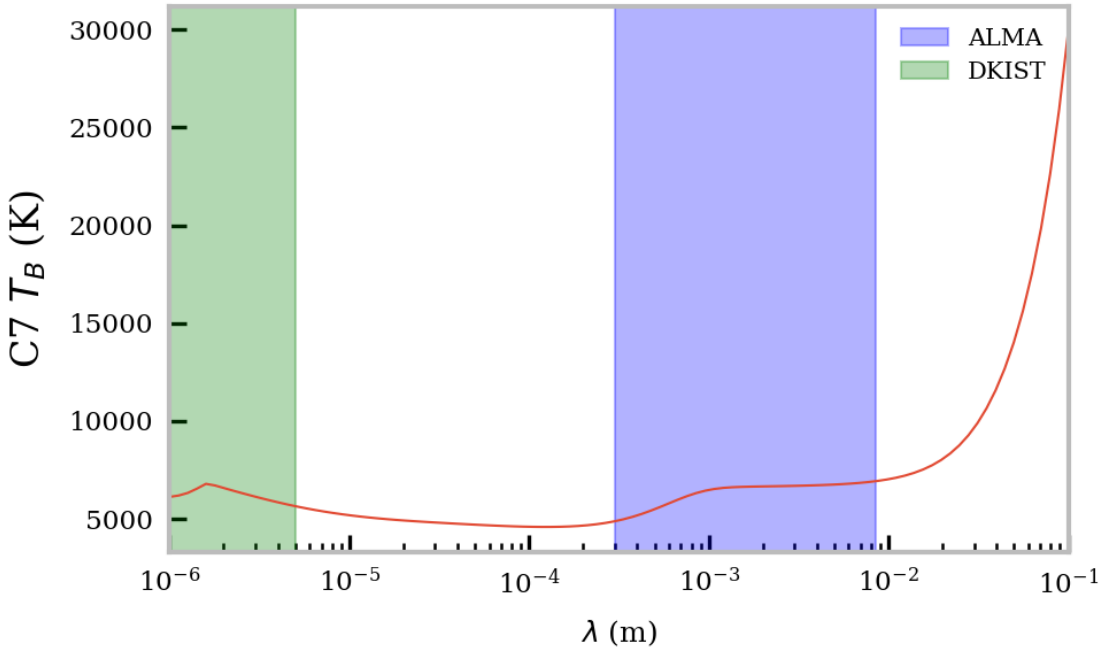

Figure 3.5: Brightness temperature spectrum produced from the C7 atmospheric model of Avrett & Loeser (2008). The blue coloured region shows the wavelength range of the ALMA observing bands, whilst the green region shows the range of DKIST's CRYO-NIRSP and DL-NIRSP instruments within the dimension of the x-axis.

thickness, whilst T is the electron temperature of the plasma. In more complex models, where the radiative transfer between filament and the surrounding atmosphere is considered, this parameter would be calculated within the radiative transfer. Here however, two options were available to use: observed values (i.e. as calculated by White et al. (2017)), or values calculated from an empirical model atmosphere. Both methods were found to have their own disadvantages. If observed values for the quiet Sun millimetre-continuum were to be used, the modelling would thus have to be restricted to the ALMA observing bands which have been used to observe the Sun so far, i.e. Band 3 and 6. This problem would not exist if an empirical solar atmospheric model was used, as any wavelength could be calculated for. However, it would be less clear whether the calculated values would be representative of the true quiet sun brightness temperature, as in White et al. (2017) the authors state that the ALMA observed brightness temperatures are typically above those expected by chromospheric models.

To begin with, the brightness temperature spectrum was produced from an empirical

atmospheric model. The model chosen for this was the C7 model of Avrett & Loeser (2008). The brightness temperatures were calculated using the heights, temperatures and densities provided by the C7 model for a pure hydrogen plasma. The absorption mechanisms are assumed to be inverse thermal bremsstrahlung (Equation 3.5), using the interpolated value of the Gaunt factor from the table of values from van Hoof et al. (2014) as discussed in Section 3.1, and H^- absorption (Equations 2.5 and 2.6). The resulting brightness temperature spectrum is shown, along with the ALMA and part of the DKIST wavelength range in Figure 3.5. For ALMA Band 3 a brightness temperature of ≈ 6700K is calculated, whilst for ALMA Band 6 a value of ≈ 6600K is calculated. These values are simultaneously lower for Band 3 and higher for Band 6 than when compared to the observed values presented in White et al. (2017). This suggests that the local temperature gradients where the millimetre-continuum is formed are higher in the real solar atmosphere than the C7 model. It should be noted that the values presented here are somewhat closer together in brightness temperature than those quoted in Gunár et al. (2016) for the C7 model. A major factor in this difference will be the use of the Gaunt factor, as Gunár et al. (2016) approximate it as unity whilst I have used interpolated values from the table provided in van Hoof et al. (2014), although there may be further differences as well.

There also exists the question; what is meant by a typical quiet Sun brightness temperature? Most of the millimetre-continuum radiation is formed in the solar chromosphere, and therefore displays the cellular structure of the network and internetwork. Brajša et al. (2018) found from a Band 6 total power, full-disk image that the quiet Sun brightness temperature at the centre of the disk was 6040 ± 70K, however, these quiet sun values experience significant variation due to fine structures and centre-to-limb brightening. In Loukitcheva et al. (2019) the authors find, using defined boxes within an ALMA Band 3 quiet chromospheric observation, that the width of the brightness temperature distribution is significantly wider for chromospheric network than for the internetwork, whilst the total width of the combined distribution appears to range from ≈ 6–10×10^3K. Bastian et al. (1993) also claim that reduced network activity in filament channels could cause lower brightness temperatures within the filament channel.

Because of the fairly large discrepancy produced between the observed and simulated brightness temperatures the values chosen for these models were picked to reflect the currently observed values at ALMA Bands 3 and 6. For this, the central values were chosen to be the recommended values of 7300K for Band 3 and 5900K for Band 6 from White et al. (2017).

Table 3.1: Parameters for Isothermal-Isobaric Prominence/Filament Core Models

Parameter	Value
Temperature (K)	{6000, 8000, 10000, 15000, 20000, 30000, 40000, 50000, 65000, 80000, 100000}
Pressure (dyn cm^{-2})	0.1
Radius (km)	500
Helium Abundance	0.1

To reflect some of the large variation observed in the chromospheric network/internetwork structure and due to centre to limb effects, 13 different background brightness temperatures with offsets ranging to ±900K from said central values are considered. The choice of this value is arbitrary, but is designed to cover a large fraction of the expected variation in quiet Sun brightness temperatures.

3.2.1.3 Input Parameters

In this study both isothermal and multi-thermal temperature distributions are considered, as was done previously for off-limb prominences in Chapter 2. The isothermal-isobaric filament models which are used in this section are given in Table 3.1. As in previous model sets, the helium abundance and microturbulent velocity are set, respectively, at 0.1 and 5 $km\,s^{-1}$. These isothermal-isobaric filament models have a larger radius than the corresponding prominence fine-structure models used in Chapter 2. This was chosen as to allow for consideration of larger optical thicknesses for the filament, as fine-structure threads are unlikely to be visible on their own against the solar disk. The widths of these threads is equal to the core region within the multi-thermal models with a PCTR in Table 2.2. The altitude of the filament models is again 10000km.

The multi-thermal models used in this section are the same as defined in Table 2.2.

3.2.2 Results

Figure 3.6 shows the brightness temperature distribution across the FOV for the set of isothermal-isobaric filament models given in Table 3.1 with a selection of background brightness temperatures for the solar disk at 1.3 and 3.0mm, including the White et al. (2017) suggested value on the central row. Across both wavelengths and all models in Table 3.1, the

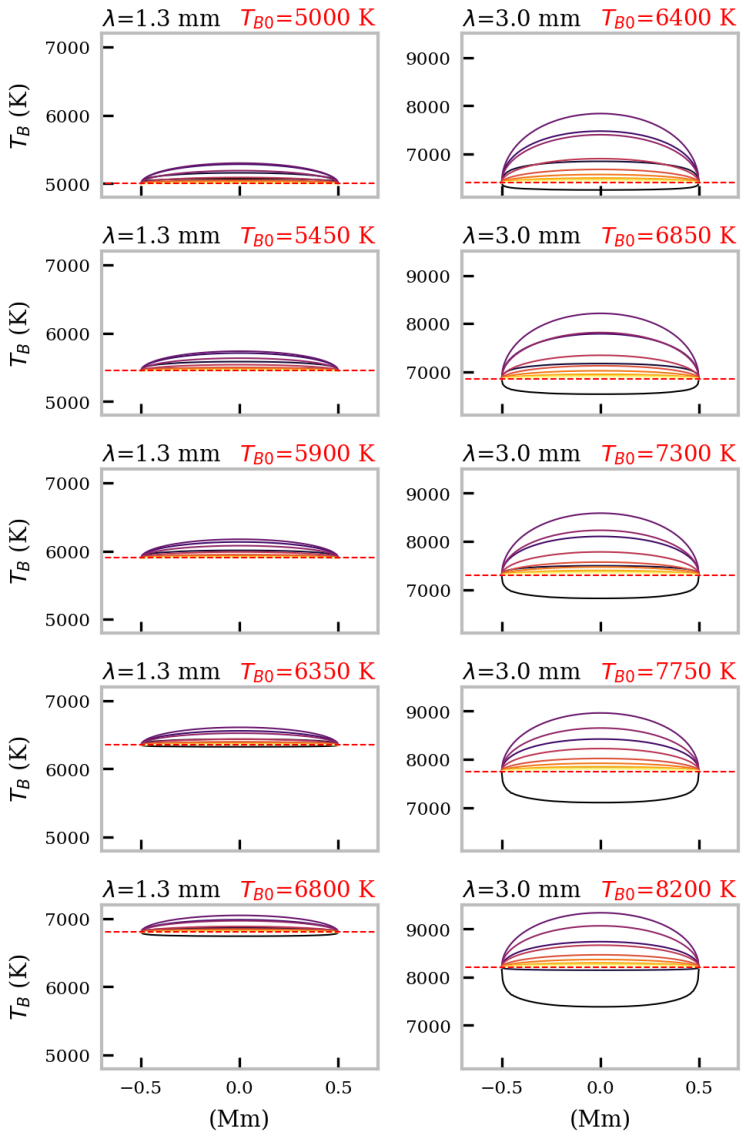

Figure 3.6: Variation of the brightness temperature across the FOV for the set of isothermal-isobaric models in Table 3.1. The *left* column shows the emission at Band 6 (1.3mm), whilst the *right* column shows the emission at Band 3 (3mm). Each plot in each column gives a different background brightness temperature for the solar disk illuminating the lower boundary of the filament LOS. The coloured solid lines in the plots show the temperature for each model, increasing from black to purple to yellow, as given in Table 3.1. The dashed red line shows the given background solar-disk brightness temperature.

filamentary plasma is optically thin. Most models appear in emission with the only cases where they are not being when the constant electron temperature of the model is lower than the brightness temperature of the solar disk. As the brightness temperature of the solar disk is directly related to the temperature of the particular region where the emission is formed within the solar chromosphere, isothermal filaments will appear dark if the filamentary material is cooler than said formation region within the chromosphere, and bright if they are hotter.

Unlike the simulated prominence observations presented in Chapter 2, the geometry of

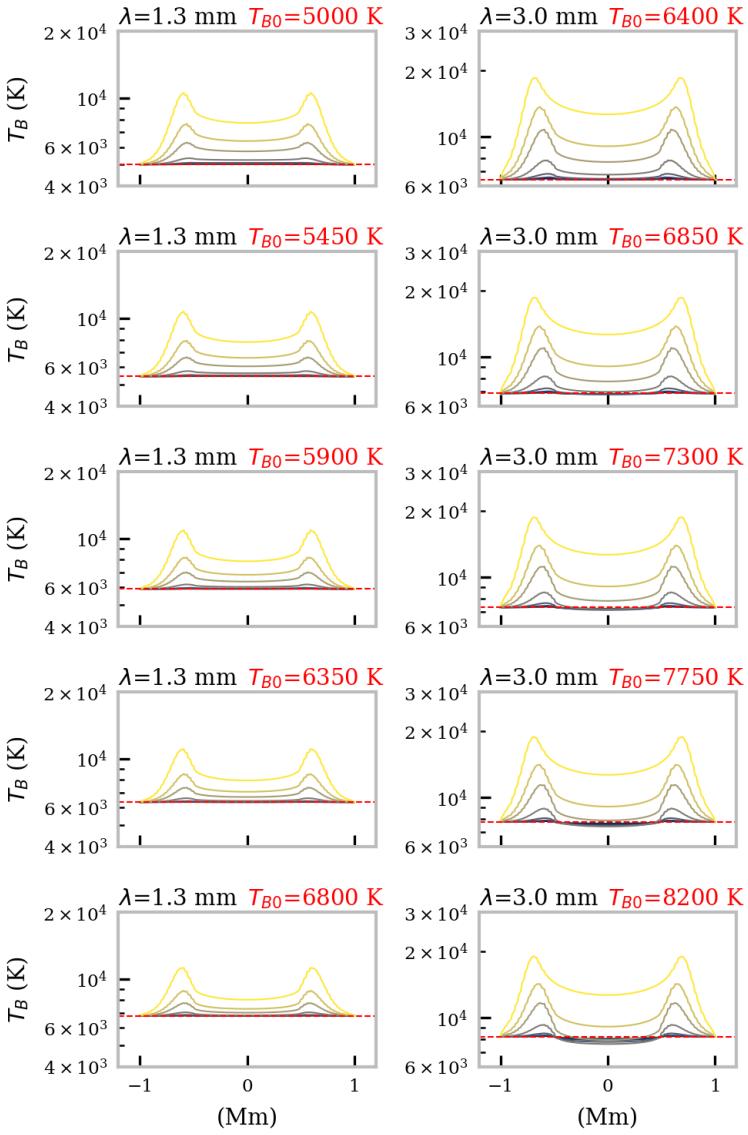

Figure 3.7: Variation of the brightness temperature across the FOV for the set of multi-thermal models in Table 2.2. The *left* column shows the emission at Band 6 (1.3mm), whilst the *right* column shows the emission at Band 3 (3mm). Each plot in each column gives a different background brightness temperature for the solar disk illuminating the lower boundary of the filament LOS. The coloured solid lines in the plots show the pressure for each model, increasing from dark blue to grey to yellow, as given in Table 2.2. The dashed red line shows the given background solar-disk brightness temperature.

the integration for these filament models results in brightness temperature profiles which are symmetrical across the FOV, as the incident radiation penetration is similarly symmetrically distributed.

The same figure for the set of multi-thermal plasmas is shown in Figure 3.7, with the central row again showing the background brightness temperature as suggested by White et al. (2017). Because of the hot PCTR material, as the density of the filament increases with the pressure of each model, the edges of the filament FOV become increasingly bright against the background solar disk, irrespective of the said background's value. When the

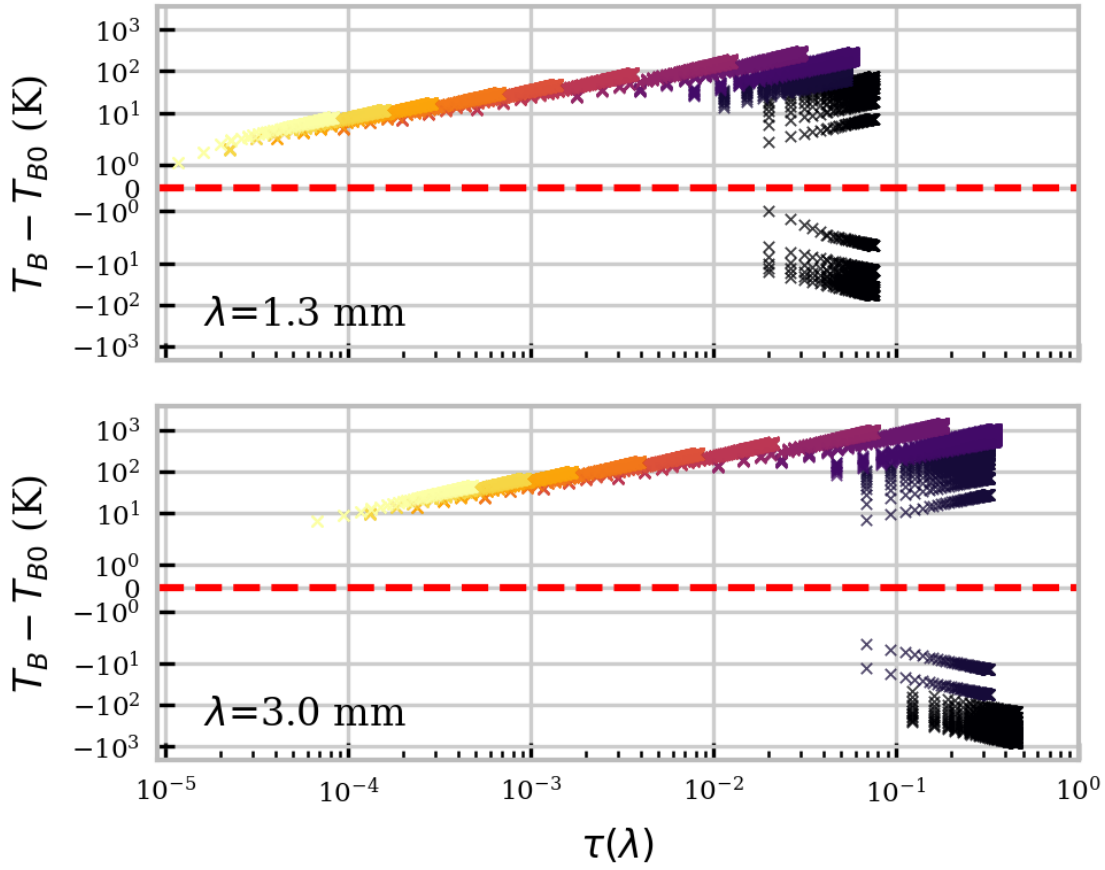

Figure 3.8: Relationship between the filament contrast, defined as the difference between the brightness temperature from the filament and from the background solar disk, and with the optical thickness of the LOS. Each colour represents a different constant temperature, as defined in Table 3.1, with values increasing from black to purple to yellow. For each isothermal model a range of different solar disk brightness temperatures is considered as described in Section 3.2.1.3

filament's density is increased with the pressure, the optical thickness increases, causing the formation layer of the millimetre-continuum to be located further away from the filament's core, thus increasing the brightness temperature. For optical thick filaments this prevents the brightness temperature at the centre of the FOV from reaching down to the temperature of the filament core value which is 6000K. What this then means in terms of the filament's visibility is that low pressure, low optical thickness models will appear faint, and potentially dark if the solar disk is particularly bright (see bottom right hand panel of Figure 3.7), and that at high pressure, high optical thickness, the filament's visibility will be strong, and

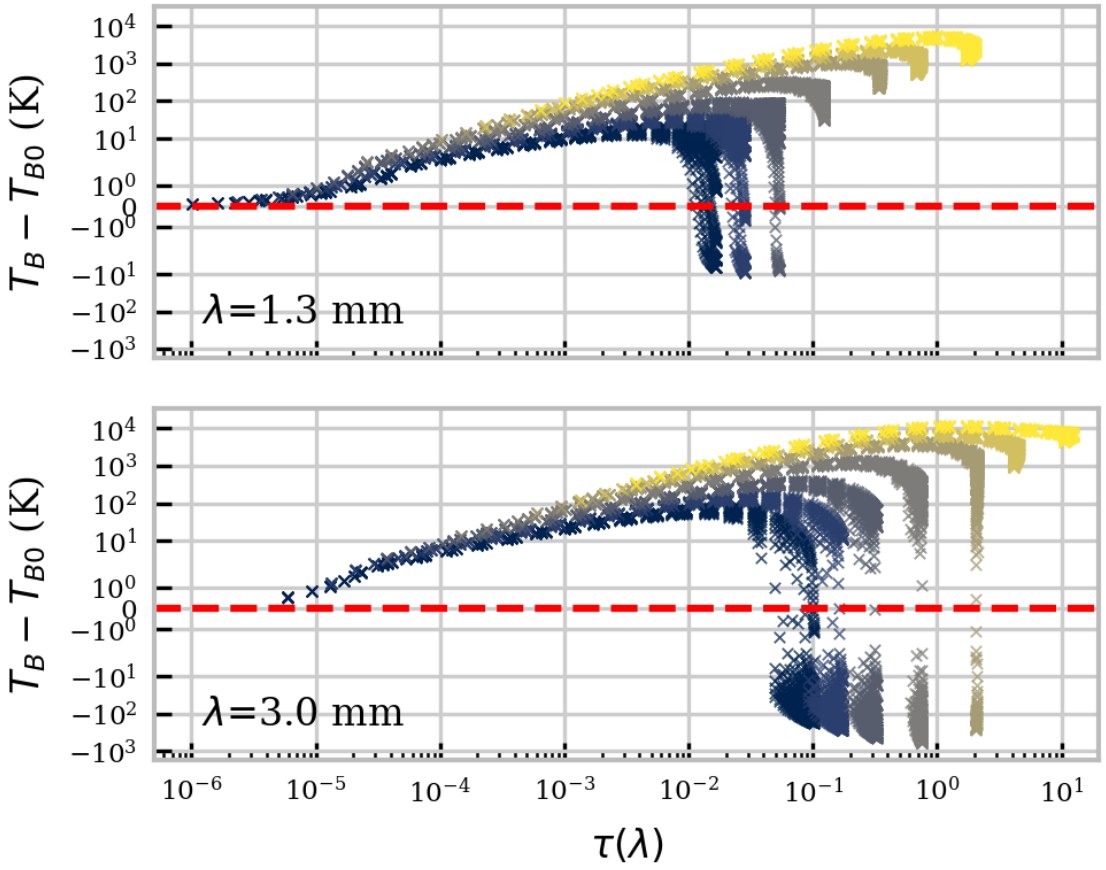

Figure 3.9: Relationship between the filament contrast, defined as the difference between the brightness temperature from the filament and from the background solar disk, and with the optical thickness of the LOS. Each colour represents a different pressure, as defined in Table 2.2, with values increasing from dark blue to grey to yellow. For each multi-thermal model a range of different solar disk brightness temperatures is considered as described in Section 3.2.1.3

bright, particularly in LOS where more PCTR material is located. Therefore these models suggest that the PCTR region would be expected to produce a better visibility against the solar disk than the denser core region, which for low pressure models may be faint, or perhaps dark against the background.

In this study I measure the filament's visibility using the contrast it would display against the background quiet Sun. To calculate the contrast I use the difference between the brightness temperature of the filament and the brightness temperature of the background solar

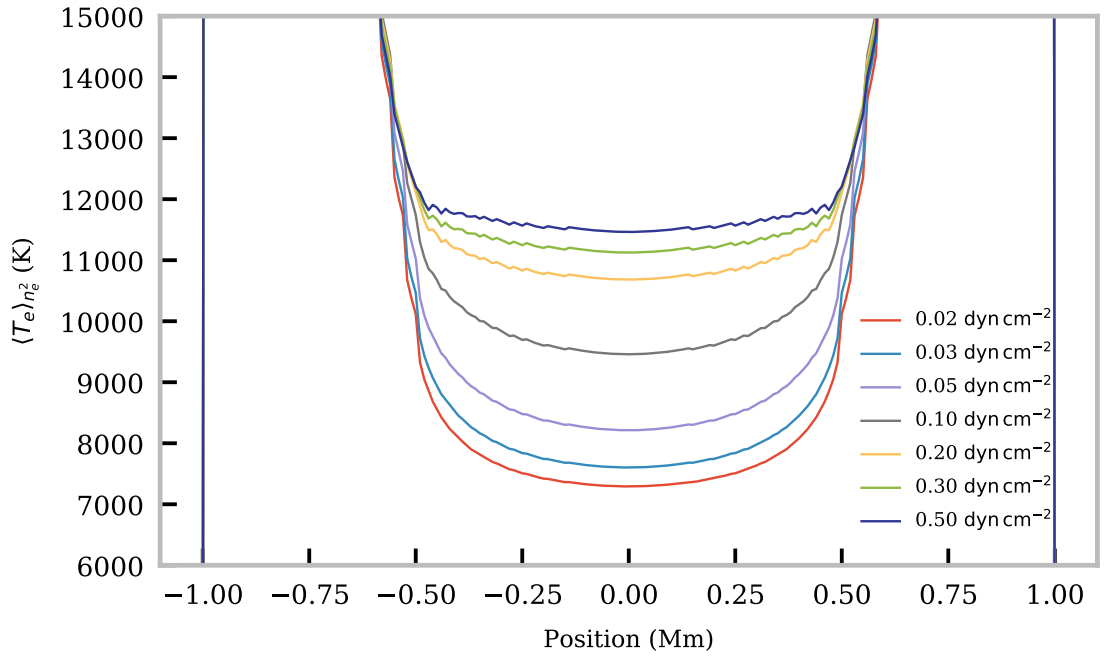

Figure 3.10: Distribution of the electron density squared weighted mean temperature across the FOV for the set of multi-thermal filament models from Table 2.2. Each model pressure is represented by a colour given in the legend.

atmosphere. The relationship between the filament's contrast against the solar disk brightness temperature is shown for isothermal models in Figure 3.8, and for multi-thermal models in Figure 3.9. As is expected from a predominantly thermal bremsstrahlung emission mechanism, and as was previously discussed in Section 2.4.1, the optical thickness of the isothermal models decreases with increasing temperature. The isothermal models in Figure 3.8 also all display optically thin plasma, which generally leads to a relationship where the lower the temperature, the higher the contrast seen between the filament and the solar disk. Again it is seen that only the models with electron temperatures below the solar disk brightness temperature will appear as dark, negative contrast, structures. If an uncertainty on ALMA's observable brightness temperature was taken to be 100K for a filament observation of these models, only a few of these models would be visible in ALMA Band 6 (1.3mm). A larger set of models would be observed in Band 3 with models either displaying as bright or dark structures against the disk, depending on the temperature of the given model thread.

In Figure 3.9 it is seen that the contrast of the multi-thermal filaments generally increases with pressure/density. Low pressure/density models are, however, more likely to appear

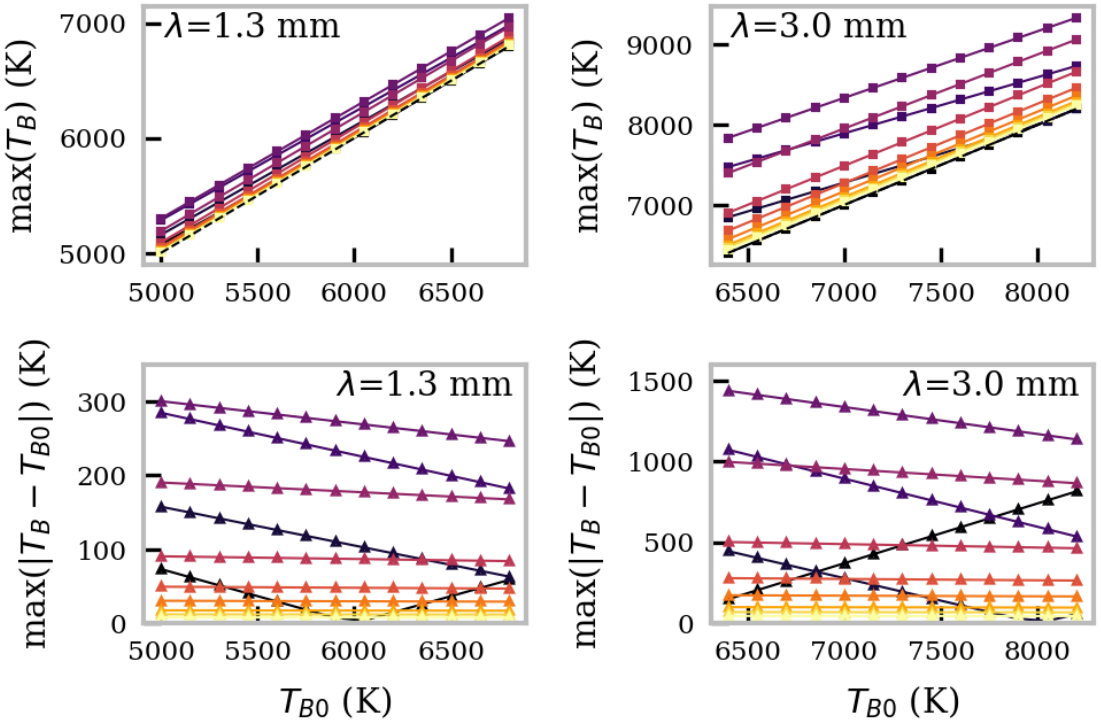

Figure 3.11: Effect of the solar disk background brightness temperatures for isothermal models. The *top* panels show the relationship between the maximum brightness temperature of the filament and the background brightness temperature of the solar disk, whilst the *bottom* panels show the relationship between the maximum absolute contrast between the filament and background with increasing background brightness temperature. The results for ALMA Band 6 (1.3mm) are shown on the *left* hand side, whilst the results for ALMA Band 3 (3mm) are shown on the *right*. The colors represent the temperature of the isothermal models, with the values (given in Table 3.1) increasing from black to purple to yellow.

as a dark structure within the plasma core. This is caused by the optical thickness and the representative temperature of the LOS, which I consider here to be the electron density squared weighted mean temperature. As the pressure/density of each model increases, so too will the electron density squared weighted mean temperature ($\langle T_E \rangle_{n_e^2}$) within the filament core, this is demonstrated in Figure 3.10. Therefore, whilst in the optically thin regime, increasing the pressure/density of a solar filament will produce a higher brightness temperature due to having both a higher optical thickness and a higher representative temperature for the LOS. Assuming an uncertainty of 100K for ALMA interferometric data,

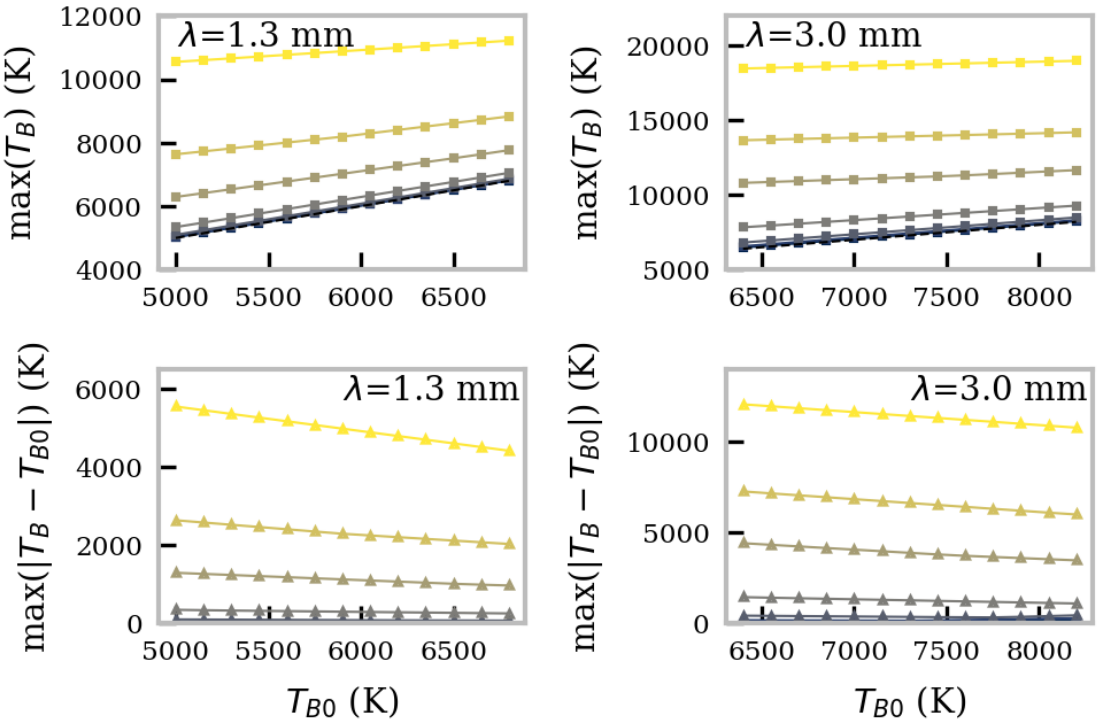

Figure 3.12: Effect of the solar disk background brightness temperatures for multi-thermal models. The *top* panels show the relationship between the maximum brightness temperature of the filament and the background brightness temperature of the solar disk, whilst the *bottom* panels show the relationship between the maximum absolute contrast between the filament and background with increasing background brightness temperature. The results for ALMA Band 6 (1.3mm) are shown on the *left* hand side, whilst the results for ALMA Band 3 (3mm) are shown on the *right*. The colors represent the pressure of the multi-thermal models, with the values (given in Table 2.2) increasing from dark blue to grey to yellow.

only the highest pressure models will be visible using ALMA Band 6 (1.3mm), with all of these cases appearing as bright features. A wider range of pressures should be visible using ALMA Band 3, however, they may appear as both dark and bright structures against the solar disk dependent on the optical thickness and whether the LOS is predominantly through the core or PCTR regions. If this were to be observable with ALMA's spatial resolution this would provide a significantly different picture to what is usually observed in solar filaments in spectral line emission, and may present a more direct observation of the structure of the PCTR than has previously been available. It should, however, be noted that the PCTR

structure in these models is defined by an ad-hoc temperature gradient between the cool core and the corona, and that real PCTR may be expected to be significantly narrower in extent, depending on the angle between it and the magnetic field direction. Small scale brightenings due to the PCTR may not then be observable with low spatial resolution observations, such as have been conducted up to now.

This result is consistent with what is found in Gunár et al. (2016), where they find that in one observing band part of a filament may be dark, but simultaneously bright in another. Because of this they emphasise the need for simultaneous multiple wavelength observations which test the plasma where it is both optically thin and optically thick. It is, however, important to note that from these results it is clear that the contrast between the filament and the solar disk is often low (less than 100 K) in suitably optically thin cases. This problem may be answered through coordinated observation with spectral lines such as Hα, such that the location of the cool material within the filamentary structure can be discerned.

The effect of the variation in background brightness temperature for the solar disk is shown for isothermal models in Figure 3.11 and for multi-thermal models in Figure 3.12. As all the isothermal models in Figure 3.11 are optically thin the solar disk brightness temperature is seen to have a clear linear relationship with the maximum brightness temperature emitted by the filament (top panels). This linear relationship has a gradient of close to 1 for the high temperature, low optical thickness models. As the temperature decreases, and the optical thickness increases, the relationship moves away from the $x = y$ line, shown as the dotted black line in the plots. For the lowest temperature models, where the plasma is closest to being optically thick, the slope of the correlation decreases, and thus the background brightness temperature is seen to have less of an effect on the emitted radiation. These changes are seen more clearly in the 3mm emission, as the optical thickness is greater than for 1.3mm.

The bottom panels of Figure 3.11 show the effect the background brightness temperature has on the maximum contrast/visibility of the filament (maximum $T_B - T_{B0}$). The highly optically thin (high temperature) models show little to no variation with background brightness temperature, whilst the closer to optically thick (low temperature) models unsurprisingly increase or decrease in contrast with increasing background brightness temperature, depending on whether the temperature of the isothermal model is below or above the solar disk brightness temperature, respectively.

The same relations when investigated for multi-thermal models (Figure 3.12) are found

to display a weaker effect of the background brightness temperature. The lowest optical thickness (lowest pressure) models once again display a slope close to 1 and near the $x = y$ line, however, the models where the plasma is optically thick show the brightness temperature to be independent of the background, perhaps unsurprisingly. The contrast between the filament and background solar disk is found to vary only weakly with increasing background brightness temperature, with this only occurring for the models where the brightness temperature of the filament is nearly independent of the background brightness temperature.

3.2.3 Summary and Discussion

In summary I have used the millimetre-continuum prominence models defined in Chapter 2 to model the visibility of solar filaments with ALMA. I have considered a LOS which integrates vertically from the solar disk to the observer. To account for the varying quiet Sun brightness temperature across the solar disk, a range of background brightness temperatures of up to ±900 the recommended mean values of 7300 K and 5900 K for ALMA Bands 3 and 6 from White et al. (2017), respectively, is used.

For a set of isothermal prominence core models (Table 3.1) it is found that only models with electron temperatures below the background brightness temperature of the solar disk will appear as dark structures. The contrast between these model filaments and the solar disk will also decrease as said electron temperature increases, as the optical thickness of the plasma will decrease. For ALMA Band 6 only a few of the lower temperature models were found to display contrasts against the disk with values of greater than 100K, with all of these models displaying as bright features. ALMA Band 3 would be able to observe a larger set of filaments with contrasts of 100K or greater, with these models displaying as either dark or bright structures depending on the constant electron temperature.

The multi-thermal models including a PCTR (Table 2.2) yield similar results, however, due to having a larger physical extent, a larger fraction of these models would be visible with ALMA Bands 6 and 3 within 100K accuracy. Band 6 shows structures which are mostly bright against the solar disk, however, in Band 3 it is found that a singular filament structure may appear both dark and bright against the disk, depending on the plasma's optical thickness, or the particular LOS. If this is observable with ALMA's spatial resolution this could provide a more direct observation of the PCTR structure in solar filaments than has previously been available with high resolution spectral line observations.

Due to the geometry of the C2D2E model it was not possible to consider the effect on the

emission from the filament channel, or any potential overlying cavity. Therefore the results from this study consider the emission from the solar filamentary material solely. The models presented here where the filament is in emission and optically thin may have their contrast affected by the inclusion of a filament cavity in the corona. A decreased optical thickness of the corona caused by a filament cavity could effect the filament visibility in the following ways:

a) Optically thin filament: Any enhancement caused by the filament could be negated, or perhaps appear as a dark (absorption) feature due to the $\tau = 1$ line lying lower within the chromosphere.

b) Optically thick dark, cool material: This material, likely from the filament core, should appear dark irrespective of whether there is a cavity in the corona or not. However, if the width of the cavity is wider than the cool material, its contrast against the solar disk may be diminished due to the dimming of the chromospheric emission.

c) Optically thick bright, hot material: If the PCTR material is optically thick and hot enough to appear bright against the solar disk this should be unaffected by the existence of a coronal cavity, or it could perhaps appear with improved contrast due to the surrounding chromospheric dimming. Depending on the width of a potentially bright PCTR, this may not have been observable with the pre-ALMA spatial resolutions.

For the potential effect of a cavity to be considered in more detail, in the future a more sophisticated atmosphere+filament+cavity modelling approach will be required.

3.3 Correlations between the Millimetre Continuum and Emission from Hydrogen and Helium

In Chapter 2 I described the development and results found when modelling the emission in the millimetre/sub-millimetre continuum from 2D cylindrical cross-section, non-LTE radiative transfer prominence models. In doing so I discussed the capability for millimetre brightness temperature measurements to be used as diagnostics for the plasma kinetic temperature, amongst other parameters. In all instances, be the plasma isothermal or multi-thermal, optically thin or thick, knowledge of the optical thickness of the plasma at millimetre wavelengths is important to understand the reliability or applicability of the

chosen plasma diagnostic. In this section I discuss whether it may be possible to estimate the optical thickness of a plasma in the millimetre regime if coordinated observation in other wavelength domains is available. In particular I investigate the relationship between emission from the millimetre continuum and a few important lines from both hydrogen and helium, as well as the hydrogen Lyman continuum. In my discussion I also discuss the potential use of lines from minority species such as Mg II, which could be investigated in a future work.

To model the hydrogen and helium line emission from our solar prominence/filament models, the capability of C2D2E developed in Gouttebroze (2006) and Gouttebroze & Labrosse (2009) is used. The list of neutral hydrogen spectral lines which are modelled using this code are: Lyman-α, Lyman-β, Lyman-γ, H-α, H-β, and Paschen-α. The modelled neutral helium lines include: 584 Å, 537 Å, 10830 Å, 6678 Å, and 5876 Å(D3), with He II 304 Å also modelled.

In Subsection 3.3.1 I investigate the correlations between Balmer series emission (Hα and Hβ) and the millimetre continuum, comparing the modelled results with derived expressions for optically thin plasma. Subsection 3.3.2 discusses any potential correlations with the strong Lyman series of neutral hydrogen resonance lines and continua, with plasma parameters and the millimetre continuum. Subsection 3.3.3 shows the same for the commonly investigated He I 5876 Å(D3) line of helium. In Subsection 3.3.4 I give a summary of the results found in this study and discuss the potential for other minority species spectral lines, such as those observed using IRIS, as plasma diagnostics and any potential relationship they may have to the millimetre continuum.

3.3.1 Balmer Series Emission and the Millimetre/sub-millimetre Continuum

The Balmer series has been spectroscopically observed from solar prominences since the eclipse observation of Rayet (1869), where the Hβ line was clearly visible (Vial & Engvold 2015). Balmer imaging of solar prominences was greatly improved with the invention of the coronagraph in the 1930s, as previously eclipse observations were required to provide significant contrast from the much brighter solar disk (Vial & Engvold 2015). Since then, Hα and Hβ spectral lines have been frequently observed in emission from solar prominences, and as dark absorption structures as filaments against the solar disk, using ground based observatories. Space based observations of Hα have also been conducted by the *Solar Optical Telescope* (SOT) on board Hinode (Tsuneta et al. 2008). The images of solar prominences

in Hα generally show the structure of the cool, dense material found at the core of the prominence. Numerically modelled Hα spectral lines from solar prominences are generally have a single peak, however, they can have more complicated shapes in real observations. In general scattering plays a lesser role in the formation of the Balmer lines than the Lyman lines with thermal emission providing a non-negligible component.

It has been postulated by Rutten (2017), that the opacity of the millimetre continuum as observed by ALMA should be equal to, or greater than the opacity in Hα, and should increase with both temperature, and wavelength. In Rutten (2017) the author hypothesises that the fibril canopy observed in Hα on the solar disk will similarly be observed in the millimetre continuum. Analogously, if Hα and millimetre observations come from plasma of similar optical thickness, it is thus reasonable to hypothesise that the visibility of solar prominences in the millimetre continuum may be similar to that observed in the intensity of the Hα line; at least when they are mutually emitted from optically thin plasma. Unlike the millimetre-continuum, however, radiative interactions between bound states have an effect on the Hα line emission, such as the coupling that is seen between the Lyβ line and Hα.

In Heinzel et al. (2015a) the authors attempted to predict the visibility of prominences when viewed through ALMA by converting an image of a prominence taken in Hα by the *Multichannel Subtractive Double Pass* (MSDP) spectrograph on the Large Coronograph at the Astronomical Observatory of the University of Wrocław. From the observed spectra they calculated the line-integrated Hα intensity for each pixel in their chosen image. Through citing an analytical expression for the emission measure in terms of Hα integrated line intensity derived from a set of isobaric-isothermal NLTE prominence models (Gouttebroze et al. 1993), the authors estimated the millimetre wavelength brightness temperature, by assuming an isothermal/isodense prominence for the LOS of each pixel. Following Jejčič & Heinzel (2009), the expression they use for the Hα intensity with regards to the emission measure was:

$$E(\mathrm{H}_\alpha) = 3.96 \times 10^{-20} b_3 T^{-3/2} e^{17534/T} n_e n_{\mathrm{H_{II}}} L, \tag{3.7}$$

where b_3 is the departure coefficient for the third hydrogen atomic level which is the upper state of the Hα transition. They assumed an isothermal, isodense prominence, with a purely hydgrogen thermal bremsstrahlung emission mechanism, thus the millimetre optical thickness they estimated was as follows:

$$\tau_\nu \approx 0.018 g_{\mathrm{ff}} \nu^{-2} T^{-3/2} n_e n_{\mathrm{H_{II}}} L \tag{3.8}$$

Thus combining Equations 3.7 and 3.8 they found the expression:

$$\tau_\nu \approx 4.55 \times 10^{17} g_{\rm ff} e^{-17534/T} E(\mathrm{H}_\alpha)/(\nu^2 b_3(T)). \tag{3.9}$$

Taking the natural logarithm of Equation 3.9 the following expression is obtained:

$$\ln(\tau_\nu) \approx \ln(E_{\mathrm{H}_\alpha}) + \ln(g_{\rm ff}) - \frac{17534}{T} - 2\ln(\nu) - \ln(b_3(T)) + 40.7. \tag{3.10}$$

In Heinzel et al. (2015a) the authors use previously calculated values for the departure coefficient from Jejčič & Heinzel (2009). The authors proceeded to use Equation 3.9 to calculate the brightness temperature for a set of sub-millimeter/millimeter wavelengths, assuming an isothermal prominence, see Equation 1.18. They then estimated how the prominence would look through ALMA by inputting their converted brightness temperature map through CASA's (*Common Astronomy Software Applications*) simobserve() and simanalyze() procedures. Whilst the construction of Equation 3.9 required a significant number of assumptions, the ability to be able to determine the optical thickness regime for a millimetre/sub-millimetre observation, independent of the millimetre observation itself, would help significantly in understanding how to use the brightness temperature as a plasma diagnostic.

Equation 3.9 can be derived more generally for any optically thin hydrogen line, or for non-hydrogen lines, although for this to be useful, information about the elemental and ionization abundances must be known. To get an equivalent to Equation 3.7 the integrated line intensity needs to be estimated assuming an optically thin LOS, where a representative upper energy level density can be found using Saha-Boltzmann statistics. Performing this for a non-specific neutral hydrogen line transition, from energy level j to i, the following equation is found:

$$\tau(\mathrm{mm}) \approx 0.018 E_{ji} \frac{g_{\rm ff}}{\nu^2 T^{3/2}} \left(\frac{2\pi m_e k T}{h^2}\right)^{3/2} \frac{4\pi}{h\nu_{ij} A_{ji} b_j} \frac{2 g_{\mathrm{H_{II}}}}{g_j} e^{-\chi_j/kT}, \tag{3.11}$$

where E_{ji} is the integrated intensity of the neutral hydrogen transition from upper energy level, j, to lower energy level, i. A_{ji} and ν_{ij} are the Einstein coefficient for spontaneous emission and the frequency of the emitted photon, respectively. g_j and $g_{\mathrm{H_{II}}}$ are the statistical weights for the neutral hydrogen upper level of the transition and for ionized hydrogen, respectively. χ_j is the ionization energy from level j.

Unlike in Heinzel et al. (2015a) the C2D2E models consider a combined hydrogen and helium plasma. Thus in our case the optical thickness of the millimetre-continuum is related

to the electron-proton emission mechanism ($n_e n_{\mathrm{H_{II}}} L$) as follows:

$$\begin{aligned}\tau(\mathrm{mm}) \propto n_e \sum_i Z_i^2 n_i L &= n_e(n_{\mathrm{H_{II}}} + n_{\mathrm{He_{II}}} + 4n_{\mathrm{He_{III}}})L \\ &= n_e(n_{\mathrm{H_{II}}} + \frac{A_{\mathrm{He}}\eta_1}{\xi} n_{\mathrm{H_{II}}} + \frac{4A_{\mathrm{He}}\eta_2}{\xi} a n_{\mathrm{H_{II}}})L \\ &= n_e n_{\mathrm{H_{II}}} L(1 + \frac{A_{\mathrm{He}}(\eta_1 + 4\eta_2)}{\xi})\end{aligned} \tag{3.12}$$

where A_{He} is the helium abundance ratio equal to the total density of helium divided by the total density of hydrogen, ξ is the ratio of ionized hydrogen to total hydrogen density, η_1 is the ratio of singly ionized helium density over the total helium density, and η_2 is the ratio of twice ionized helium density over the total helium density. In the case where helium is nearly completely neutral, τ(mm) will tend towards the assumption used by Heinzel et al. (2015a). Whilst at very high temperatures, with a fully ionized plasma, τ(mm) will tend towards being proportional to $(1 + 4A_{\mathrm{He}})n_e n_{\mathrm{H_{II}}} L$. In general it would be expected that the helium abundance would be fairly low, e.g. ~ 0.1 (Heasley & Milkey 1978; Labrosse & Gouttebroze 2001). In all the prominence models presented in Chapter 2 I assumed an helium abundance of 0.1. Due to the presence of helium in our models it can therefore be expected whilst using the Hα integrated intensity to estimate the optical thickness of the millimetre-continuum (Equation 3.9), the estimated value may underestimate the optical thickness, down to $\sim 70\%$ the true value, if considering for a fully ionized plasma with a helium abundance ratio of 0.1.

In Figures 3.13 and 3.14 I show the relationships between several different forms of the electron, hydrogen, and helium emission measure with the optical thickness of the 3 mm emission for isothermal and multi-thermal models, respectively. As the electron density is very highly linked to the density of ionized hydrogen, both the electron–proton ($n_e n_{\mathrm{HII}} L$) and electron–electron ($n_e n_e L$) emission measures present a similar correlation with the optical thickness of the millimetre-continuum at 3 mm for both isothermal and multi-thermal models. This correlation shows a clear power law relationship for each isothermal and multi-thermal prominence model, with the spread between different models caused by the temperature-dependence of the millimetre absorption coefficient. There is also clear power-law correlation between the optical thickness at 3 mm and the total hydrogen ($n_{\mathrm{H}}^2 L$), and helium ($n_{\mathrm{He}}^2 L$) emission measures at low densities, however, the trend appears to flatten at higher densities. For isothermal models (Figure 3.13) there appears to be model dependent power law correlation between the electron–singly ionized helium density emission measure ($n_e n_{\mathrm{HeII}} L$) and the optical thickness at 3 mm, whilst the multi-thermal models (Figure 3.14) show a more complex distribution where there appears to be a power law relationship for

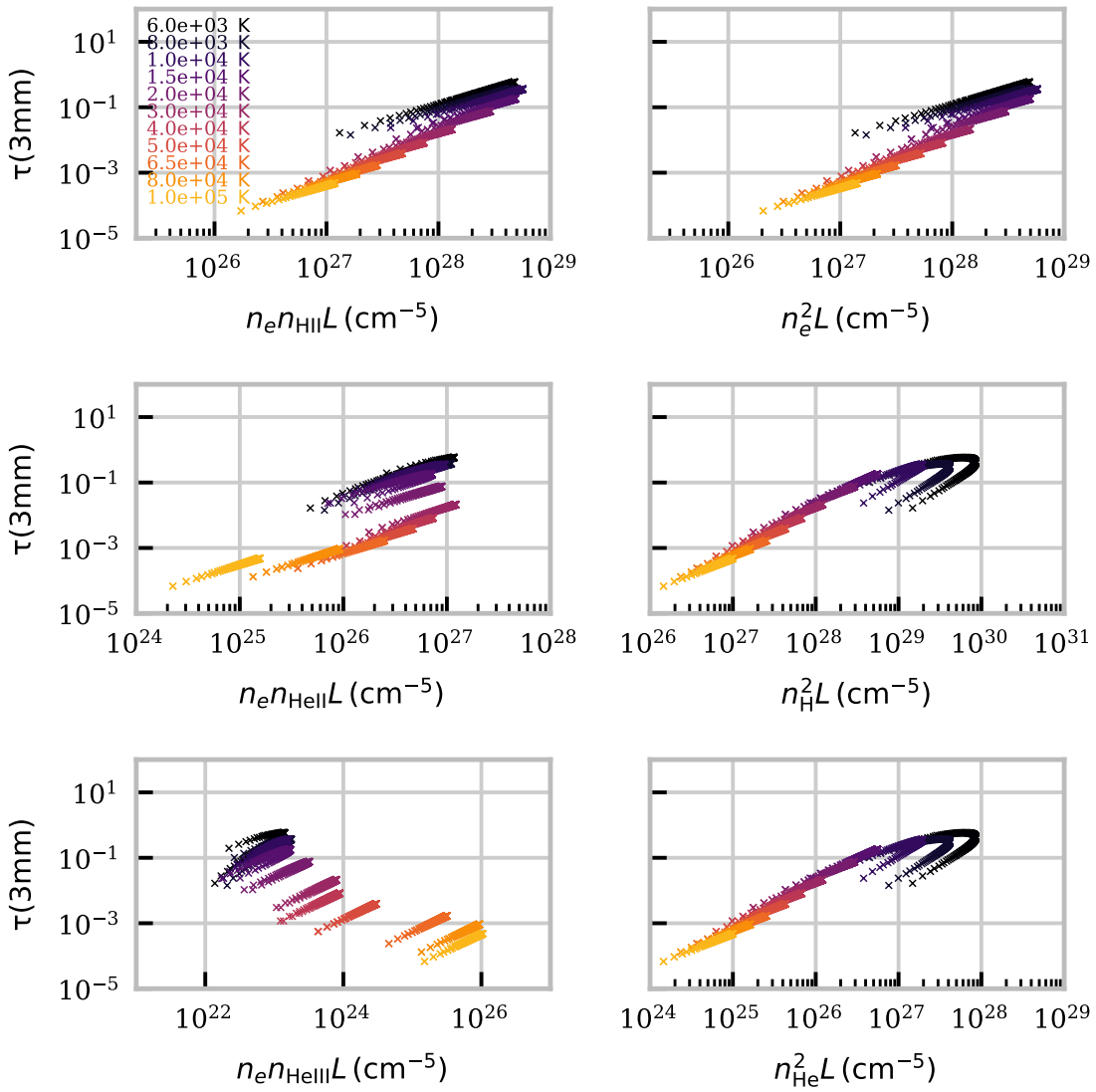

Figure 3.13: Correlation between six forms of the emission measure for electron, hydrogen and helium species, and the optical thickness of the 3 mm continuum for the set of isothermal prominence models from Table 3.1. The colour of each scatter plot corresponds to a given constant temperature for each model, as given on the top-left panel.

low but not high optical thicknesses. For the electron–twice ionized helium density emission measure ($n_e n_{\mathrm{HeIII}} L$) there is again model dependent power law relationships for isothermal models with no global trend, whilst there is no clear correlation for the multi-thermal models. In all instances the correlation becomes unclear once the optical thickness at 3 mm exceeds unity.

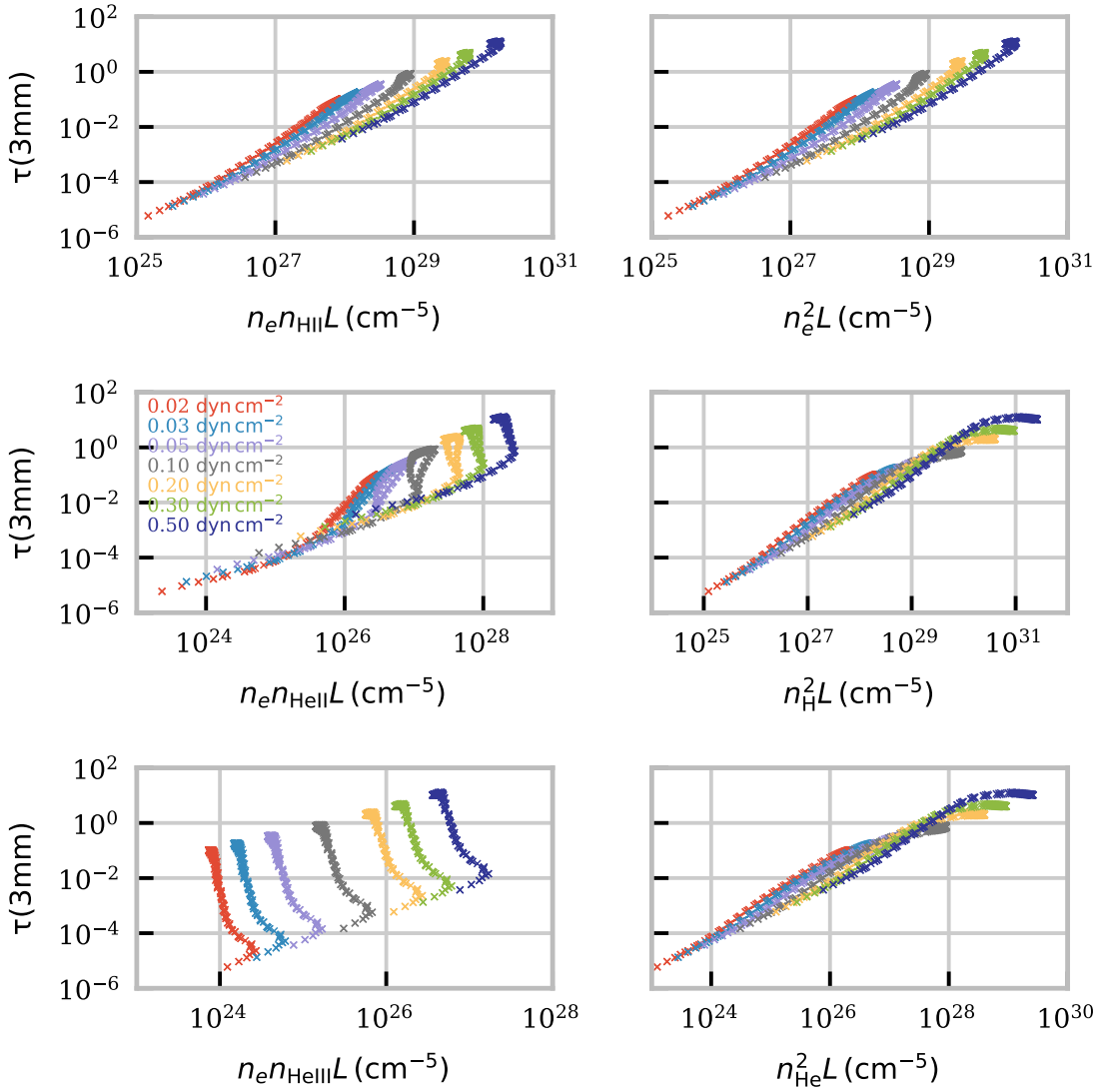

Figure 3.14: Correlation between six forms of the emission measure for electron, hydrogen, and helium species, and the optical thickness of the 3 mm continuum for the set of multi-thermal prominence models from Table 2.2. The colour of each scatter plot corresponds to a given constant pressure for each model, as given on the middle-left panel.

In the remainder of this section I address the relationships between millimetre optical thickness and brightness temperature with the Hα and Hβ integrated intensities produced from the same set of models, whilst comparing these results to the expression given by Heinzel et al. (2015a). To do this, sets of isothermal-isobaric and multi-thermal structures are used, where the multi-thermal models aim to represent the case where the prominence

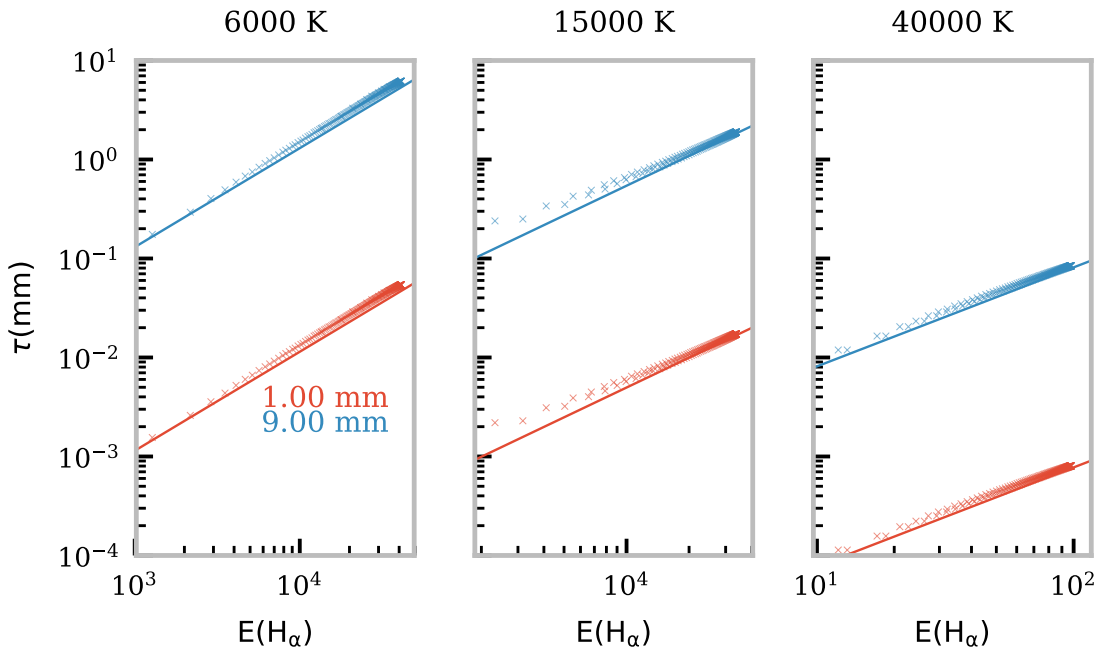

Figure 3.15: Relationship between-millimetre continuum optical thickness and integrated Hα intensity for three isothermal prominence models from Table 3.1. The colours represent different millimetre wavelengths as given on the left panel. The solid-lines show the expected relationships calculated using Equation 3.9.

has a clear PCTR. The results for isothermal-isobaric models are given in Section 3.3.1.1, whilst Section 3.3.1.2 gives the results for multi-thermal structures.

3.3.1.1 Results from Isothermal Models

In Figure 3.15 I show the relationship between two different millimetre wavelength optical thicknesses and the integrated Hα intensity for three models from Table 3.1 with different temperatures. For each model the expected expressions according to Equation 3.9 are also plotted as solid straight lines of colour corresponding to the representive millimetre wavelength. Whilst in Heinzel et al. (2015a) the authors use a singular value for the departure coefficient as calculated for a plasma of 8000 K in Jejčič & Heinzel (2009), here a mean value for the departure coefficient as calculated for each model is used. The definition of the departure coefficient used in this study is:

$$b_j = \frac{n_j}{n_j^{\mathrm{LTE}}}, \tag{3.13}$$

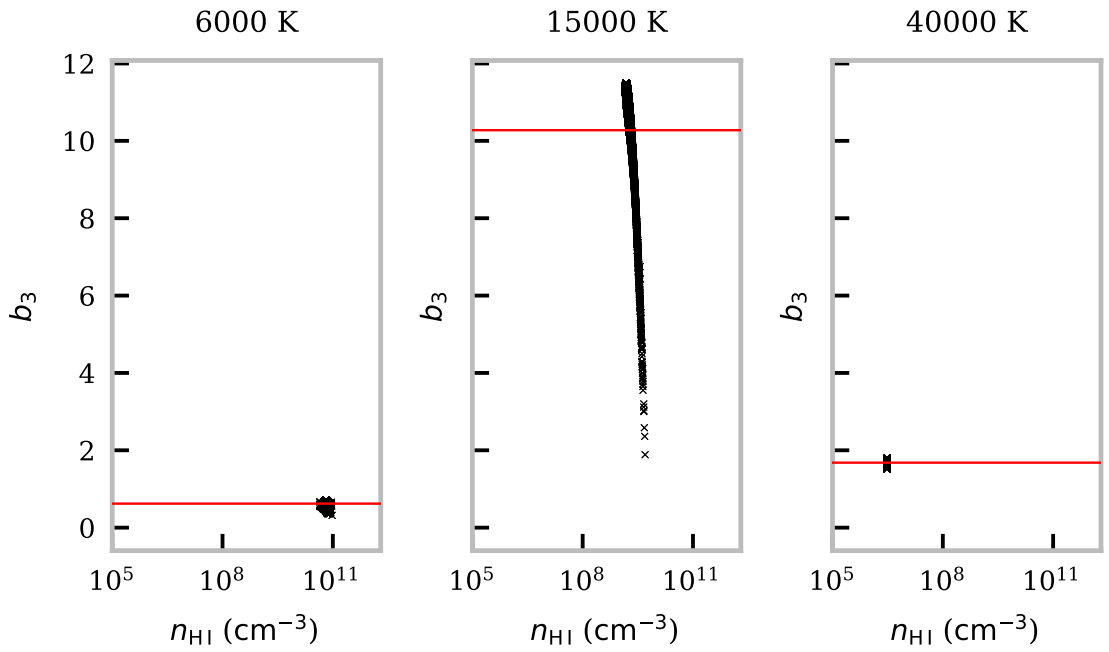

Figure 3.16: Relationship between the departure coefficient for level 3 with the number density of neutral hydrogen for 3 isothermal models. Each point represents a point in the 2D model, whilst the red straight line shows the value for b_3 used to calculate the analytical expressions used in Figure 3.15.

where j denotes the energy level of interest, with n_j then being the number density of the given energy level and n_j^{LTE} being the same value but for a plasma in LTE. n_j^{LTE} is calculated using Equation 1.12.

Whilst the temperature and pressure is constant across the whole cylinder, the departure coefficient will vary due to the effects of the ionizing incident radiation. I calculate this value by first finding the LOS integrated mean for each point in the FOV before taking the mean across the FOV to get a singular value. The LOS integrated mean, $\bar{x}$, is defined as follows for a given parameter, x:

$$\bar{x} = \frac{\int_0^L x \mathrm{d}s}{L}. \tag{3.14}$$

It can be seen from Figure 3.15 that for low temperature, isothermal models, the relation in Equation 3.9 follows well the relationship found in our models. The two wavelengths shown in the figure were chosen to represent values across ALMA's observing range whilst not overlapping on the plot. There does exist some small but noticeable deviations between

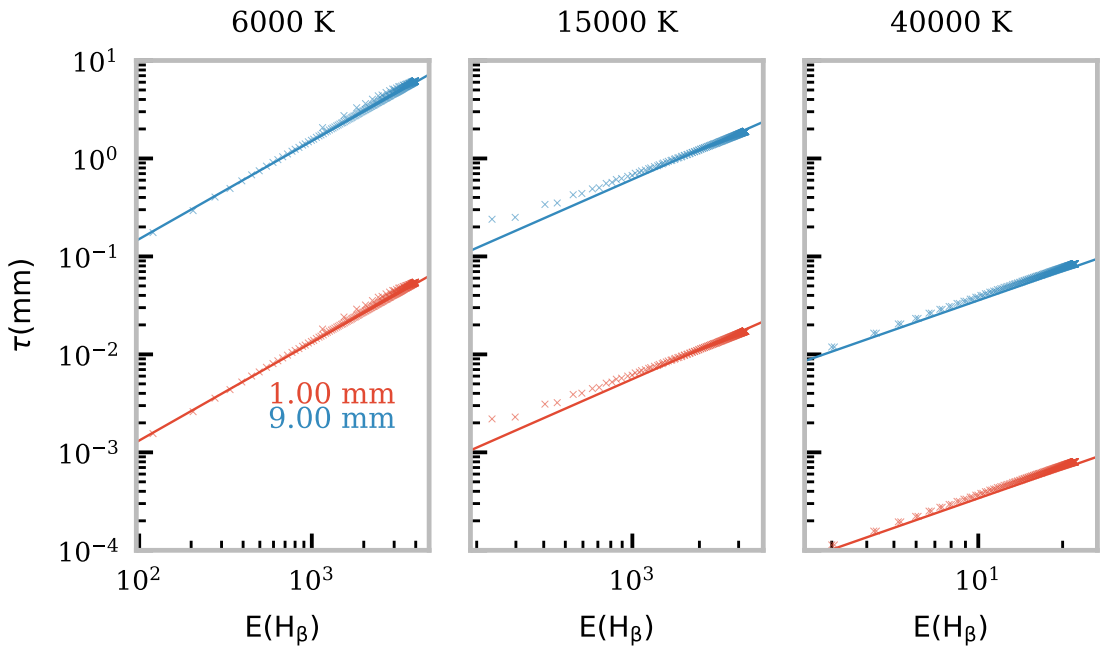

Figure 3.17: Same as Figure 3.15, however, showing the relationship between millimetre-continuum optical thickness and integrated Hβ intensity for three isothermal prominence models from Table 3.1, instead.

the numerical results and the analytical expression. This will be caused by the non-uniform b_3 distribution caused by the incident radiation, as well as to a lesser extent the presence of ionized helium within the prominence cylinder. The variation of the departure coefficient for level 3 versus the neutral hydrogen density is shown in Figure 3.16, with the values used in the analytical expression used in Figure 3.15 shown as red straight lines. It can be seen that for 15000K, the isothermal model which shows the largest departure from the analytical expression in Figure 3.15, corresponds to a model which shows a significant variation in b_3 across the cylinder. The increase in neutral hydrogen density seen in the central panel of Figure 3.16 is found at the edges of the prominence cylinder. This appears to be due to an increased recombination in this model as proton and electron densities decrease at the same locations. The effect of the presence of helium on the optical thickness of the millimetre-continuum can most clearly be seen in the right hand panel which shows the results from the highest temperature model. Here there will be the highest proportion of singly and twice ionized helium within the prominence which clearly causes the analytical expression to systematically underestimate the numerical results by a small amount.

Across all models given in Table 3.1 the optical thickness in Hα at line centre is below unity, such that the optically thin assumption remains valid. As a wide range of constant temperatures is considered within the model grid, for an isothermal-isobaric prominence of this width to become optically thick in Hα would require a pressure greater than 0.1 dyn cm^{-2}. Alternatively a wider prominence with a longer LOS through the plasma would provide a larger Hα optical thickness.

In Figure 3.17 the same relationship for the Hβ neutral hydrogen line transition is shown. This transition occurs between upper electron energy level $j = 4$ and lower energy level $i = 2$. Using Equation 3.11 the numerical expression for the millimetre continuum optical thickness in terms of integrated Hβ intensity ($E(\mathrm{H}_\beta)$) is:

$$\tau_\nu \approx 9.95 \times 10^{17} \frac{g_{\mathrm{ff}}}{\nu^2 b_4} e^{-9863/T} E(\mathrm{H}_\beta), \tag{3.15}$$

where b_4 is the departure coefficient for the 4$^{\mathrm{th}}$ energy level of neutral hydrogen and the upper level of the Hβ transition. Again this equation assumes that the optical thickness of the millimetre-continuum is proportional to the electron–proton emission measure ($n_e n_{\mathrm{H_{II}}} L$) and assumes that the helium contribution is minimal. Figure 3.17 shows that Hβ presents a very similar result to that of Hα with regards to their relationship with the electron-proton emission measure and thus the optical thickness at millimetre continuum wavelengths. Again, the same deviations from the analytical expression are seen due to the non-uniform departure coefficient. Whilst as the temperature of the isothermal prominence increases, so does the helium ionization, and thus the millimetre optical thickness is underestimated by a relative amount. The prominence plasma is less optically thick at the line centre of Hβ than Hα, so it is more likely to be valid for the optically thin assumption required for this technique, although, both lines do present optically thin emission from all models in the set given in Table 3.1.

3.3.1.2 Results from Multi-thermal Models

The multi-thermal structures used in this section are the same set as used in Chapter 2, given in Table 2.2. The purpose of these models is to simulate a prominence with a PCTR. The structure of the prominence has an inner, isothermal core of the same size as the isothermal models presented in the previous section (3.1), however with an additional PCTR where the temperature increases from the core to coronal temperatures. In these models the fraction of the radius which the core and the PCTR occupy are set to be equal lengths, i.e. 500 km each,

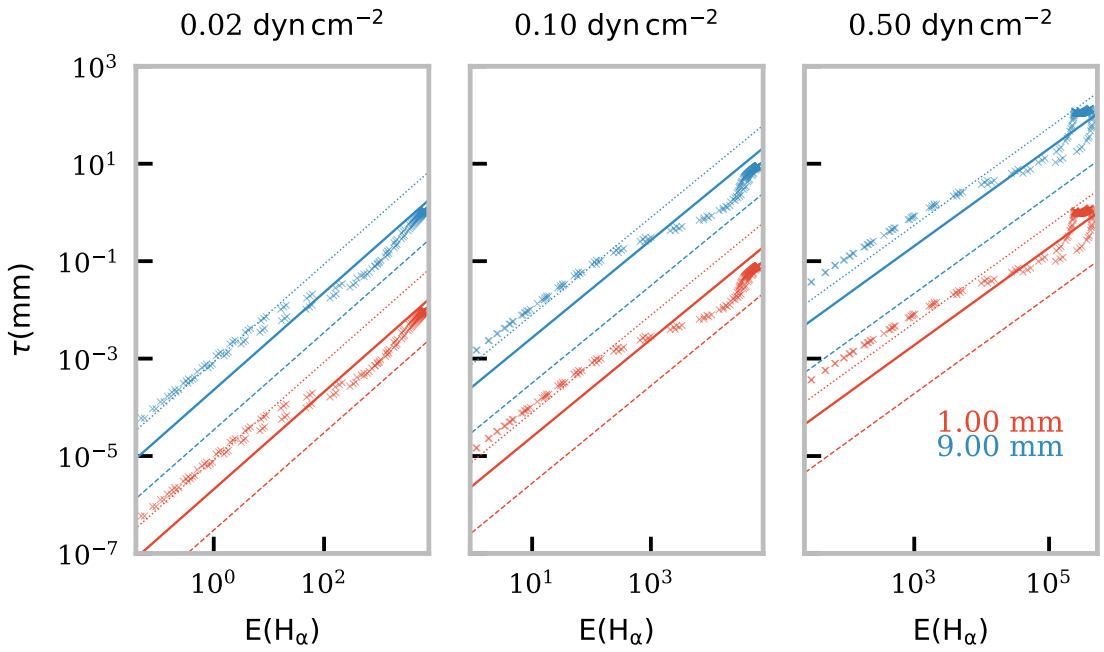

Figure 3.18: Optical thickness of the plasma at two millimetre wavelengths versus the integrated intensity of the Hα line for three different multi-thermal prominence models with different pressures from Table 2.2. Each point represents a different LOS in each 2D model, with their colour representing the wavelength of the millimetre continuum as given on the figure. The three straight lines represent calculations of the estimated relationship through Equation 3.9, with the dotted line calculated using a temperature of T1, from Table 2.2, the dashed line calculated using T0 from Table 2.2, and the solid line calculated using the electron density weighted mean temperature.

making a total prominence radius of 1000 km.

In Figure 3.18 I present the relationship found between two different millimetre-continuum optical thicknesses and the integrated intensity of the Hα line, for three models of different pressure from across the set given in Table 2.2. For each wavelength/colour, the three straight lines represent different calculations of the estimated relation as described in Equation 3.9. As there is no single representative temperature for these multi-thermal models the lines are calculated using the temperature of the core (dashed line), the corona (dotted line), and the electron density weighted mean temperature (solid line). The departure coefficient is calculated in the same manner as in Section 3.3.1.1.

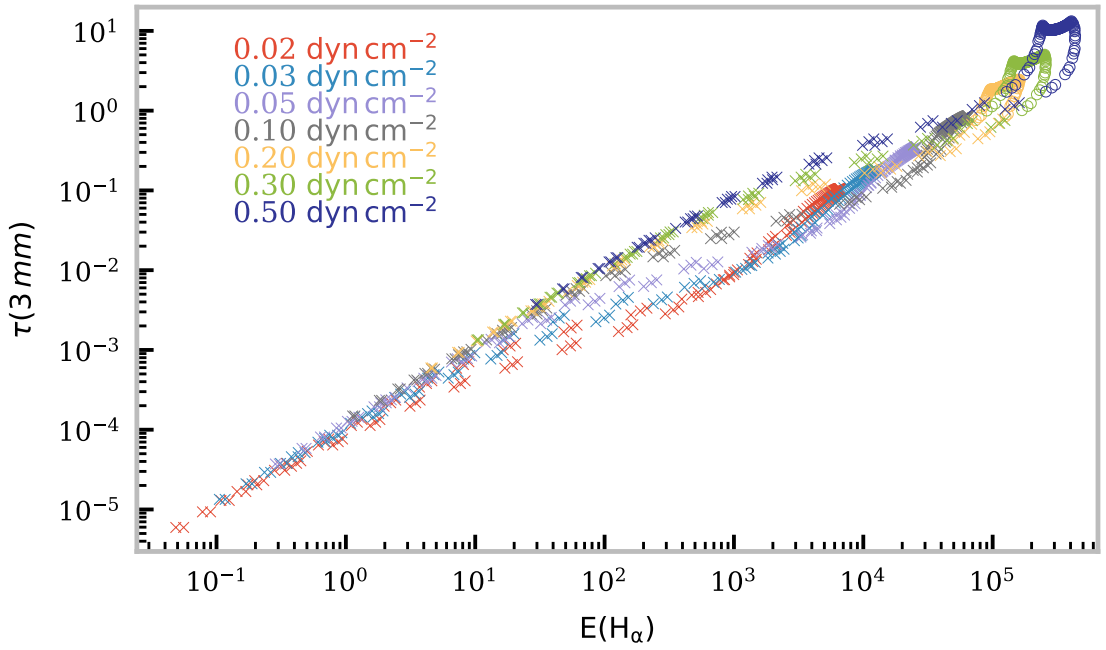

Figure 3.19: Optical thickness at 3mm versus integrated intensity of Hα for a set of multi-thermal prominence models as described in Table 2.2. Each point represents a different LOS in each 2D model, with their colour representing the constant pressure of each model as given on the plot. Points marked with an 'x' describe LOS where the optical thickness at the centre of the Hα line is less than 1, whilst points marked by an 'o' represent LOS where it is greater or equal to 1.

It can be seen from Figure 3.18 that the distribution is somewhat more complicated than the isothermal case, as there are up to two parts of the distribution where the relationship may be approximated as a power law relationship ($y = mx + c$ in log-space), as shown in Equation 3.9. At the lower millimetre optical thickness end of each distribution the relationship can be most closely approximated by the analytical expression using the temperature of the very edge of the PCTR. These points come from LOSs which are extremal within the FOV of the simulated observation where the path only crosses through a small section of the prominence, and only through high temperature material. For this part of the distribution, at higher pressures, it can be seen that the optical thickness becomes underestimated, as expected from Equation 3.9 due to the increased density of twice ionized helium.

At the high millimetre optical thickness ends of the distributions, the relationship falls closer to the solid line calculated using the electron density weighted mean temperature

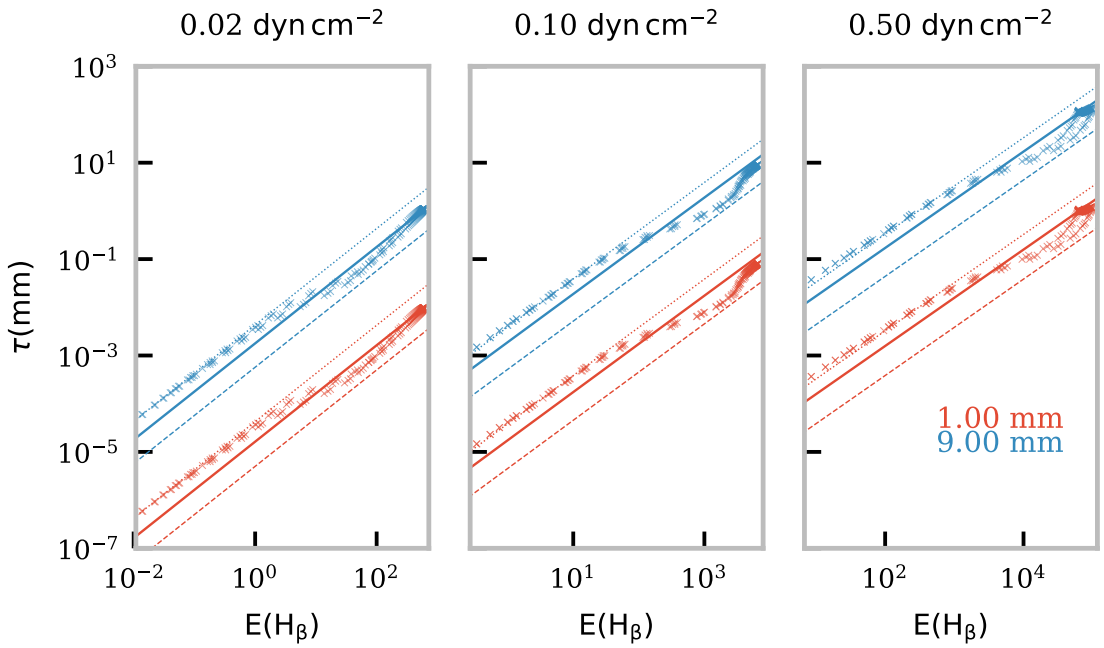

Figure 3.20: Optical thickness at two millimetre wavelengths versus the integrated intensity of Hβ for three multi-thermal prominence models with different pressures from Table 2.2. Each point represents a different LOS in each 2D model, with their colour representing the wavelength of the millimetre continuum as given on the figure. The three straight lines represent calculations of the estimated relationship through Equation 3.15, with the dotted line calculated using a temperature of T1, from Table 2.2, the dashed line calculated using T0 from Table 2.2, and the solid line calculated using the electron density weighted mean temperature.

of the LOS. This analytical expression again underestimates the numerical results which could be due to the same reasons as previously, i.e. non-uniform departure coefficient and the presence of helium, or it could be due to the lack of a representative temperature for the LOS. These points in the distribution do, however, occur from the LOSs in the centre of the FOV where the path crosses through large sections of the isothermal core of the prominence.

In the central region of the millimetre optical thickness distributions there is the region where the LOS crosses through mostly large sections of PCTR material, and less of the isothermal core. Here it can be seen that a much less clear relationship between the optical thickness of the millimetre-continuum and the integrated intensity of the Hα line exists, due to the plasma being furthest from the isothermal condition. In the right most panel of

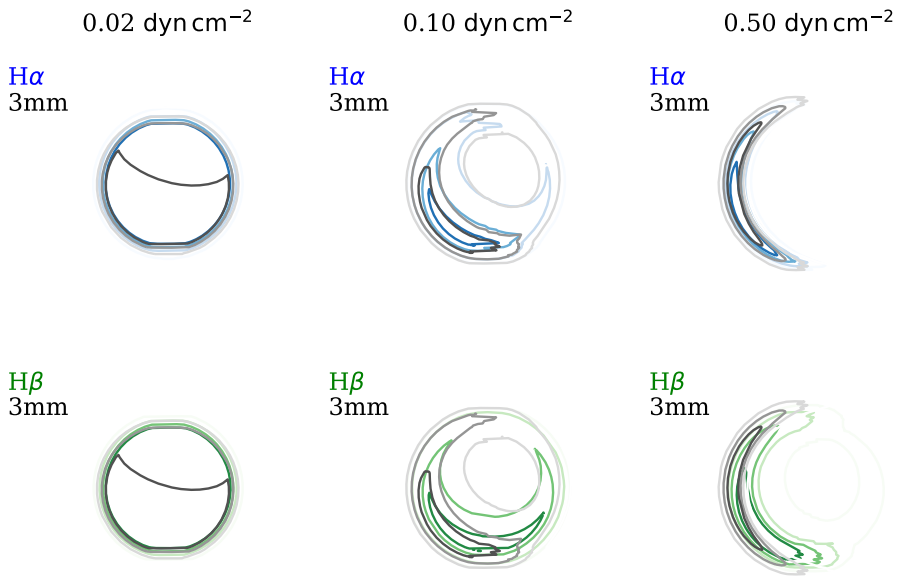

Figure 3.21: Contour maps for contribution function for the Balmer Hα and Hβ lines, compared to the continuum at 3 mm, for three multi-thermal prominence models, each with different constant pressure. The LOS is directed such that the "observer" is to the left of each cylinder. The coloured contours show the Balmer lines, as given on the plot, whilst the black contours describe the millimetre continuum. The contour levels correspond to {20, 40, 60, 80, 100}% the maximum of the contribution function in the model prominence.

Figure 3.18 the prominence model has a sufficiently high pressure/density that the LOSs crossing the cylinder near to the axis are optically thick in the line centre of Hα. Here the assumptions required for Equation 3.9 are broken and the quality of the correlation becomes less clear the more optically thick the line becomes.

A combined view of the results from all seven multi-thermal models is given in Figure 3.19 compared to the optical thickness at 3mm. The 3mm wavelength was chosen as it is within ALMA Band 3 which the most likely band to be emitted at a higher optical thickness from the bands which are currently available to solar physics. It can be seen clearly that, with a small scatter in the data, a power law dependence occurs at very low optical thickness and again towards the point when the plasma becomes optically thick for 3 mm emission. In this plot I also represent the optical thickness regime of the Hα line-centre emission through different markers for the points, i.e. 'x' represents $\tau < 1$, and 'o' represents $\tau \geq 1$.

Although it is model dependent, it can be seen that the transition between optically thin, and optically thick plasma for the line-centre of Hα occurs roughly at the same point as for the millimetre-continuum at 3 mm. Within the regime where the centre of the Hα line is optically thin, the maximum spread across the y-axis for the optical thickness at 3 mm in Figure 3.19 is roughly 1 order of magnitude.

Figure 3.20 again shows the relationship between optical thickness of the millimetre-continuum and the integrated intensity of Hβ, although in this case for multi-thermal models. The straight line expressions are once again calculated using Equation 3.15, with the temperatures used the same as was previously in this section for Hα. As would be expected, the relationship in Hβ closely resembles that seen in Hα, however with the overall optical thickness of the Hβ line centre lower than that seen in Hα for the same model prominences.

In Figure 3.21 I show a comparison between the contribution function maps of Hα and Hβ with the millimetre continuum at 3 mm, at three multi-thermal models of different pressure. In the two low pressure models the plasma is optically thin for both Balmer lines and the millimetre-continuum. This results in the contour maps showing contribution function components from across both sides of the cylinder axis. Similar to the 3 mm emission, the Balmer lines also show increased contribution from the lower boundary of the cylinder, where ionising EUV radiation is incident on the prominence plasma. In the highest pressure model, the plasma is optically thick for both the Balmer lines and the 3 mm emission. Here the contribution function is highly peaked towards the side of the cylinder nearest the observer, as was previously discussed in Section 2.4.2 for the millimetre emission. In all instances in these models there is clear and consistent overlap between the contribution function maps of the millimetre emission and the Balmer lines, with Hα showing a slightly improved overlap compared to Hβ, such that it can be concluded that both types of emission are formed in the same regions of the solar prominence plasma.

3.3.2 The Lyman Series and the Millimetre/sub-millimetre Continuum

The Lyman series contains the set of resonance lines for neutral hydrogen. These lines display large intensities from the main body of solar prominences due to large optical thicknesses and light scattering from the bright solar disk. The high optical thicknesses are due to the prominence densities and the Lyman series presenting large cross-sections for interaction. Because of their high intensities and optical thickness, the Lyman lines play an important role in the energy balance within the prominence plasma. A lot of the observed knowledge

of the Lyman series spectra was obtained using the *Solar Ultraviolet Measurements of Emitted Radiation* (SUMER) (Wilhelm et al. 1995) spectrometer on the *Solar Heliospheric Observatory* (SOHO) satellite. This instrument was a UV spectrograph capable of scanning the range 500–1600 Å. A review of the solar prominence science performed using SUMER, amongst the other instruments on board SOHO, was given by Patsourakos & Vial (2002). Prior to SUMER observations of the Lyα and Lyβ in prominences, there were observations obtained using the LPSP instrument on OSO-8 which are discussed in Vial (1982).

Observations of the higher order Lyman lines (Lyδ–Ly9) were presented in Schmieder et al. (1999). They found the intensities of the lines from the solar prominence to be roughly half the intensity on the solar disk, which they attributed to dilution of the incident radiation. Through comparison with three different sets of non-LTE prominence models, both isothermal and with a temperature gradient representing a PCTR, they found that whilst individual lines could be replicated using isothermal-isobaric models, to replicate the set of higher order Lyman lines they required models with a varying temperature gradient, thus confirming the need for a PCTR in prominence modelling of Lyman lines. By varying the intensity of the incident radiation in the non-LTE models they found that the higher order Lyman lines (Lyϵ and above) were highly dependent on the incident intensity, whilst Lyα intensity was only reduced by half the reduction factor. Gunár et al. (2007) showed across the range of lines in the Lyman series that the SUMER observations were better represented by multi-thread fine-structure modelling than singular slab models, except for Lyα which is unaffected by multiple fine-structures due to its high optical thickness.

Observations across the whole Lyman series were presented by Heinzel et al. (2001b). These data sets showed variation in both the intensity and the shape of the Lyman spectral lines, with the discovery that surprisingly the profiles did not always present strongly reversed profiles. It was postulated by these authors that the cause of this could be the viewing angle with respect to the magnetic field and the PCTR, i.e. that viewing the PCTR along the magnetic field lines would produce unreversed profiles, whilst viewing across the magnetic field would produce reversed profiles, as expected. Gunár et al. (2010) were able to replicate the shape of parts of the Lyman spectra by conducting a statistical comparison between observed Lyman line emission and synthetic profiles from three sets of 2D multi-thread models with different PCTR temperature distributions. They did, however, find that their simulated profiles displayed too sharp peaks compared to the observations. This is attributed to either issues in the frequency redistribution within the radiative transfer in

their 2D models compared to the real 3D case, or due to the lack of mutual interaction considered between their model threads. The authors did perform some minor tests on the effect of mutual interaction between threads and found that this exaggerated the sharpness of the peaks, however, these tests neglected LOS velocities which would be present between threads.

In this section I cover the relationships found using the C2D2E model for the Lyman series and the millimetre-continuum. I begin by investigating any correlation between the emergent intensities of the Lyman lines and continua with various forms of the emission measure in Section 3.3.2.1. Section 3.3.2.2 presents the correlations found between the Lyman series emission and optical thickness with the millimetre-continuum. Finally Section 3.3.2.3 considers the colour temperature of the Lyman continuum and how this relates to the electron temperature of the model prominences and the brightness temperature of the millimetre-continuum.

3.3.2.1 The Lyman Series and the Emission Measure

Whilst an expression relating the integrated intensity of the Lyman lines to the electron–proton emission measure of an optically thin plasma, as discussed in the section on the Balmer series (Equation 3.11) exists, realistically prominences will always be predominantly optically thick in the major Lyman lines. This is due to the density of the solar prominences and the large cross-sections for interaction. Because of this the analytical electron–proton emission measure relation is not calculated here. As there is no need for an isothermal assumption, this section focuses on the distributions found when considering a multi-thermal prominence structure including a PCTR (Table 2.2).

In Figures 3.22 and 3.23 I show the relationship between three different forms of the emission measure: the electron–proton emission measure ($n_e n_{\mathrm{H_{II}}} L$), the total hydrogen density emission measure ($n_{\mathrm{H}}^2 L$), and the electron–singly ionized helium emission measure ($n_e n_{\mathrm{He_{II}}} L$), with the integrated intensities of the first three lines of the Lyman series (Lyα, Lyβ, and Lyγ), as well as the intensity at the head of the Lyman continuum (912 Å). As expected for Lyα, the strongest and most optically thick resonance line of neutral hydrogen, the low pressure models show that both the electron–proton and the total hydrogen density emission measures are uncorrelated with the integrated intensity of the line. This is because the emission mechanism is heavily dominated by scattering of incident radiation. At the highest pressures there is an increased collisional element to the emission mechanism,

causing a slight increase in correlation. The electron–singly ionized helium emission measure relationship has a more complex distribution, this is unsurprising as the Lyman emission will not be directly related to the helium densities, but rather that the helium populations will also be related to the neutral hydrogen density through the ionization equilibrium. Lyβ and Lyγ show similar relationships to each other with respect to the various emission measures, as seen in the low pressure models for Lyα.

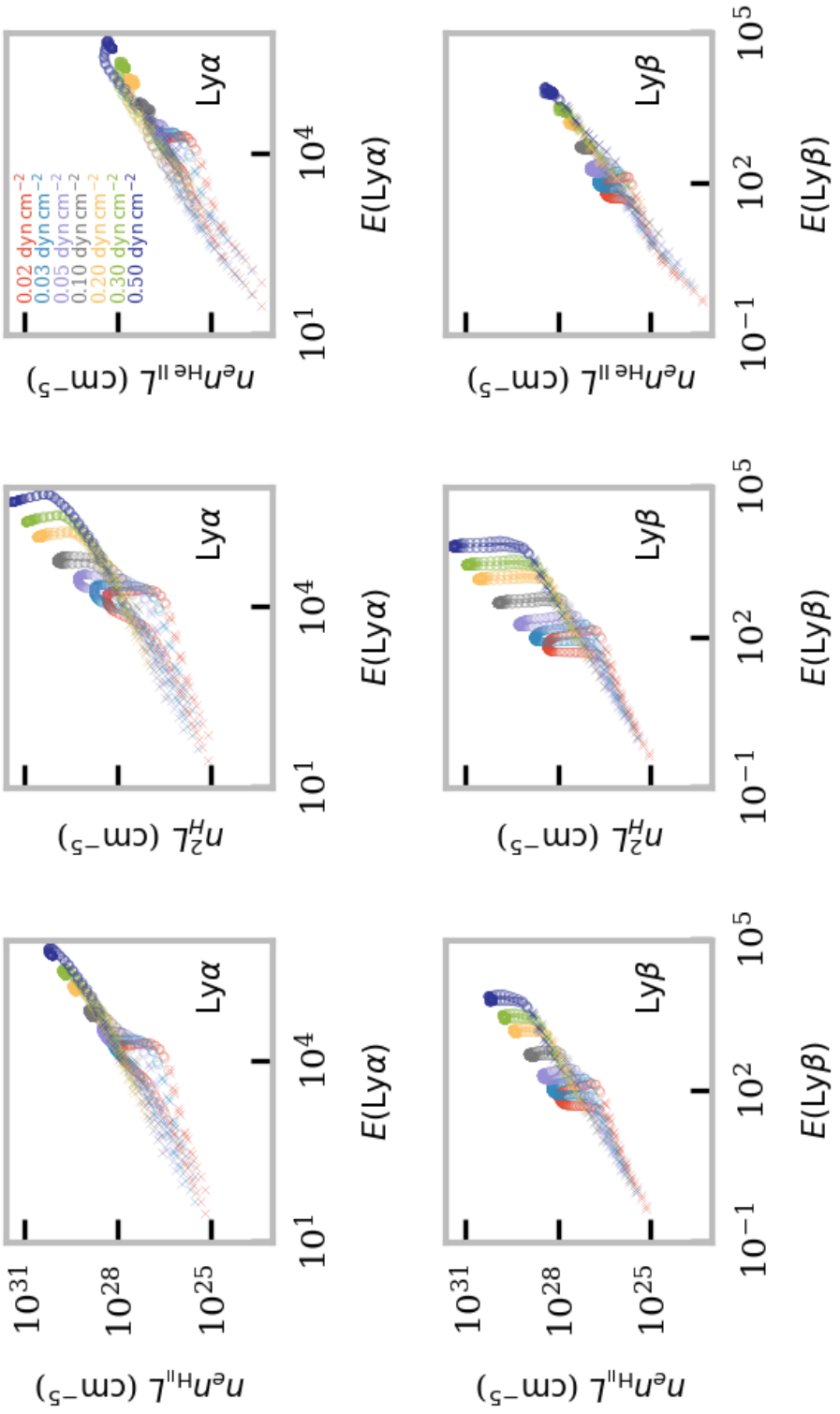

Figure 3.22: Relationships between different forms of the emission measure with the Lyman α and β intensities. The columns show: the electron/proton emission measure ($n_e n_{\mathrm{H_{II}}} L$), the total hydrogen density emission measure ($n_{\mathrm{H}}^2 L$), and the emission measure for singly ionized helium ($n_e n_{\mathrm{He_{II}}} L$). Each colour represents a pressure from Table 2.2. The markers represent the optical thickness for the line-centre/continuum head ("x" for $\tau < 1$, and "o" for $\tau \geq 1$).

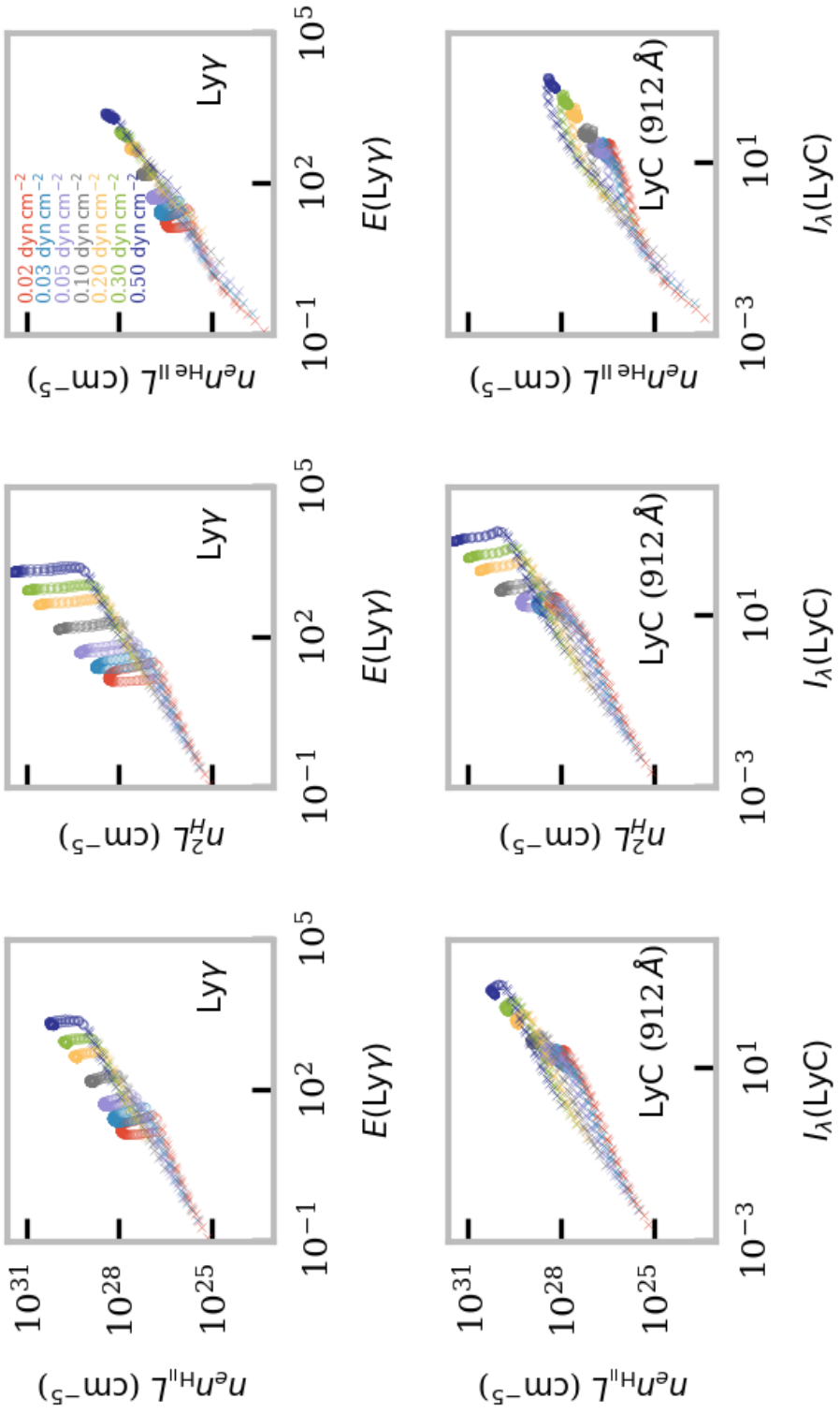

Figure 3.23: Same as Figure 3.22 but for Lyman γ and continuum at 912Å intensities.

Lyα at high pressures is optically thick even into some of the shortest LOSs through PCTR and produces a more symmetrical FOV across the cylinder axis than the other Lyman lines. This appears to increase correlation between Lyα integrated intensity and the electron-proton emission measure for high pressure models.

The Lyman continuum emission appears to have a larger region within the FOV for which it is optically thinner than the three line centres, thus leading to a somewhat correlated distribution, although once optically thick it is clear that the scattering does play a significant role in the emission mechanism here.

3.3.2.2 The Lyman Series and the Optical Thickness of the Millimetre-continuum

In Figure 3.24 the relationship between the optical thickness and brightness temperature of the millimetre continuum at 3 mm and the intensities of the Lyman series for the same set of multi-thermal prominence models is shown. It is immediately clear from this figure that emission from optically thin LOSs from Lyβ, Lyγ, and the Lyman continuum will have a power law relation with the optical thickness of the millimetre-continuum. This is slightly less clear with Lyα at low pressures as it appears the ionization asymmetry across the FOV has a larger affect here. This is because Lyβ and Lyγ are formed under more collisional conditions giving them a more symmetrical FOV. On the other hand, at low pressures Lyα is scattered straight from the lower boundary of the prominence, whilst for high pressures collisional excitation occurs across the FOV. When the Lyman emission emanates from an optically thick plasma the relationship between the intensity and the optical thickness of the millimetre-continuum appears mostly uncorrelated. The one exception to this statement potentially being that seen in Lyα at high pressures. This will be caused by the relationship found between the electron-proton emission measure and the Lyα intensity found for the same pressures in the previous subsection.

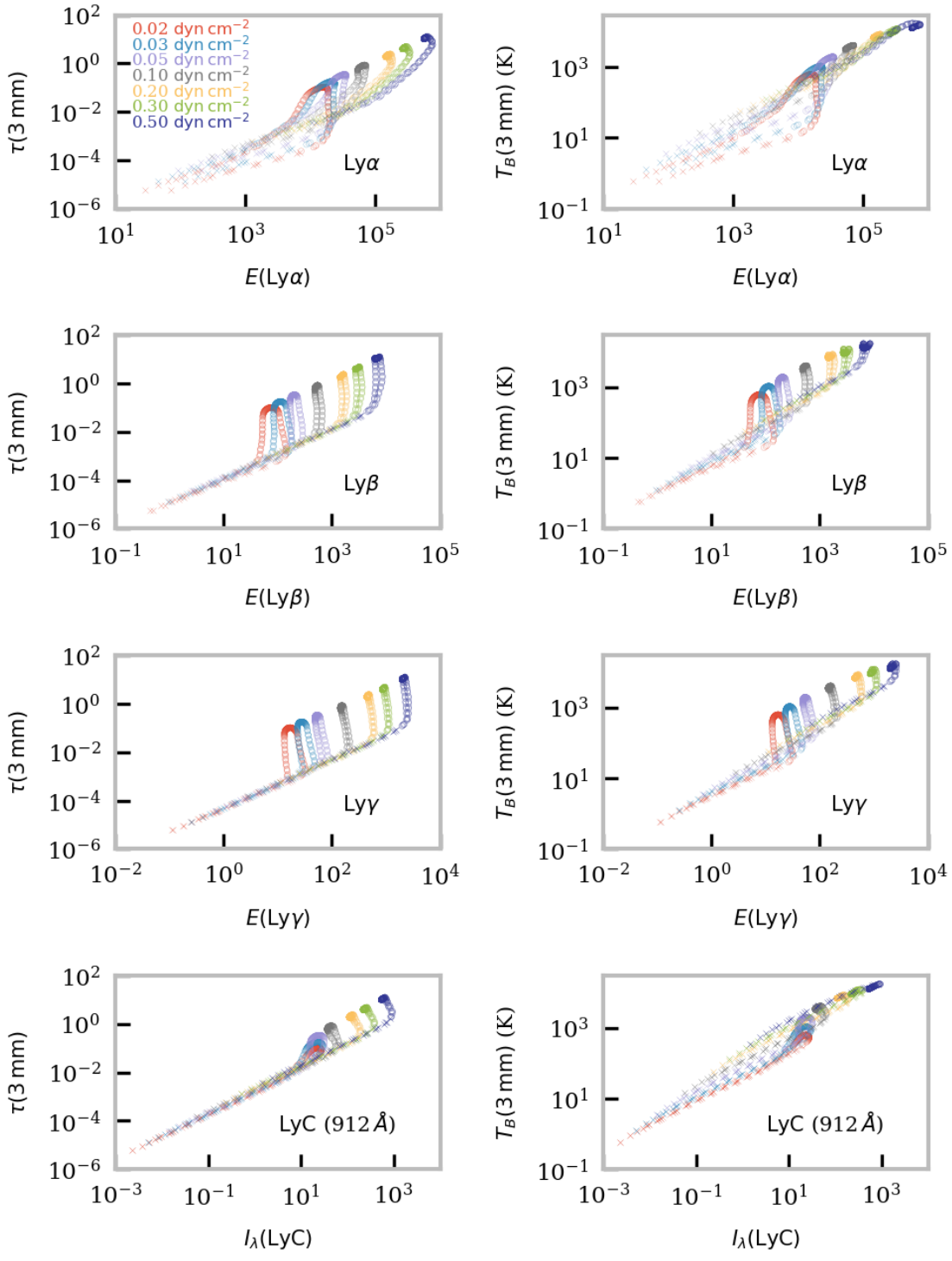

Figure 3.24: Relationships between the millimetre-continuum at 3 mm optical thickness and brightness temperature versus the intensities of the Lyman series. Each row represents a different part of the Lyman series which are in descending order: Lyman-α, Lyman-β, Lyman-γ, and the Lyman continuum at 912 Å. The colours represent the pressure of each isobaric model, whilst the markers represent the optical thickness for the line-centre/continuum head ("x" for $\tau < 1$, and "o" for $\tau \geq 1$).

In Figure 3.25 the relationship between the various optical thicknesses of the Lyman line centres, as well as at the head of the Lyman continuum with the optical thickness of the millimetre-continuum is shown. In all cases the same trend is observed, where there is a clear, yet model-dependent and thus pressure/density-dependent correlation.

Using contour maps of the contribution function of the line centre of the Lyα, Lyβ and Lyγ lines and the millimetre-continuum at 3mm the formation layer of the radiation is analysed in Figure 3.26. It is clear that the emission from all three Lyman lines is emitted from near the edge of the prominence cylinder. This is significantly different from what has been seen for the millimetre-continuum, especially for low pressure/density models. As the millimetre-continuum at 3mm becomes optically thick, as witnessed in the right hand column of Figure 3.26, the forming regions take on a similar shape to that of the Lyman lines, however, closer to the cylinder axis. Lyγ is the closest to having an overlapping formation region with the 3mm emission, although they are still clearly distinct, whilst Lyα is furthest from overlapping.

Due to the highly optically thick and scattering-dominated emission mechanism in the formation of the Lyman lines in prominences, there is no clear correlation between the integrated intensities of the lines with the emission measure, and thus the optical thickness of the millimetre-continuum. However, the emission across the line-profile will vary, with the plasma being less optically thick in the line wings. This could lead to an increase to the contribution of the intensity formed from collisional effects here.

3.3.2.3 Temperature and the Lyman Continuum

The Lyman *Extreme Ultraviolet* (EUV) continuum has an important role in the ionization and energy structure of solar prominences. Incident radiation in the EUV range is primarily responsible for the ionization of the neutral species within the cool prominence structure. Emission from prominences in the Lyman continuum is thus dominated by the radiative ionization, and subsequent photo-recombination processes. Measurement of photo-recombination (bound-free) spectra has the capability to diagnose the temperature of the emitting plasma through a variable known as the *colour temperature* (T_c). The colour temperature, unlike the brightness temperature, is defined by the slope of the continuum spectrum. Orrall & Schmahl (1980) presented the measurement of the colour temperature from nine sets of Lyman EUV continuum observed in hedgerow prominences. They define the colour

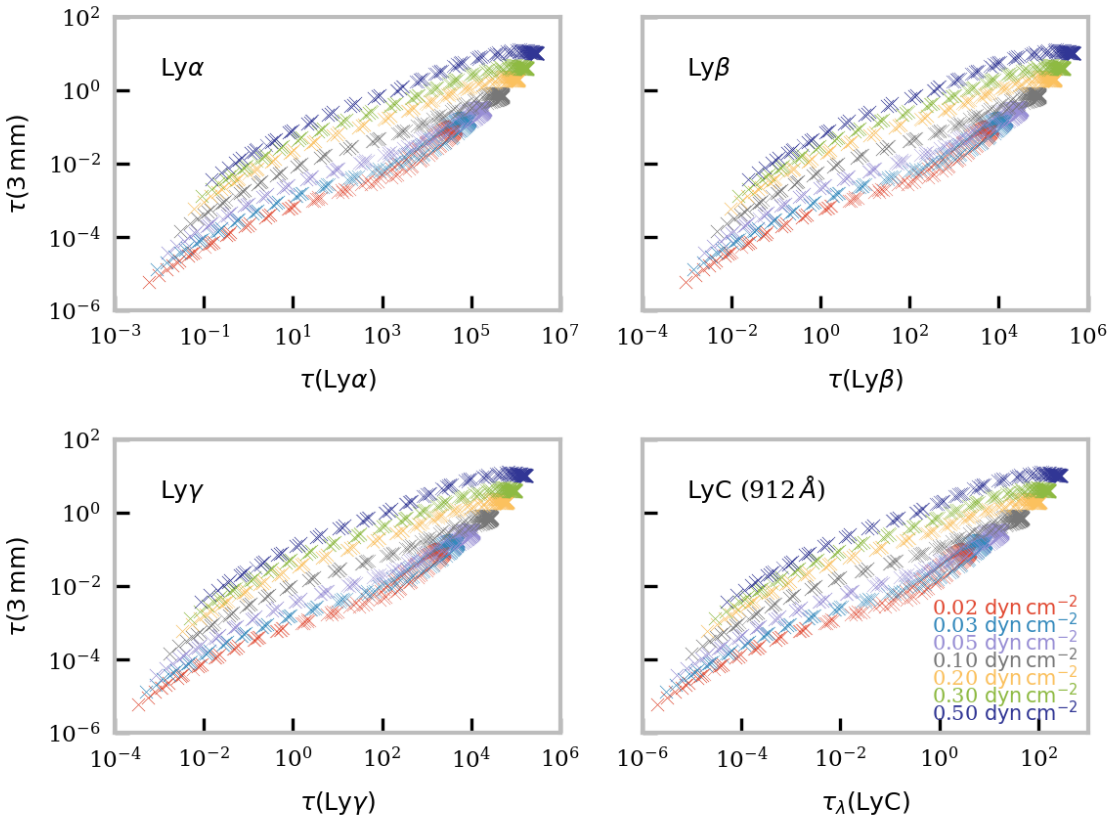

Figure 3.25: Relationships between the optical thicknesses at the line centres of the Lyman-α, Lyman-β, and Lyman-γ lines, as well as the optical thickness of the Lyman continuum at 912 Å, with the optical thickness of the millimetre-continuum at 3 mm. These plots were produced using the multi-thermal prominence models defined in Table 2.2. The colours represent the pressure of each isobaric model.

temperature, including contribution from stimulated emission as:

$$T_c = -\frac{hc}{\lambda_0 k_B B} \quad , \tag{3.16}$$

where λ_0 is the wavelength at the head of the photo-recombination continuum, which for the Lyman continuum is at 912 Å. The parameter B is found by fitting the logarithmic spectrum:

$$\ln(I_\lambda \lambda^5) = A + B\left(\frac{\lambda_0}{\lambda} - 1\right) + C\left(\frac{\lambda_0}{\lambda} - 1\right)^2. \tag{3.17}$$

As derived in Orrall & Schmahl (1980) for an isothermal plasma, with a uniform departure coefficient across the LOS, the coefficients to this quadratic expression would be expected to be:

$$A = \ln(I_{\lambda_0} \lambda_0^5), \tag{3.18}$$

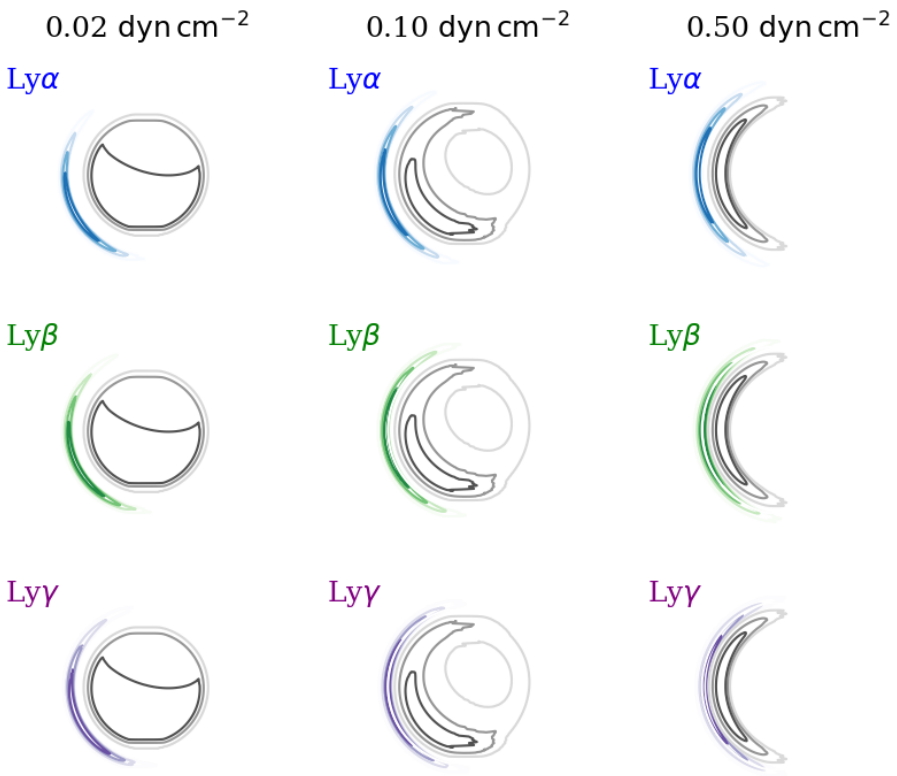

Figure 3.26: Contour maps for the Lyα, Lyβ and Lyγ lines, compared to the continuum at 3 mm, for three multi-thermal prominence models, each with different constant pressure. The LOS is directed such that the "observer" is to the left of each cylinder. The coloured contours show the Lyman lines, as given on the plot, whilst the black contours describe the millimetre continuum. The contour levels correspond to {20, 40, 60, 80, 100}% the maximum of the contribution function in the model prominence.

$$B = \epsilon\gamma\xi_1 - \frac{hc}{\lambda_0 k_B T} \quad , \tag{3.19}$$

and

$$C = (\epsilon\gamma)^2\xi_2. \tag{3.20}$$

γ is ≈ 3 for the Lyman continuum where it arises from the expected relation $\frac{\tau(\lambda)}{\tau_0} \approx (\frac{\lambda}{\lambda_0})^{-\gamma}$, whilst ϵ is a small correcting factor added in the derivation. ξ_1 and ξ_2 are terms dependent on the optical thickness at the head of the continuum solely. If $\xi_1 \neq 0$, then the measured colour temperature will differ from the electron temperature by a value dependent on the optical

thickness. In Noyes et al. (1972) the authors presented results for the colour temperature of solar prominences and filaments in the Lyman continuum using observations taken using the *Orbiting Solar Observatory* (OSO) 4 and 6 instruments. In this study they used a simpler expression for the colour temperature than Orrall & Schmahl (1980) by neglecting any contribution from stimulated emission. They measured a continuum colour temperature of 6800 K which was found to increase with height. They also found that due to the Lyman continuum opacity, filaments have a high visibility contrast with respect to the surrounding quiet Sun for lines shortward of the recombination edge at 912 Å, whilst at wavelengths longer than 912 Å, filaments will display a lower contrast, although still being visible.

The colour temperature of prominences has been calculated for isothermal-isobaric models by Heasley & Milkey (1983). From their models they found that the Lyman continuum brightness was only dependent on the optical thickness of the plasma and the incident EUV radiation. When calculating the colour temperature of the prominence models, they found that the colour temperature from an optically thick slab equaled the electron temperature, whilst the colour temperature from an optically thin slab was less than the electron temperature.

In Parenti et al. (2005) the authors used observations of the Lyman continuum with SUMER on board SOHO to measure the brightness and colour temperature from a solar prominence in order to find information on the electron temperature of the emitting plasma at two different parts of the prominence structure. In this study they found that their values agreed quite well with the average values that were presented in Orrall & Schmahl (1980). The temperature of the prominence plasma, in an observation where the prominence is seen to disappear in the EUV, has also been estimated using the Lyman continuum observed by SUMER in Ofman et al. (1998). The authors compared the ratio of intensities at 876Å, and 907Å to computed values using the isothermal-isobaric prominence models of Gouttebroze et al. (1993). They attribute the variation in the temperature structure they observed to Alfvén wave heating, such that the cool material required for the EUV Lyman continuum emission is heated towards coronal temperatures. Heinzel et al. (2001a) used coordinated observations of the Lyman EUV emission, and Hα from THEMIS/MDSP to address why solar filaments are observed to have significantly greater width in EUV lines, than in Hα. They concluded that the reason for this is the enhanced opacity found in the Lyman continuum, compared to Hα, such that less of the cool material required for the filament to be visible in Hα is necessary to observe in the EUV lines. They speculate thus that the observed Hα

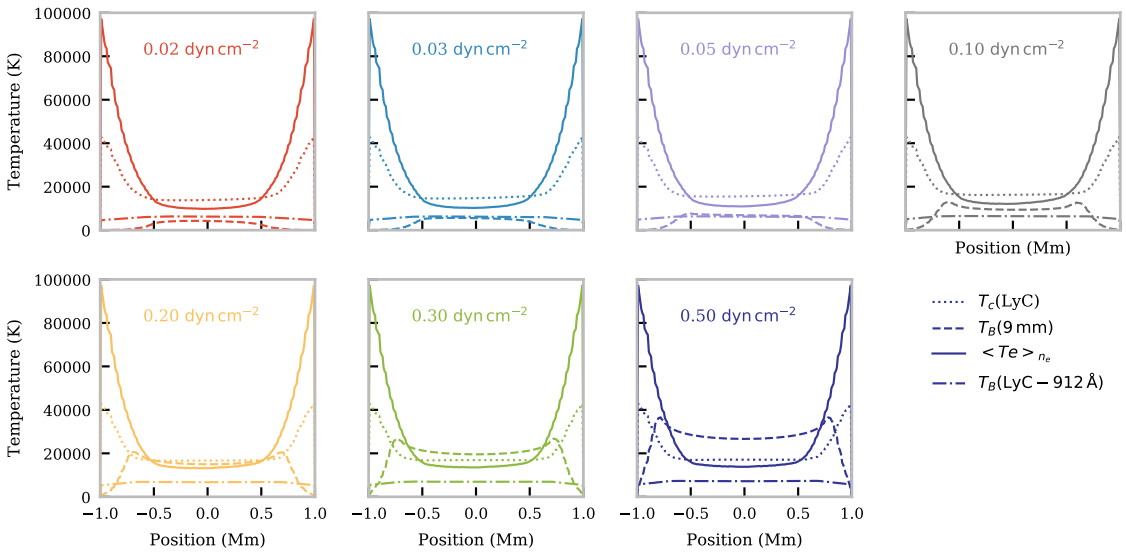

Figure 3.27: Variation across the FOV of the colour (*dotted line*) and brightness temperatures (*dot-dashed line*) of the Lyman continuum compared to the brightness temperature of the millimetre continuum (*dashed line*) for a set of multi-thermal prominence models (Table 2.2). The Lyman continuum brightness temperature is calculated at 912Å, whilst the millimetre continnuum is calculated at 9 mm. The electron density weighted mean temperature is also shown for each LOS in the FOV using the *solid line*.

filaments represent the lower altitude, higher density parts of a prominence, which are observed in off-limb observations, whilst the significantly wider EUV filaments encompass the more diffuse, irregular, cool material that is observed at higher altitudes in off-limb observations.

For the rest of this section I shall present the results found in testing the colour and brightness temperature of the Lyman continuum using the multi-thermal C2D2E models defined in Table 2.2, presenting also how these quantities compare to the brightness temperatures as observed in the millimetre-continuum. The colour temperature is defined in this study using Equation 3.16 following Orrall & Schmahl (1980) by fitting the output Lyman continuum spectrum of C2D2E using Equation 3.17.

In Figure 3.27 I show the variation across the FOV for the Lyman continuum colour and brightness temperatures, as well as the brightness temperature at 9 mm and the electron density weighted mean temperature of each LOS for the set of multi-thermal prominence models. The brightness temperature of the Lyman continuum was calculated using the

intensity of the continuum at 912Å and the Planck function as defined in Equation 1.13. At the edges of the FOV where the LOS through the cylinder is shortest, the colour temperature of the Lyman continuum increases with radial distance from the cylinder axis, however at a less steep gradient than is seen for the electron density weighted mean temperature. The magnitude of the value here is also somewhat lower than the electron density mean temperature, which is not unexpected for when the LOS is optically thin (Heasley & Milkey 1983). In the centre of the FOV, where each LOS is optically thick at 912 Å the colour temperature flattens out at a value a little higher than the electron density weighted mean temperature. Here, the quadratic fit to the spectrum (Equation 3.17) becomes less good due to the material having increased optical thickness whilst also not meeting the isothermal condition. The millimetre brightness temperature varies as described in Section 2.4.2; where whilst optically thin, the brightness temperature is less than the mean temperature of the LOS; and whilst optically thick, it gives a representative measure of the temperature of a given formation layer, which may be higher than the mean temperature of the LOS. The models with pressures of 0.1–0.3 dyn cm^{-2} yield colour temperatures of the Lyman continuum and brightness temperatures of 9 mm emission which are similar to the electron density weighted mean temperature. This may be due to the emission being formed in similar regions of the cylinder.

To test this, in Figure 3.28 the contribution function of the emission at 912 Å is shown overlaid with that at 9 mm. It can be seen here that at pressures of 0.1–0.3 dyn cm^{-2} both the Lyman, and millimetre continuum are optically thick, with similarly highly peaked, crescent shaped contribution function maps. At the higher pressure of 0.5 dyn cm^{-2}, however, the contribution function of the millimetre-continuum has moved further from the cylinder axis than that of the Lyman continuum, and is thus sampling plasma at a significantly higher temperature within the PCTR, thus leading to the higher brightness temperatures seen in the final panel of Figure 3.27. For the models with pressures of < 0.1 dyn cm^{-2}, the prominence plasma has a lower optical thickness at 9mm resulting in a significantly wider contribution function distribution across the cylinder. There is thus a larger contribution in these models' brightness temperatures from the electron temperature of the cool prominence core, resulting in values which are below the Lyman continuum colour temperature for the same LOS.

The variation of the brightness temperature at 912 Å is a lot smaller than the other measurements, with its maximum value significantly below that of the electron density weighted mean temperature. The relationship between both the brightness temperature

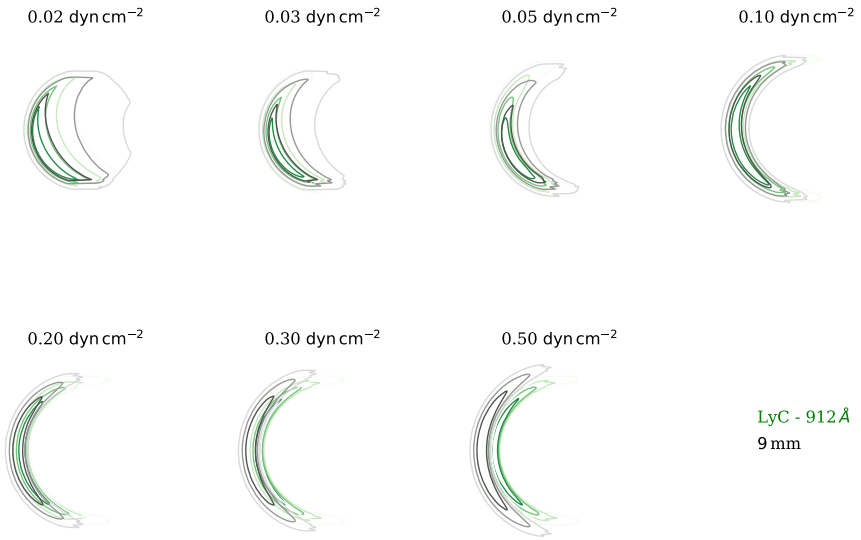

Figure 3.28: Contribution function maps for the Lyman- (912Å) and millimetre -continuum (9 mm) emission in a set of multi-thermal prominence models (Table 2.2). The Lyman continuum is shown in green, whilst the mm continuum is shown as black contours. The levels of both contours are set as [20, 40, 60, 80, 100]% of the maximum value.

of the millimetre continuum at 9 mm and the Lyman continuum at 912 Å is shown in Figure 3.29. The emission at 912 Å from optically thick LOSs is displayed using a different set of markers. It can be seen that whilst optically thin there lies a model dependent correlation between both measurements, although the variation in magnitude for the Lyman continuum is significantly less than the millimetre equivalent. The reason why their is a lower variation in the Lyman continuum brightness temperature is because it is heavily scattered, resulting in a brightness temperature which is predominantly related to the value of the incident radiation. Correlation ceases to exist once the brightness temperature of the millimetre continuum flattens out for optically thick LOSs.

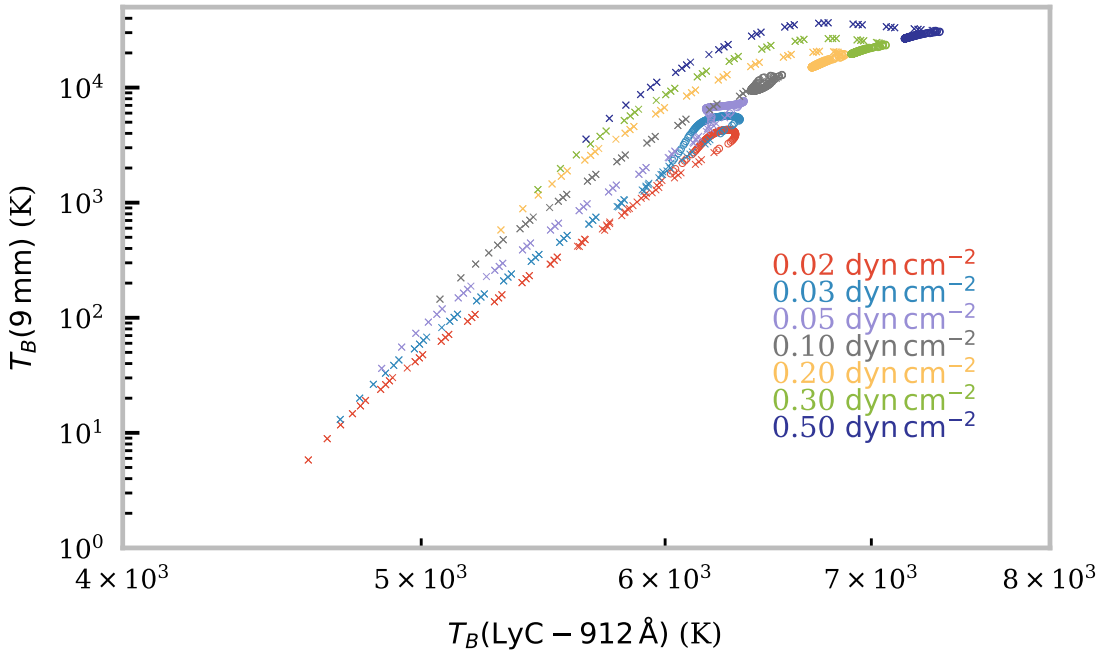

Figure 3.29: Brightness temperature of the millimetre-continuum at 9 mm versus the brightness temperature calculated at the head of the Lyman continuum (912Å). Trend is shown across the set of multi-thermal prominence models (Table 2.2). The points with 'o' as markers represent LOSs where the emission at 912Å is produced from optically thick ($\tau \geq 1$) plasma.

3.3.3 Helium and the Millimeter/sub-millimeter Continuum

In the previous sections it has been shown that the most important parameter in the calculation of the optical thickness of the millimetre-continuum is the charge squared weighted electron–ion emission measure. As the integrated intensity of optically thin neutral hydrogen emission is closely related to the electron–proton emission measure, there is thus a fairly clear correlation between them and the optical thickness of the millimetre-continuum, even for multi-thermal models containing a PCTR. The next question to arise is thus: do similar correlations exist between the millimetre-continuum and spectral line emission from other elemental species?

The second most abundant element in the solar atmosphere after hydrogen is helium. Helium spectral line emission has long and frequently been observed from solar prominences; indeed the neutral helium D3 line (5876 Å) was observed in an off-limb solar structure as far back as 1868, 27 years before the discovery of helium in the Earth's atmosphere (Vial &

Engvold 2015).

The helium abundance ratio, A_{He}, is defined as the ratio of number densities of total helium to hydrogen ($\frac{n_{\mathrm{He\,total}}}{n_{\mathrm{H\,total}}}$). In solar prominences this has been calculated by Heasley & Milkey (1978) to be 0.1 ± 0.025, through the comparison between observational data and 1D numerical models. The abundance ratio has also been calculated by Iakovkin et al. (1982) as 0.05 through solving integral diffusion equations, however their method only considered low temperature plasma, and thus neglects the higher temperatures found in prominences, and in particular the PCTR. Hirayama (1971) calculated the ratio to be 0.065 observationally, assuming a fully ionized hydrogen and helium plasma.

The atomic model for neutral helium is significantly more complicated than for hydrogen; containing two distinct and separate systems, known as the singlet and triplet systems. The two systems correspond to differing spin angular momentum numbers with $S = 0$ for the singlet and $S = 1$ for the triplet, respectively. Transitions between these two systems are forbidden, however, the energy level populations are linked through collisions via the equations of statistical equilibrium and through photoionization-recombination.

Lines such as He I 584Å and He II 304Å are also commonly observed from solar prominences, however, both these lines are strong resonance lines of neutral helium and singly ionized helium, respectively, which results in them being formed under optically thick conditions. In the previous section it was found for the Lyman lines that it was difficult to determine any clear relationship between the optical thickness of the millimetre-continuum with the integrated intensity from a line when it is produced in said optically thick conditions. Therefore, in this study I restrict my analysis to the frequently observed neutral helium line: He I 5876Å (D3). He I 5876Å, or D3, is created within the triplet system of neutral helium and is generally an optically thin line when observed from solar prominences. There exists strong correlations between the integrated intensities of D3 and the other optically thin, triplet system transition line He I 10830Å (Labrosse & Gouttebroze 2001, 2004). Thus any correlation found between the integrated intensity of D3 and the millimetre-continuum will also exist for He I 10830Å.

In this section I consider again the same set of isothermal-isobaric and multi-thermal prominence models with a PCTR as used in Section 3.3.1.

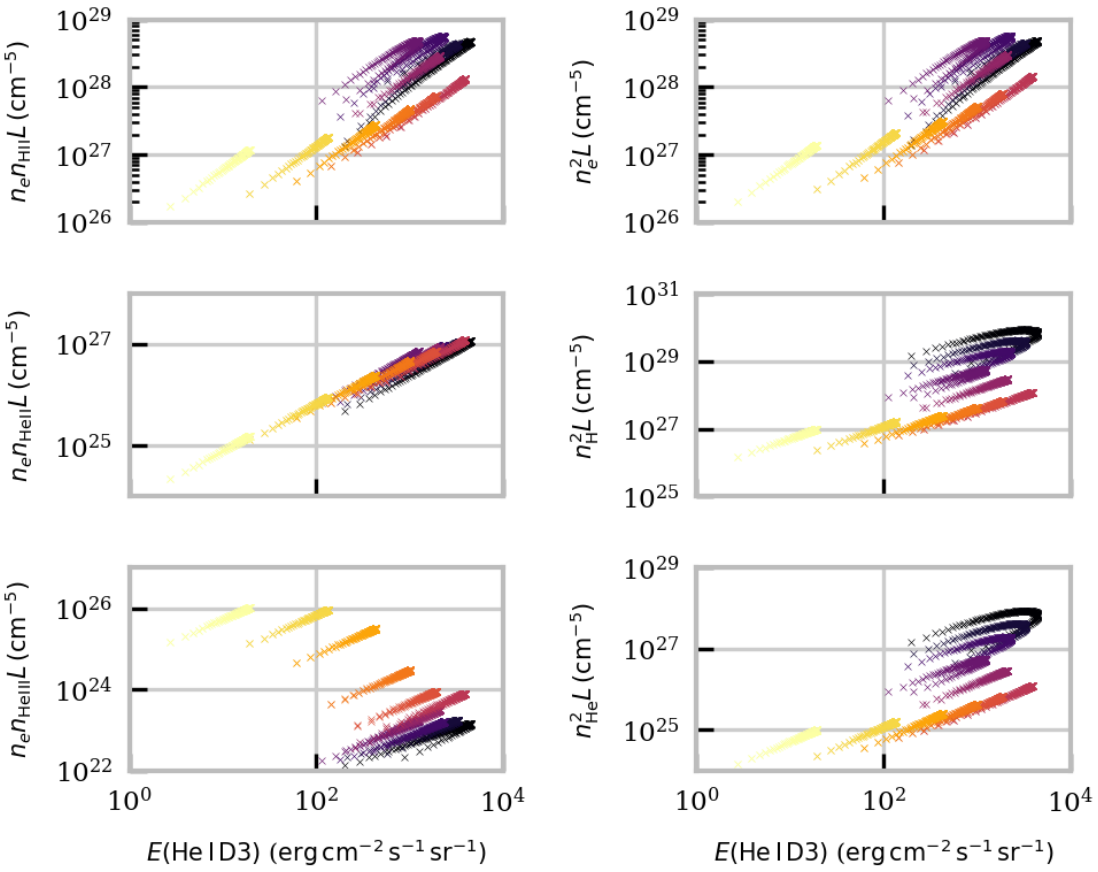

Figure 3.30: Relationships between various forms of the emission measure with the integrated intensity of the He I D3 line produced by isothermal-isobaric models (Table 3.1). Each panel shows a different form for the emission measure as labelled on the y-axis. The colour in the scatter plots represents the constant temperature of each isothermal model from Table 3.1 with temperature values increasing from black to purple to yellow.

3.3.3.1 Results from Isothermal Models

As was done previously for the hydrogen Balmer and Lyman lines, I start by considering the relationship between the integrated intensity emitted by the model prominence with various forms of the emission measure for each LOS. For the isothermal-isobaric models of Table 3.1, these results can be seen in Figure 3.30. The most important form of the emission measure to the formation of millimetre radiation is the electron-proton emission measure (top-left panel). From Figure 3.30 it can be seen that for the He I D3 integrated intensity, although there is a correlation, there is no simple trend as the correlation changes for each

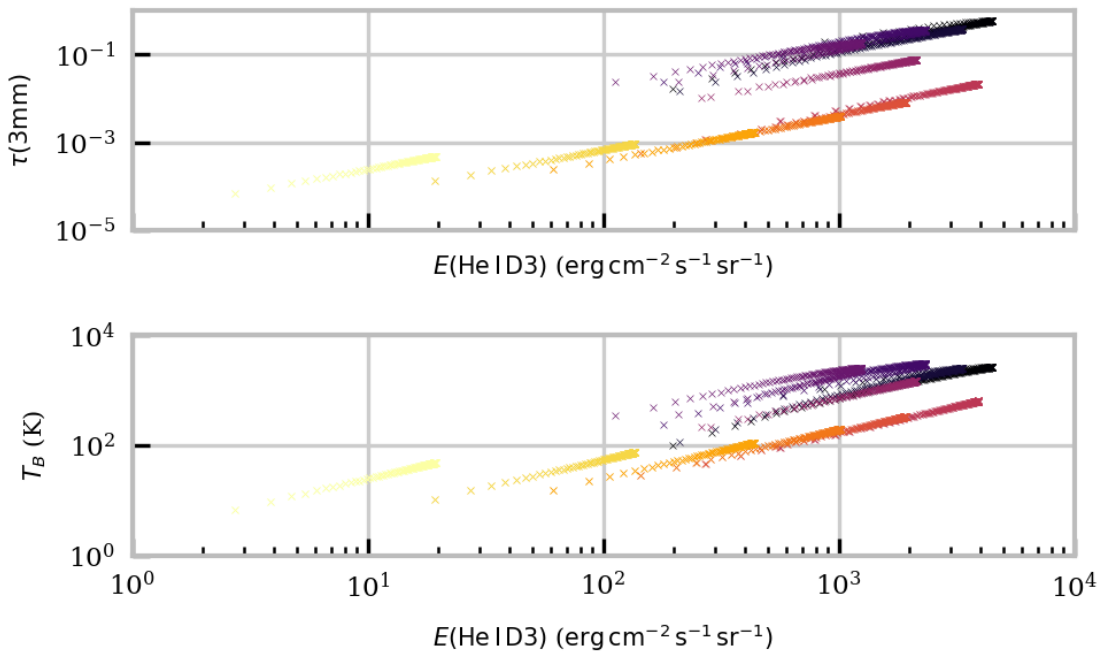

Figure 3.31: Relationships between the optical thickness (top panel) and brightness temperature (bottom panel) of the millimetre-continuum at 3mm with the integrated intensity of the He I D3 line. The colours represent the constant temperature of each isothermal model from Table 3.1, with the temperature increasing from black to purple to yellow.

model temperature, whilst there is also a noticeable effect of the incident radiation on the low temperature models. The electron-electron emission measure is very closely linked to the electron-proton form due to hydrogen making up the majority of the plasma ($A_{\mathrm{He}} = 0.1$). The total hydrogen squared, total helium squared and electron-twice ionized helium forms for the emission measure exhibit a similar result to the top panels where there are clear model dependent correlations, but no overarching trend in the relationship with the integrated intensity of He I D3. There is, however, a very clear power law trend across all models for the electron-singly ionized helium emission measure. This is not surprising: as the prominence plasma is generally optically thin for He I D3, there should exist a relationship similar to the relationship between the integrated intensity of Hα and the electron-proton emission measure through Equation 3.11. With this relationship, a measurement of the integrated intensity of the He I D3 line could be used to estimate the electron-singly ionized helium emission measure. With a separate diagnostic for the electron density/LOS length, this could be used to give an estimate of the density of singly ionized helium in the LOS.

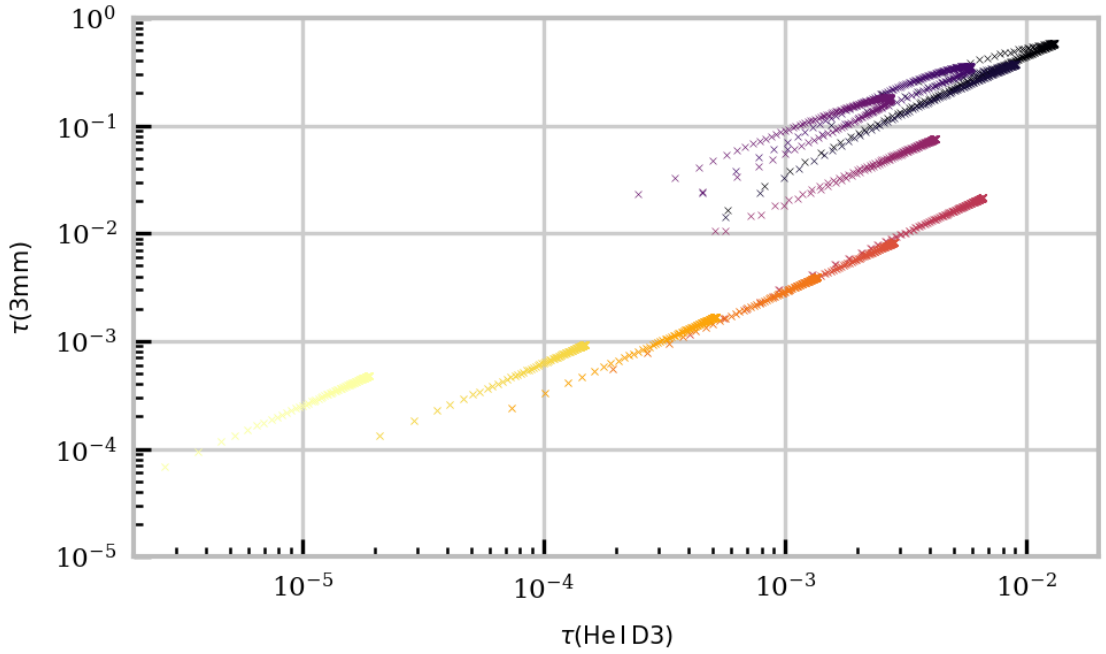

Figure 3.32: Relationship between the optical thicknesses of the line centre of the He I D3 line and the millimetre-continuum at 3mm for the set of isothermal models from Table 3.1. The colours on the graph represent the temperature of each model with the values increasing from black to purple to yellow.

For the same set of isothermal-isobaric models, the relationship between the integrated intensity of He I D3 with the optical thickness of the millimetre-continuum and brightness temperature of the millimetre-continuum at 3mm is shown in Figure 3.31. The relationship between the optical thickness at 3mm and the integrated intensity of He I D3 is fairly similar to that seen for the electron-electron and electron-proton emission measures in Figure 3.30. There are clear model-dependent correlations, but no unique trend across the range of temperatures of the isothermal models. As these models are all optically thin for millimetre wavelength emission, the distribution with brightness temperature is very similar in shape to that of the optical thickness with only a small amount of flattening observed in the coldest, highest optical thickness models.

The relationship between the optical thickness of the He I D3 line and that of the millimetre-continuum at 3mm is given in Figure 3.32. This distribution is very similar to that seen in the top panel of Figure 3.31 for the integrated intensity of He I D3 suggesting that there is a linear relationship between the optical thickness at line centre for He I D3 and

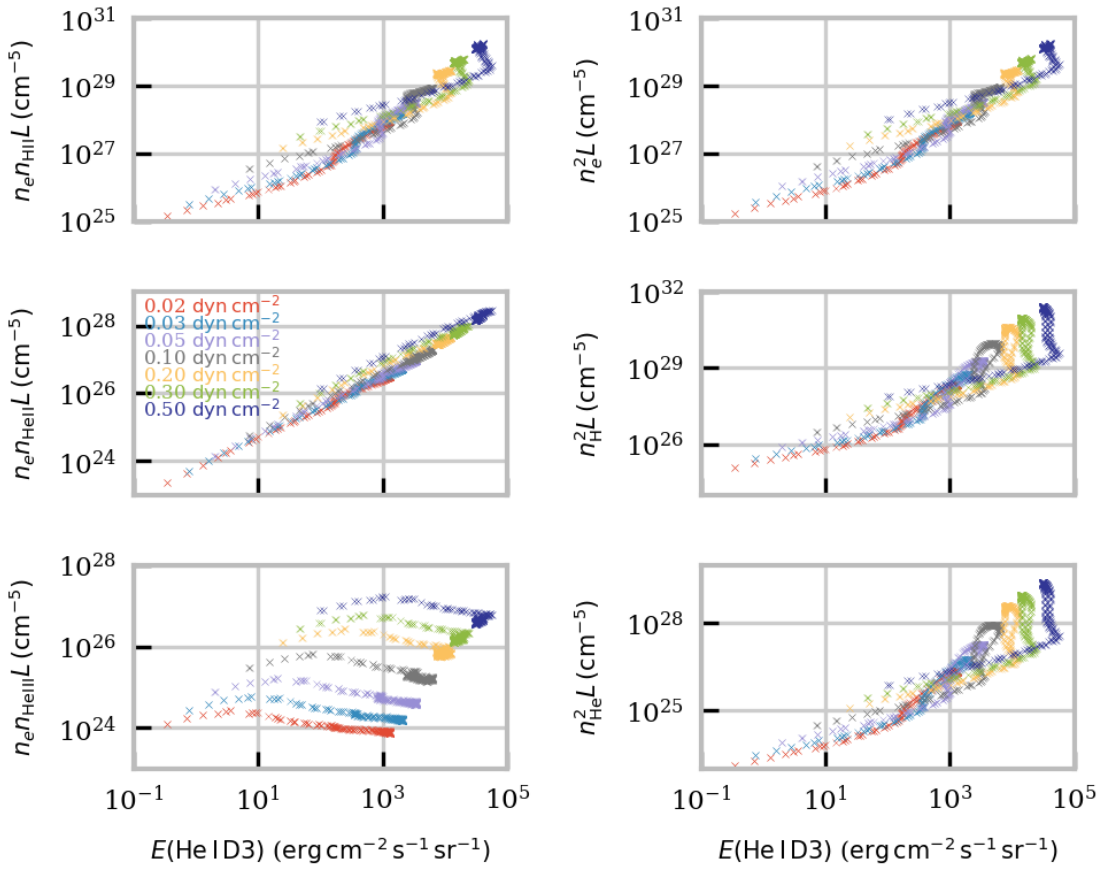

Figure 3.33: Relationships between various forms of the emission measure with the integrated intensity of the neutral helium D3 line produced by multi-thermal prominence models (Table 2.2). Each panel shows a different form for the emission measure as labelled on the y-axis. The colours of the scatter plots represent the pressure of each multi-thermal model from Table 2.2 as given on the middle-left panel.

its integrated intensity, at least for optically thin emission.

3.3.3.2 Results from Multi-thermal Models

Figure 3.33 shows the relationship between the same various forms of the emission measure as used in the previous section with the integrated intensity of the He I D3 line produced by the multi-thermal models of Table 2.2. The electron-electron and electron-proton emission measures show model-dependent correlations across large parts of the distribution. There is little to no correlation found, however, for the electron-twice ionized helium emission

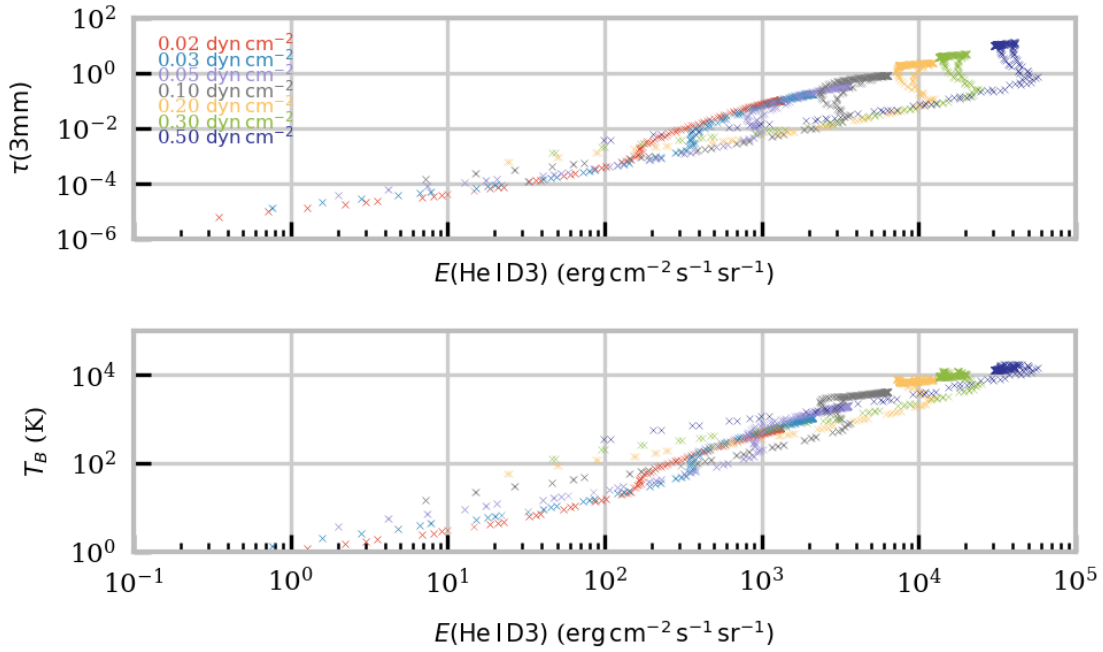

Figure 3.34: Relationships between the optical thickness (top panel) and brightness temperature (bottom panel) of the millimetre-continuum at 3mm with the integrated intensity of the He D3 line. The colours represent the pressure of each multi-thermal model from Table 2.2 as given on the plot. The LOSs through the prominence are represented as the areas where the points are densely located. The very sparsely packed points represent the edges of the cylinder FOV.

measure in the bottom left hand panel. The distributions found for the total hydrogen/helium emission measures show model-dependent correlation at the edges of the FOV (mostly PCTR material), however, the correlation is lost in the core region. Similarly to the isothermal models there is a clear trend across all models found for the relationship between the integrated intensity of the He I D3 line and the electron-singly ionized helium emission measure.

The relationships between the He I D3 integrated intensity with the optical thickness and brightness temperature of the millimetre-continuum at 3mm is shown in Figure 3.34. There appears to be two distinct power law trends found in the relationship between the He I D3 integrated intensity and the millimetre-continuum optical thickness: one for the emission from close to the edge of the prominence FOV, and one from the denser core region. The lower optical thickness branch corresponds to the regions where the LOS is closest to replicating

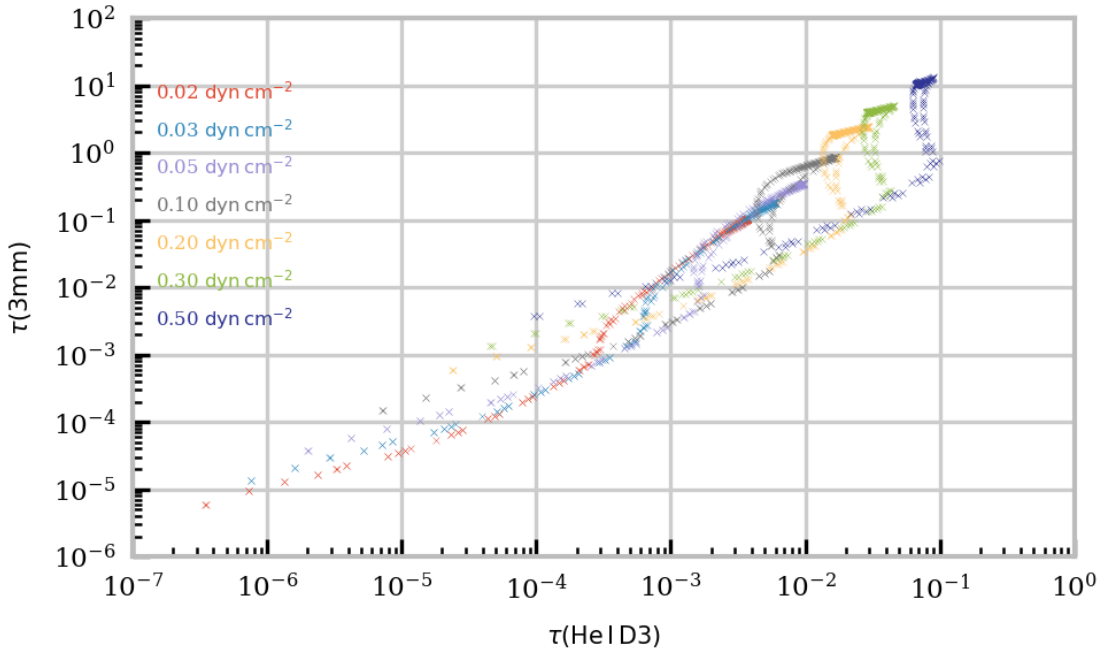

Figure 3.35: Relationship between the optical thicknesses of the line centre of the He D3 line and the millimetre-continuum at 3mm for the set of multi-thermal models from Table 2.2. The colours on the graph represent the pressure of each model as given on the plot.

the isothermal condition when it crosses PCTR material only, at the edge of the cylinder. The brightness temperature distribution shows a similar result, however, with distinct flattening due to the high pressure models becoming optically thick at 3mm, and thus producing a brightness temperature representative of the millimetre-continuum formation layer in the prominence plasma.

The optical thickness of He I D3 at line centre is compared to that of the millimetre-continuum at 3mm in Figure 3.35. As before, the optical thickness distribution found in Figure 3.35 is very similar to the distribution found for the integrated intensity of He D3 in Figure 3.34, suggesting again that the integrated intensity of He I D3 is closely linked to the optical thickness at line centre, at least for optically thin emission.

The formation region of He I D3 is compared to that of the millimetre-continuum at 3mm in Figure 3.36. At the lowest pressure (left hand panel), both types of emission are optically thin with contribution occurring from across the whole cylinder cross-section. By the middle panel, however, the plasma is beginning to become optically thick at 3mm

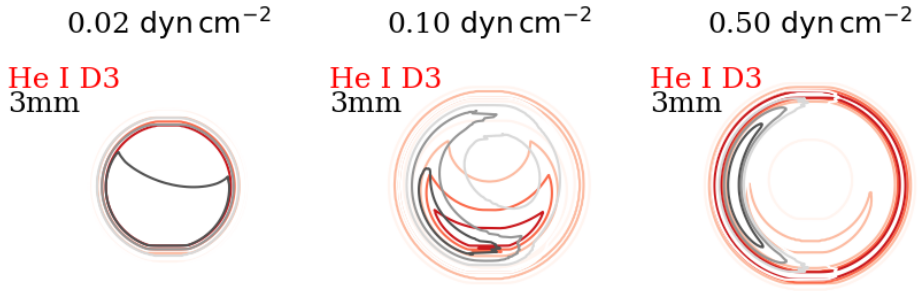

Figure 3.36: Contour maps for the He I D3 line, compared to the continuum at 3 mm, for three multi-thermal prominence models, each with different constant pressure. The LOS is directed such that the "observer" is to the left of each cylinder. The red contours show the He I D3 line, whilst the black contours describe the millimetre-continuum. The contour levels correspond to {20, 40, 60, 80, 100}% the maximum of the contribution function in the model prominence.

resulting in a contribution skewed towards the observer, whilst the He I D3 contribution function distribution remains symmetrical across the vertical axis, although showing a significant increase at the bottom side of the prominence due to the incident radiation. At the highest pressure model (right panel), the plasma is optically thick for 3mm emission, leading to the crescent shaped distribution as seen in previous sections. The He I D3 distribution is still symmetrical here due to it emerging from an optically thin plasma. There is, however, a strong ring structure to this contribution plot, suggesting that, despite being optically thin, much of the He I D3 emission is formed from a specific region in the PCTR here.

3.3.4 Summary and Discussion of Future Work

In this section I have presented relationships between some of the major lines and continua of neutral hydrogen and helium with the optical thickness and brightness temperature of the millimetre-continuum. To do this I have used the millimetre-continuum model discussed in Chapter 2. It has previously been shown that the most important factor in determining the optical thickness of the millimetre-continuum is the charge squared weighted electron-ion emission measure, which because hydrogen is the majority species means that the electron-proton emission measure will have the greatest contribution.

It was found that the integrated intensity of the Balmer lines, Hα and Hβ, displayed a power-law relationship with the optical thickness of the millimetre-continuum for isothermal models, although the isothermal models in question were optically thin. It is expected, however, that this relationship would breakdown once the LOS becomes optically thick. The inclusion of helium in the plasma was found to cause a small, yet noticeable variation from the expected, analytical expression. This was then confirmed for multi-thermal models as, whilst optically thin, it was found that both Balmer lines displayed clear correlations with the millimetre-continuum optical thickness, but no clear correlation once the line centre became optically thick. The correlations for multi-thermal models are more complicated than that of the isothermal models, with two separate power-law relations found for different sections of the FOV. The extremal parts of the PCTR followed most closely the analytical expression using the temperature of the corona, whilst the core region was closest to the analytical expression using the electron density weighted mean temperature.

The integrated intensities of the first three lines from the Lyman series: Lyα, Lyβ and Lyγ, were also compared to various forms of the emission measure, as well as the optical thickness and brightness temperature of the millimetre-continuum. The vast majority of the LOSs displayed optically thick emission from all three Lyman lines considered, which resulted in no correlation between the integrated intensity and the emission measure or the optical thickness of the millimetre-continuum. In the few LOSs where the emission was optically thin, a clear power-law relationship between the integrated intensity of the lines and the optical thickness of the millimetre-continuum is found.

I also investigated the relationship between the temperature diagnostics using the Lyman continuum and the brightness temperature of the millimetre-continuum. It was found that the colour temperature of the Lyman continuum, defined by a polynomial fit to the continuum spectrum, provided a fairly good representation of the electron density weighted mean temperature of the optically thick core region of the multi-thermal prominence models, irrespective of the pressure of the isobaric models. Whilst in the optically thin PCTR, the color temperature underestimated the mean value while still roughly following the temperature structure. As was shown previously the brightness temperature of the millimetre-continuum is representative of the electron temperature of a given formation within the LOS, when the plasma is optically thick. Through comparing the contribution function distributions of both continua it was found that the models where the brightness temperature of the millimetre-continuum most closely matched with the colour temperature of the Lyman continuum were

when the two forming regions most closely overlapped. The optical thickness of the Lyman continuum was found to be higher than that of the millimetre-continuum, however, for the highest pressure model considered the formation region of the millimetre-continuum was found to be further from the cylinder axis than that of the Lyman continuum.

A power-law trend was found between the integrated intensity of the optically thin neutral helium line He I 5876Å , or D3, line with the electron–singly ionized helium emission measure ($n_e n_{\mathrm{He\,II}} L$). This parameter, however, only contributes a small factor to the total charge squared weighted electron-ion emission measure, due to the large abundance of hydrogen. This results in an unclear relationship between the helium lines intensity and the millimetre-continuum emission. Although, if the electron density were to be measured through a separate mechanism, this relationship could be used to estimate the number density of the singly ionized state of helium within the prominence plasma. It is likely that this kind of relationship exits for other optically thin emission lines; such that if a given line's intensity were found to have usable correlations with a respective form of the emission measure it could be used with coordinated millimetre-continuum observations to:

a) Estimate the optical thickness of the millimetre continuum, or

b) If the electron density can be inferred independently, be used to estimate the densities of the particular atomic species or ionization state in question.

Of course hydrogen and helium lines are not the only frequently observed spectral lines from solar prominences. For instance, the Ca II resonance lines are easily observable from prominences using ground based observatories and from space using the SOT (Tsuneta et al. 2008). Gouttebroze et al. (1997) modelled the emission produced by Ca II ions from 1D solar prominence models. Gouttebroze & Heinzel (2002) built on this work whilst using a larger set of models. In Gouttebroze & Heinzel (2002) a fairly clear correlation was found between the intensity from the infra-red Ca II 8542Å line and that of the Balmer Hβ line, when considering only models of temperature less than 10000K. It could then be assumed from the results of this study that, due to the correlation between Hβ emission and the electron-proton emission measure and thus the optical thickness of the millimetre-continuum, there should be a correlation between said parameters at low temperatures and the integrated intensity of the Ca II 8542Å line.

Other minority species which have been of particular interest to solar prominence observations lately are those which are observable using the *Interface Region Imaging Spectrograph*

(IRIS) (De Pontieu et al. 2014) due to the instrument's high spatial resolution and particularly high spectral resolution. Nominally IRIS's spatial resolution is 0.167″ per pixel, however, the actual observable resolution is closer to ≈ 0.4″, whilst the spectral resolution is 0.05Å. IRIS observes in both the Far Ultraviolet (FUV 1332–1348 and 1390–1406Å) and Near Ultraviolet (NUV 2783–2834Å) ranges. This includes interesting spectral lines from Mg II, C II and Si IV. Many of the studies conducted so far have focussed on the results from the Mg II h and k lines due to the strength in intensity of the lines and due to an approximately linear response between k/h line ratio and the temperature of the plasma for low temperatures. The formation of the Mg II h and k lines from solar prominences has been considered for 1D slab models by Heinzel et al. (2014), Vial et al. (2019) and Levens & Labrosse (2019). Vial et al. (2019) derived a unique correlation between the integrated intensities of the Mg II h and k lines with the electron–electron as well as the total hydrogen density squared emission measures for isothermal–isobaric 1D slab models. These models were also used to diagnose the plasma electron density, hydrogen density and temperature of an eruptive prominence in Zhang et al. (2019). Levens & Labrosse (2019) confirmed that there is an approximate linear correlation between the k/h ratio and the temperature for both isothermal-isobaric and PCTR models up to ≈ 25000K, where the ratio saturates at between 2 and 2.4. The authors also found in their Figure 13 a fairly clear correlation between the integrated intensity of the Mg II k line with the electron-electron emission measure, for low mean temperature plasmas. The C2D2E code, used in this study, is currently unable to account for atomic species other than hydrogen or helium, therefore, for further study to be conducted into whether the intensity from minority species such as Ca II or Mg II correlate with aspects of the millimetre continuum in 2D, appropriate expansions will need to be made to the existing code in a future work.

Chapter 4

Millimetre Continuum Spectral Diagnostics

The purpose of this chapter is to present and discuss techniques for the inference of plasma properties from multiple observations of the millimetre-continuum brightness temperature. The techniques discussed in this chapter focus on estimating the optical thickness of the plasma at millimetre wavelengths, however, through the estimated optical thickness further estimations into properties such as the electron temperature, emission measure and electron density are made. The chapter begins by discussing how the ratio of two brightness temperatures from an isothermal plasma may be used to estimate the optical thickness, and thus the emission measure for a given LOS in Section 4.1. The emission measure in this chapter refers to the charge squared weighted ion-electron emission measure. Section 4.2 expands on this through the derivation of an expression relating the spectral gradient of the millimetre-continuum to the LOS optical thickness, for both logarithmic-, and linear-scale spectra. The section then continues by showing tests of the applications of this expression using non-LTE prominence modelling. Finally Section 4.3 presents a case study where the spectral gradient of a brightness temperature enhancement during a solar eruptive event observed with ALMA is used to estimate the optical thickness of the enhancing plasma, and subsequently other important plasma properties. Sections 4.1, 4.2 and 4.3 present work and adaptations of work previously published in Rodger & Labrosse (2017), Rodger & Labrosse (2018) and Rodger et al. (2019), respectively. In each of these publications I contributed through the production of all numerical modelling and data analysis codes. This included the production of the figures, except where it is explicitly stated otherwise. The analyses

were reached through the discussions between myself and my co-authors. Because of this, much of each of this chapter directly follows from the material previously published in the publications stated above. The findings of this chapter are summarised in Section 4.4.

4.1 Millimetre-Brightness Temperature Ratio as a Plasma Diagnostic

In this section I discuss the use of a ratio of two brightness temperatures, observed in the millimetre-continuum, as a diagnostic for the optical thickness, and subsequently the emission measure of the emitting plasma, provided an isothermal assumption is valid. The work presented in this section has been published previously in Rodger & Labrosse (2017); it has been adapted for this chapter using a slightly different set of models using the calculated values of the Gaunt factor of van Hoof et al. (2014), as discussed previously in Section 3.1. The approach for using a brightness temperature ratio used in this section is similar to that presented in Bastian et al. (1993). In Gunár et al. (2018), the authors present a method for deriving the kinetic temperature of the plasma from two different millimetre wavelength observations, provided one is reliably optically thick, and the other optically thin. Since ALMA began accepting proposals for solar observations (cycle 4) the only two wavelength bands available to solar physicists has been Band 6 (1.3 mm) and Band 3 (3.0 mm), with Band 7 (0.9mm) becoming available in the current cycle 7. For the purposes of this investigation an observation where a solar prominence is observed in both bands 3 and 6 is considered. The ratio of the brightness temperatures between these two observing bands, R, is thus defined as:

$$R = \frac{T_{\mathrm{B},1.3}}{T_{\mathrm{B},3.0}}, \tag{4.1}$$

where T_{B} is the brightness temperature and the subscripts 1.3 and 3.0 denote the wavelengths at 1.3 mm and 3.0 mm, respectively. For ease these subscripts are used throughout the rest of this section.

If a constant temperature can be assumed across the LOS through the prominence, Equation 4.1 can be expanded to include terms solely dependent on the optical thicknesses of the two observed wavelength bands:

$$R \approx \frac{T(1-\mathrm{e}^{-\tau_{1.3}})}{T(1-\mathrm{e}^{-\tau_{3.0}})} = \frac{1-\mathrm{e}^{-\tau_{1.3}}}{1-\mathrm{e}^{-\tau_{3.0}}}. \tag{4.2}$$

The optical thickness, at a given wavelength i, can then be approximated as:

$$\tau_i \approx \langle \kappa_i \rangle L, \tag{4.3}$$

where κ_i is the absorption coefficient and L is the length of the LOS. This approximation assumes that a mean value for κ_i can represent the LOS. Following on from this, the optical thicknesses of the plasma at the two observable wavelengths are related to each other as follows:

$$\tau_{1.3} \approx \frac{\langle \kappa_{1.3} \rangle}{\langle \kappa_{3.0} \rangle} \tau_{3.0} = K \tau_{3.0}, \tag{4.4}$$

where K has been defined here as the dimensionless opacity ratio.

As discussed earlier in Section 2.3.2, the dominant mechanism for photon absorption within the millimetre-continuum is inverse thermal bremsstrahlung (Equation 3.5, or Equation 2.2 when considering the classical assumption). Due to this dominance, it is therefore a reasonable assumption within this wavelength range, for most electron temperatures, to calculate the opacity ratio while considering contribution from inverse thermal bremsstrahlung solely. Using this assumption, and Equation 3.5, K is defined as:

$$K = \frac{\nu_{3.0}^2 g_{\mathrm{ff}}(\nu_{1.3}, T)}{\nu_{1.3}^2 g_{\mathrm{ff}}(\nu_{3.0}, T)} \tag{4.5}$$

In this case the opacity ratio is therefore only dependent on the known observational frequencies, and the Gaunt factor which depends on a constant temperature for the LOS. In Rodger & Labrosse (2017) we used the classical assumption for the thermally-averaged Gaunt factor, however, here the interpolated value from the table of calculated values of van Hoof et al. (2014) is used instead, as discussed in Section 3.1.

A representation for how the opacity ratio, K, will vary with temperature in a prominence plasma is shown in Figure 4.1. This figure was calculated according to Equation 4.5 and the two observing wavelengths: 1.3 mm, and 3.0 mm, at a range of temperatures simulating low core temperatures of around 5000 K to extreme PCTR temperatures of 10^5 K. From Figure 4.1, it is clear that the variation in the size of K is only small across this temperature range. If the electron temperature of the prominence is known, or can be suitably assumed, a bound on the magnitude of the opacity ratio can be set.

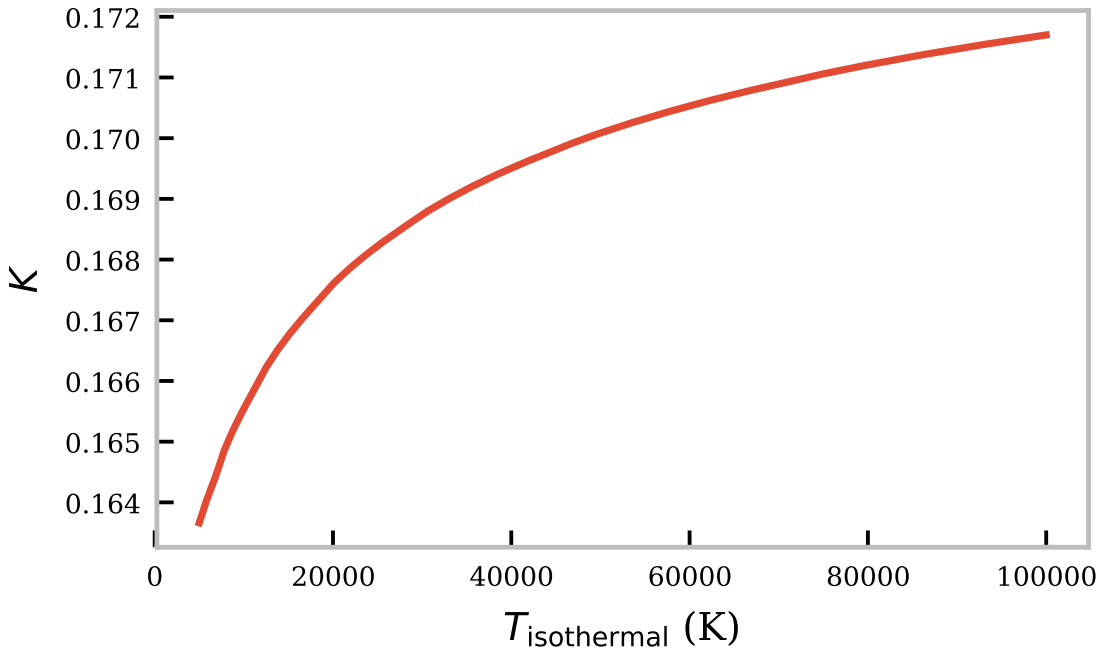

Figure 4.1: Variation of opacity ratio for ALMA wavelengths $\lambda_1 = 1.3$ mm and $\lambda_2 = 3.0$ mm with temperature (Equation 4.5). This figure is a replication of a figure in Rodger & Labrosse (2017), with the difference that this figure was produced without the use of the classical assumption for the calculation of the thermal Gaunt factor.

4.1.1 Estimating the Optical Thickness – Isothermal Models

If a value for the opacity ratio is known, the optical thickness of the plasma at either wavelength can be estimated by substituting Equation 4.4 into Equation 4.2, which yields:

$$R \approx \frac{1 - e^{-K\tau_{3.0}}}{1 - e^{-\tau_{3.0}}}. \tag{4.6}$$

An analytical solution to this equation exists through the expansion of the exponential terms to the 2nd order only. This leads to:

$$\tau_{3.0} = \frac{2(K - R)}{K^2 - R}. \tag{4.7}$$

Whilst this solution is satisfactory for high temperatures and low optical thicknesses, it was found to underestimate the optical thickness as the latter increased. In an attempt to improve the estimation of higher optical thicknesses a numerical method for the solution of Equation 4.2 was used. This involved finding the roots of the function:

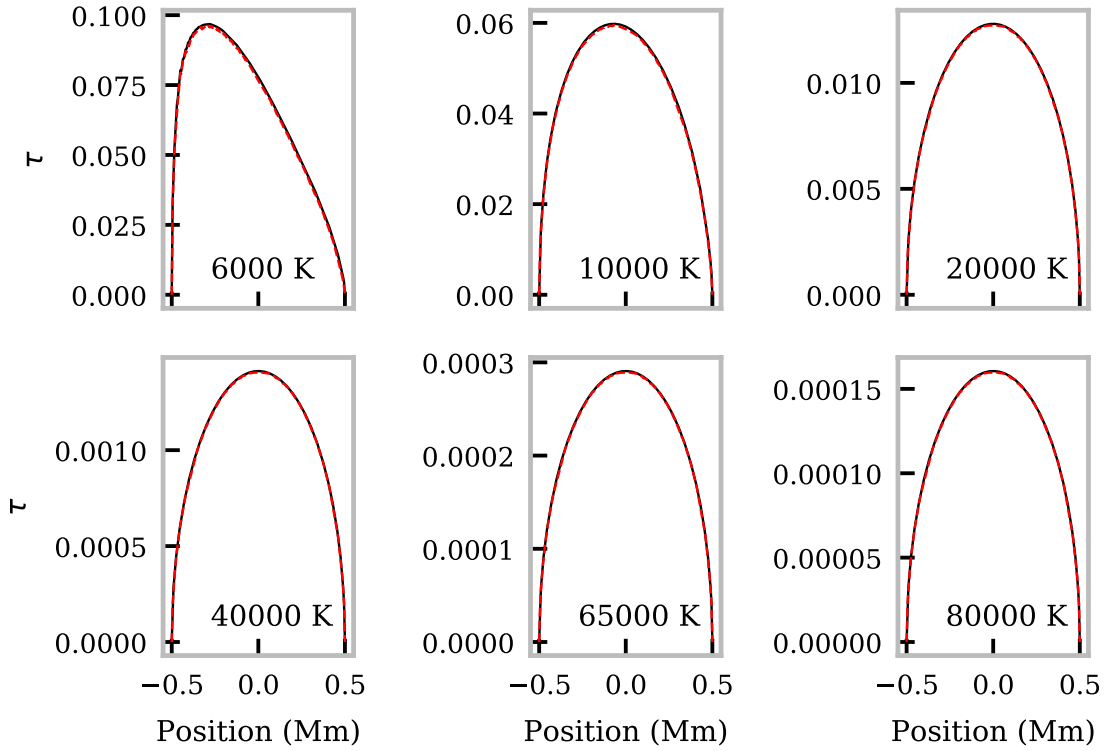

Figure 4.2: Variation of estimated (*solid black line*) and "true" (*dot-dashed red line*) optical thickness with the FOV, for six isothermal prominence models at $\lambda = 1.3$ mm. The FOV is orientated vertically in the solar atmosphere with the positive x-axis directed radially away from the Sun. Adaptation of a figure previously published in Rodger & Labrosse (2017) but using the interpolated value of the Gaunt factor as discussed in Section 3.1.

$$f(\tau_{3.0}) = \sum_{n=1}^{N} \frac{(-1)^n (K^n - R)}{n!} \tau_{3.0}^{n-1}, \tag{4.8}$$

using the Newton-Raphson method. N is the order to which the exponential terms are expanded. For the purpose of these estimations N was set to 20 throughout.

This method was tested using the set of isothermal-isobaric models outlined in Chapter 3 in Table 3.1. They are equivalent to the size of a prominence core (radius of 0.5 Mm), without a PCTR. The orientation used describes an off-limb prominence orientated horizontally in the solar atmosphere as described in Section 2.3.3. Brightness temperatures were obtained at both 1.3 mm and 3.0 mm and were subsequently used to calculate the ratio R for all points in the FOV.

Figure 4.2 presents the variation of both the estimated LOS optical thicknesses at 1.3 mm and the "true" optical thickness outputted by the simulation. This is given for a sub-set of different temperatures in the set of isothermal-isobaric models (Table 3.1). The opacity ratio, K, used in the production of these estimations, was calculated using Equation 4.5, and the known constant temperature for each model. It is clear from the figure that the optical thickness estimation matches well the "true" values across a large range of isothermal temperatures. Using the opacity ratio again, the estimation is as accurate for $\lambda = 3.0$ mm.

It is important to note that these computed brightness temperatures are idealised and noiseless, and that an attempt to use this method with real brightness temperature measurements would have an associated uncertainty. This uncertainty would likely have a significant effect if both observation wavelengths are emitted from highly optically thin plasma, *i.e.* $\tau \ll 1$. Both brightness temperatures will be low, and will hence present a small SNR. In the regime where $\tau \ll 1$ is true, Equation 4.2 can be simplified to $R \approx K(T)$. In the highly optically thick regime an increasingly high accuracy in the brightness temperature ratio will also be necessary. This will be caused by the brightness temperatures asymptotically tending toward the electron temperature of the plasma, which in the case of the estimations in Figure 4.2 is constant for each model. If both wavelengths are emitted from a sufficiently optically thick plasma ($\tau > 4$–5, see Figure 2.9), R will tend towards 1, and this method will no longer be able to discern between the differing optical thicknesses (Equation 4.2).

In Figure 4.3 the relative difference between the brightness temperature ratio estimated and "true" optical thickness for every LOS in the set of isothermal models in Table 3.1 is shown for different levels of noise in the data. This figure was produced by adding a uniformly distributed random noise to each of the output brightness temperatures. The width of the uniform distributions were set from $-\sigma$ to $+\sigma$, where noise levels of 25, 50 and 100 K have been considered. For the highest noise level it can be seen that the method is approximately correct within 10% of the true value when the optical thickness is greater than 2×10^{-2}, yet still optically thin.

4.1.2 Estimating the Emission Measure from the Optical Thickness

With an estimation of the plasma's optical thickness at a given wavelength it becomes possible to estimate the emission measure of the particular LOS. Continuing the assumption that within the quiet solar atmosphere the millimetre-continuum opacity is greatly dominated by free-free inverse thermal bremsstrahlung, and substituting Equation 2.2 into the approxi-

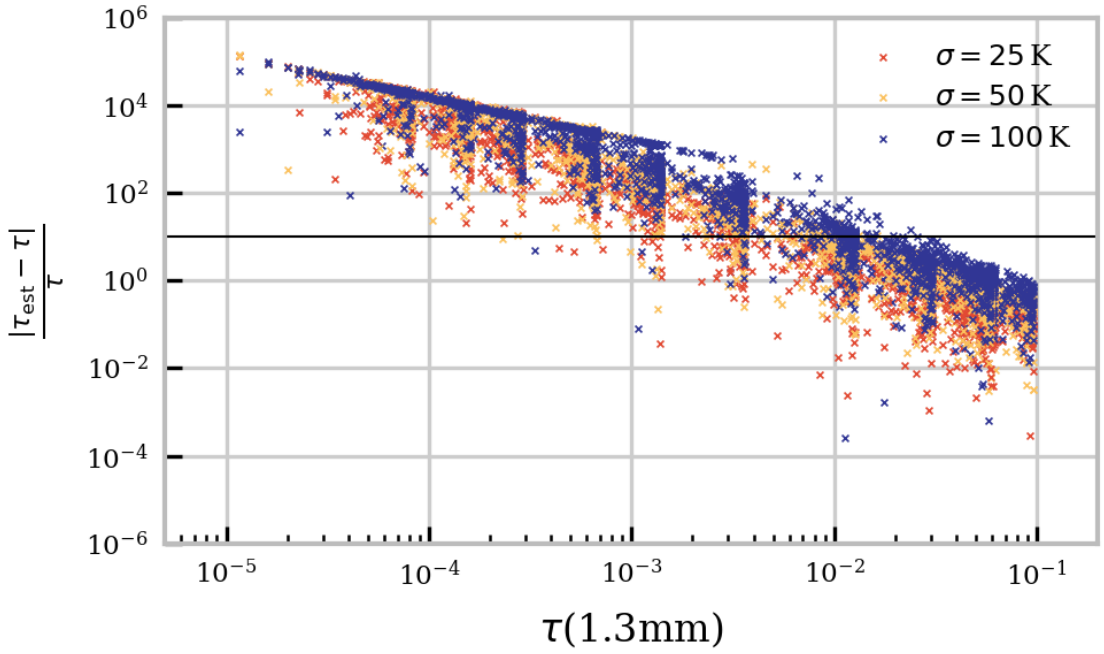

Figure 4.3: Relative difference between the brightness temperature ratio estimated and "true" optical thickness at 1.3 mm for the full set of isothermal models in Table 3.1. The output brightness temperature for each LOS in each model has had a random noise added to it from a uniform distribution of width = 2σ around zero as given by the colour in the plot's legend. The solid black line displays where the estimated optical thickness has a 10% difference from the "true" value.

mation of the optical thickness of a homogeneous LOS (Equation 4.3), the mean emission measure can be written as:

$$\langle \mathrm{EM} \rangle = \frac{\tau_\nu \nu^2 T^{3/2}}{1.77 \times 10^{-2} g_{\mathrm{ff}}(\nu, T)} \tag{4.9}$$

where EM in this chapter is the charge squared weighted ion-electron emission measure, defined as:

$$\mathrm{EM} = n_\mathrm{e} \sum_j Z_j^2 n_j L. \tag{4.10}$$

In this equation n_e is the electron density, whilst Z_j and n_j are the charge and density of ion species j, respectively. The value for the mean emission measure was calculated using the integrated mean over the LOS using Equation 3.14.

The optical thicknesses estimated in Section 4.1.1 have been used to estimate the mean

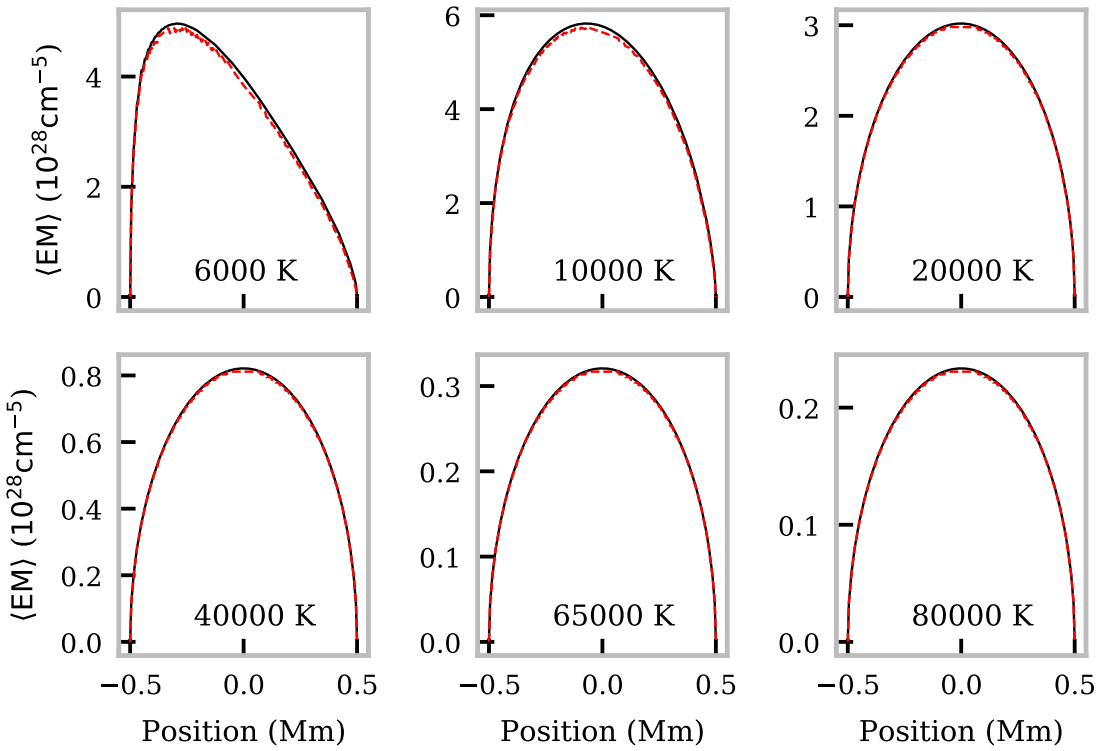

Figure 4.4: Variation of estimated (*solid black line*) and "true" (*dot-dashed red line*) mean emission measure across the FOV, for six isothermal prominence models. The FOV is orientated vertically in the solar atmosphere with the positive x-axis directed radially away from the Sun. Adaptation of a figure previously published in Rodger & Labrosse (2017).

emission measure, as seen in Figure 4.4. Once again, the estimated value is very close to the value calculated straight from the simulation, with only a very small underestimation noticeable in the low temperature models. This small underestimation may be due to the presence of neutral hydrogen absorption, in the models with cooler, denser plasma. Since the same value for K was used, both 1.3 mm and 3.0 mm produced the same estimates for $\langle \mathrm{EM} \rangle$. As these estimates of $\langle \mathrm{EM} \rangle$ rely on the optical thickness estimates of Section 4.1.1, the same requirements on the uncertainty of the brightness temperature ratio are necessary.

So far in this section it has been shown that the optical thickness, and the emission measure, can be well estimated for isothermal prominence models with known temperatures, and assuming a sufficiently low uncertainty on the brightness temperature ratio. However, it is expected in general that prominences will display a significantly more complex temperature

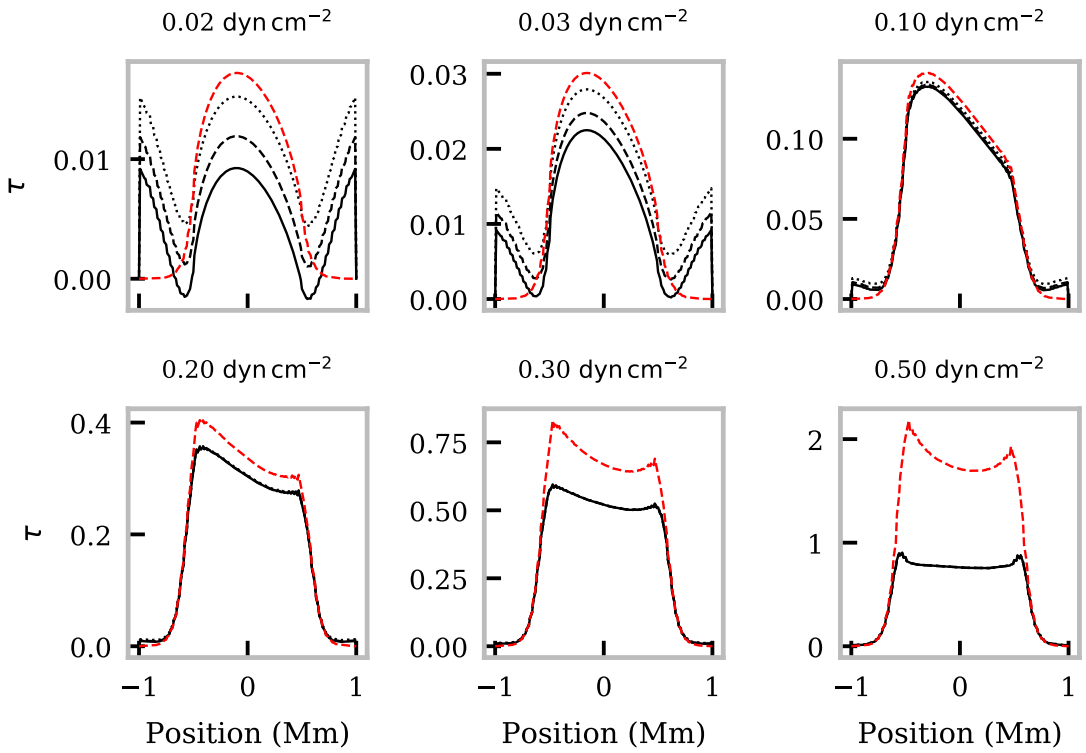

Figure 4.5: Variation of the estimated (*black lines*) and "true" (*dashed red line*) optical thickness across the FOV, for six multi-thermal prominence models each including a PCTR. The FOV is orientated vertically in the solar atmosphere with the positive x-axis directed radially away from the Sun. The different black lines correspond to the estimation using different representative temperature estimations for the prominence, including; the mean temperature (*solid*), the electron density weighted mean temperature (*dashed*), and the electron density squared weighted mean temperature(*dotted*). This figure is an adaptation of figure previously published in Rodger & Labrosse (2017).

distribution. The next step in this investigation was thus to test the method using a set of multi-thermal prominences with radially increasing temperature distribution representing a PCTR.

4.1.3 Estimating the Optical Thickness – Multi-thermal Models

The optical thickness and emission measure were estimated for the plasma in each LOS of the set of prominence models with a radially increasing temperature from an isothermal core (see

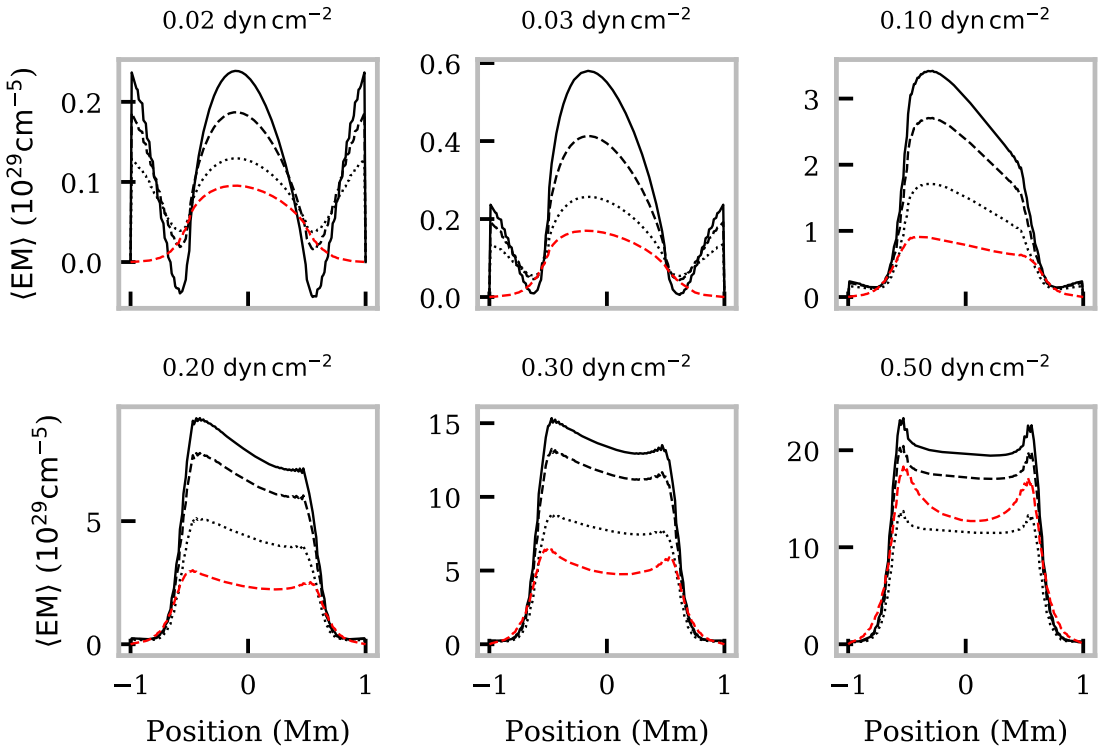

Figure 4.6: Variation of estimated (*black lines*) and "true" (*dashed red line*) mean emission measure across the FOV, for six multi-thermal prominence models each including a PCTR. The FOV is orientated vertically in the solar atmosphere with the positive x-axis directed radially away from the Sun. The different black lines correspond to the estimation using different representative temperature estimations for the prominence, including; the mean temperature (*solid*), the electron density weighted mean temperature (*dashed*), and the electron density squared weighted mean temperature (*dotted*). This figure is an adaptation of figure previously published in Rodger & Labrosse (2017).

Table 2.2 in Chapter 2). The brightness temperature measurements at 1.3 mm and 3.0 mm from each model were used to estimate the respective optical thicknesses and the mean emission measure using the brightness temperature ratio method described in Section 4.1.1. As an attempt to consider a representative temperature for the model, three different values were used; the mean temperature, the electron density weighted mean temperature, and the electron density squared mean temperature. The results for the estimation of the optical thickness at 1.3 mm is shown in Figure 4.5. From this figure it is clear that the similarity

between the estimated and "true" optical thickness changes given the model pressure, and thus density/optical thickness. In the low pressure/density models, the prominence is optically thin, such that the variation between the estimated and "true" values will be caused by an insufficiently representative temperature for the LOS. In each case the electron density squared mean temperature provides the best estimation of the optical thickness in the centre of the FOV, whilst optical thickness at the edges of the FOV are overestimated as the different mean temperatures are all too low. In the highest pressure/density model, the prominence has become optically thick in the paths which cross the central region of the FOV. Here the brightness temperature ratio will be increasingly defined by the temperature of the different formation layers of the two wavelengths, thus the estimation is poor passed the $\tau = 1$ transition.

The average emission measure calculated using these optical thickness estimations is shown in Figure 4.6. The estimated values of the average emission measure are seen to overestimate the values as calculated from the model densities by up to a factor ≈ 3, particularly in the models with an optically thin plasma (pressures $\geq 0.5\,\mathrm{dyn\,cm^{-2}}$ in Figure 4.6). Once again the electron density squared weighted mean temperature proves to provide the best estimation compared to the "true" values as calculated from the simulated output. In optically thin cases the resultant brightness temperature is produced from an integration of the contribution function across the whole LOS. Since each LOS has a multi-thermal temperature distribution, the temperature dependence of the millimetre-continuum contribution function will cause different layers to present different contributions to the emitted brightness temperature. It is possible, when using unrepresentative temperatures in the calculation of the opacity ratio to estimate negative optical thicknesses, this is obviously unphysical and is caused by the brightness temperature ratio exceeding the opacity ratio (Equation 4.7), see the solid black line for estimations using simple mean temperature during calculation in top left panel of Figure 4.5. The emission measure estimate in the bottom right panel, where the plasma is known to be optically thick from Figure 4.5, shows a better similarity to the "true" value than the optically thin cases, however, this is likely caused by the relative underestimation of the optical thickness, rather than being an improvement to the diagnostic.

4.2 The Millimetre-Continuum Spectral Gradient as a Diagnostic of Optical Thickness

In this section I discuss how the gradient of the quiet Sun logarithmic millimetre-continuum spectrum can be used to estimate the optical thickness of the emitting plasma at the central frequency of the observing band. This work has been published in the letter to the editor (Rodger & Labrosse 2018). For this publication I contributed all numerical modelling and produced each of the figures. The analysis was reached from discussions between myself and my co-author Dr N. Labrosse. Because of this, the figures and analysis presented in this Section are largely replications of that presented in said article. All figures reproduced from this article are explicitly labelled in their captions.

4.2.1 Theory

In the quiet solar atmosphere, emission in the millimetre-continuum is dominated by free-free collisional processes. As stated previously, the dominant emission mechanism amongst these processes across the millimetre regime is thermal bremsstrahlung, thus with regards to deriving the diagnostics studied in this section the emission is assumed to be produced solely from thermal bremsstrahlung. This assumption will, however, become less valid at low temperatures, below 5000 K, and at high densities where neutral hydrogen absorption becomes significant (Rutten 2017). Another assumption which is used throughout this study is that the plasma can be described by typical quiet Sun conditions, where the affect of the magnetic field can be neglected. Net linear polarization is expected to be absent from quiet Sun observations (Shimojo et al. 2017a). In the presence of strong magnetic fields, however, the emission from thermal bremsstrahlung becomes circularly polarized due to the difference in absorption coefficient for the propagating ordinary and extraordinary electromagnetic wave modes. A discussion into how the spectral gradient of the mean of the two orthogonal polarizations of the thermal bremsstrahlung continuum brightness temperature spectrum, and the difference between the left- and right-handed circularly polarized brightness temperatures can be used to estimate the magnetic field strength is given in Bogod & Gelfreikh (1980) and Grebinskij et al. (2000).

The frequency-dependent absorption coefficient, κ_ν, for thermal bremsstrahlung in the absence of a magnetic field, as previously shown in Equation 3.5, is described by (Dulk 1985;

Wedemeyer et al. 2016):

$$\kappa_{\text{ion}}^{\text{ff}} \approx 1.77 \times 10^{-2} \frac{n_e g_{\text{ff}}}{\nu^2 T^{\frac{3}{2}}} \sum_i Z_i^2 n_i,$$

in cgs units, where n_e is the electron density, T is the electron temperature, and g_{ff} is the thermal Gaunt factor. Z_i and n_i are the charge and density for the ion species i. The optical thickness of a homogeneous LOS of length L can be approximated as $\tau_\nu = \kappa_\nu L$ (Equation 4.3), such that the optical thickness, when assuming purely thermal bremsstrahlung absorption, will vary with frequency as $\tau_\nu \propto g_{\text{ff}} \nu^{-2}$, where the Gaunt factor, g_{ff}, varies with frequency and temperature, see Section 3.1.

As discussed in previous chapters, the advantage of observing the solar atmosphere in the millimetre regime is the strong potential for temperature diagnostics arising from the thermally dominated emission mechanism and the Rayleigh-Jeans limit. This results in a brightness temperature spectrum, given previously in Equation 1.17, and restated here, which can be described as:

$$T_{\text{B}}(\nu) = \int T \kappa_\nu e^{-\tau_\nu} \mathrm{d}s \,,$$

where the integration is performed over a LOS of length s with a path element of ds. For a sufficiently optically thick source the brightness temperature will tend towards saturating at the electron temperature of the plasma. For this diagnostic to be used successfully, however, knowledge of the source's optical thickness at the observing wavelength is required, as optically thin material, or not-sufficiently optically thick material, will provide brightness temperatures non-representative of the electron temperature.

To determine the optical thickness the gradient of the millimetre continuum is considered. Firstly the relationship between the logarithmic spectral gradient and the optical thickness of the emitting plasma is derived in Section 4.2.1.1, with the same for the linear spectral gradient in Section 4.2.1.2.

4.2.1.1 Derivation of the Logarithmic Millimetre Spectral Gradient

The derivation of the relationship between the gradient of the logarithmic brightness temperature spectrum and the optical thickness of the emitting plasma at the centre of the observing band begins by taking the logarithm of Equation 1.17, resulting in the expression:

$$\log_{10}(T_B) = \log_{10}\left(\int T \kappa_\nu e^{-\tau_\nu} \mathrm{d}s \right),$$

which the derivative of with respect to the logarithmic frequency is thus:

$$\frac{\mathrm{d}\log_{10}(T_\mathrm{B})}{\mathrm{d}\log_{10}(\nu)} = \frac{\mathrm{d}\log_{10}\left(\int T\kappa_\nu \mathrm{e}^{-\tau_\nu}\mathrm{d}s\right)}{\mathrm{d}\log_{10}(\nu)}.$$

Using the standard expression $\mathrm{d}\log_{10}(x) = \frac{\mathrm{d}x}{x\ln(10)}$, the expression then becomes:

$$\frac{\mathrm{d}\log_{10}(T_\mathrm{B})}{\mathrm{d}\log_{10}(\nu)} = \nu\ln(10)\frac{\mathrm{d}\log_{10}\left(\int T\kappa_\nu \mathrm{e}^{-\tau_\nu}\mathrm{d}s\right)}{\mathrm{d}\,\nu},$$

which contains the derivative of the logarithm of a function. For a function $f(x)$ the derivative of the logarithm of $f(x)$ is given by $\frac{\mathrm{d}}{\mathrm{d}x}(\log_{10}(f(x))) = \frac{\frac{\mathrm{d}f(x)}{\mathrm{d}x}}{\ln(10)f(x)}$. Using this, the expression for the logarithmic spectral gradient becomes:

$$\frac{\mathrm{d}\log_{10}(T_\mathrm{B})}{\mathrm{d}\log_{10}(\nu)} = \nu\ln(10)\frac{1}{\ln(10)\int T\kappa_\nu \mathrm{e}^{-\tau_\nu}\mathrm{d}s}\frac{\mathrm{d}\int T\kappa_\nu \mathrm{e}^{-\tau_\nu}\mathrm{d}s}{\mathrm{d}\,\nu},$$

which simplifies to:

$$\frac{\mathrm{d}\log_{10}(T_\mathrm{B})}{\mathrm{d}\log_{10}(\nu)} = \frac{\nu}{T_B}\int T\frac{\mathrm{d}\,\kappa_\nu e^{-\tau_\nu}}{\mathrm{d}\,\nu}\mathrm{d}s.$$

Using the product rule, this becomes:

$$\frac{\mathrm{d}\log_{10}(T_\mathrm{B})}{\mathrm{d}\log_{10}(\nu)} = \frac{\nu}{T_B}\int T\left(e^{-\tau_\nu}\frac{\mathrm{d}\,\kappa_\nu}{\mathrm{d}\,\nu} + \kappa_\nu\frac{\mathrm{d}\,e^{-\tau_\nu}}{\mathrm{d}\,\nu}\right)\mathrm{d}s.$$

Assuming absorption is solely caused by inverse thermal bremsstrahlung (Equation 3.5) the following equations are derived:

$$\frac{\mathrm{d}\,\kappa_\nu}{\mathrm{d}\,\nu} = -\kappa\left(\frac{2}{\nu} - \frac{g'_\mathrm{ff}}{g_\mathrm{ff}}\right), \tag{4.11}$$

and

$$\frac{\mathrm{d}\,e^{-\tau_\nu}}{\mathrm{d}\,\nu} \approx \tau e^{-\tau}\left(\frac{2}{\nu} - \frac{g'_\mathrm{ff}}{g_\mathrm{ff}}\right), \tag{4.12}$$

where g'_ff is the rate of change of the thermal Gaunt factor with frequency. Using Equations 4.11 and 4.12, the expression for the logarithmic spectral gradient becomes:

$$\frac{\mathrm{d}\log_{10}(T_\mathrm{B})}{\mathrm{d}\log_{10}(\nu)} = \frac{\nu}{T_B}\int T\left(-\kappa_\nu e^{-\tau_\nu}\left(\frac{2}{\nu} - \frac{g'_\mathrm{ff}}{g_\mathrm{ff}}\right) + \tau_\nu\kappa_\nu e^{-\tau_\nu}\left(\frac{2}{\nu} - \frac{g'_\mathrm{ff}}{g_\mathrm{ff}}\right)\right)\mathrm{d}s,$$

which can then be simplified to give the general solution for the gradient of the logarithmic millimetre continuum spectrum as:

$$\frac{\mathrm{d}\log(T_\mathrm{B})}{\mathrm{d}\log(\nu)} = \frac{\nu}{T_\mathrm{B}}\int T\mathrm{e}^{-\tau_\nu}\left(\frac{2}{\nu} - \frac{g'_\mathrm{ff}}{g_\mathrm{ff}}\right)(\tau_\nu - 1)\mathrm{d}\tau_\nu. \tag{4.13}$$

If it can be assumed that the LOS is isothermal (1.18), and the integral is evaluated from 0 to τ_ν in optical thickness, the expression becomes:

$$\frac{\mathrm{d}\log(T_\mathrm{B})}{\mathrm{d}\log(\nu)} = \frac{\nu T}{T(1-e^{-\tau_\nu})}\left(\frac{2}{\nu} - \frac{g'_\mathrm{ff}}{g_\mathrm{ff}}\right)\int_0^{\tau_\nu} e^{-t_\nu}(t_\nu - 1)\mathrm{d}t_\nu,$$

which includes the standard integral of the form $\int_0^X e^{-x}(x-1)\mathrm{d}\,x = -Xe^{-X}$. Evaluating this integral yields the following equation:

$$\frac{\mathrm{d}\log(T_\mathrm{B})}{\mathrm{d}\log(\nu)} = \left(\frac{2}{\nu} - \frac{g'_\mathrm{ff}}{g_\mathrm{ff}}\right)\frac{-\nu\tau_\nu}{\mathrm{e}^{\tau_\nu}-1}. \tag{4.14}$$

If it is valid to assume that the rate of change of the Gaunt factor with frequency, g'_ff, is ≈ 0, this equation simplifies to:

$$\frac{\mathrm{d}\log(T_\mathrm{B})}{\mathrm{d}\log(\nu)} = \frac{-2\tau_\nu}{\mathrm{e}^{\tau_\nu}-1}, \tag{4.15}$$

such that the gradient of the logarithmic spectrum is dependent on the optical thickness of the source material solely. In the high optical thickness limit, $\tau_\nu \gg 1$, Equation 4.15 reduces to 0, whilst in the low optical thickness limit, $\tau_\nu \ll 1$ it reduces to -2. Thus by measuring the gradient of a small enough frequency band, such that the measured gradient is representative of the gradient at band centre, the optical thickness regime at band centre may be estimated.

4.2.1.2 Derivation of the Linear Millimetre Spectral Gradient

The previous section showed how the logarithmic brightness temperature spectral gradient is related to the optical thickness at the centre of the observing band. For completeness I will also present the derivation of the gradient of the linear brightness temperature spectrum. Starting with Equation 1.17 again, and taking the derivative with respect to frequency, the following expression is found:

$$\frac{\mathrm{d}\,T_B}{\mathrm{d}\,\nu} = \int T\frac{\mathrm{d}\,\kappa_\nu e^{-\tau_\nu}}{\mathrm{d}\,\nu}\mathrm{d}s.$$

Using the product rule, and Equations 4.11 and 4.12 again, this expression becomes:

$$\frac{\mathrm{d}\,T_B}{\mathrm{d}\,\nu} = \int T\left(-\kappa_\nu e^{-\tau_\nu}\left(\frac{2}{\nu} - \frac{g'_\mathrm{ff}}{g_\mathrm{ff}}\right) + \tau_\nu\kappa_\nu e^{-\tau_\nu}\left(\frac{2}{\nu} - \frac{g'_\mathrm{ff}}{g_\mathrm{ff}}\right)\right)\mathrm{d}s,$$

which, when simplified yields an expression similar to Equation (4.13), such that the general form for the linear brightness temperature spectral gradient can be described as follows:

$$\frac{\mathrm{d}T_\mathrm{B}}{\mathrm{d}\nu} = \int T\mathrm{e}^{-\tau_\nu}\left(\frac{2}{\nu} - \frac{g'_\mathrm{ff}}{g_\mathrm{ff}}\right)(\tau_\nu - 1)\mathrm{d}\tau_\nu. \tag{4.16}$$

For an isothermal LOS, and a thermal Gaunt factor approximately constant with frequency, Equation (4.16) simplifies further to:

$$\frac{\mathrm{d}T_\mathrm{B}}{\mathrm{d}\nu} = \frac{-2T\tau_\nu \mathrm{e}^{-\tau_\nu}}{\nu}. \tag{4.17}$$

In the extreme optical thickness limits Equation 4.17 reduces to 0 for $\tau_\nu \gg 1$, and to $\frac{-2T(\tau_\nu - \tau_\nu^2)}{\nu}$ for $\tau_\nu \ll 1$. Hence for an optically thin source the linear scale spectral gradient will vary with both frequency and temperature, as well as optical thickness; such that the value of the gradient is non-unique for a given optical thickness. Hence, due to the relative simplicity of the two diagnostics it is concluded that the gradient of the logarithmic brightness temperature spectrum is a stronger optical thickness diagnostic than the gradient of the linear-scale brightness temperature spectrum.

4.2.2 Modelling the Logarithmic Millimetre Spectral Gradient

To test the theory presented in Section 4.2.1 a set of numerical radiative transfer models was used. The models used were the two-dimensional, cylindrical cross-section, non-local thermodynamic equilibrium (non-LTE) radiative transfer prominence models of Gouttebroze & Labrosse (2009) (C2D2E). The cylinder was orientated such that its axis was parallel to the solar surface. The brightness temperature was then calculated for a set of horizontal LOS bisecting the prominence cylinder at varying heights. This brightness temperature calculation follows the same methods as outlined previously in Chapter 2, and in Rodger & Labrosse (2017). The one notable change made in the calculation is that the thermal Gaunt factor is found by interpolating the table of calculated thermal Gaunt factors of van Hoof et al. (2014), as described in Section 3.1. Whilst the expression relating the spectral gradient of the logarithmic millimetre-continuum was derived assuming a solely thermal bremsstrahlung emission mechanism, the results from these numerical models are calculated using both thermal bremsstrahlung and neutral hydrogen absorption. To analyse the quality of the logarithmic spectral gradient as a diagnostic, a set of isothermal prominence models is firstly considered to see if there is an agreement with Equation 4.15 (Section 4.2.2.1), and then subsequently a set of multi-thermal (PCTR) models is used to see how any such agreement changes when a temperature gradient is present in the plasma (Section 4.2.2.2).

Whilst nominally the models used here describe solar prominences, the results are applicable to any off-limb solar atmospheric structure. For on-disk structures, the spectral gradient will follow a similar relation to Equation 4.15 with the addition of a second term

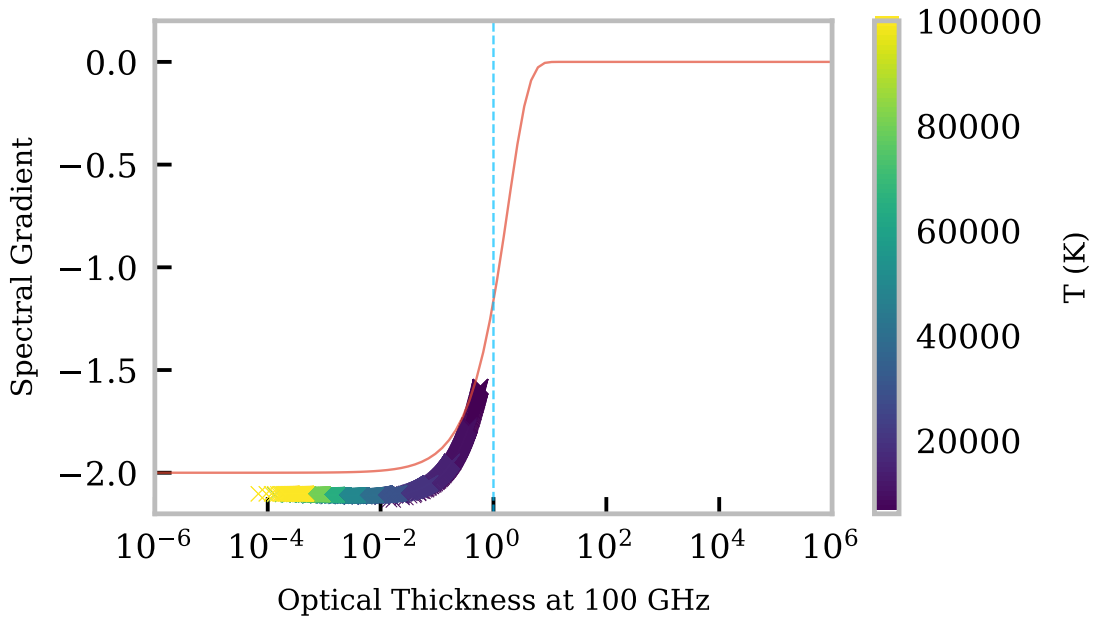

Figure 4.7: Relationship between optical thickness and logarithmic spectral gradient for a set of isothermal prominence models. The solid red line shows the simple relationship as defined by Equation 4.15. The dashed-blue line shows $\tau = 1$. Taken from Rodger & Labrosse (2018)

describing the contribution of the background solar continuum spectrum. Analysis of on-disk structures would thus require knowledge into the brightness temperature of the structure, and the background emission illuminating it. This may be difficult unless the emission is formed above the chromosphere, the forming region for most millimetre-continuum radiation, or when the observed structure is transient in nature, such that measurements of both the background and enhanced brightness temperature phases are obtainable, see Section 4.3.

4.2.2.1 Logarithmic Millimetre-Continuum Spectral Gradient from Isothermal Prominence Models

The set of isothermal models used in this section have been previously defined in Table 3.1, and are the same as the "*t*" models as described in Gouttebroze & Labrosse (2009). Each prominence model consists of cylindrical cross-section of plasma with a radius of 0.5 Mm, at

an altitude of 10 Mm above the solar surface.

The brightness temperature at the four spectral sub-bands of ALMA Band 3, i.e. 93, 95, 105 and 107 GHz (White et al. 2017) was calculated for each of the isothermal models in Table 3.1. A straight line was then fitted to the resultant sub-band 3 logarithmic millimetre-continuum spectrum for every LOS in each model. Figure 4.7 shows a scatter plot of the fitted logarithmic spectral gradient versus the optical thickness for all LOS from the set of isothermal models. Alongside this scatter plot is shown the simplified derived expression from Equation 4.15.

The modelled relationship between the spectral gradient and the LOS optical thickness in Figure 4.7 can be seen to follow a similar trend to that expected by Equation 4.15, although with the values slightly lower. This discrepancy was found to be caused by the assumption that the Gaunt factor is approximately constant over the frequency band. As a test, by re-computing the brightness temperatures with a constant Gaunt factor it was found that this discrepancy was removed entirely.

If the variation of the thermal Gaunt factor across the observing band is thus sufficiently significant to affect this relationship a method to account for it had to be found. From Equations 4.14 and 4.15 it can be found, whilst still assuming an isothermal plasma, that;

$$\frac{\mathrm{d}\log(T_\mathrm{B})}{\mathrm{d}\log(\nu)} = \left.\frac{\mathrm{d}\log(T_\mathrm{B})}{\mathrm{d}\log(\nu)}\right|_{g'=0} \alpha, \tag{4.18}$$

where α is a multiplicative offset factor described by;

$$\alpha = 1 - \frac{\nu g'_\mathrm{ff}}{2 g_\mathrm{ff}}. \tag{4.19}$$

α was evaluated at the known constant temperatures of each prominence model and at the central frequency of ALMA Band 3 (100 GHz). Dividing the modelled spectral gradient versus optical thickness relationship by this correcting factor results in the relationship as shown in Figure 4.8. It can be seen that as long as the non-zero rate of change of thermal Gaunt factor with frequency is corrected for, isothermal models provide the expected relationship between optical thickness and logarithmic spectral gradient as described in Equation 4.15.

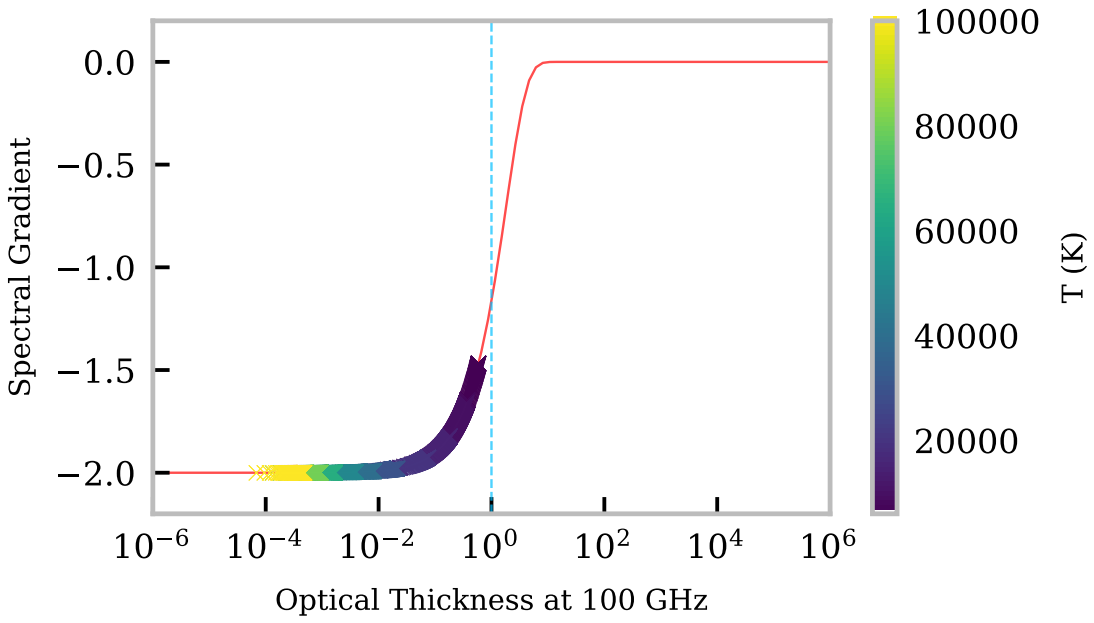

Figure 4.8: Same as Figure 4.7, however the spectral gradient has been corrected for the non-zero g'_{ff} using the known temperature of each model, through Equations 4.18 and 4.19. This figure is taken from Rodger & Labrosse (2018)

4.2.2.2 Logarithmic Millimetre-Continuum Spectral Gradient from Multi-Thermal Prominence Models

This section replicates the tests using isothermal plasmas shown previously using a set of multi-thermal prominence models. The prominence models used here, each including a PCTR, were defined in Table 2.2, and are the same as the '*p*' models as described in Gouttebroze & Labrosse (2009). The radius of these models is larger than that of the isothermal models shown above, as they contain both a core region and a PCTR. The total value for the radius of these cylinders is 1 Mm. The multi-thermal temperature distribution is ad-hoc and defined previously in Equation 2.1 (Gouttebroze 2006). Each model has a different constant pressure as described in Table 2.2. The altitude, helium abundance and microturbulent velocity for all models are the same as described for the isothermal models.

The same process as for the isothermal models was followed whereby the brightness temperature spectrum was calculated and the gradient was found for each of the sub-band wavelengths of ALMA Band 3. The relationship between logarithmic spectral gradient and

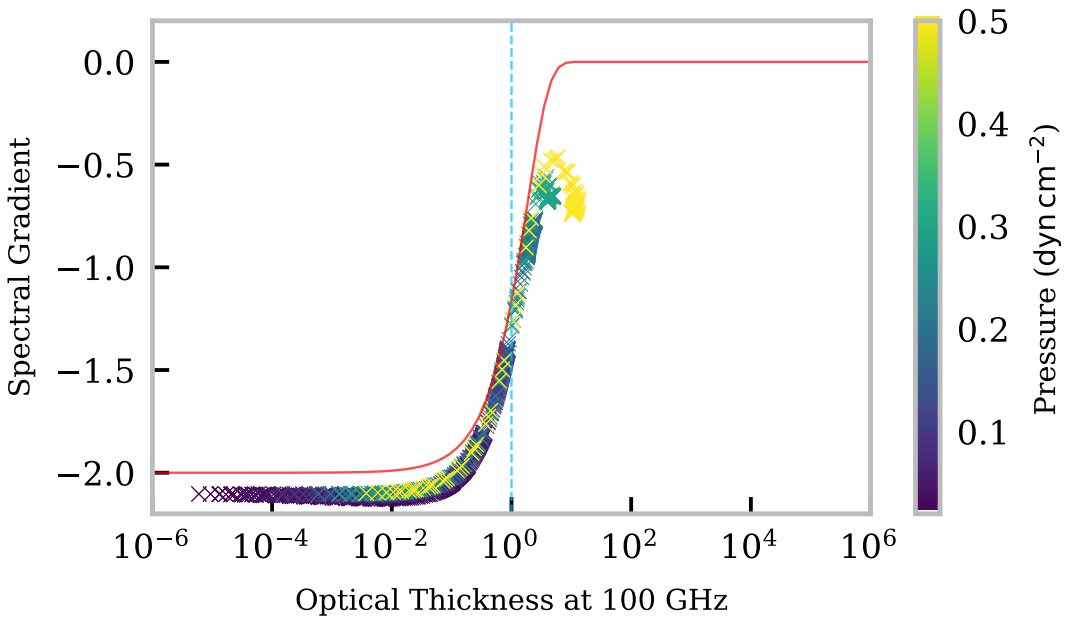

Figure 4.9: Same as Figure 4.7, for a set of multi-thermal isobaric prominence models at various pressures (Table 2.2). This figure is taken from Rodger & Labrosse (2018)

optical thickness at the central frequency of Band 3 for this set of multi-thermal models can be seen in Figure 4.9.

It is seen again in Figure 4.9 that the trend found in the simulated data is below the simplified relationship in Equation 4.15 within the optically thin regime, due to the non-zero rate of change of Gaunt factor with frequency. Unlike the isothermal case, however, it is less simple to correct for α through Equation 4.18 and 4.19 due to the lack of a single representative temperature value. This will be the case when considering any set of multi-thermal LOSs, or more generally a structure of unknown temperature. To attempt to find a solution to this, α has been calculated at all ALMA Bands and at a wide range of temperatures between 10^3 and 10^6 K.

The rate of change of the Gaunt factor with frequency was calculated by interpolating the table of calculated Gaunt factors of van Hoof et al. (2014) across each of the ALMA observing bands. For each band the aunt factor relationship with frequency was fitted with a polynomial function, and the rate of change of the Gaunt factor with frequency was found by evaluating the gradient of the fitted slope at the central frequency of the observing band.

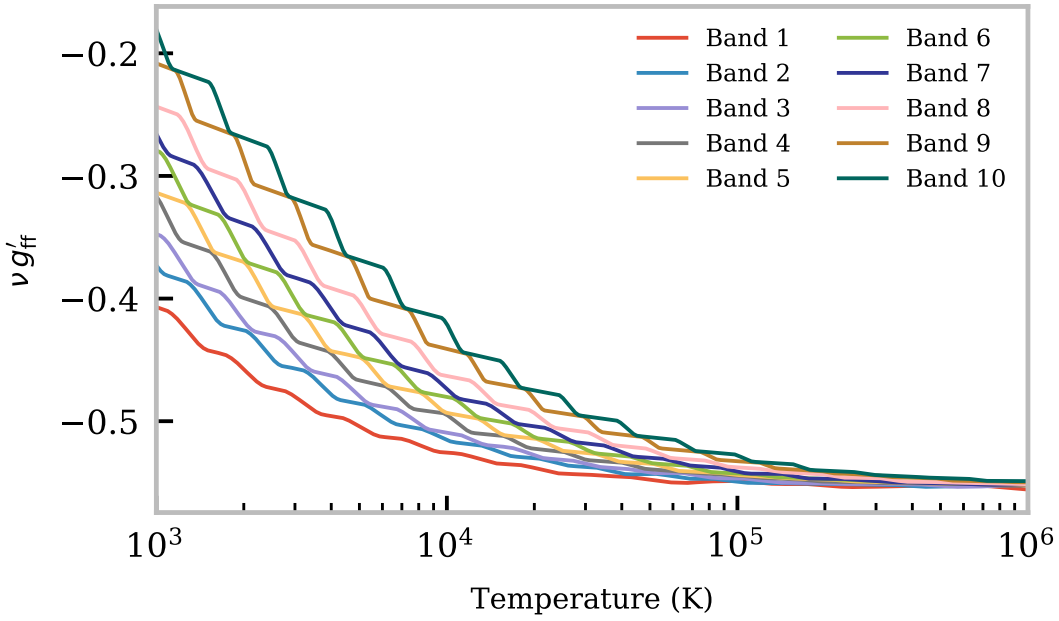

Figure 4.10: Unsmoothed relationship between the rate of change of the Gaunt factor with frequency against temperature. Each colour on the plot represents a different ALMA observing band.

This value was then used with Equation 4.19 to calculate the alpha factor. Due to the very small magnitude of the rate of change of the Gaunt factor with frequency ($g'_{\rm ff} \sim 10^{-13}$), the α variation with temperature displayed a jagged, oscillation-like pattern at low temperatures. The relationship between $g'_{\rm ff}$ multiplied by the frequency at band-centre, at each of the ALMA observing bands with temperature is given in Figure 4.10. This numerical artifact was removed by fitting $g'_{\rm ff}$ with the function;

$$g'_{\rm ff}(\nu, T) = a_\nu \frac{T^{b_\nu}}{T^{c_\nu} + d_\nu}, \tag{4.20}$$

and calculating α using the fitted values for $g'_{\rm ff}$. a_ν, b_ν, c_ν and d_ν are constants dependent on the frequency band. An example of this fit to the $g'_{\rm ff}$ relationship with temperature is shown in Figure 4.11. The resulting smoothed variation of α for each ALMA Band with temperature is shown in figure 4.12. The temperature values in figure 4.12 extend below the temperature range ($\sim$ 5000 K) where this method may be applied, as neutral hydrogen will become a more significant emission mechanism there.

Applying the maximum and minimum values for α(100GHz) across the range 10^3–10^6 K

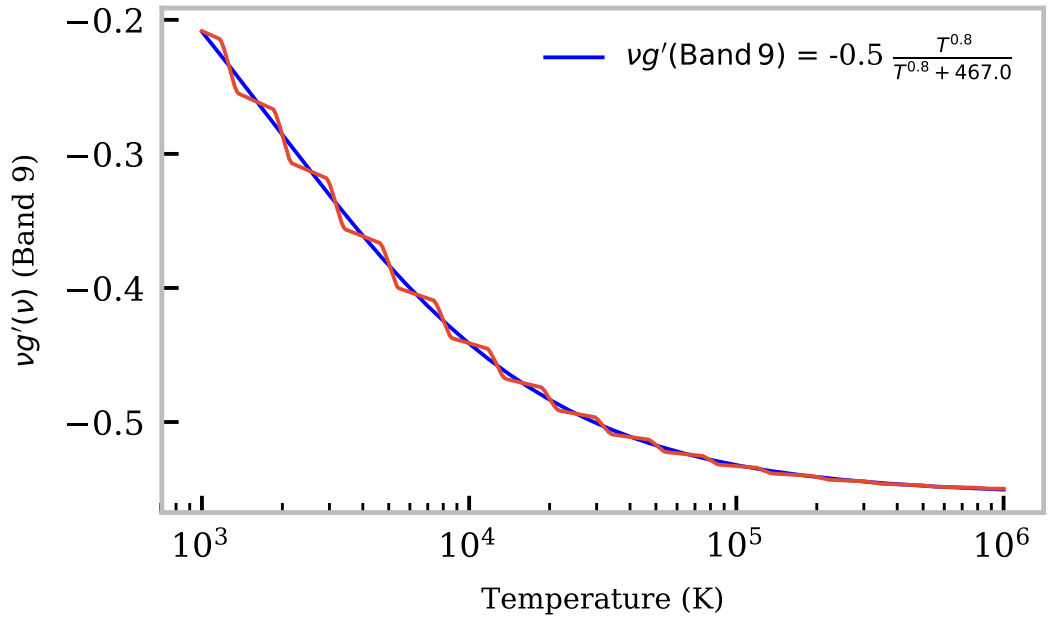

Figure 4.11: Relationship between the rate of change of the Gaunt factor with frequency and temperature, fitted with the function given in Equation 4.20. This relationship was evaluated at ALMA Band 9 (661 GHz).

to Equation 4.18 the corrected relationship is compared to the results from the multi-thermal models. The results from this method are shown in Figure 4.13.

Figure 4.13 shows that the $\alpha(100\ \mathrm{GHz})$ correction can produce a fairly close agreement to the values found from the multi-thermal numerical models, although the relationship notably differs at higher optical thickness. This is primarily due to the breakdown in the assumption that the LOS is isothermal as the spectral gradient becomes dependent on the temperature gradient of the LOS in addition to the optical thickness. Using the non-zero g'_{ff} corrected logarithmic spectral gradient may, however, be used to discern whether the emission is (a) optically thin, (b) the optical thickness of the material if it is in the range $\tau \approx 0.1 - 1$, or (c) whether it is optically thick and the gradient is defined by the temperature gradient of the plasma.

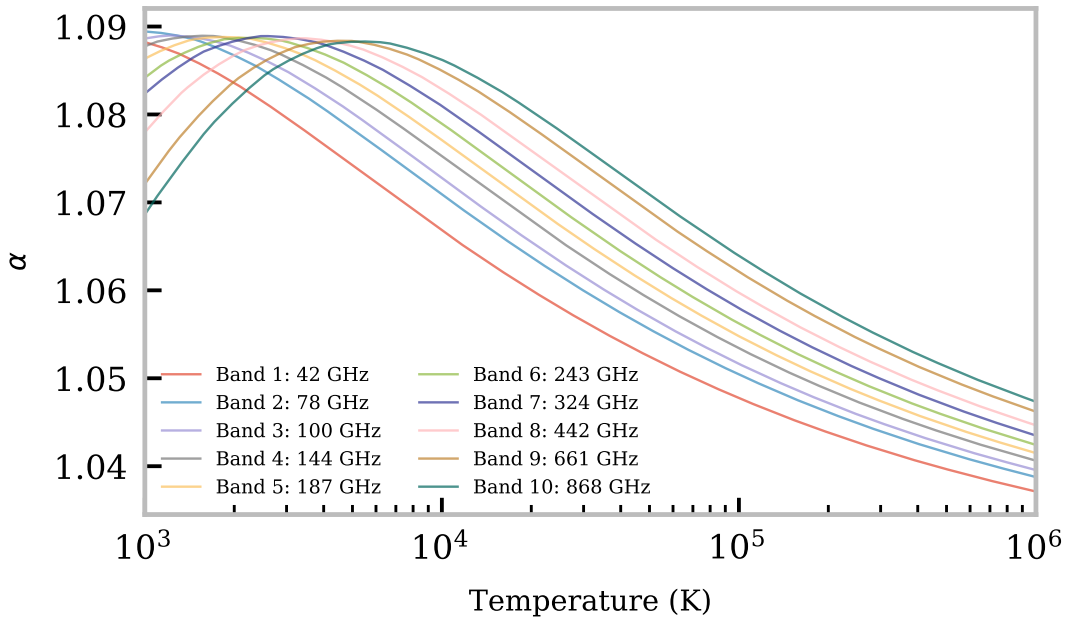

Figure 4.12: Smoothed variation of α correction, evaluated at all ALMA bands over a wide range of temperatures. This figure is taken from Rodger & Labrosse (2018)

4.2.2.3 Minimum Required Uncertainty in Brightness Temperature Measurement

Estimating the optical thickness regime using the logarithmic spectral gradient of the millimetre-continuum will require suitably precise measurements of the brightness temperature across the ALMA sub-band. Ideally for the gradient of the logarithmic spectrum to be calculated the uncertainty in the brightness temperature should be significantly less than the brightness temperature difference across the sub-band spectrum. Higher precision will thus be necessary when the brightness temperature is very low, or when the spectral gradient tends towards 0 for fully optically thick material. In Figure 4.14 the brightness temperature difference across ALMA Band 3 for both the sets of isothermal and multi-thermal models used in this study is shown. As may be expected, very low optical thickness, and therefore very low brightness temperature models, will require significantly better precision in the brightness temperature measurements than models with higher brightness temperatures.

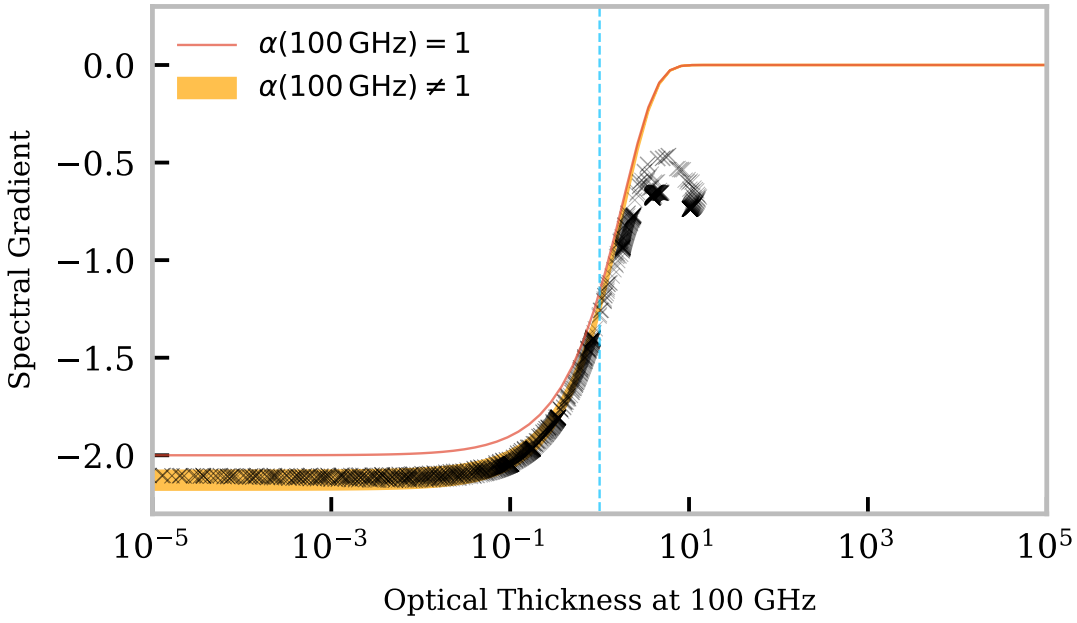

Figure 4.13: Relationship between millimetre-continuum logarithmic spectral gradient and optical thickness for multi-thermal numerical models (black points). The simple, isothermal expression from Equation 4.15, without the correction for α factor is shown in red. The orange region shows the corrected relationship from Equation 4.18, where α is evaluated for ALMA Band 3 at temperatures between 10^3 and 10^6 K. The dashed-blue line shows $\tau = 1$. This figure is taken from Rodger & Labrosse (2018)

4.2.3 Summary

In this section I have described how the gradient of the logarithmic millimetre-continuum spectrum can be used as a diagnostic of the optical thickness regime at the centre of the observing band when a purely thermal bremsstrahlung emission mechanism may be assumed. The derivation of the expected relations for both a logarithmic and linear scale spectral gradient with respect to the LOS optical thickness is shown. From this it is clear that the logarithmic scale provides a better, simpler diagnostic. Through testing the theoretical expression with both isothermal and multi-thermal numerical prominence simulations it was found that the spectral gradient can be used to estimate the optical thickness regime at band centre provided that a suitable correction is made to account for a non-zero rate of change of the Gaunt factor with frequency over the observing band.

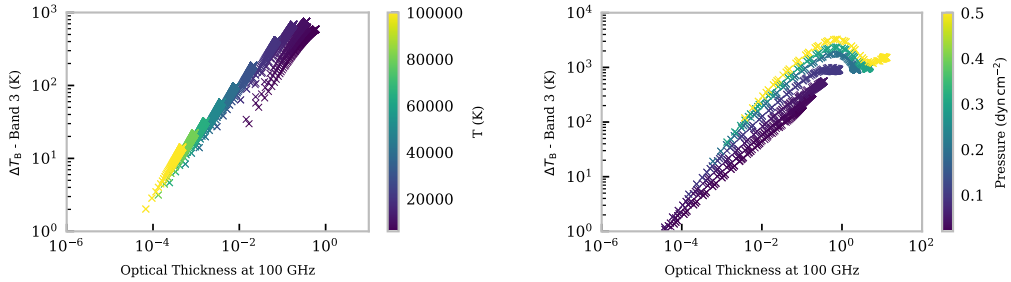

(a) **(b)**

Figure 4.14: Brightness temperature difference across the ALMA Band 3 sub-band spectra created by the set of isothermal models (left panel) and multi-thermal models (right panel). These figures are taken from Rodger & Labrosse (2018).

It is found that, for an isothermal plasma, when the optical thickness of the emitting material lies within the range $\tau \approx 10^{-1}$–10^{1}, this method may be used to estimate the optical thickness of the material, and that this relationship should always hold. However, for a more realistic multi-thermal plasma the relationship will not be able to tell directly the optical thickness for $\tau > 1$ where the optical thickness is sufficiently high for the spectral gradient to also be defined by the temperature distribution as opposed to the optical thickness solely.

These results were determined using a set of prominence models, however, this method will be more generally applicable to any off-limb solar structure. Enhancement from on-disk structures will follow a similar relationship with the addition of a term dependent on the gradient of the background continuum spectrum. This will thus require knowledge of both the structure's brightness temperature spectrum, but also of the background brightness temperature spectrum illuminating it from the solar disc. This may be problematic unless the structure is clearly observed to be above the formation region of the millimetre regime, or where the observed structure is transient in nature. In the next section (4.3) I present a case study for the analysis of the sub-Band 3 ALMA spectrum of such a transient event, using an ALMA solar observation of a brightness temperature enhancement, and plasma ejection.

4.3 Diagnostic Case Study: Spectral Diagnostics of a Solar Eruptive Event using ALMA

Here I present a case study which I conducted on the use of the spectral gradient of ALMA Band 3 as a plasma diagnostic. Much of the work in this section has previously been published in Rodger et al. (2019). As stated previously, my contribution to this publication included the construction and running of all numerical modelling and data analysis codes, as well as most of the figures. Because of this, much of the content of this chapter follows directly from this publication. All figures from this publication are explicitly labelled in their captions, and in the few cases where I did not produce the figure the co-author who did is also explicitly stated.

The first ALMA solar observing cycle (Cycle 4) was conducted in 2016–2017. In cycle 4 the ALMA modes and capabilities available for solar physics were Bands 3 (84–116 GHz) and 6 (211–275 GHz) using the most compact-array configurations (maximum baselines < 500m) at an imaging cadence of ~ 2 s. This study, however, makes use of dataset from the ALMA solar science verification (SV) campaign of 2015, the successes of these verification campaigns led directly to the opening of proposals for solar observing in ALMA's Cycle 4. Shimojo et al. (2017a) give an account of the SV efforts including descriptions of the required Mixer-Detuning method of receiver gain reduction and calibration processes for ALMA solar data. They also discuss how to estimate the noise level for interferometric images using the difference between cross-correlated orthogonal linear polarization measurements. Absolute brightness temperature measurements from ALMA require the interferometric images to be "feathered" with measurements taken using a set of up to four separate total-power (TP) antennas. White et al. (2017) provide a description of the Fast-Scanning Single-Dish Mapping technique employed by ALMA's TP antennae. For information on other publications using the SV data sets see Section 1.5.

ALMA bands are formed of four constituent sub-bands, also known as *spectral windows* (or spw). Through the measurement of the brightness temperature spectrum at several frequencies within one ALMA Band it is possible to construct a millimetre-continuum spectrum providing more constraints to the emission mechanism from a given region, which could be used to refine any diagnostic made of the plasma conditions. To do this, the relationship between the optical thickness of an emitting material and the logarithmic spectral gradient, which is discussed for an off-limb case in Rodger & Labrosse (2017), is

used. This study demonstrates this using ALMA Band 3, although the method is applicable to other solar observing bands. The observation used is of a plasmoid ejection from the active region NOAA12470 taken on the 17th of December 2015. This was an interesting case to study due to the enhancement in brightness temperature caused by the plasmoid observed. This event was first analysed by Shimojo et al. (2017b) where the authors set limits on the possible density and thermal structure of the plasmoid using the brightness temperature integrated across Band 3, observations at EUV wavelengths from *SDO*/AIA and soft X-rays using *Hinode*/XRT. The authors calculated the average enhancement observed from the plasmoid in brightness temperature at ALMA Band 3 (100 GHZ) and in intensity in the 171, 192 and 211 Å AIA bands. From these measurements they considered the required density/temperature curves for formation, aiming to find the areas where cross-over occurred between the ALMA and AIA bands. Finally, the authors concluded that the plasmoid consisted of either an isothermal 10^5 K plasma that was optically thin at 100 GHz, or a multi-thermal plasmoid with a cool 10^4 K core and a hot EUV emitting envelope.

Section 4.3.1 describes the data used, the methods for image synthesis and the calculation of the plasmoid brightness temperature enhancement, whilst the results are presented in Section 4.3.2. A discussion of the method and the results found is given in Section 4.3.3.

4.3.1 Observation

On the 17th of December 2015, ALMA observed during a science verification campaign near to the large leading sunspot of active region NOAA12470. During this observation, the ALMA array consisted of a reduced interferometer setup of 22×12 m and 9×7 m antennas instead of up to the 50×12 m and 12×7 m which will be the maximum possible array configuration available during full scientific campaigns. A temporal brightness temperature enhancement was measured simultaneously near to an X-ray bright point (XBP) observation, with this brightness temperature enhancement showing the ejection of a moving bright blob of plasma or *plasmoid* (Shimojo et al. 2017b). The interferometer observed in ALMA Band 3 which has a central frequency of 100 GHz in the bandwidth of 84 – 116 GHz. ALMA Band 3 observations at 100 GHz have FOVs of 60″. The observing beam was found to be elliptical with a semi-major axis of 6.2″and semi-minor axis of 2.3″. This is due to the shape of the beam depending on the location in the sky and thus the shape will change for different observations. This dataset, along with other SV data sets, has been publicly released by the

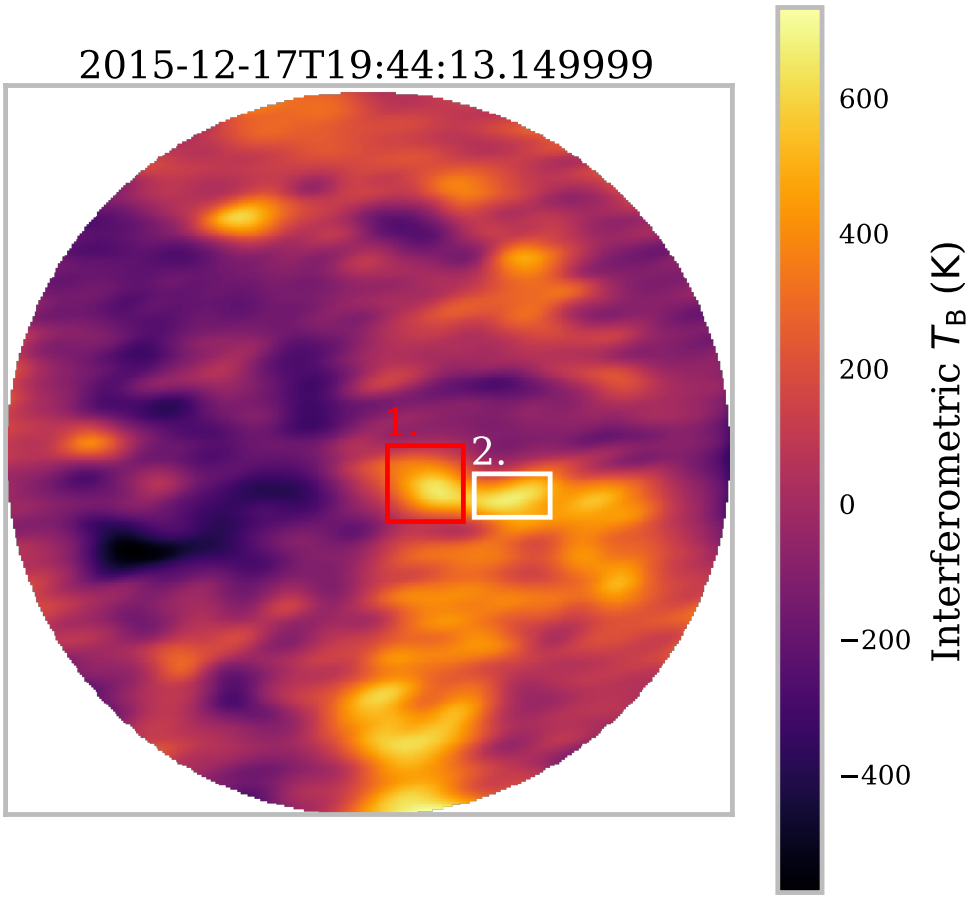

Figure 4.15: High resolution interferometric image of active region NOAA12470 observed on the 17th of December 2015 by ALMA during a science verification campaign. This figure shows a synthesised ALMA Band 3 spectral window 0 (93 GHz) image produced over a single 2s interval. The interferometric relative brightness temperature change is represented in Kelvin in the colourbar to the left of the plot. The two numbered boxes on the image show the locations of the regions of interest discussed throughout this section. This figure is a reproduction of a figure previously published in Rodger et al. (2019).

joint ALMA observatory[1].

[1] https://almascience.eso.org/alma-data/science-verification

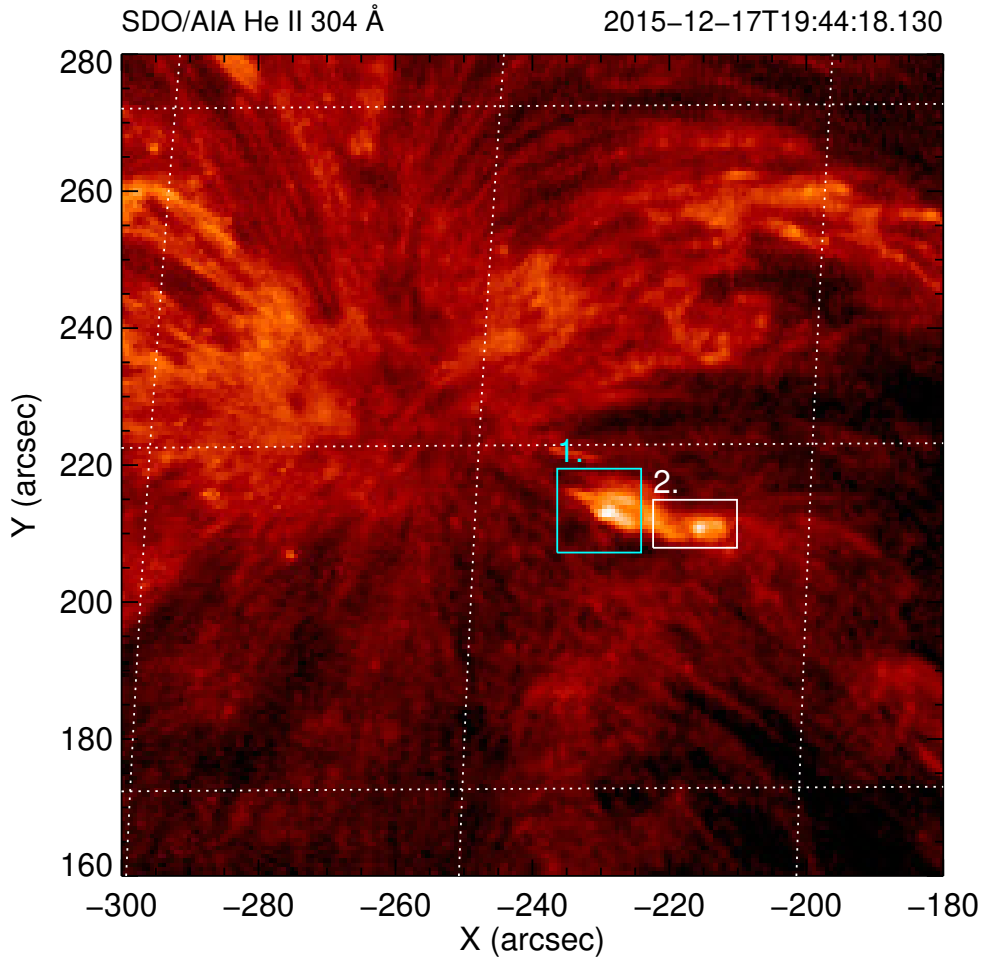

Figure 4.16: Image viewed using SDO/AIA at 304 Å taken on the 17th of December 2015 used to provide context to the ALMA observation shown in Figure 4.15. The two regions of interest shown in Figure 4.15 are again displayed on this figure. This image was previously published in, and was produced on request by co-author Dr P.J.A. Simões, for Rodger et al. (2019).

The first test which I attempted was to replicate the results of Shimojo et al. (2017b). To do this I used the data reduction scripts provided with the test data[2] to calibrate the data and synthesise each image using the full bandwidth of Band 3 at a cadence of 2 s.

[2] https://almascience.eso.org/almadata/sciver/2015ARBand3/

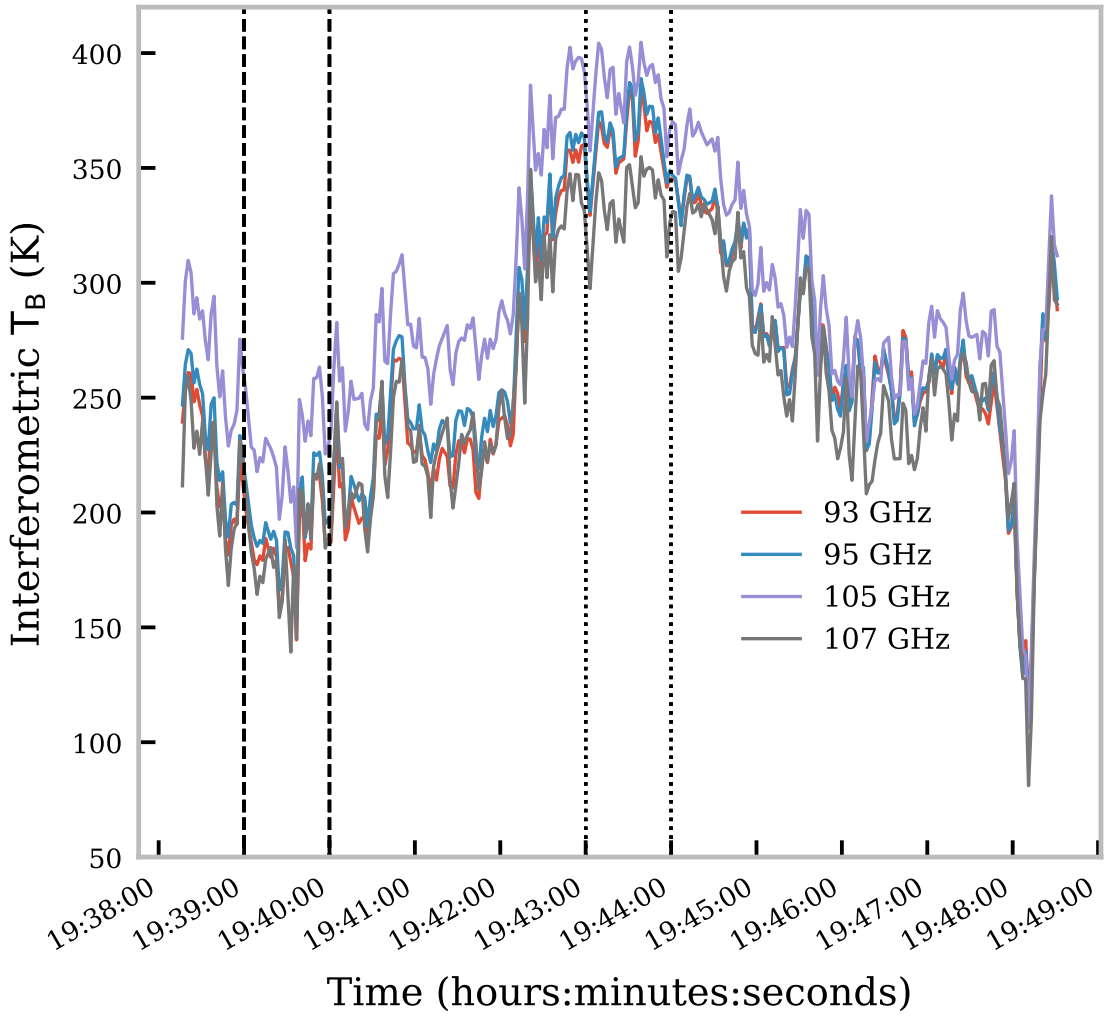

Figure 4.17: Lightcurve of the interferometric brightness temperature within the region coincident with an XBP (Box 1 in Figure 4.15), for all sub-bands in ALMA Band 3. The dashed lines represent the time range defining the pre-enhancement background level, whilst the dotted lines represent the same for the plasmoid enhancement time range used in this analysis. This figure is a reproduction of a figure previously published in Rodger et al. (2019).

Following Shimojo et al., two boxes within the FOV were defined (Box 1 and Box 2 in Figure 4.15) in the resulting time-series images. An SDO/AIA 304 Å image shows the context for the observation in Figure 4.16 (Lemen et al. 2012). Box 1 covers the region containing the stationary brightness temperature enhancement coincident with an XBP, whilst Box 2 shows the region where the moving brightness temperature enhancement from the plasmoid ejection was observed. These boxes were chosen to replicate as well as possible the same

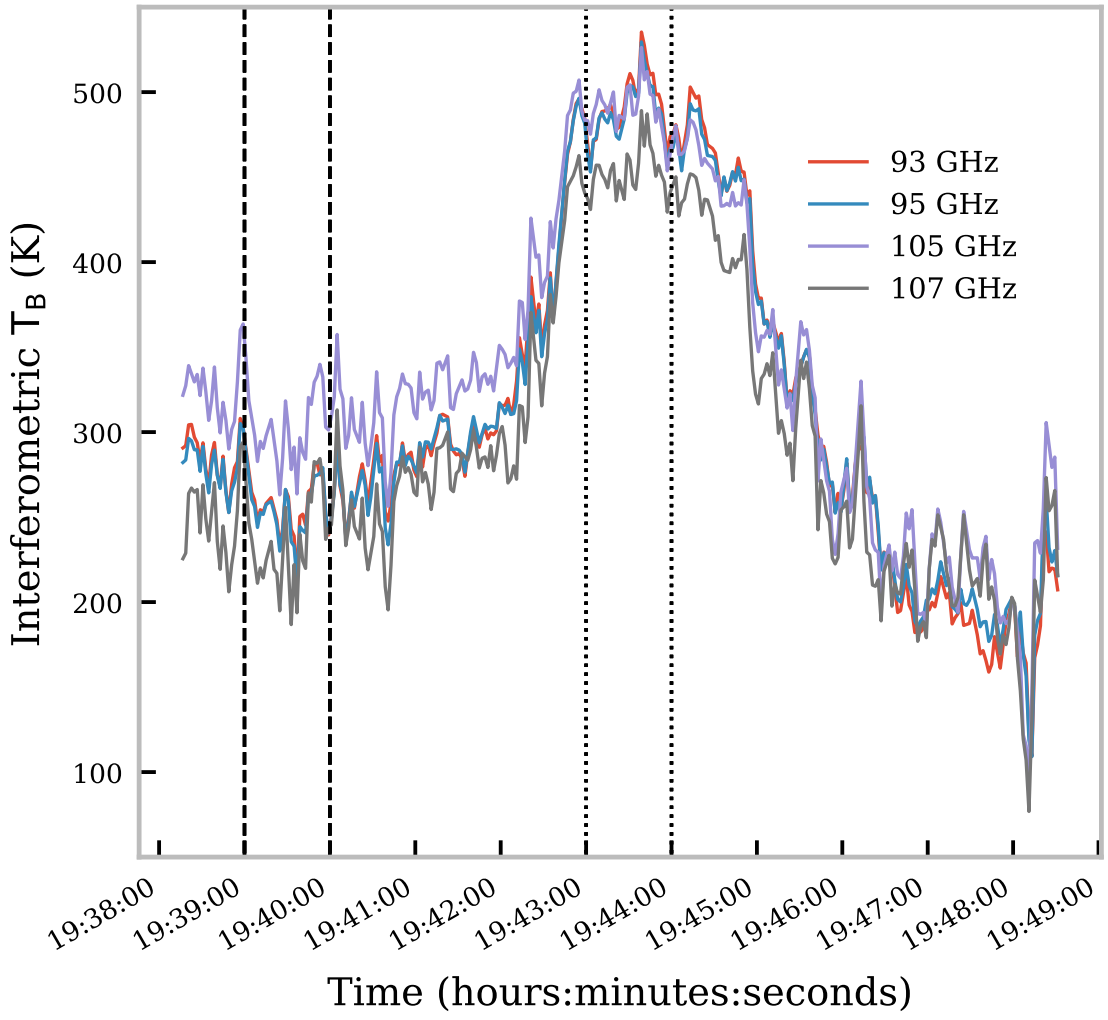

Figure 4.18: Same as Figure 4.17 but for Box 2 in Figure 4.15. This figure is a reproduction of a figure previously published in Rodger et al. (2019).

location and extent of those used Shimojo et al., however, it is likely that there was some differences in execution. The mean brightness temperature was calculated within each of Box 1 and 2 at each time step during the observing scan covering the plasmoid ejection.

Due to the lack of zero-spaced data, purely interferometric measurement can only provide the relative change in brightness temperature to some background value described by the very largest spatial scales for the particular frequency-band observed. As the FOV for this observation (60″ for Band 3) is completely filled by the Sun, a background or quiet Sun measurement was not possible using solely interferometric. It is possible, however, for

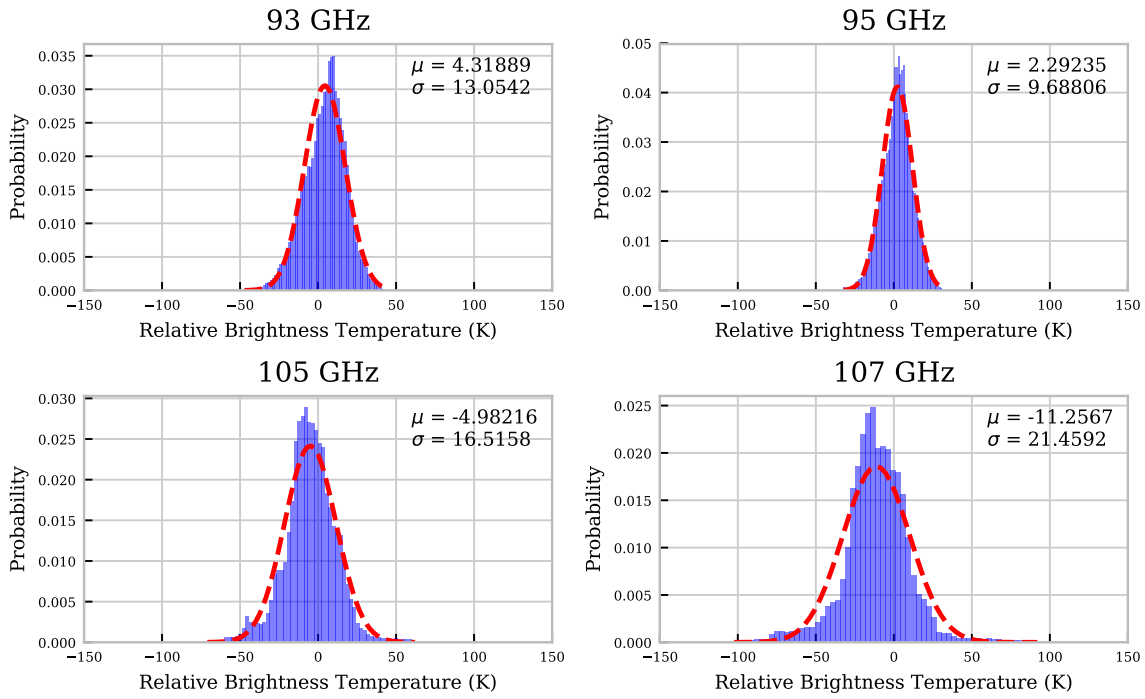

Figure 4.19: Histograms of the noise distributions for each sub-band of ALMA Band 3. Distributions calculated using the respective difference between XX and YY cross-correlated linear polarisation data of each sub-band. Each image was synthesised across the whole bandwidth of each sub-band over a single time stamp of duration 2s. Each histogram is fitted with a gaussian function (dashed red), with the fitted mean and standard deviation given on each panel. This figure is a reproduction of a figure previously published in Rodger et al. (2019).

ALMA to produce absolute brightness temperature measurements through a process called "feathering", where the interferometric images are combined with full-dish total power images (Koda et al. 2011). Feathering would add an increased level of uncertainty to the data set (White et al. 2017), and in agreement with Shimojo et al., for Rodger et al. (2019) it was decided to focus on interferometric results solely.

Using this method, relative brightness temperature lightcurves for boxes 1 and 2 were produced. The absolute brightness temperature enhancement was then calculated by taking the difference between the relative brightness temperatures at two separate periods within the scan; one representative of a quiet/background phase and the other of the enhanced phase. These time ranges are shown on Figures 4.17 and 4.18.

This procedure was repeated to calculate the brightness temperature of the four constituent spectral windows of Band 3: 93, 95, 105 and 107 GHz (White et al. 2017). The resulting brightness temperature curves can be seen in Figures 4.17 and 4.18.

4.3.1.1 Noise Level Calculation

The noise level of the synthesised images was estimated by calculating the difference image between XX and YY cross-correlations of the two orthogonal linear polarisation measurements, X and Y (Shimojo et al. 2017a). Net linear polarization should be absent from quiet solar observation and any such polarization in Band 3 or Band 6 should be negligible in comparison to current instrumental precision. Knowing this it is then possible to attribute any observed difference between the solar synthesised images of XX and YY-data to noise. The noise level measurement was calculated as the standard deviation of a gaussian function fitted to the distribution of the XX-YY image.

Shimojo et al. (2017b) quoted a brightness temperature enhancement for the moving plasmoid (box 2) of 145 K with a calculated noise level for the dataset of 11 K. The 11 K noise level value presented by Shimojo et al. (2017b) was found to be replicated in this study when estimating for the full Band 3 bandwidth image synthesised over the entire observations duration. The noise estimates used in this study are, however, representative of the noise level in the images at a single time 2 s cadence observation within the particular scan of interest. Following the method described above a brightness temperature enhancement of 220 K was calculated with respective noise level of 14 K. Whilst the overall lightcurves are very similar, the calculated brightness temperature enhancement in this study (Rodger et al. 2019) differs from the value quoted by Shimojo et al. (2017b). These differences may be attributed to the definitions of the box dimensions or time ranges used in either study, or through differences in calibration. For example, in Rodger et al. (2019) we used only the calibration methods presented in the reference reduction scripts for the SV data, these do not contain further correction methods such as self-calibration.

The noise level of each sub-band was then calculated using the method given in Shimojo et al. (2017a), again the images used were synthesised for a single time interval of 2s. The gaussian fitted noise distributions can be seen in Figure 4.19. It can be seen that the gaussian fit to the data is noticeably better for spectral windows 0 and 1 than when compared to 2 or 3. Through analysing the kurtosis of each dataset it was found that spectral windows 2 and 3 have non-gaussian distributions. Reasons for the departure from a gaussian distributed

noise distribution include either a component from an unknown source of linear polarisation in the signal, or the introduction of a disbalance in XX and YY polarisations from the radio antennas themselves. The former is unlikely due to the general understanding of the solar millimetre emission mechanism, whilst the latter has been found in the prominence observation investigated in Chapter 5. None the less, the reason behind this was not known when Rodger et al. (2019) was published and it remains an issue which should be investigated further in a future study.

Table 4.1: Brightness temperature enhancements for Boxes 1 and 2 in figure 4.15 with the standard deviations of the respective normally distributed uncertainty for each box, as observed in Rodger et al. (2019). Data is provided for each constituent spectral window of ALMA Band 3.

Spectral Window (GHz)	Box 1 $E \pm \sigma(E)$ (K)	Box 2 $E \pm \sigma(E)$ (K)
Spw0 – 93 GHz	174 ± 6.8	235 ± 9.3
Spw1 – 95 GHz	170 ± 6.9	233 ± 9.2
Spw2 – 105 GHz	156 ± 7.5	188 ± 9.9
Spw3 – 107 GHz	150 ± 6.7	218 ± 9.3
Full Band – 100 GHz	159 ± 6.8	221 ± 9.4

The noise levels quoted above represent the noise in the image as a whole and are thus used as the detection limit of the image. These values, however, cannot be used as the uncertainty of the brightness temperature observed from a specified region in the image. To calculate the brightness temperature enhancement noise at the four constituent spectral windows of Band 3, within each observational box, the value for the noise in each sub-band was calculated using half of the average of the absolute difference between the XX and YY data in said specified region, and for each of 2s interval image in the scan. This method found that the noise was different between observational boxes but did not evolve in time, remaining at a constant value, $\sigma_{box}(\nu)$. As the number of images used within both the background and enhanced phases were kept equal at $N = 29$, the propagated noise for the enhancement at each sub-band for each box was calculated using the equation:

$$\sigma_{E,noise}(box, \nu) = \sqrt{\sigma_{box}(\nu)^2 \frac{2}{N}} \tag{4.21}$$

4.3.1.2 Flux Scale Accuracy

Section 10.4.8 of the ALMA Cycle 6 Technical Handbook[3] (Warmels et al. 2018) states that there is a limit to the accuracy of the flux, and thus brightness temperature, scale of an observation with ALMA. In Warmels et al. (2018) it is said that this limit to the accuracy increases with frequency. For ALMA Band 3 this limit is quoted to be 5% of the flux scale. This 5% value is a conservative estimate as the flux scale uncertainty is built on a combination of sources, including: system temperature measurement, absolute flux calibration, and temporal gain calibration. Because of this conservative estimate, the true uncertainty in the flux scale accuracy may well be less than this quoted value. To model this, in Rodger et al. (2019) we assumed a gaussian-distributed random uncertainty where the mean is zero and 3σ is equal to the 5% limit. Including this scaling accuracy limit as a systematic error the standard deviation of the normally-distributed brightness temperature enhancement error becomes:

$$\begin{aligned}\sigma_E(box,\nu)^2 &= \sigma_{E,noise}(box,\nu)^2 + \\ (\frac{0.05}{3} &\times T_{B,background}(box,\nu))^2 + \\ (\frac{0.05}{3} &\times T_{B,enhanced}(box,\nu))^2,\end{aligned} \tag{4.22}$$

where $T_{B,background}(box,\nu))$, and $T_{B,enhanced}(box,\nu))$ are the interferometric brightness temperatures of the background and enhanced phases shown in figures 4.17 and 4.18 for a given box and spectral window, respectively.

The resulting enhancement at each spectral window and the standard deviation of their respective normally-distributed uncertainties are given in Table 4.1.

4.3.1.3 Brightness Temperature Enhancement Spectrum

Throughout this case study the brightness temperature enhancement is defined as the difference between the brightness temperature emitted during a period of enhancement and its background value. Assuming an isothermal enhancing plasma the equation for the frequency dependent brightness temperature enhancement, $E(\nu)$ is;

$$E(\nu) = (T - T_{\mathrm{B0}}(\nu))(1 - \mathrm{e}^{-\tau(\nu)}), \tag{4.23}$$

where T is the temperature of the enhancing plasma, $T_{\mathrm{B0}}(\nu)$ and $\tau(\nu)$ are the frequency-dependent background quiet Sun brightness temperature and optical thickness, respectively.

[3] https://almascience.eso.org/documents-and-tools/cycle6/alma-technical-handbook

The sign of the enhancement, i.e. whether the structure is observed as a bright or dark feature, depends on whether the temperature of the plasma is greater (positive enhancement) or less (negative enhancement) than the background brightness temperature value.

The logarithmic-scale gradient of the enhancement spectrum (Equation 4.23) follows a similar relation with optical thickness to the off-limb version described in Equation 4.14, again using the previously defined α term (Equation 4.19), but with an additional term, β, dependent on frequency and on the background solar spectrum:

$$\frac{\mathrm{d}\log(E)}{\mathrm{d}\log(\nu)} = \beta - \alpha\frac{2\tau_\nu}{\mathrm{e}^{\tau_\nu}-1}, \tag{4.24}$$

where,

$$\beta = \frac{-\frac{\mathrm{d}T_{\mathrm{B0}}}{\mathrm{d}\nu}\nu}{T - T_{\mathrm{B0}}}. \tag{4.25}$$

Due to the structure of the solar chromosphere where the background emission is formed, and the width of the observing band, the gradient of the background spectrum, $-\frac{\mathrm{d}T_{\mathrm{B0}}}{\mathrm{d}\nu}$, is expected to be a small negative value, this assumption is discussed more in Section 4.3.3. β will thus be a negative or positive factor depending on whether the constant temperature, T, is less than or greater than the brightness temperature of the background emission at band centre, T_{B0}, respectively. Through Equation 4.23 the magnitude of the β term will decrease with increased brightness temperature enhancement. When the gradient of the background is small, so too should the β term, except when near the discontinuity at $T = T_{\mathrm{B0}}$.

For a fully optically thin plasma, $\tau \ll 1$, the gradient of the enhancement spectrum will tend towards $\frac{\mathrm{d}\log(E)}{\mathrm{d}\log(\nu)} = \beta - 2\alpha$. For fully optically thick plasma, $\tau \gg 1$, it shall tend towards $\frac{\mathrm{d}\log(E)}{\mathrm{d}\log(\nu)} = \beta$. Due to the structure of the solar chromosphere, the quiet Sun background brightness temperature in the millimetre-continuum is expected to decrease with increasing frequency, thus to reach the same magnitude of the electron temperature across the entire wavelength range, the enhancement spectrum would have to increase with frequency. There is therefore a transition between a negative-gradient enhancement spectrum and a positive-gradient enhancement spectrum when the enhancing plasma's optical thickness increases significantly above unity. A schematic graph of this mechanism is given in Figure 4.20.

4.3.2 Results and Analysis

The brightness temperature enhancement spectra were produced from the lightcurves shown in Figures 4.17 for the stationary enhancement coincident with an XBP(Box 1) and 4.18 for the moving plasmoid (Box 2), see Figure 4.15 for the locations of both structures. All values

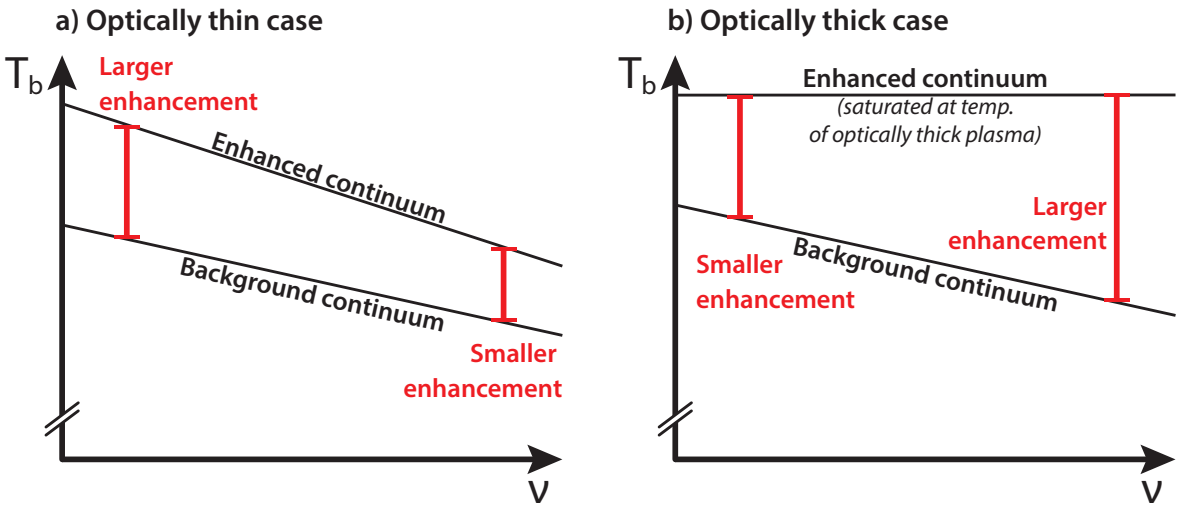

Figure 4.20: Schematic diagrams showing the change in brightness temperature enhancement with frequency for an optically thin or optically thick enhancing isothermal material. This figure is a reproduction of a figure previously published in Rodger et al. (2019). Figure was produced on request by co-author Prof S. Wedemeyer.

for the brightness temperature enhancements and the respective standard deviations of their assumed normally distributed errors are shown in Table 4.1. From these spectra the respective logarithmic spectral gradient for both boxes is calculated so that the optical thickness may be estimated using the method described in Section 4.3.1.3. The estimated optical thickness was then used to further estimate other plasma properties, such as the emission measure and temperature. The results and analysis for Box 1 are shown in Section 4.3.2.1, whilst the same for Box 2 is given in Section 4.3.2.2.

4.3.2.1 Analysis of Box 1: Stationary Enhancement Coincident with an XBP

In Figure 4.21 the logarithmic enhancement spectrum is plotted for the stationary enhancement seen in Box 1. Due to the relatively small separation in frequency across the spectrum a straight line is assumed for the fit to the curve. The fitting function is thus:

$$\log_{10}(E) = m\log_{10}(\nu) + c, \tag{4.26}$$

where m is the gradient and c is the y-intercept, regardless of the optical thickness regime. A bayesian linear regression method was chosen to fit this function to the observed spectrum. The rationale for this decision was that this method allows for the best use of the uncertainty distributions defined in Sections 4.3.1.1 and 4.3.1.2, whilst having the advantage of produc-

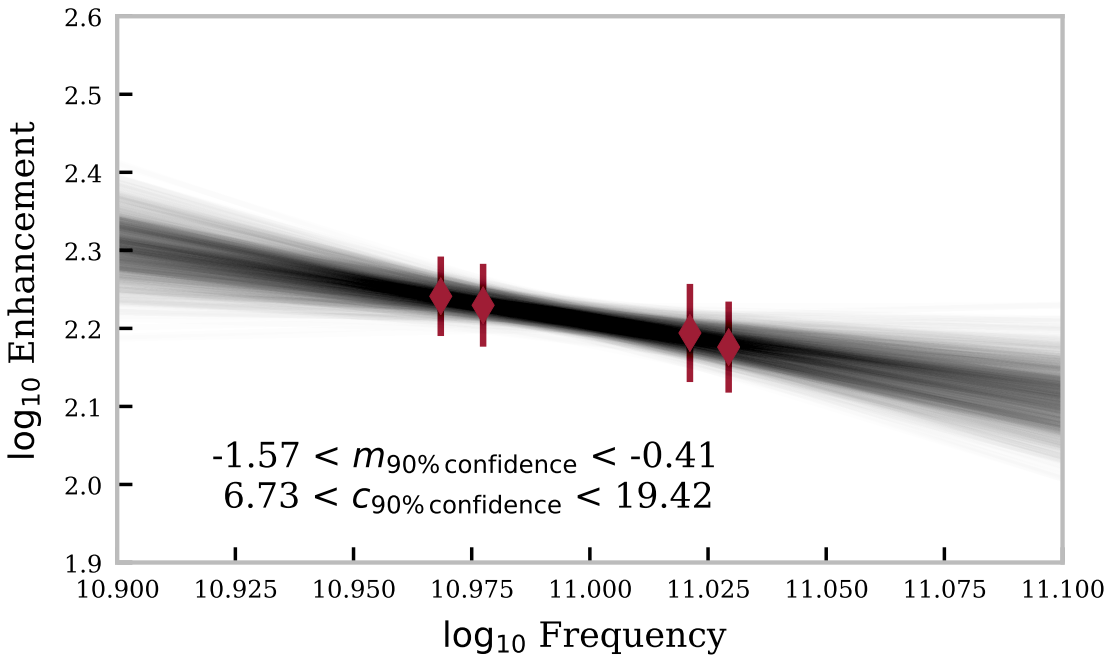

Figure 4.21: A subset of the MCMC fitted logarithmic-scale mean millimetre-continuum brightness temperature enhancement spectra for the Box 1 region coinciding with the XBP from figure 4.15 is shown as overlaid grey lines. The red data points show the observed brightness temperature measurement, with the bars representing the 3σ value of the normally-distributed likelihood functions used in the statistical model. The values of σ for these error bars are propagated in logarithmic space from the values given in Table 4.1. The range of values for the gradient and intercept of the spectral fits to 90% confidence are shown on the plot. This figure is adapted from Rodger et al. (2019), although, it has been calculated using a larger number of MCMC samples, thus allowing for the fitting parameters to be quoted to a higher precision.

ing a posterior probability distribution for the estimated spectral gradient. The bayesian statistical model used here is defined as:

$$p(m,c|\{\text{data}\}) \propto p(\{\text{data}\}|m,c)\,p(m,c), \tag{4.27}$$

where $p(m,c|\{\text{data}\})$ is the posterior probability distribution, i.e. the probability for a specific fit to the spectrum (m,c), given the observed enhancements at each frequency ($\{\text{data}\}$). $p(\{\text{data}\}|m,c)$ is the likelihood function defined as the probability of finding the observed enhancements given the hypothesized m and c. $p(m,c)$ is the prior distribution which defines

any previously known information with regards to the expected m and c (Bayes & Price 1763).

To fit the spectrum a statistical model was made with suitable logarithmic likelihood and prior functions. For the likelihood function a normal distribution was chosen, such as that the logarithmic likelihood is described by:

$$\ln\Big(p(y|x,\sigma_{y,n},m,c)\Big) = -\frac{1}{2}\sum_{n}\left[\frac{(y_n - mx_n - c)^2}{\sigma_{y,n}^2} + \ln(2\pi\sigma_{y,n}^2)\right], \tag{4.28}$$

where $y = \log_{10}(E)$, $x = \log_{10}(\nu)$ and the standard deviation, $\sigma_{y,n}$, is equal to the values given in Table 4.1 propagated into logarithmic space. The prior distributions for both the gradient (m) and the y-intercept (c) were set as uninformative uniform distributions. The logarithmic uniform priors were therefore set as:

$$\ln\left(p(m)\right) = \begin{cases} 0.0, & \text{if } -20 < m < 20 \\ -\infty, & \text{otherwise,} \end{cases} \tag{4.29}$$

and

$$\ln\left(p(c)\right) = \begin{cases} 0.0, & \text{if } -10 < c < 30 \\ -\infty, & \text{otherwise,} \end{cases} \tag{4.30}$$

for the gradient, m, and the y-intercept, c, respectively. The widths of these uniform prior distributions were set to cover all possible values for these parameters.

With the model defined, it was then sampled using a python implementation of the *affine-invariant ensemble sampler for Markov-chain Monte-Carlo (MCMC)* method (EMCEE) defined in Foreman-Mackey et al. (2013) (Goodman & Weare 2010). The advantage of this algorithm over simpler MCMC algorithms, such as Metropolis–Hastings (Sivia & Skilling 2006), is that due to being affine-invariant, it will perform equally well under all linear transformations, such that it becomes insensitive to covariances in the parameters. As the gradient and y-intercept of a straight line are by definition highly correlated, this method performs a better inference within a much reduced computational time. The ensemble part of the method means that the sampling of the posterior distribution occurs multiply in parallel. The statistical model was sampled using this method with 1000 chains, each consisting of 10000 steps, including tuning. This is a larger set of samples than was used in the published work in Rodger et al. (2019). The larger number of samples reduces the variation in the output posterior distribution, so reflecting this improvement, the fitting parameters are quoted to a higher precision and thus the ranges presented in the results

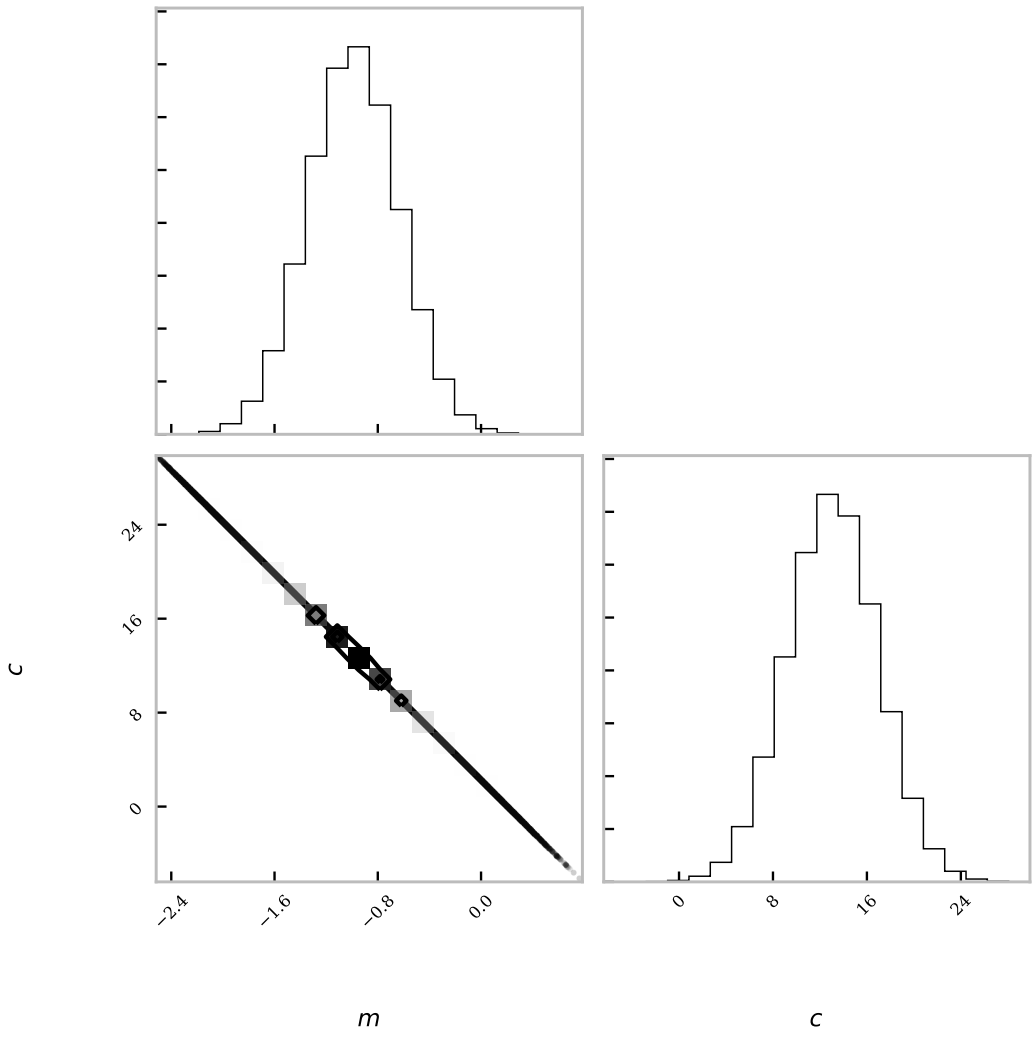

Figure 4.22: This corner plot shows the posterior probability distributions for the logarithmic spectral gradient, and y-intercept after sampling. The upper panel shows a representation of the normalised posterior probability distributions of the spectral gradient, m, whilst the right most panel shows the same for the y-intercept c. The bottom left panel shows a 2D histogram of the joint probability distribution of both parameters, the plot consists of both greyscale points and contours. This plot was produced using the python software package *corner.py* (Foreman-Mackey 2016)

are slightly narrower. Figure 4.22 shows the output probability distributions for the fitting parameters after the model was sampled. A subset of the sampled fits to the spectrum using

this method are displayed, alongside the observed enhancements, in Figure 4.21.

The first and simplest deduction from the spectrum made in Rodger et al. (2019) from Figure 4.21 was that, as the enhancement is positive, the electron temperature of the plasma must be greater than the brightness temperature of the background atmosphere. Within 90% confidence intervals, the posterior probability distribution for the spectral gradient was found to range between −1.57 and −0.41. This signifies that the optical thickness of the plasma likely lies within the transition between fully optically thin and optically thick material, as discussed in Section 4.3.1.3 and Figure 4.20. The confidence intervals were estimated using the percentile method. From the calculated posterior probability for the logarithmic spectral gradient, the optical thickness was then estimated by defining a diagnostic curve for the observation using Equation 4.24.

The multiplicative α correcting factor, dependent on the non-zero rate of change of the Gaunt factor across the frequency band, defined in Equation 4.19, was estimated as discussed in Section 4.2. This was done by finding the Gaunt factor and calculating its rate of change with respect to frequency for ALMA Band 3 at a wide range of temperatures ($T = 10^3 - 10^6$ K). The Gaunt factors used were interpolated from the table of calculated values from van Hoof et al. (2014) as discussed in Section 3.1. Without any prior knowledge of the temperature structure, it was assumed that all such potential temperatures were equally likely. This resulted in the minimum and maximum values for α being 1.04 and 1.09, respectively (Rodger & Labrosse 2018), see the curve for Band 3 in Figure 4.12.

As this observation was on the solar disk, it was also necessary to estimate the β factor defined in Equation 4.25. This required an estimate of the linear-scale gradient of the background brightness temperature spectrum. As the solar atmosphere is optically thick this will be defined by the temperature structure of the solar chromosphere where the millimetre-continuum is predominantly formed. Due to the current lack of absolute brightness temperature sub-band observations, this value had to be estimated using numerical modelling. This was done by adopting the 1D quiet-Sun atmospheric model C7 from Avrett & Loeser (2008) to provide an example continuum spectrum in ALMA Band 3. For this calculation a purely hydrogen plasma and a solely thermal bremsstrahlung emission mechanism were assumed. The absorption coefficient was calculated from the C7 data using Equation 3.5 (Dulk 1985). From this and using the temperature structure for the solar atmosphere defined in C7, the brightness temperature emitted across Band 3 was calculated using the integral defined in Equation 1.17. This method is similar to Heinzel & Avrett (2012) and Simões et al.

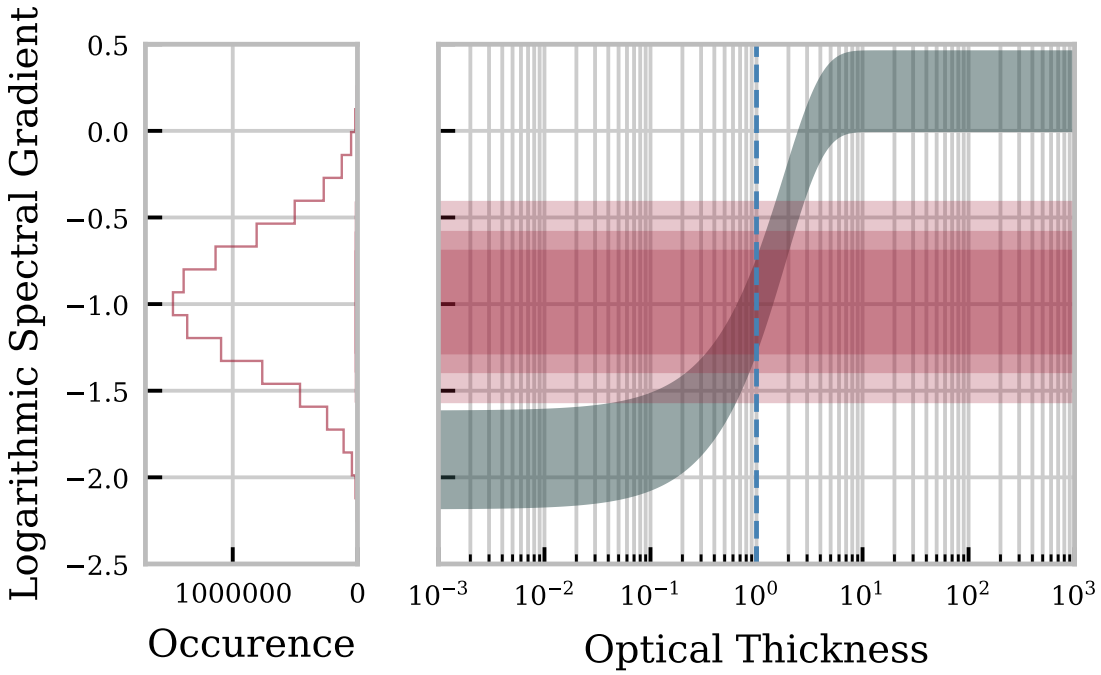

Figure 4.23: Relationship between the optical thickness and logarithmic-scale millimetre-continuum spectral gradient for the structure in Box 1 of Figure 4.15. The left panel shows a histogram of the MCMC sampled probability distribution for the spectral gradient. The red shaded regions represent the 90, 75, and 60% confidence intervals for the MCMC fitted observed logarithmic continuum enhancement gradient, calculated as shown in Figure 4.21. The right panel shows the region between the two diagnostic curves displaying the relationship between optical thickness and spectral gradient defined by Equation 4.24, and calculated for Box 1, in green. Where the red and green regions overlap represents the range of possible optical thicknesses for the structure given the observed data, the degree of confidence in the fitted spectral gradient and the assumptions made. The dashed blue line shows the location of the $\tau = 1$ line. This figure is adapted from a figure in Rodger et al. (2019), although is produced using a larger number of MCMC samples.

(2017). The linear-scale background spectral gradient for ALMA Band 3 found for the C7 atmosphere was calculated to be $\sim -9 \times 10^{-10}\,\mathrm{K\,Hz^{-1}}$.

From Equation 4.23, it can be seen that $(T - T_{\mathrm{B0}}(\nu))$ must always be $\geq E(\nu)$, therefore it was only necessary to evaluate the β term within the range of values $E(\nu) \leq (T - T_{\mathrm{B0}}(\nu)) \leq 10^{6}$, where the full-band ALMA Band 3 enhancement value for Box 1 (Table 4.1) was used for $E(\nu)$. This restriction in the range of $(T - T_{\mathrm{B0}}(\nu))$ values considered allowed for the avoidance

of the discontinuity found in Equation 4.25. Using this method the minimum and maximum for β were found to be ~ 0.00 and 0.46, respectively.

The diagnostic curves for the optical thickness of the enhancing plasma were made by taking the maximum and minimum values for the two factors; α and β with Equation 4.24. From this the optical thickness, or optical thickness regime, of the plasma was estimated through finding the positions where the distribution of the fitted spectral gradient intersects the diagnostic curves. The results from this method are presented in Figure 4.23. The maximum and minimum optical thickness of the stationary enhancement coincident with an XBP was inferred by using the regions where the 90% confidence logarithmic spectral gradient and the diagnostics curves overlapped in Figure 4.23 using the results of the Newton-Raphson method. Within 90% confidence, it was found that the optical thickness lies within the range $0.05 \leq \tau_{90\%} \leq 2.74$. Due to the finite number of samples in the MCMC process the maximum and minimum values are subject to some small change, which is of the order $\sim \pm 0.01$. These small fluctuations will thus have an affect on any further estimations, e.g. the electron density, made using these optical thickness limits.

The estimated optical thickness of the plasma in Box 1, within 90% confidence, is partially greater than 1, however, it is not high enough to be in the regime where the brightness temperature may be used as a direct analog of the electron temperature, which from isothermal-isobaric prominence models is expected to be around $\sim$ 4–5, see Figure 2.9. It is possible, however, to estimate the difference between the electron temperature of the plasma and the background brightness temperature ($T - T_{B0}$) using the optical thickness confidence intervals and Equation 4.23. Using this estimation, the temperature difference is calculated to be within the range $170 \leq T - T_{B0} \leq 3010$ K. If the background brightness temperature for Band 3 emission is assumed to be similar to the typical value of $\approx 7300 \pm 100$ K quoted for quiet Sun observations in White et al. (2017), this would result in an expected electron temperature for the plasma in Box 1 of between $\approx 7370 - 10410$ K. To test this assumption the ALMA single-dish images taken during this observation were used to check that the White et al. (2017) quoted value for the typical millimetre-continuum background value in Band 3 was an applicable value to use for this study. If the plasma had the maximum or minimum possible optical thicknesses, as estimated using our method, the expected maximum charge squared weighted ion-electron emission measure would be in the range $\sim 0.09 - 3{\times}10^{29}\,\mathrm{cm}^{-5}$, following Equation 4.9.

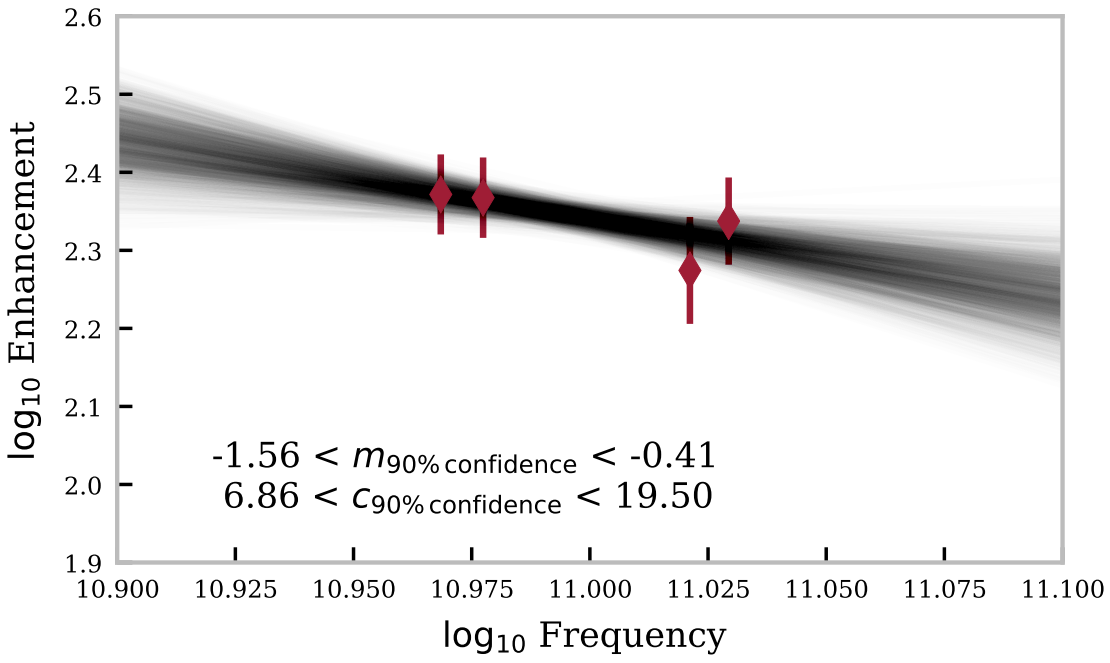

Figure 4.24: Same as in Figure 4.21 for the moving plasmoid ejection observed in Box 2 of Figure 4.15. This figure is adapted from a figure in Rodger et al. (2019), although, is produced using a larger number of MCMC samples, the fitting parameters are quoted to a higher precision.

4.3.2.2 Analysis of Box 2: Moving Plasmoid Ejection

The moving enhancement caused by the plasmoid ejection observed in Box 2 was analysed using the same method outlined previously for Box 1 in section 4.3.2.1. A subset of the MCMC fitted continuum brightness temperature enhancement spectra for Box 2, including the 90% confidence interval results for the two fitting parameters, are presented in Figure 4.24, whilst the corner plot showing the resultant posterior probability distributions for the two fitting parameters is shown in Figure 4.25. Once again, the first noticeable indicator for the plasma conditions is that, as the enhancement is positive and the gradient of the spectrum is negative, the temperature of the structure must be greater than the background brightness temperature value, and that the plasma is either optically thin or near the transition to optically thick.

The optical thickness diagnostic curves (Equation 4.24) were created for Box 2 using the same method as described in Section 4.3.2.1. The same bounds for the α factor were used here as were used for Box 1, whilst bounds for the β factor are slightly different at

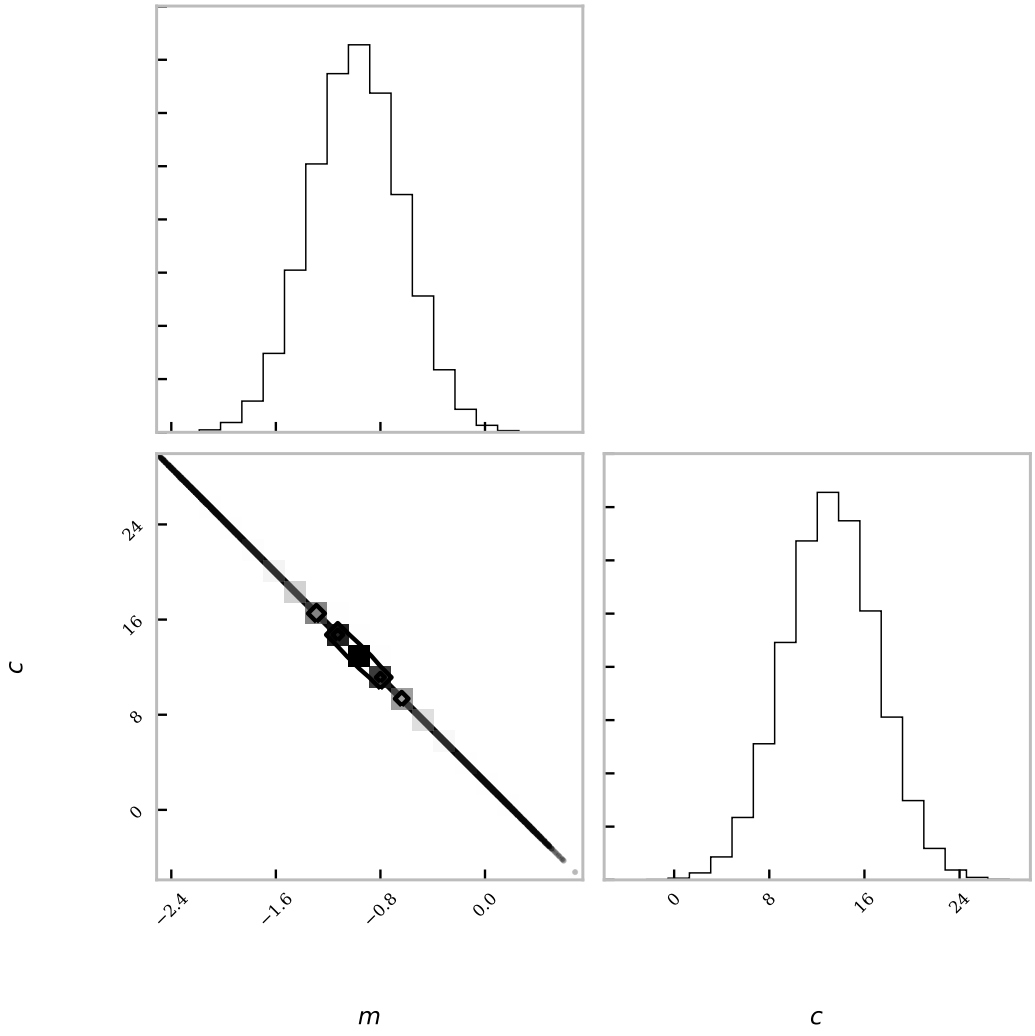

Figure 4.25: Same as given in Figure 4.22, however, for the moving plasmoid ejection observed in Box 2 of Figure 4.15. This plot was produced using the python software package *corner.py* (Foreman-Mackey 2016)

$\sim 0.00 - 0.37$, due to the difference in the enhancements at the central frequency of Band 3. The plots showing the diagnostic curve and the 90% confidence interval estimates for the spectral gradient for Box 2 is shown in figure 4.26. The regions where the 90% confidence interval logarithmic spectral gradient and the diagnostic curve overlap were found and the optical thickness for Box 2 was estimated using the Newton-Raphson method. It was found that the optical thickness of the moving plasmoid is expected to range between 0.15 and

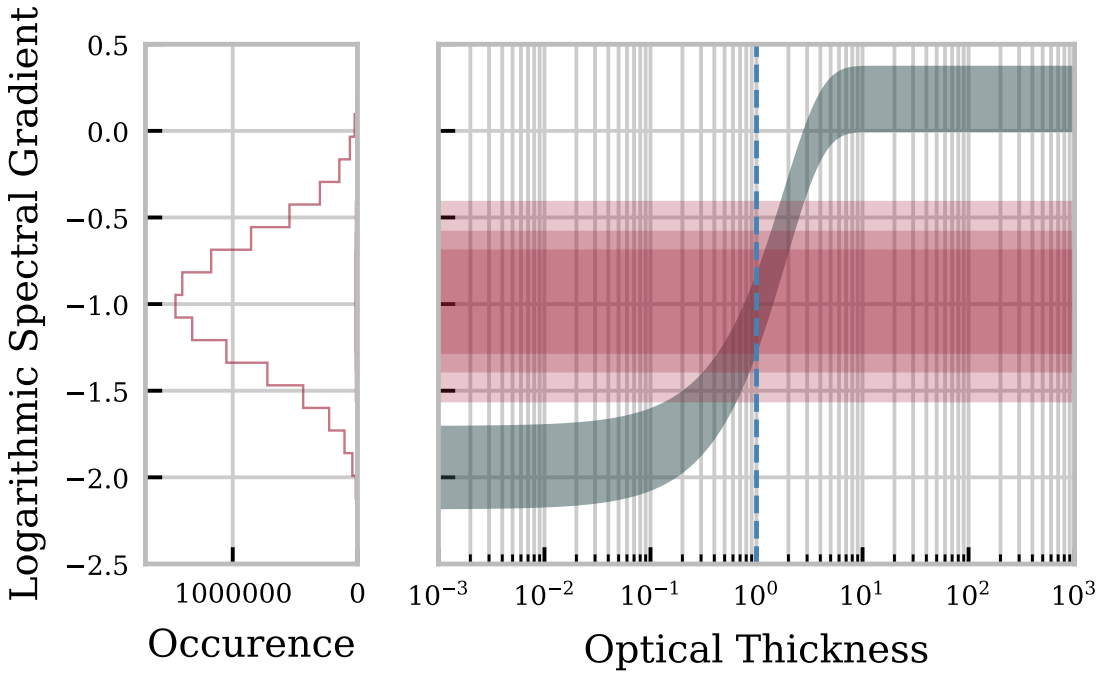

Figure 4.26: Same as given in Figure 4.23, although for the moving plasmoid ejection observed in Box 2 of Figure 4.15. This figure is adapted from a figure in Rodger & Labrosse (2018), although, it is produced using a larger number of MCMC samples.

2.74. Therefore, the plasmoid also lies within the region between fully optically thick and optically thin material. Again, due to the finite number of MCMC samples, these optical thickness limits may vary by $\sim \pm 0.01$, and therefore all subsequent estimations using these limits are similarly affected. Using the brightness temperature enhancement at band centre, this optical thickness range would result in a temperature difference between the plasma and the background brightness temperature ($T - T_{B0}$) of 240 – 1610 K.

In the same manner as used in the previous section further plasma properties such as the temperature and the emission measure were estimated. If again a typical background brightness temperature of 7300 ± 100 K (White et al. 2017) is assumed, the electron temperature of the plasma would be expected to range from 7440 – 9010 K. The maximum charge squared weighted ion-electron emission measure for this plasma would be estimated to range from $\sim 0.2 - 3 \times 10^{29}\,\mathrm{cm}^{-5}$, when using the estimated temperature and optical thickness. The electron density was then estimated by assuming that the width of the plasmoid on the disk ($\sim 4'' \approx 3000$ km) was approximately equal to the LOS length. This resulted in an estimated electron density ranging between $0.8 - 3 \times 10^{10}\,\mathrm{cm}^{-5}$.

In Shimojo et al. (2017b) the authors concluded that the moving plasmoid was roughly consistent with either an isothermal $\approx 10^5$ K plasma that is optically thin at 100 GHz (density of $\approx 10^9$ cm^{-3}), or a cool optically thick plasma core of temperature $\approx 10^4$ K and density $\geq 2 \times 10^{10}$ cm^{-3}. Whilst the results of this analysis (Rodger et al. 2019) more closely follow the Shimojo et al. (2017b) case where the plasma in the moving ejection is cool and optically thick, the estimated optical thickness quoted here suggests that it could lie somewhere across the transition from optically thin to optically thick material.

4.3.3 Discussion

In this case study I have presented the work originally published in Rodger et al. (2019). I have shown how the logarithmic spectral gradient of the millimetre brightness temperature continuum may be used as a diagnostic of the optical thickness of the emitting plasma. The plasma in consideration was viewed on-disk, and thus had more complications to the radiative transfer considerations than the simpler off-limb equivalent. There were also several assumptions made in this study which are required so that a suitable estimation could be made. For example, the equations used throughout this analysis were derived assuming an isothermal LOS through the enhancing plasma. It is possible that the objects observed in either Boxes 1, or 2 were in some way multi-thermal, however, in Rodger & Labrosse (2018) (Section 4.2) it was found that the isothermal assumption in the relationship between logarithmic spectral gradient and optical thickness holds well for a multi-thermal plasma with optical thicknesses ≤ 1. Beyond the $\tau = 1$ the logarithmic spectral gradient relationship with optical thickness is expected to deviate from the isothermal case increasingly with increasing optical thickness. In such a case the estimated optical thickness for a multi-thermal plasma passed the $\tau = 1$ line could be expected to be under-estimated compared to its true value. From this analysis it was found that both observational boxes have optical thicknesses around the $\tau = 1$ line, where the expected relationship derived under the isothermal assumption should mostly agree with a multi-thermal case.

A source of uncertainty not considered within the scope of this analysis was the gradient of the background brightness temperature spectrum. Estimating this value was necessary for the calculation of the β factor in Equation 4.24. Due to the lack of published results on the spectral gradient of the Band 3 millimetre-continuum, it was necessary to estimate this value using brightness temperature spectrum produced from a numerical model. The numerical model chosen for this calculation was the 1D atmospheric Quiet-Sun model C7 of Avrett &

Loeser (2008). At the time of this study it was not known how good an approximation this method produced as, as White et al. (2017) states, atmospheric models tend to underestimate the brightness temperature value compared to the typical observed values. It was also unknown to what degree the spectral gradient is affected by the small scale temperature structure of the solar chromosphere, e.g. the variation across the network and internetwork cells, and how much this variation changes across the solar disk. If this method of analysis were to be repeated in a future study, i.e. when the uncertainties on absolute brightness temperatures are better understood, it will likely be beneficial to observe the background spectral gradient directly from the feathered total-power and interferometric ALMA data. A similar assumption was made in the estimation of the emission measure and the temperature of the plasma structures, i.e. assuming the typical ALMA Band 3 background brightness temperature of 7300 ± 100 suggested by White et al. (2017). Similarly, improved knowledge of this value shall be addressed through future absolute brightness temperature observations.

The largest source of uncertainty to the data which is considered in this study is the accuracy limit to the flux scale determination. As this uncertainty is a limit suggested from the combination of several different uncertainty sources in the calibration of the data, if the distribution of this uncertainty source would become smaller, or better understood in future ALMA cycles, this would greatly improve the width of the estimations made using this diagnostic method. Warmels et al. (2018) also states that this source of uncertainty is expected to increase with increasing frequency, such that, once lower frequency ALMA Bands (Bands 1 and 2) become available to solar observations, they may provide a more suitable wavelength range for this technique. Future efforts to determine the slope of the logarithmic millimetre continuum could also be improved through the additional sampling of the brightness temperature across a wider range of frequencies.

4.4 Conclusions

In this chapter I have discussed and presented methods for the estimation of the millimetre-continuum optical thickness using multiple wavelength/frequency observations of the millimetre brightness temperature. In Section 4.1 I began by considering the ratio of two brightness temperature measurements of the same LOS at different observing wavelengths (Rodger & Labrosse 2017). It was found that for an idealised, noiseless, isothermal plasma this method produced excellent results for both the estimation of the LOS optical thickness,

but also its emission measure. As this method becomes asymptotically more sensitive to variation in uncertainty of the brightness temperature ratio once the plasma becomes optically thick ($\tau > 1$), it was found that this method was better suited for optically thin plasmas. Higher frequency observations, such as observed with Band 6, are more likely to be optically thin than lower frequency measurements (Band 3). The method presented in Section 4.1 does, however, have the disadvantage that it requires an estimation of the temperature for the LOS. When testing multi-thermal prominence models, different representative temperatures were used: the mean, electron density weighted mean, and electron density squared weighted mean temperatures. It was found that the electron density squared weighted mean temperature produced the closest estimations for the optical thickness. Whilst, for optically thin LOSs the representative temperatures chosen could cause either an underestimation or overestimation of the optical thickness depending on the location within the FOV. In models with optically thick LOSs, however, it was found that this method could not successfully estimate the optical thickness when it was greater than 1.

In Section 4.2 I derived the relationship between the spectral gradient of the millimetre-continuum and the optical thickness of the plasma in the millimetre-continuum, for both logarithmic-, and linear-scale spectra (Rodger & Labrosse 2018). It was found that the logarithmic-scale spectral gradient and the optical thickness of the plasma provided a very simple relationship for the isothermal case, where it is only dependent on the optical thickness, and a multiplicative factor (α) depending on the rate of change of the Gaunt factor with frequency. This derived expression was tested against both isothermal and multi-thermal prominence models. It was found, with estimation of the α factor, that the spectral gradient is a clear indicator of the optical thickness regime of an isothermal plasma, and that within the range $\sim 10^{-1} \leq \tau \leq 10^{1}$ the optical thickness can be estimated directly from the logarithmic spectral gradient. The results from multi-thermal models were somewhat more complicated as passed $\tau = 1$ the logarithmic spectral gradient becomes increasingly dependent on the temperature structure of the regions of formation for millimetre-continuum within the model. Below $\tau = 1$, however, multi-thermal models proved to act similarly to isothermal models, such that the logarithmic spectral gradient acts as a clear indicator of the optical thickness regime and the optical thickness itself for $\sim 10^{-1} \leq \tau \leq 10^{0}$.

Finally, in section 4.3 I presented a case study for the use of the logarithmic-scale millimetre-continuum spectral gradient as a diagnostic of an on-disk brightness temperature enhancement and plasma ejection observed in an ALMA science-verification (SV) observ-

ing campaign. This work, previously published in Rodger et al. (2019), used an on-disk extension of the theory for the spectral gradient derived for off-limb plasma in Section 4.2 and presented the first sub-band spectral analysis of an ALMA solar observation. From this analysis it was proved that sub-band analysis of the logarithmic millimetre-continuum spectrum can provide a powerful technique for diagnosing plasma optical thickness, and thus other plasma parameters such as electron temperature and emission measure, provided that suitable uncertainties are defined and necessary assumptions are made. The ALMA observation was conducted in Band 3 on the 17th of December 2015 and contained two regions with temporally enhanced brightness temperatures; one associated with an X-ray Bright Point (XBP), and the other with a plasmoid ejection event. The observed logarithmic brightness temperature enhancement was fitted using a bayesian linear regression method to find the posterior probability distribution for the spectral gradient. The results presented in this chapter used an increased number of samples compared to those used in Rodger et al. (2019), this allowed the values for the spectral gradient to be quoted at higher precision, and thus the estimated plasma properties are given over narrower ranges. The 90% confidence regions for this distribution were then compared to the expected spectral gradient versus optical thickness curve. A width for the curve was designed for an ALMA Band 3 observation by considering an on-disk structure of given band-centre brightness temperature enhancement, over a large range of possible temperatures. Using this method it was found that the optical thickness of the stationary enhancement was between 0.05–2.74, whilst the moving enhancement had 0.15–2.74, thus both lying entirely within the transition region between optically thin and fully optically thick plasma. If a typical quiet Sun background brightness temperature of 7300 ± 100 K (White et al. 2017) is assumed the electron temperature for the stationary enhancement would be expected to be in the range $\sim$ 7370–10410 K and between $\sim$ 7440–9010 K for the moving plasmoid enhancement. The analysis presented here for the moving plasmoid feature was compared to the results given in Shimojo et al. (2017b), and it was found that it supports better the case presented by Shimojo et al. (2017b) where the structure has a cool core of $\approx 10^4$ K with density of $\geq 2 \times 10^{10}$ cm^{-3} against the option of a fully optically thin plasmoid with a temperature of $\approx 10^5$ K and a density of $\approx 10^9$ cm^{-3}.

Chapter 5

The First High Resolution Interferometric Observation of a Solar Prominence Using ALMA

In this chapter I present preliminary results from the first observation of a solar prominence using the high resolution interferometric imaging of ALMA. The ALMA observation was coordinated with measurements using both space- and ground-based instruments, including: AIA, ground-based Hα spectral imaging, and IRIS. In this section I will cover: the data reduction performed to construct the ALMA Band 3 time-averaged images for each full observing block; an analysis of the integrated intensity of the coordinated Hα observation to estimate the millimetre-continuum optical thickness as discussed in Chapter 3; and a pixel by pixel analysis of the correlation between an ALMA image and co-temporal imaging from the various AIA filters. Analysis of the UV imaging using IRIS and a discussion into the coordinated view of the prominence dynamics from different wavelengths and viewing angles will be given in a future publication, Labrosse et al. (In Prep).

Section 5.1 covers descriptions of the observations and data-reduction procedures for the coordinated observations of ALMA, ground-based Hα, and AIA. Whilst Section 5.2 presents the preliminary brightness temperature results, a millimetre optical thickness diagnostic using the Hα integrated intensity, as well as a discussion into the prominence morphology observed in ALMA compared to Hα and co-aligned imaging with each of the AIA bands. Finally, Section 5.3 presents the conclusions of this work so far, as well as discussing some of the additional analysis which could be conducted using this data set.

5.1 Observations and Data Reduction

5.1.1 ALMA Band 3

ALMA observed off the solar limb, near the heliocentric coordinates (+650″, −750″), between 15 : 20 and 17 : 45 UTC on the 19th of April 2018. The mode of operation planned for this observation was a mosaic with a proposed total field of view (FOV) of 40″ by 80″. This FOV was produced through cycling through a total of 5 pointings, each with a smaller FOV determined by the observing wavelength and array configuration. In this case the observing band was band 3 (84–116 GHz) and the array configuration was C43-3, the largest possible array configuration available for solar physics at the time of this observation. This was chosen because the longer the widest baseline between antennas in the array, the higher the resolution in the resulting images produced by the observation.

The ALMA observation of the prominence was split into two main observing blocks; the first observing the Sun from 15 : 38 – 16 : 32 (Block 1) and the second from 16 : 51 – 17 : 45 (Block 2). Within each of these main blocks ALMA conducted 7 scans of the total solar FOV, with off-target calibration occurring between each scan. The average time taken for each scan was ∼ 6 minutes.

Issues with the system temperature were found from some of the antennas where their XX and YY polarisations were too large resulting in very large estimates for the noise in the synthesised images[1]. To combat this, the problem antennas were identified, which included 8 antennas for Block 1 and 10 for Block 2, which were subsequently removed from the image synthesis. Whilst the reliability of the data is improved by removing the antennas, the resolution suffers somewhat due to the reduction in overall baseline number.

5.1.1.1 Image Synthesis and Cleaning

For every image produced from an interferometer a deconvolution algorithm must be used to find the true image from the imperfectly sampled visibility data, see Section 1.4. For this process the *Common Astronomical Software Applications* (CASA) program tclean() is used.

[1] The reason for these differences in the XX and YY data, according to the ALMA helpdesk is: when using the mixer detuning mode, the receiver temperature dominates the system temperature. Hence the difference between the XX and YY system temperatures is caused by the difference in the receiver temperature. Because the bias voltage of the mixer detuning mode is not optimized for the balance between XX and YY, there is a possibility of a dis-balance between the receiver temperatures of XX and YY.

This is a parallelized version of the older CASA clean() routine. When using clean() a *clean box* would often be defined for which the deconvolution algorithm would work on. It would be expected that the clean box would have a primary beam coverage during the observation which was sufficiently good that the data within it could be trusted. Clean() would then work on that box solely, ignoring the less reliable data outwith it. The tclean() routine is somewhat more sophisticated than this, and rather than requiring a pre-defined clean box calculates itself the regions with good primary beam coverage, thus choosing which regions in the observation meet a certain minimal threshold for coverage. The default minimum threshold for the primary beam coverage used in this study was 0.2 primary beam gain level. This process, while more efficient, does result in non-standard, irregular dimensions for the resulting ALMA images.

The particular deconvolution algorithm which I used for this data set was the multiscale extension to the CLEAN algorithm (Högbom 1974) presented in Cornwell (2008). The CLEAN algorithm of Högbom (1974) is the most widely used deconvolution algorithm and works well for point sources and collections of point sources. However, as stated in Cornwell (2008) the algorithms performance for use on extended objects can be improved using a multiscale approach. The multiscale CLEAN algorithm of Cornwell (2008) works simultaneously on a range of specified spatial scales. Because of the improved performance of multiscale CLEAN it was the chosen deconvolution algorithm for image synthesis throughout this study.

Despite the improvements presented by tclean(), the process of cleaning the data for each image can still be quite time intensive unless running the program across a large number of cores. Due to this and the need to tune the particular tclean() parameters, as a first look into how the prominence appears in the millimetre-continuum a time-averaged image was produced for both observations in Blocks 1 and 2. The purpose of running deconvolution algorithms on interferometric data is essential to solve for the gaps in the u-v plane produced by having a finite number of baselines in the array. A satisfactory image is produced by iteratively producing a solution for the image to reduce the maximum of the residual image within the FOV. The residual image is the difference between the "Dirty image" and the solution for the cleaned image convolved with the point spread function, i.e.:

$$\text{residual} = I^D - B * I^C, \tag{5.1}$$

where I^C is the solution for the cleaned image (Cornwell 2008).

Tuning the tclean() parameters turned out to be quite time consuming, as the default

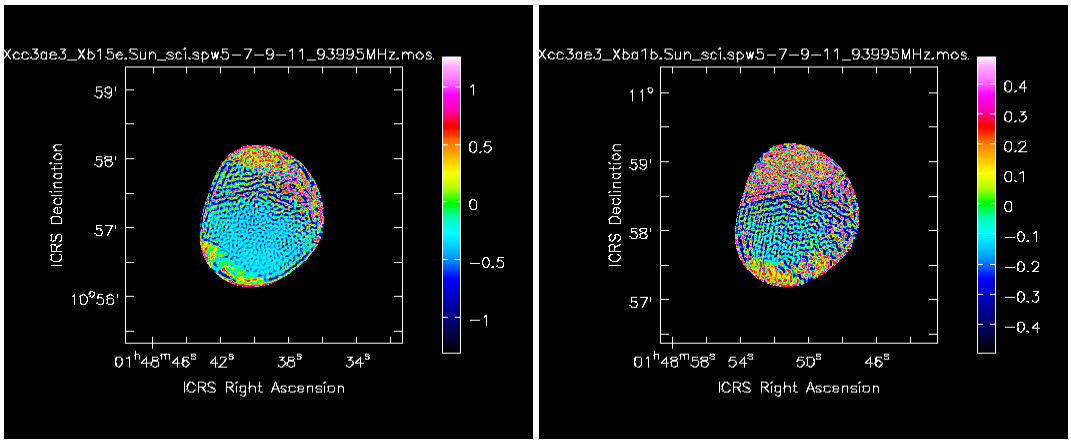

(a) Block 1 **(b)** Block 2

Figure 5.1: Residual images for synthesised ALMA interferometric prominence observation produced using default parameters, before tuning tclean() parameters and before removal of all antennas with too large XX/YY system temperature ratio. The default parameters are given in Table 5.1.

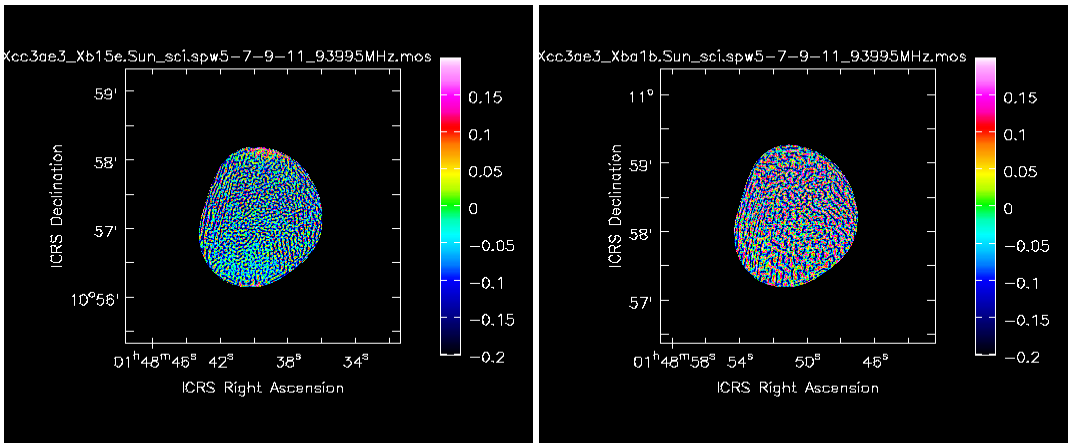

(a) Block 1 **(b)** Block 2

Figure 5.2: Residual images for synthesised ALMA interferometric prominence observation produced after tuning tclean() parameters and removal of all antennas with too large XX/YY system temperature ratio. Parameters used in tclean() summarised in Table 5.1.

parameters did not manage to produce satisfactory residual images, see the residual images Figure 5.1. These residuals show distinct structures across the FOV, suggesting that the deconvolution was not fully successful. This may be due to the algorithm finding the solution

Parameter	Block 1	Block 2	Default
maximum iterations	1.2×10^6	1.2×10^6	1.0×10^5
scales (pixels)	{0,7,21}	{0,7,21,42}	{0,7,21}
residual threshold (Jy)	0.2	0.2	0.3

Table 5.1: Parameters used in multiscale version of tclean() for observations during Blocks 1 and 2. The default values used to produce the residual images are given in Figure 5.1.

difficult due to the shape of the solar limb, as it appears somewhat step-function like. In an attempt to improve how the algorithm ran, tclean() was tested using different parameters including lower thresholds for the maximum residual in the dataset and increased numbers of iterations. The best results found using tclean() were with the total number of iterations equal to 1.2×10^6 and the threshold for the maximum residual set at 0.2Jy, where 1Jy = $10^{-26}\mathrm{Wm^{-2}Hz^{-1}}$ or $10^{-23}\mathrm{erg\,s^{-1}cm^{-2}Hz^{-1}}$. For both deconvolutions the maximum residual threshold was reached before the total number of iterations. The image synthesis in Block 2 was found to be improved by using an increased number of the spatial scales considered by the multiscale CLEAN. This, however, did not work for Block 1 as the algorithm failed to find a solution in this case. A summary of the tclean() parameters used for the image synthesis is given in Table 5.1. The resultant cleaned interferometric images for the full-observation time range are shown in Figure 5.3, with the residuals of both image shown in Figure 5.2.

It can be seen from Figures 5.2 and 5.1 that the new parameters used in Table 5.1 have performed better than the default values. This is because the maximum residuals in the images are significantly lower, as well as the images presenting a significant reduction in observable structure. The deconvolution has performed better in the Block 2 observation than Block 1 as there is some small remaining structure in the residual image of Block 1. From this deconvolution, the resulting interferometric synthesised images of the prominence observed on the 19th of April 2018 are presented in Figure 5.3.

5.1.1.2 Feathering Interferometric and Total Power Images

Interferometric images on their own do not present absolute brightness temperatures, but rather relative brightness temperature values around some background value determined by the largest spatial scales. Because of the finite minimum separation between antennas it is impossible to sample the u-v plane at these scales. To produce absolute brightness

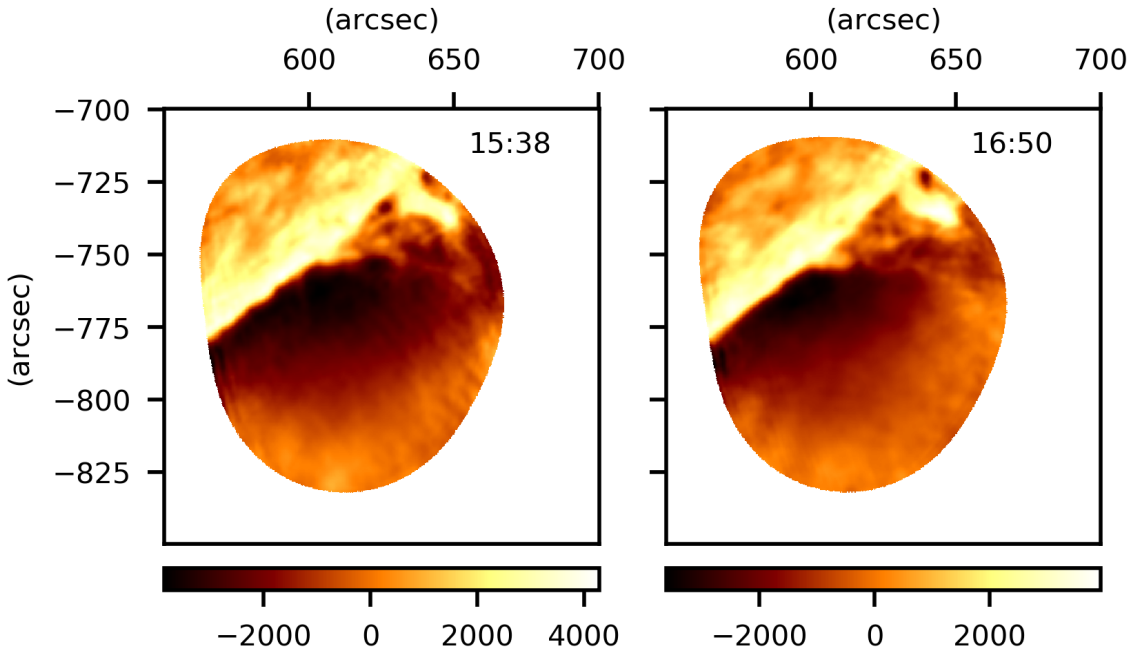

Figure 5.3: Synthesised interferometric images for the prominence observation with ALMA on the 19th of April 2018. Each image is produced over a time-range spanning an entire observing block, with the start time of each observation given in the image titles. The axes are in heliocentric coordinates, whilst the colorbars are in Kelvin.

temperature images the interferometric images must be combined with single dish images to provide measurements of the total flux in the image (Koda et al. 2011). The process currently used by ALMA is to combine the interferometric and the single dish measurements from the Total Power (TP) array is called "feathering". Feathering involves combining two images together through the weighted sum of the Fourier transform components in the *uv*-plane. This will also provide the low spatial resolution component of the image due to the limitations in the shortest possible baseline in the interferometer array. Across the entire observation ALMA conducted a total 14 observing scans of the entire solar disc, each taking ~ 10 minutes. The method for TP full-disc observation is described in White et al. (2017). For each interferometric synthesised image a corresponding TP image was chosen to feather with it to produce an absolute brightness temperature image. The choice of corresponding TP image was chosen by either having the longest period of co-temporal observation, or if that was not possible, the shortest difference in time between it and the synthesised interferometric image.

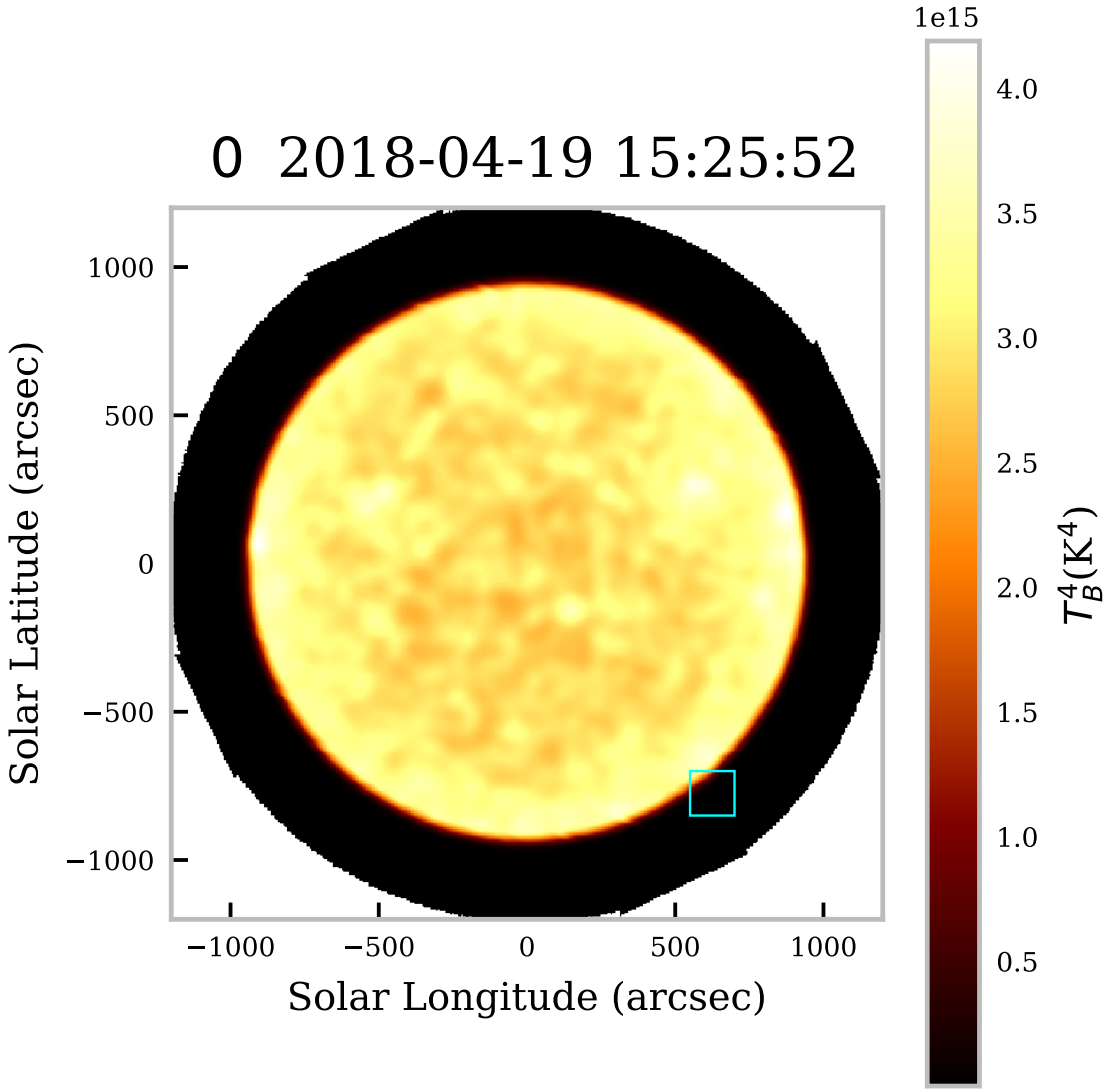

Figure 5.4: Total power image of the whole solar disk in ALMA Band 3. The brightness temperature is scaled to T_B^4 to improve contrast. The cyan box shows the location of the high resolution ALMA interferometric FOV.

Figure 5.4 presents an example of one of the full-disk images produced from ALMA's TP array at the start of the observation. The map is scaled to T_B^4 to improve the contrast of the image. The box highlighted in cyan at the bottom right of the image shows the location within which the interferometer array constructed the high resolution mosaic FOV as seen in Figure 5.3. The prominence, whilst clearly observed in the high resolution image, is unresolved in the lower resolution TP map.

Each TP image is produced for a single sub-band within Band 3, in the case of Figure 5.4 the sub-band used is spw 1. Because of this, feathered images across the whole of Band 3 must be feathered with a TP image at a single sub-band. As the TP maps are by default produced in spw 1, which is one of the two central sub-bands within the Band 3, this sub-band was used throughout all feathered images.

In the feathering process there is a weighting factor known as the "sdfactor" which determines how to scale the single-dish flux to the interferometric data. Attempts were made using the interactive CASAfeather task to tune the sdfactor such that the flux in the dirty image convolved with the low resolution TP image matched the flux of the TP image convolved with the high resolution interferometric image. These attempts have been so far unsuccessful, therefore the feathered images presented later in this section are produced with a default sdfactor of 1 and can only be considered as preliminary results.

5.1.2 Hα

A coordinated ground-based observation was conducted to find the Hα line intensities using the MSDP telescope at Białkow in Poland by Dr K. Radziszewski. The observation consisted of 739 scans and was taken between 10 : 02 and 15 : 54 UTC on the 19th of April 2018. In this study I am only investigating a singular scan from this observation with the aim to gain an estimation of the optical thickness of the Band 3 emission. The scan in question was taken between 15 : 35 : 08 and 15 : 35 : 24 UTC, which is roughly 3 minutes before the start of the first ALMA observation. The data in this scan has been calibrated and the contribution to the intensity from scattered light has been subtracted by Prof P. Rudawy. This particular scan was chosen due to poor seeing being present in later scans, creating a smearing effect on the images. An image of the prominence at the line-centre of Hα, with the disk masked and the intensities converted from DNS to erg s^{-1}cm^{-2}sr^{-1}Å^{-1}, is shown in Figure 5.5.

5.1.3 AIA

In Section 5.2.3 I compare the image of the prominence synthesised with ALMA in Band 3 (100GHz) across observing Block 2 (16 : 50–17 : 44) to simultaneously observed imaging from the *Atmospheric Imaging Array* (AIA) on board the *Solar Dynamics Observatory* (SDO) (Lemen et al. 2012). The aim of this was to compare the morphology of the prominence in the millimetre-continuum to the various AIA bands which are each produced at different layers within the solar atmosphere, as well as investigating any potential correlation between

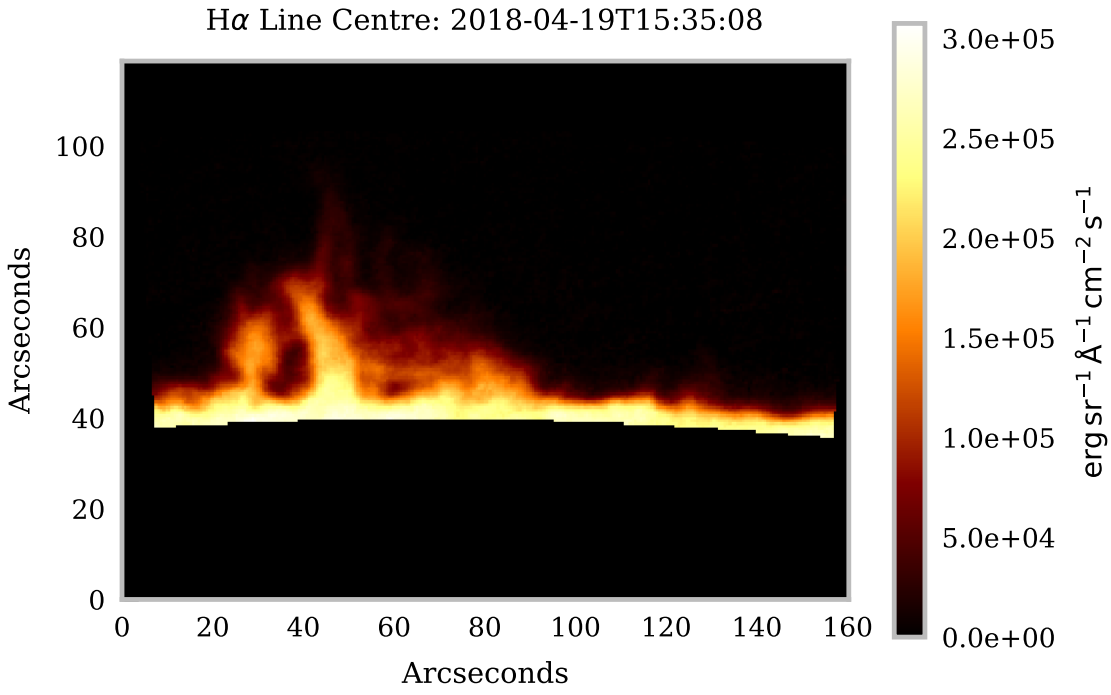

Figure 5.5: Image of the 19th of April prominence taken in the line centre of Hα between 15 : 35 : 08 and 15 : 35 : 24 UTC using the MSDP telescope at Białkow, Poland.

the brightness temperatures and intensities observed. To do this I downloaded all the data observed by AIA in each band within the time-range considered in Block 2. These images were then calibrated using standard *AIAprep* routines using IDL. As the ALMA image for Block 2 is time-averaged, much small scale motions will be undetectable. To allow for direct comparison with this ALMA image and the prepped AIA images, the AIA images were too averaged over the full time range. In AIA bands where the prominence is faint, or there was a low SNR, this time-averaging produced a more distinct view of the prominence to compare to the ALMA image. Bands where the signal was strong, e.g. 304Å, were also averaged with respect to time so that any time-dependent fine structure will be unresolved in a similar manner to the lower temporal resolution ALMA image.

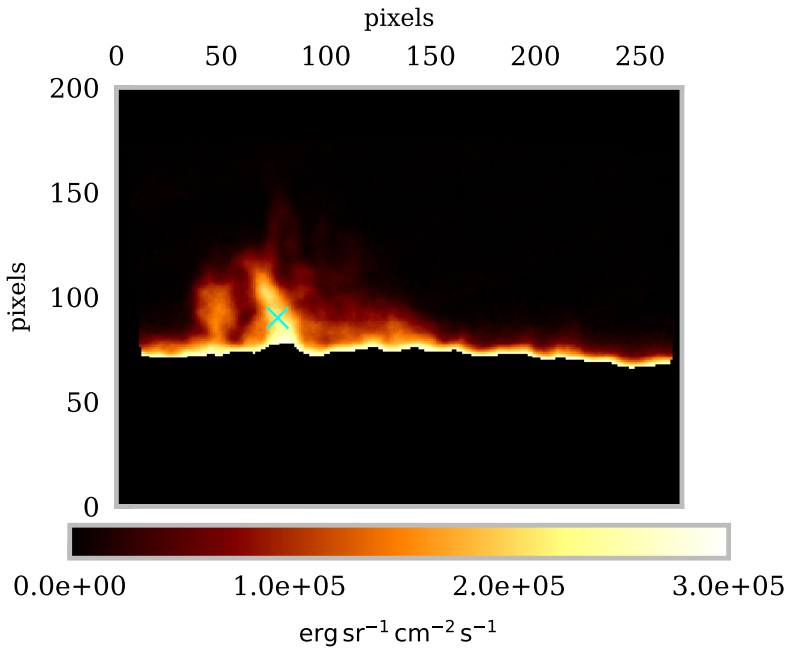

Figure 5.6: Image of the prominence FOV in Hα integrated intensity observed by the MSDP in Białkow and produced from the scan taken between 15 : 35 : 08 and 15 : 35 : 24 UTC. The cyan cross marks the pixel which is used for the intensity at the centre of the prominence in Figure 5.9. To improve contrast, solar disk pixels with intensities over $3\times10^5\,\mathrm{erg\,s^{-1}cm^{-2}sr^{-1}}$ are masked with zeros.

5.2 Results and Analysis

5.2.1 Hα Integrated Intensity and the Millimetre Optical Thickness

Using the method investigated in Section 3.3.1 of Chapter 3 I have used the coordinated Hα spectral imaging of the 19th of April 2018 prominence observation to estimate the optical thickness of the prominence in ALMA Band 3 emission. The first step in doing this was to calculate the integrated intensity in the image from across the Hα line profile. The MSDP telescope measured the intensity at 23 different wavelengths ranging from –1.1Å to +1.1Å from the line-centre. An image of the integrated Hα intensity from the parts of the MSDP FOV where the prominence is observed is shown in Figure 5.6. Bright solar limb pixels with intensities greater than $3\times10^5\mathrm{erg\,s^{-1}cm^{-2}sr^{-1}}$ are masked in this image.

The optical thickness of the millimetre-continuum is related to the integrated intensity of

the Hα line for an isothermal LOS through Equation 3.9, which for ease I shall repeat here:

$$\tau_\nu \approx 4.55 \times 10^{17} g_{\rm ff} e^{-17534/T} E(\mathrm{H}_\alpha)/(\nu^2 b_3(T)).$$

Any optical thickness estimation using this expression will thus be effected by variation of a constant temperature for the LOS through the proportionality:

$$\tau_\nu \propto g_{\rm ff}(\nu, T) f(T),$$

where $f(T)$ is defined:

$$f(T) = \frac{e^{-17534/T}}{b_3(T)}. \tag{5.2}$$

In Heinzel et al. (2015a) the authors use 3 values for the $f(T)$ factor calculated using 1D prominence models at constant temperatures of 6000, 8000 and 10000K. These values, multiplied by the respective Gaunt factor as interpolated from the calculations of van Hoof et al. (2014) are shown on Figure 5.7. This figure also plots the same values as calculated from the 2D C2D2E isothermal models of Table 3.1 and multi-thermal PCTR models of Table 2.2. It can be seen that the values used in Heinzel et al. (2015a) agree well with the values from the 2D isothermal and multi-thermal models of similar temperatures, with the spread seen in the 2D models caused by the density variation and the non-uniform incident radiation. The temperature variation of the optical thickness estimation using Hα integrated intensity ($g_{\rm ff}(\nu, T) f(T)$) can be seen to be fairly stable around ≈ 0.25 for low temperatures, with values greater that 0.5 only being observed frequently for models with temperatures greater than 20000K.

As Equation 3.9 requires an isothermal assumption and thus singular values for $g_{\rm ff}(\nu, T) f(T)$ it was decided to use the values as quoted in Heinzel et al. (2015a) as they were proven to be in line with the results of the C2D2E models. From the resulting estimation, the optical thickness and brightness temperature (also calculated as for an isothermal plasma) FOV are shown for each of 6000, 8000 and 10000 constant temperature plasmas in Figure 5.8.

From Figure 5.8, it can be seen that if the observed prominence were to have a constant temperature between 6000 and 10000K, the optical thickness of the millimetre-continuum should lie between ≈ 1 and 3, with the value at the centre of the prominence spine (cyan cross) at ≈ 2. However, an optical thickness of 2 has been shown to be too low to make a direct electron temperature diagnostic from the millimetre-continuum brightness temperature for isothermal prominence models, see Figure 2.9.

If the temperature of the plasma is higher than the 10000K considered here, which is perhaps unlikely due to the intensities observed in the Hα emission, the optical thickness

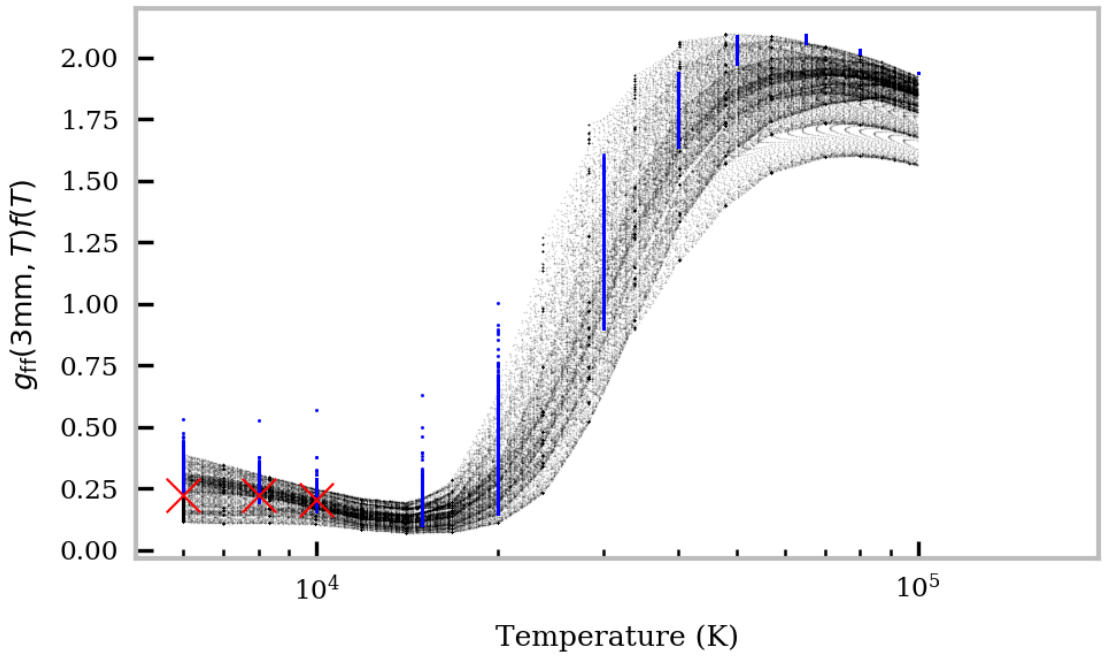

Figure 5.7: Relationship between the Gaunt factor multiplied by the f factor (Equation 5.2) versus temperature. The blue dots show the values as calculated from C2D2E using isothermal-isobaric models from Table 3.1, whilst the black dots show the same for multi-thermal PCTR models from Table 2.2. The red crosses show the values from 1D isothermal models as used in Heinzel et al. (2015a).

of the millimetre-continuum could be higher due to an increased magnitude of the f factor (Figure 5.7). For these cases I show the effect on the optical thickness at the centre of the prominence (pixel highlighted in cyan on Figure 5.6) with increasing $g_{ff}(\nu, T)f(T)$ in Figure 5.9. The values used for $g_{ff}(\nu, T)f(T)$ range up to 0.5 which covers the majority of temperatures up to 20000K within the isothermal and multi-thermal models of Figure 5.7. This shows that, even for the unlikely case where the prominence plasma is up to 20000K in temperature, the optical thickness of the millimetre-continuum would only range up to ≈ 4.5.

5.2.2 Time Averaged ALMA Images

Through comparison between the Band 3 interferometric image (Figure 5.3) and the Hα integrated intensity image (Figure 5.6) it is clear that the prominence has a very similar

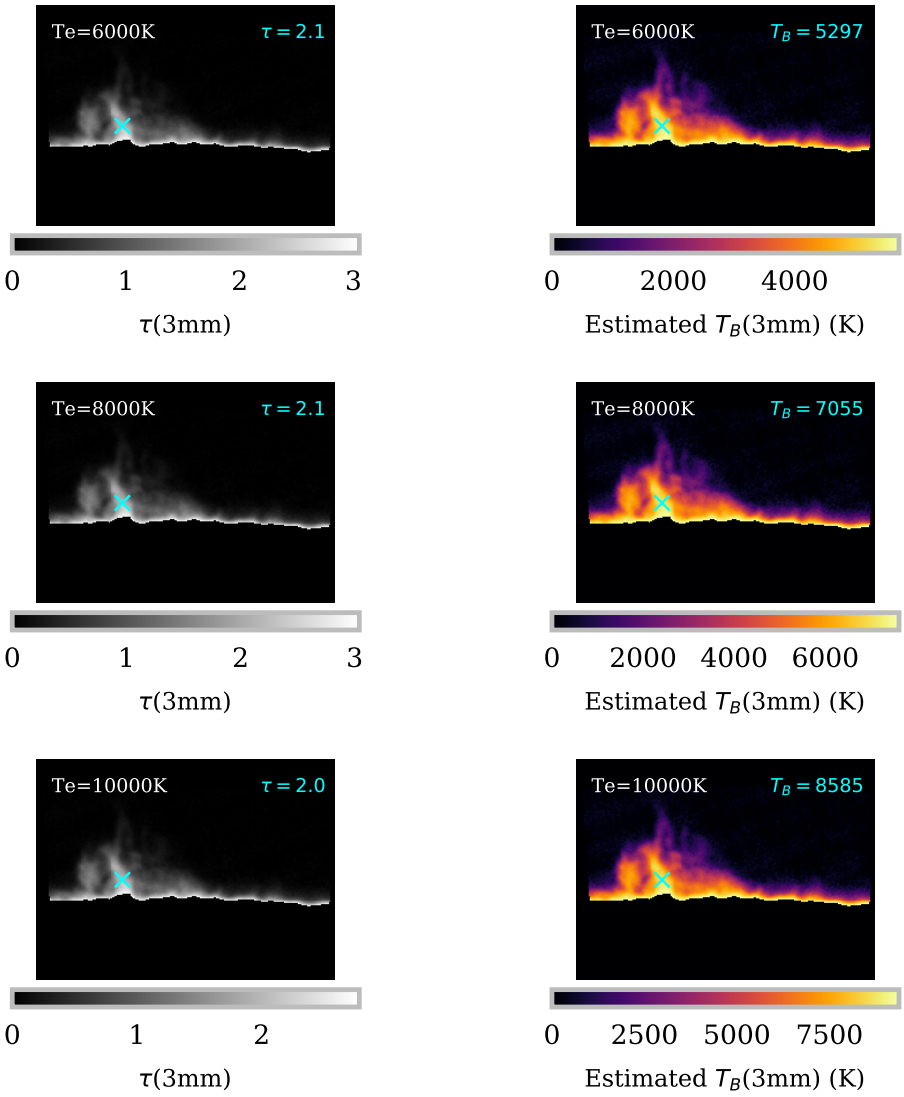

Figure 5.8: Optical thickness and brightness temperature estimations for ALMA Band 3 emission as calculated using the Hα integrated intensities from Figure 5.6 and an isothermal assumption. The estimation was calculated at 3 constant temperatures, where the values for the f-factor (Equation 5.2) were the same as quoted in Heinzel et al. (2015a).

morphology in both observing bands. This is true despite the most solar northerly part of the prominence observed in the Hα image being cut off in the ALMA FOV. This suggests either that the emission in ALMA Band 3 is formed: by the same cool, dense material which forms the Hα emission; in a closely fitting hot plasma sheath around the cool, dense core; or it is formed by the contribution of multiple, unresolved hot and cold fine-structures. This is in

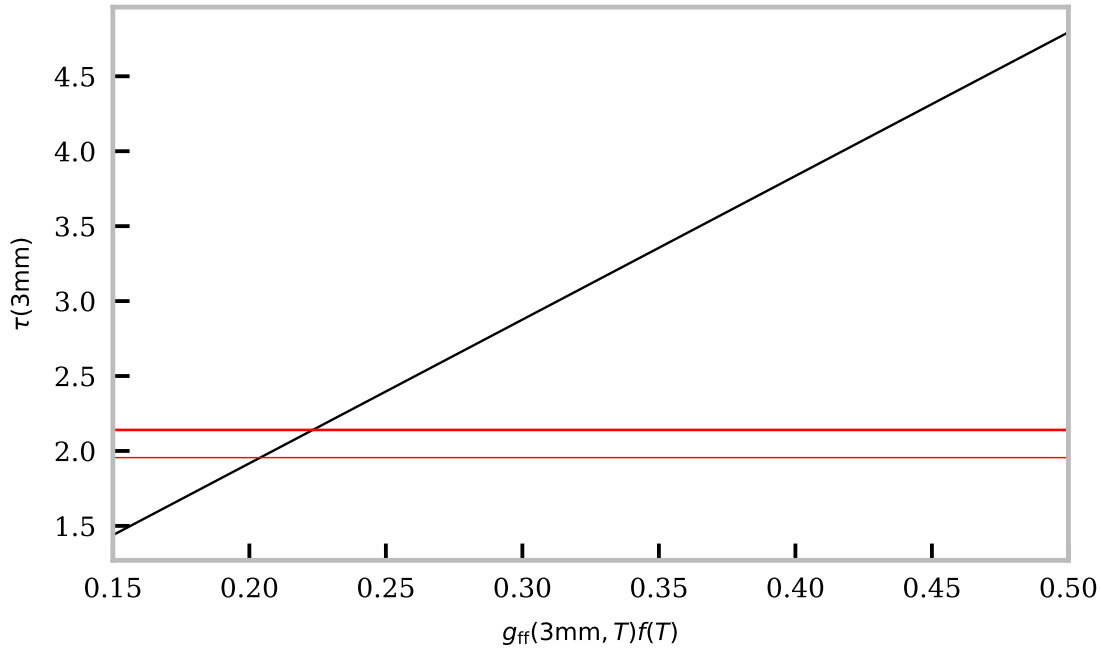

Figure 5.9: Variation of the ALMA Band 3 optical thickness estimation for the centre of the prominence spine (pixel highlighted by cyan cross in Figure 5.6) from the Hα integrated intensity with increasing values for $g_{ff}(\nu, T)f(T)$. The red horizontal lines show the 3 estimations using the 6000, 8000 and 10000K values from Figure 5.8.

agreement with what has been shown previously using the contribution function maps for Hα and 3mm emission given in Figure 3.21 of Chapter 3. The two contribution function maps show clear and consistent overlap across a wide range of prominence pressures. As the width of the millimetre-continuum contribution function map is slightly larger than that of of the Hα emission it is possible there is an increased contribution from hotter plasma at the base of the PCTR. In both observations the prominence spine is clearly visible, with what looks to be some barb-like structures at the sides, although the ALMA FOV only catches the solar southward side of the full prominence observed in Hα.

The brightness temperature appears to be fairly uniformly distributed across the width of the prominence spine. As the results from our prominence models in Chapter 2 suggest that the millimetre-emission should peak in LOSs passing through optically thick PCTR material, this suggests either that the PCTR is either optically thin in this observation or that the PCTR is not resolved. The resolution of the ALMA maps is defined by the semi-major and semi-minor axes of the synthesised beam, which is 1.98″ x 1.52″ for Block 1 and 2.17″

x 1.56″ for Block 2. The visibility of fine-structures will also be effected by the long time range used in the production of this image, as well as the frequency bandwidth as different frequency emission will be produced from different layers in the fine-structure.

Assuming constant electron temperatures up to 10000K, the previous section estimated that the maximum optical thickness of the prominence spine was ~ 2 from the integrated intensity of the Hα emission. This is in agreement with the hypothesis that the LOSs through the sparser PCTR material are optically thin for this observation. As an optical thickness of 2 is below that which is required for a direct measurement of the local electron temperature of the emitting plasma (Figure 2.9) an absolute brightness temperature measurement will present a lower boundary to the electron temperature measurement.

Figure 5.10 shows the preliminary results for the feathered absolute brightness temperature images using both high resolution interferometric imaging as well as slow resolution TP maps. As these images have been produced using a default single-dish weighting of 1 the true absolute brightness temperature values may vary somewhat from those presented here. However, the preliminary brightness temperatures for the prominence spine are still within what would be expected at between 6000 and 7000K.

Negative brightness temperatures are observed in the dark regions of Figure 5.10, just off the solar limb. Further from the limb there is observed to be some brightness temperature enhancement in the background corona. Both the negative values and the enhanced brightness temperature are likely to be caused by imaging artifacts caused by the step-function like brightness temperature variation of the solar limb and the finite sampling of the u-v plane. Artifacts like these have been previously observed in other off-limb ALMA observations (Shimojo et al. 2017a; Yokoyama et al. 2018).

5.2.2.1 Noise Level in Band 3 Images

The noise level in the interferometric ALMA images was calculated by finding the distribution of the difference between the XX and YY cross-correlated linear polarization signal as suggested by Shimojo et al. (2017a) and described previously in Section 4.3.1.1. As was stated previously in Section 5.1.1, analysis of the noise level in the images initially produced very large uncertainties due to the presence of too large disbalance between the XX and YY components of the system temperature in some of the antennas. Removal of these antennas for the image synthesis greatly improved the level of the noise estimates. The noise estimates for observing Blocks 1 and 2 are shown in Figures 5.11 and 5.12, respectively.

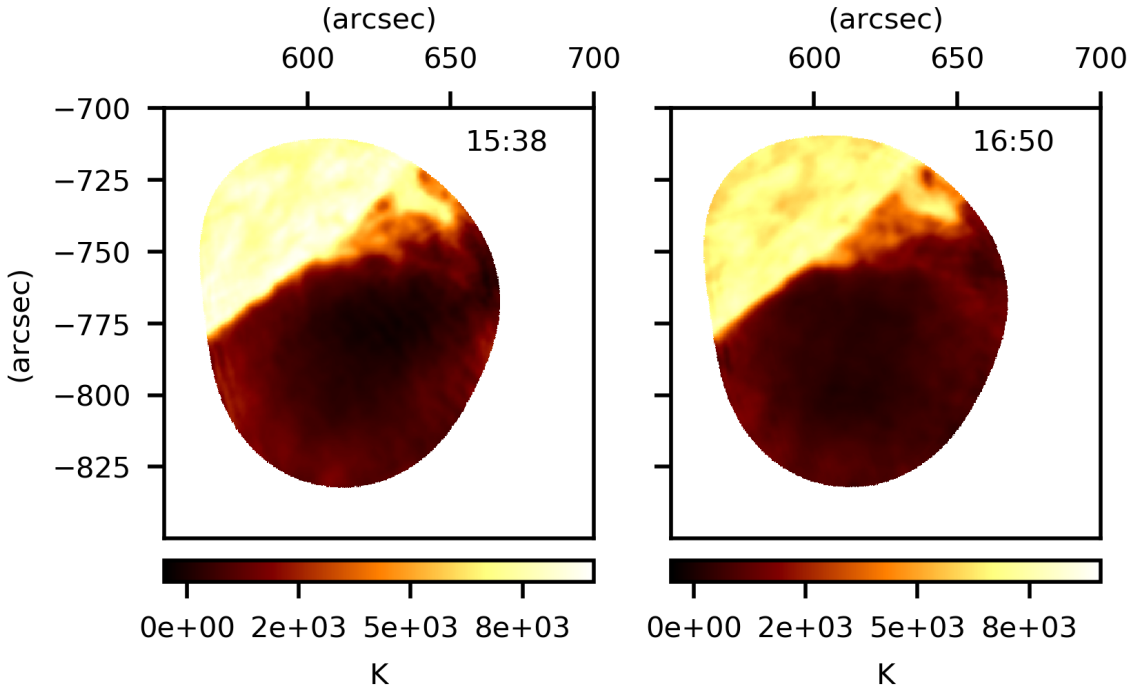

Figure 5.10: Preliminary absolute brightness temperature images of the prominence observed with ALMA on the 19th of April 2018. The images have been produced by feathering high resolution interferometric synthesised images with low resolution TP maps. The results are preliminary because the maps have been feathered with a default single-dish weighting of 1.

From Figures 5.11 and 5.12 it can be seen that the noise distributions are still non-gaussian, despite the removal of the problem antennas. The second observation (Block 2) has a peak within the distribution caused by a localised off-limb region in the lower left hand side of the difference image. The reason for the remaining sizeable difference in XX and YY distributions is unknown. Further reduction of the array size used in the image synthesis, beyond the removal of the antennas with the clear XX/YY system temperature disbalance, was decided against due to the negative effects this would have on the image quality. Although the distributions are irregularly shaped, a fitted gaussian to the data was used to find an estimated width for the distributions. This gave an estimated noise in Block 1 at $\sim$ 68K and $\sim$ 91K for Block 2.

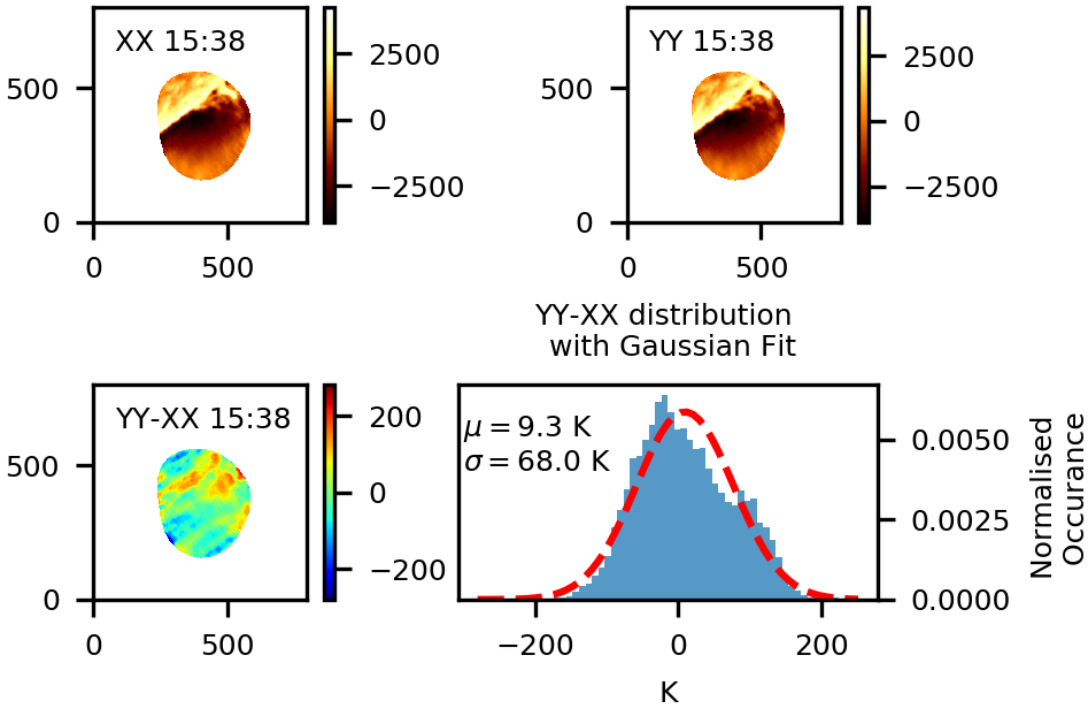

Figure 5.11: Noise distribution as calculated from the time-averaged ALMA observation of the prominence taken during Block 1. The *top* panels show the XX and YY images, with the *bottom left* panel showing the difference between the two. The *bottom right panel* shows the noise distribution defined as the distribution in the difference image fitted with a gaussian function. The mean and standard deviation of the fitted gaussian is printed on the same panel.

5.2.3 ALMA–AIA Cross-correlations

The ALMA observations were co-aligned with the SDO/AIA images using SunPy (SunPy Community et al. 2015). To do this the ALMA images needed to be converted from right ascension and declination to heliocentric units. This was done using the methods and routines outlined in ALMA Memo 611[2] Skokić et al. (2018). For this analysis I use time-averaged AIA images for each band, as the 3 mm images in Figure 5.3 were produced across the whole time range of both observations. Due to the better residuals after de-convolution the image chosen to co-align with AIA was the second ALMA observation taken during Block 2. To co-align the images from the two instruments the FOV of the data sets were set to be equal using SunPy's submap() feature. An example of the co-aligned images can be seen in Figure 5.13, where the

[2] https://library.nrao.edu/public/memos/alma/main/memo611.pdf

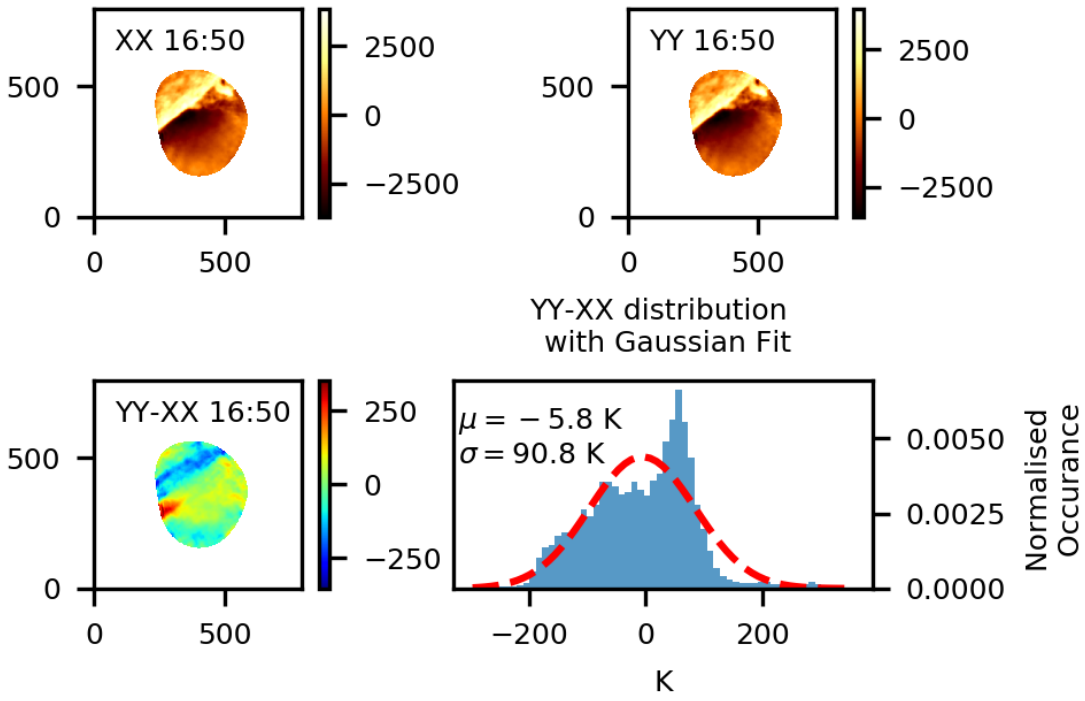

Figure 5.12: Same as Figure 5.11, but produced for the observation taken during Block 2.

ALMA observation is displayed as a contour map on top of the various time-averaged AIA band images.

In Figure 5.13 it can be seen that contours of the Band 3 prominence spine follow clearly the dark structures observed in AIA Bands 171, 193 and 211Å. This finding agrees well with previous knowledge of the optical thicknesses of ALMA Band 3 and the lyman continuum at 195Å. The optical thickness of Band 3 emission has already been shown to be similar to that of the Hα at line centre through the models in Section 3.3.1 and the observed morphologies in Figures 5.3 and 5.6, whilst it has been previously shown by Heinzel et al. (2008) that the opacity of the Lyman continuum at 195Å is comparable to that of the line centre of Hα. The bright prominence structure in 304Å is, however, significantly wider than that observed in either the Band 3 or Hα images. This is not surprising as 304Å is expected to be formed under optically thick conditions in prominences, thus allowing fine-structures away from the main body of the prominence to be more easily observed. The 94Å 131Å 335Å 1600Å and 1700Å bands show similar results to Bands 171, 193 and 211Å, however, in these bands the prominence is significantly fainter regardless of whether it is observed in absorption or emission.

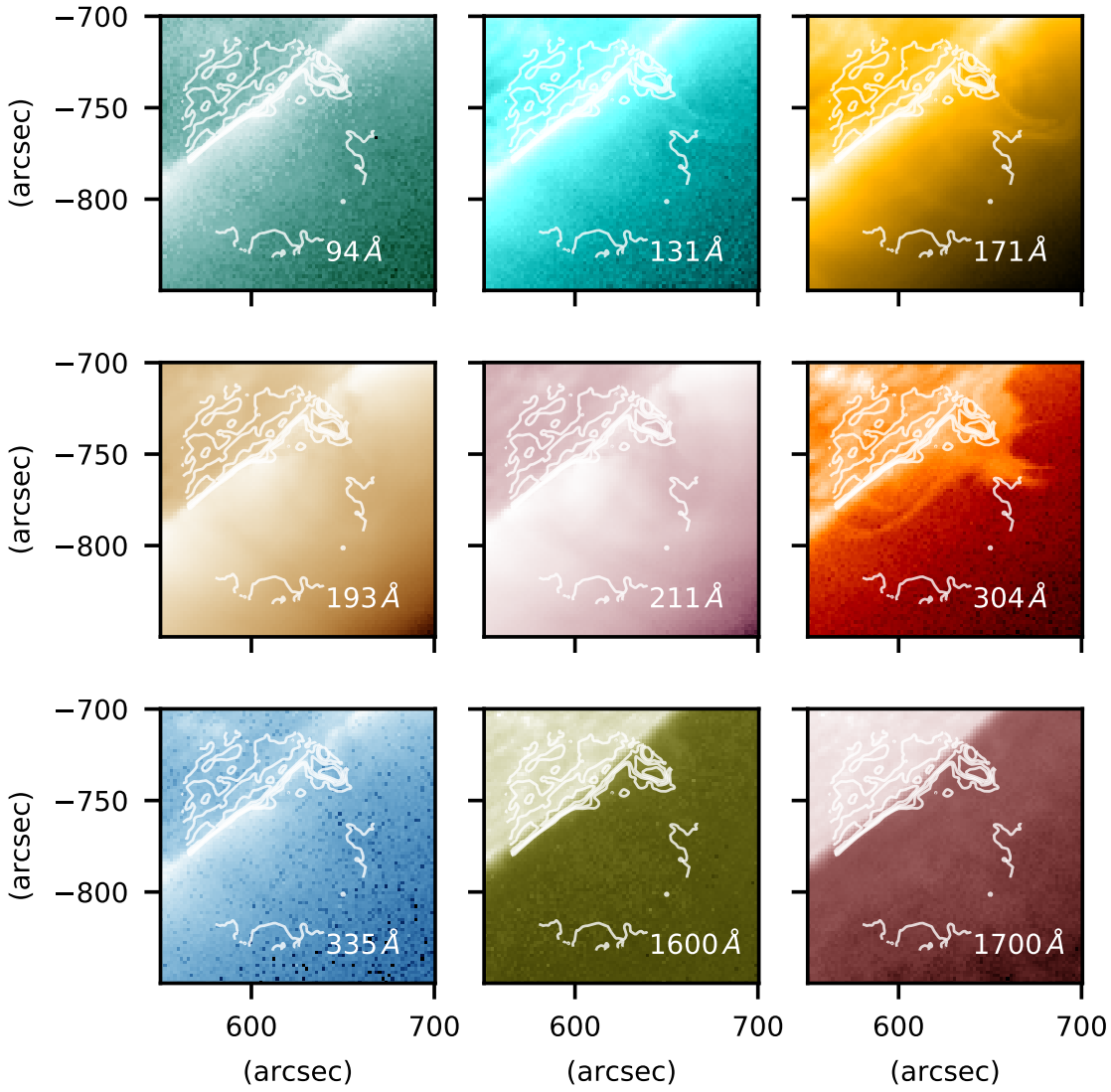

Figure 5.13: Co-aligned time-averaged images of the 19th of April 2018 prominence observed with ALMA and AIA bands during the second ALMA observing block (Block 2). The ALMA image is displayed as the white contours overlaid on the AIA images. The contours show the bright parts of the synthesised image with relative brightness temperatures of $\{0, 1000, 2000, 3000\}$K.

To do a pixel by pixel comparison of the brightness temperature/intensities from both datasets the resolution of both images needed to be matched. The original ALMA image had a finer spatial resolution (500 x 500pixels) than that of the AIA images (250 x 250) so was thus degraded to match AIA's lower spatial resolution. This was achieved using SunPy's

resample() function with the default mechanism of linear interpolation. The FOV of the ALMA image is a non-standard shape as it is defined by the primary beam coverage during the tclean() procedure. To match the AIA FOV to that of the ALMA image a mask array was produced from the degraded ALMA image which displayed values of 1.0 within the ALMA FOV and NaN outwith the FOV. The final AIA FOV image matching the ALMA FOV was produced by multiplying the AIA submaps by the mask array.

To restrict the analysis to the prominence and off-limb material only, the dataset was split into off-limb and on-disk parts by detecting the solar limb for the 3 mm emission. This was done using SunPy's draw_limb method() and manually altering the radius of the Sun until it was found to be $\approx .267°$. 2D histograms comparing the brightness temperature of the 3mm image with the intensity of each of the AIA bands are shown in Figure 5.14 for the off-limb data.

Because of the brightening artifacts observed off the solar limb, much of the 2D histograms in Figure 5.14 appear to be uncorrelated, or show a slight anti-correlation. The most clear anti-correlations are seen for AIA bands 193 and 211Å, suggesting that the dark structures observed in these bands, follow the bright Band 3 prominence closer than the other AIA bands.

5.3 Discussion and Conclusions

In this chapter I have presented preliminary results of the first high resolution ALMA interferometric observation of a solar prominence. In doing so, I have also considered co-ordinated observations using Hα spectral imaging from the Białkow MSDP instrument and AIA.

As discussed throughout this chapter, the preparation and data reduction of the ALMA observations has faced a myriad of problems at different steps in the process. This included the necessity to tune the deconvolution parameters to ensure a sufficiently non-structured residual image. Another problem arose from finding large, non-gaussian XX-YY distributions when investigating the noise levels in the interferometric imaging. This problem was solved by the identification and subsequent removal of a subset of the array's antennas from the image synthesis. This included 8 antennas for Block 1 and 10 antennas for Block 2. Unfortunately, addressing these issues proved to take quite a lot of time, and thus the breadth of analysis of this prominence observation possible within the scope of my PhD thesis was

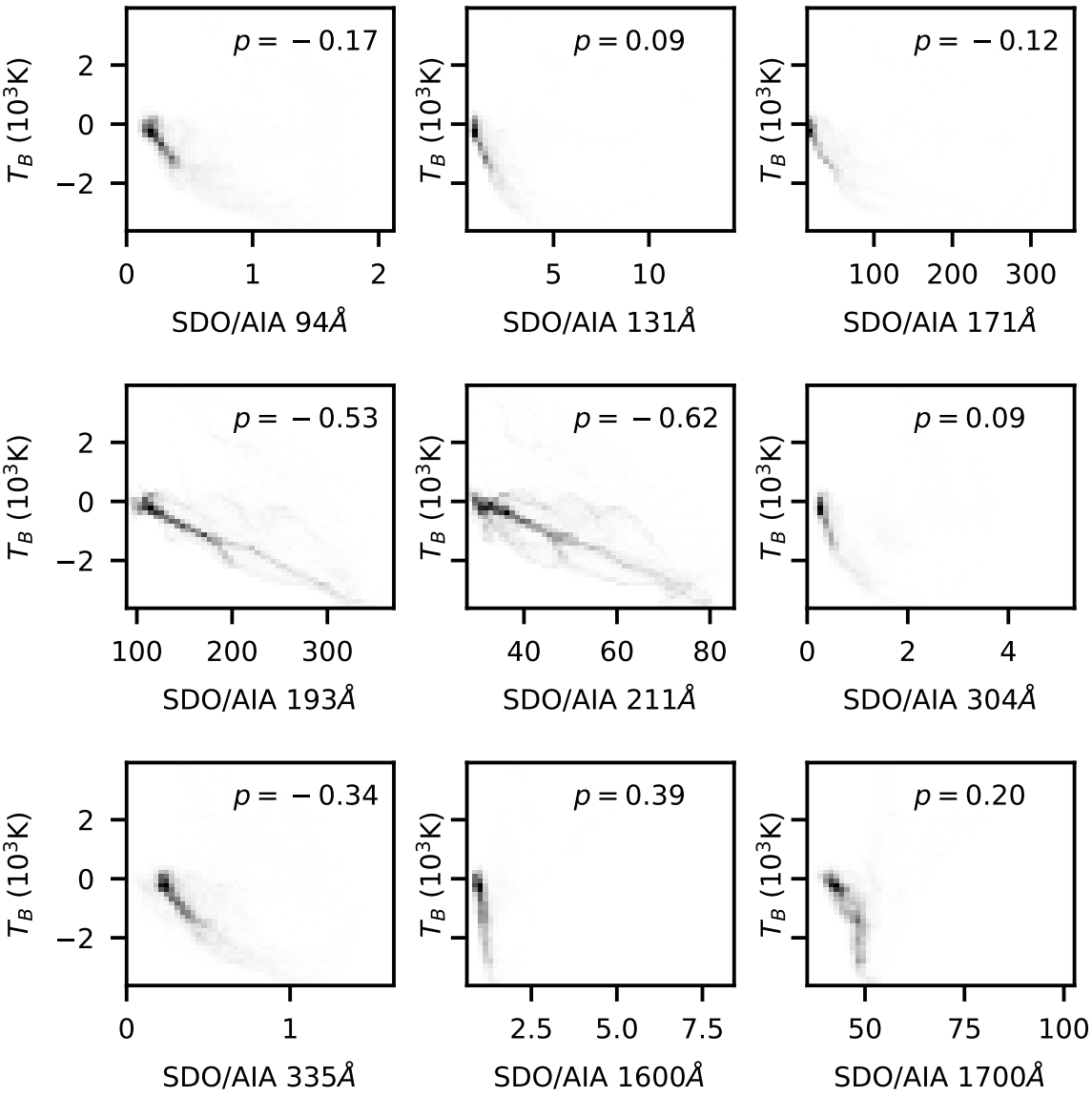

Figure 5.14: 2D histograms showing the correlation between the emission in ALMA Band 3 interferometric brightness temperature and the intensities observed using each of the AIA bands for the prominence and surrounding corona observed during Block 2. The units of intensity for the bands observed in AIA is DNs^{-1}.

greatly reduced. Issues were also found when attempting to tune the single-dish weighting in the feathering process to produce absolute brightness temperature measurements. Because of this, only preliminary results for the absolute brightness temperatures produced using the default weighting factor of 1 are included within this study.

Despite the issues encountered in the ALMA data reduction, it has been possible to

produce some results from this study which are primarily focussed on the morphology of the prominence rather than specific quantitative measurements. Through comparison between the ALMA Band 3 and Hα images it is possible to conclude that both forms of emission present very similar morphologies for this prominence observation, with both images showing clear prominence spine and barb-like structures. This suggests that the millimetre-continuum at Band 3 must then be formed from the same cold, dense plasma which is known to emit in Hα, or it is formed from hotter material contained within a similarly shaped structure. This could either be explained by a structure with a cool, dense core surrounded by a tight hot plasma sheath; or a structure consisting of multiple unresolved cold and hot plasma fine-structures. The first two options fit well with what was found using the contribution function maps modelled for Hα and 3mm emission in Section 3.3.1 of Chapter 3, where both forms of emission had largely overlapping formation regions. Longer millimetre wavelengths than Band 3 are likely to be more optically thick and would then be expected to be formed further from the cylindrical axis.

The Hα integrated intensities were then used, assuming an isothermal plasma, to estimate the optical thickness of the prominence in the millimetre-continuum. This estimated that the maximum Band 3 optical thickness would be ≈ 2, which is too low for absolute brightness temperature measurements to be used as a direct analogue of any local electron temperature. This optical thickness and the view of the prominence in Band 3 are in good agreement with what would be expected for a solar prominence from our models discussed in Chapter 2. Fully optically thick prominences would be expected to show brightness temperature enhancement from the higher temperature LOSs through predominantly PCTR material. As no such brightening is observed the prominence must either be optically thin for Band 3 in such high temperature LOSs, or that this material is unresolved. The preliminary absolute brightness temperatures lies within $\approx 6000 - 7000$K, which is in agreement with previous prominence modelling and observations.

The Band 3 prominence observation was also compared to co-aligned images from each of the nine AIA bands. The AIA bands which appeared to be most highly correlated with the millimetre-continuum emission were the 193 and 211Å bands, where the bright ALMA prominence spine appeared as clear dark structures against the bright surrounding corona. The 304Å prominence is also clearly visible, however, the extent of this structure is considerably larger than the corresponding millimetre-continuum image. This indicates that there is a significant amount of unresolved material which is optically thin in the millimetre-

continuum beyond the core of the prominence spine/barbs observed in the ALMA Band 3 image.

In addition to the work presented here, future studies could be used to find more from this dataset by considering either time-series imaging or sub-band 3 spectra. Analysing the time-series may allow study into the motions of the prominence plasma and how the temperature structure changes with time. Measuring the sub-band spectra on the other-hand would allow for a second estimate, alongside the co-ordinated Hα intensities, of the prominence's optical thickness in the millimetre-continuum. This would, however, require the use of a temporal or spatial enhancement in the brightness temperature, or be conducted using absolute brightness temperature measurements. If significant analysis were to be conducted using absolute brightness temperature measurements, further investigation into the feathering process between the interferometric and TP images and the noise distributions should be done first.

Future observations of prominences with ALMA could be improved once solar observations using Bands 1 and 2 are available. Prominence plasma is likely to be formed under higher optical thickness conditions for these wavelengths, thus allowing the plasma temperature structure to be probed at different formation layers. Knowledge of the temperature structure at different layers within the prominence will help improve understanding into the prominence energy balance and how they are sustained within the solar corona.

Chapter 6

Conclusions

Throughout my PhD I have investigated the millimetre-continuum emission from solar prominences and how it may relate to the internal parameters of the emitting plasma. The impetus behind this work was the advent of the solar observering capability of the *Atacama Large Millimeter/sub-millimeter Array* (ALMA). It has long been known that millimetre wavelength emission from the Sun carries the potential for strong direct temperature diagnostics through the complementing aspects of a collisional emission mechanism and lying within the Rayleigh-Jeans limit. Until ALMA, however, millimetre observations had been hampered by low spatial resolutions, thus negating the possibility to investigate the small-scale temperature structures which are involved in solar prominence energy balance.

Prominences generally consist of large areas of relatively cool, dense plasma suspended by strong magnetic fields within the hot, sparse solar corona. The magnetic field protects these objects from gravity and dissipation to the corona, however for this to succeed there is a necessity for delicate energy balance and dynamic equilibrium within the prominence structure. Understanding into these equilibria, as well as the triggers to when they are broken resulting in the end of the prominence's lifespan, are not fully known, with major questions still left open with regards to heating/cooling mechanisms and locations. Because of this, reliable and direct temperature diagnostics, such as are obtainable with millimetre observations, are desirable within the field of solar prominence research.

The first study I conducted was to investigate what the millimetre-continuum emission from a solar prominence should be expected to look like. This was done using the 2D cylindrical non-LTE radiative transfer code C2D2E and was described in Chapter 2. The majority of this chapter covered material previously published in Rodger & Labrosse (2017). In this

work I considered two sets of prominence models; isothermal-isobaric fine-structure models and multi-thermal prominence width models including a *prominence to corona transition region* (PCTR). The results from the isothermal-isobaric models found that the brightness temperature of the plasma directly measured the electron temperature of the isothermal model once the prominence was sufficiently optically thick, i.e. with $\tau \gtrsim 4-5$. Below these optical thicknesses the brightness temperature would measure some fraction of the electron temperature dependent on the particular optical thickness. Multi-thermal models, on the other hand, showed that the brightness temperature of the millimetre-continuum was related to the electron temperature of a given formation region whilst optically thick, and to some representative temperature for the entire line of sight (LOS) when optically thin. In all instances it was found to be clear that to be able to ascertain the relevant usable temperature diagnostic to use for a particular observation, knowledge of the optical thickness or optical thickness regime of the millimetre-continuum would be necessary.

In Chapter 3 of my thesis I focussed on further applications to the millimetre-continuum prominence modelling discussed in the previous chapter. The first of these applications to be considered was how prominences could be expected to appear when viewed as filaments against the solar disk in Section 3.2. This involved a change in the model's geometry as well as consideration of the background brightness temperature from the quiet Sun. Unlike solar prominences where coronal contributions are generally considered to be negligible, the illuminating radiation on solar filaments is integral to how the filaments appear to the observer. To simulate the brightness temperature from the quiet solar disk I considered variations on the typical ALMA Band 3 (100GHz) and 6 (230GHz) brightness temperatures as measured using the total power (TP) maps of White et al. (2017). Again I considered two sets of prominence models, isothermal-isobaric prominence models and the same set of multi-thermal whole prominence width models including a PCTR. It was found from this study that isothermal-isobaric models would only appear as dark absorption structures against the solar disk when the electron temperature of the given model was below the particular background quiet Sun value, and that the contrast against the background would decrease as the filament's electron temperature increased due to a reduction in the overall opacity of the filament. By considering an assumed 100K uncertainty on the synthetic brightness temperature it was found that only a few of the lower temperature models would be visible against the disk with all of these appearing as features in emission. A larger subset of models would be visible in Band 3 emission, however, with some appearing as dark and some as bright features. The results from multi-thermal prominences yielded largely similar results,

however, it was found that a singular multi-thermal filament could be observed in Band 3 both in absorption and in emission dependent on the particular LOS. It was concluded that, if this was observable within ALMA's spatial resolution, this could provide a direct observation of the PCTR structure of solar filaments. At the end of Section 3.2 I gave a discussion into how the results of these filament models could be affected by the presence of a coronal cavity above the filament structure.

The latter half of Chapter 3 presents a study into the relationship between the intensities observed from solar prominences in important lines of neutral hydrogen and helium, as well as the Lyman continuum, with the emission observed from the millimetre-continuum. The purpose of this investigation was to find correlations between spectral line observations and the optical thickness of the millimetre-continuum, such that they may be used to help determine the best available temperature diagnostics. The first set of lines considered were the Balmer Hα and Hβ lines of neutral hydrogen. It had previously been discussed in Heinzel et al. (2015a) that a known relationship from isothermal-isobaric models between the integrated intensity of Hα and the emission measure could be used to estimate the optical thickness of the millimetre-continuum. This theory was investigated using 2D prominence models from the same set used in Section 3.2. It was found for isothermal-isobaric models that a clear power-law relationship existed between the Hα and Hβ integrated intensities with the optical thickness of the millimetre-continuum, with only slight deviations caused by the presence of helium in the models and non-uniform incident radiation. Multi-thermal models, on the other hand, revealed that different power-law correlations existed for different parts of the prominence FOV, depending on the particular representative frequency for the LOS. In LOSs where the Hα emission was produced under optically thick conditions there ceased to be a correlation between the integrated intensity and the millimetre optical thickness. The integrated intensities from the Lyman lines (Lyα, Lyβ and Lyγ) were discovered to be mostly uncorrelated with either various forms of the emission measure or the optical thickness of the millimetre-continuum. This is due to the majority of LOSs being formed under optically thick conditions. Whilst no clear correlation was found between the integrated intensity of the neutral helium D3 line and the optical thickness of the millimetre-continuum, a clear power-law relation was identified between it and the electron-singly ionized helium emission measure ($n_e n_{HeII} L$). Investigation into the colour temperature of the Lyman-continuum proved it to be a good diagnostic of the electron density weighted mean temperature of the emitting plasma, with the Lyman-continuum colour temperature lying close to the millimetre-continuum brightness temperature when the formation regions of both forms of

emission overlapped.

The purpose of Chapter 4 was then to investigate the use of multiple millimetre wavelength observations as a means to estimate the optical thickness of the emitting plasma in the millimetre-continuum. It was also investigated how optical thickness estimations could be used to find other plasma parameters such as the charge squared weighted emission measure or the electron temperature. The first diagnostic considered was the brightness temperature ratio from two millimetre-wavelength observations. Again this study covered material previously published in Rodger & Labrosse (2017). This method required both the assumption of an isothermal plasma and some knowledge into said temperature so that an estimate of the absorption coefficient ratio between the observed wavelengths could be made. For isothermal models the brightness temperature ratio proved to be a good estimate of the optical thickness when the plasma was optically thin, however, once the plasma becomes optically thick it is expected that the method will become increasingly sensitive to any uncertainty in the brightness temperature. For multi-thermal models, different temperature estimations were used due to the lack of a single representative value. From this it was found that the best results were obtained using the electron density squared weighted mean electron temperature.

Chapter 4 continued with a study, covering material previously published in Rodger & Labrosse (2018), into the relationship between the spectral gradient of the millimetre-continuum and its optical thickness. This study began by deriving analytical expressions relating the linear-scale and logarithmic-scale spectral gradient and the optical thickness for an off-limb plasma. From this it was revealed that the logarithmic-scale gradient yielded a clear, singular relationship with the optical thickness when the plasma was isothermal, provided that estimation could be made into a multiplicative factor determined by the rate of change of the Gaunt factor over the observing band. Multi-thermal plasmas were found to react similarly to isothermal plasmas when the plasma was optically thin, however, once the plasma becomes optically thick the spectral gradient became increasingly defined by the temperature gradient of the plasma within the formation region of the observing band. An on-disk extension to this theory was then tested using the case study of a small plasma eruption and plasmoid ejection as observed using sub-band ALMA Band 3 observation conducted during a science verification campaign in December 2015. This case study mostly covered work which was published in Rodger et al. (2019). This observation had first been analysed by Shimojo et al. (2017b) who, using simultaneous observations using

XRT/Hinode and AIA/SDO set constraints on the electron temperature and density of the ejected plasmoid. Two boxes were defined within the observation which corresponded to a stationary brightness temperature enhancement and to the moving plasmoid ejection. For each of these boxes, brightness temperature lightcurves were used to produce subtracted absolute brightness temperature enhancement spectra for ALMA Band 3. The logarithmic gradient of these spectra were then calculated using a method of bayesian linear regression. The 90% confidence intervals of the resultant posterior probability distributions for the spectral gradients were used to estimate the optical thickness with the aid of curves derived from the relationship between said spectral gradient and the optical thickness for an on-disk observation. The results from this study agreed with one of the suggested outcomes of Shimojo et al. (2017b) where the plasmoid consisted of a cool $\sim 10^4$K core, surrounded by a hot EUV emitting envelope. This study proved this method's potential to estimate the optical thickness regime of an ALMA observation, however, in doing so highlighted the necessity for improved understanding into the uncertainty into ALMA interferometric brightness temperature methods, as well as calling for more detailed observation of the spectral gradient and brightness temperature of the quiet Sun at millimetre wavelengths.

Finally, in Chapter 5 I presented results from the first high resolution interferometric observation of a solar prominence using ALMA. This observation was taken on the 19th of April 2018 in ALMA Band 3 (100GHz). Co-ordinated observation was also conducted using Hα spectral imaging from the MSDP telescope in Białkow in Poland, and the space-based instruments IRIS and AIA. In this work a number of significant problems were encountered during the data reduction and preparation of the ALMA synthesised images. Due to the time constraints of my PhD project this resulted in only singular interferometric images being produced for ALMA Band 3 across two major observing blocks running from approximately 15 : 38–16 : 31 and 16 : 51–17 : 45UTC. I was only able to present preliminary absolute brightness temperature images, therefore the majority of the analysis conducted was qualitative and based around the observed prominence's morphology. Using the method defined in Heinzel et al. (2015a) and investigated in Chapter 3, a coordinated Hα integrated intensity image was used to estimate the maximum optical thickness of the prominence in ALMA Band 3. This returned a value of ~ 2 for the centre of the prominence spine, which, while optically thick, is too low for an absolute brightness temperature measurement to directly measure the electron temperature of the emission's formation region. The Band 3 image also proved to display a very similar morphology to how the prominence looked in Hα with the same spine and barb-like structures visible. This, along with the estimation of

the prominence's optical thickness tells us something about the prominence's temperature structure where the Band 3 emission is formed. This means that, as the morphologies are similar, the millimetre emission must either be produced: in the same cold, dense material that emits the Hα emission; from a tight sheath-like layer of hotter plasma around the cool core; or from the cumulative effects of LOS integration from any unresolved hot and cold fine-structures. From the models presented in Chapter 2 it is expected that LOSs at the edges of the prominence, through mostly PCTR material, should be observed at hotter brightness temperatures than the prominence centre when said LOSs are optically thick. As this is not observed, it can be concluded that these PCTR LOSs are either unresolved or optically thin for this prominence observation. An ALMA image was also co-aligned with time-averaged AIA images for the same observing period, with the resolution of the ALMA image degraded to match that of the AIA images. From this it was found that the AIA bands which correlated best with ALMA Band 3 were the 193 and 211Å bands, where the dark absorption feature in AIA fairly closely matched the bright emission feature observed with ALMA. The AIA 304Å band was observed in emission similarly to the ALMA image, however, the size and extent of the 304Å image was considerably larger than the prominence spine as observed with ALMA. This indicated that, despite the maximum optical thickness of the prominence spine being greater than one, large swathes of the prominence outer fine-structure is optically thin and unresolved for ALMA Band 3.

In conclusion, high resolution observations of the millimetre-continuum, as are now available using ALMA, provide the potential to determine new information on the temperature structure of solar prominences and their PCTR. However, for this potential to be fully realised will require estimations of the plasma's optical thickness and improved understanding into the error estimations and noise levels involved in ALMA observations. Solar science using ALMA is still in its infancy and thus the volume of published scientific content is low. Published off-limb solar observations are particularly few, with only a singular publication to date (Yokoyama et al. 2018) addressing a specifically solar limb observation. Further observations of the limb and off-limb structures will be necessary to understand the role and effect of artifacts in ALMA's synthesised images of these structures. As the knowledge base grows we can hope for improvements into the understanding of the noise in ALMA solar images from using the XX-YY difference image method, and into whether this method is always applicable as well. Another large area where understanding with ALMA solar science could be improved is the use of the TP maps and the method for their combination with the synthesis images to produce absolute brightness data. Due to variability in the

brightness temperatures observed TP maps are currently scaled to the typical values as observed in White et al. (2017). This is not ideal, as to detect long-term changes in the millimetre-continuum brightness temperature will require this scaling to be removed.

Within this thesis it has been shown that the optical thickness of the millimetre-continuum can be estimated in several different ways. These estimations will require either coordinated observations with the Balmer or other suitable optically thin spectral lines, or multiple wavelength millimetre-continuum observations with suitably small and reliable uncertainty measurements. Inevitably, however, observations of optically thick plasma will be desired so that the brightness temperature may be used as a direct measurement of the electron temperature of a given formation layer. From the models presented in Chapter 2, and from the prominence observed in Chapter 5, it is expected that ALMA Band 3 will only be sufficiently optically thick for very large or dense prominences. Therefore, for more regular observations of optically thick prominences in the millimetre-continuum the longer wavelength ALMA Bands 1 and 2 will need to become available to solar physics observations. These observations will come with the caveat that longer wavelengths will produce lower spatial resolution images, although this may be improved as more extended array configurations also become available.

Improved undestanding into how the millimetre-continuum is formed in solar prominences will also come through comparison with plasma diagnostics from coordinated observations in spectral lines, such as Mg II as is currently observed with IRIS, and continua, such as is produced by the balmer continuum. An improvement to coordinated observations will arrive once DKIST sees first light, as it shall be able to provide very fine spatial and spectral resolution of the prominence structure in Hα, and other visible lines, using its Visible Spectropolarimeter (ViSP), Visible Broadband Imager (VBI) and Visible Tunable Filter (VTF) instruments, whilst also having the capability to observe in the infra-red using its CRYO-NIRSP and DL-NIRSP instruments.

The numerical modelling conducted throughout my PhD has been limited to the 2D cylindrical models of Gouttebroze & Labrosse (2009). These models are, however, limited by their simple geometry and arbitrary temperature structure for the PCTR. Therefore, future modelling efforts could be improved through the consideration of 3D prominence models with more realistic temperature/pressure distributions.

Bibliography

Alissandrakis, C. E., Patsourakos, S., et al. 2017, *Astronomy and Astrophysics*, 605, A78

Antiochos, S. K. & Klimchuk, J. A. 1991, *The Astrophysical Journal*, 378, 372

Anzer, U. & Heinzel, P. 1999, *Astronomy and Astrophysics*, 349, 974

Anzer, U. & Heinzel, P. 2000, *Astronomy and Astrophysics*, 358, L75

Auer, L., Bendicho, P. F., et al. 1994, *Astronomy and Astrophysics*, 292, 599

Auer, L. H. & Paletou, F. 1994, *Astronomy and Astrophysics*, 285

Avrett, E., Landi, E., et al. 2013, *The Astrophysical Journal*, 779, 155

Avrett, E. H. & Loeser, R. 2008, *The Astrophysical Journal Supplement Series*, 175, 229

Ballester, J. L. 2015, in Astrophysics and Space Science Library, Vol. 415, Solar Prominences, ed. J.-C. Vial & O. Engvold, 259

Bastian, T. S. 2002, *Astronomische Nachrichten*, 323, 271

Bastian, T. S., Chintzoglou, G., et al. 2017, *The Astrophysical Journal*, 845, L19

Bastian, T. S., Ewell, Jr., M. W., et al. 1993, *The Astrophysical Journal*, 418, 510

Bayes, T. & Price, R. 1763, *Philosophical Transactions of the Royal Society of London*

Berger, T. 2014, in IAU Symposium, Vol. 300, Nature of Prominences and their Role in Space Weather, ed. B. Schmieder, J.-M. Malherbe, & S. T. Wu, 15–29

Bogod, V. M. & Gelfreikh, G. B. 1980, *Solar Physics*, 67, 29

Brajša, R., Sudar, D., et al. 2018, *Astronomy and Astrophysics*, 613, A17

Brown, G. M. & Labrosse, N. 2018, *Solar Physics*, 293, 35

Butz, M., Fuerst, E., et al. 1975, *Solar Physics*, 45, 125

Chiuderi, C. & Chiuderi Drago, F. 1991, *Solar Physics*, 132, 81

Chiuderi Drago, F., Alissandrakis, C. E., et al. 2001, *Solar Physics*, 199, 115

Cornwell, T. J. 2008, *IEEE Journal of Selected Topics in Signal Processing*, 2, 793

De Pontieu, B., Title, A. M., et al. 2014, *Solar Physics*, 289, 2733

Dulk, G. A. 1985, *Annual Review of Astronomy and Astrophysics*, 23, 169

Engvold, O. 2015, in Astrophysics and Space Science Library, Vol. 415, Solar Prominences, ed. J.-C. Vial & O. Engvold, 31

Fontenla, J. M., Avrett, E. H., et al. 1993, *The Astrophysical Journal*, 406, 319

Fontenla, J. M., Rovira, M., et al. 1996, *The Astrophysical Journal*, 466, 496

Foreman-Mackey, D. 2016, *The Journal of Open Source Software*, 24

Foreman-Mackey, D., Hogg, D. W., et al. 2013, *Publications of the ASP*, 125, 306

Gary, D. E., Zirin, H., et al. 1990, *The Astrophysical Journal*, 355, 321

Gayet, R. 1970, *Astronomy and Astrophysics*, 9, 312

Gilbert, H. 2015, in Astrophysics and Space Science Library, Vol. 415, Solar Prominences, ed. J.-C. Vial & O. Engvold, 157

Goodman, J. & Weare, J. 2010, *Communications in Applied Mathematics and Computational Science*, 5, 65

Gopalswamy, N. 2015, in Astrophysics and Space Science Library, Vol. 415, Solar Prominences, ed. J.-C. Vial & O. Engvold, 381

Gopalswamy, N., Hanoka, Y., et al. 1998, in Astronomical Society of the Pacific Conference Series, Vol. 150, IAU Colloq. 167: New Perspectives on Solar Prominences, ed. D. F. Webb, B. Schmieder, & D. M. Rust, 358

Gopalswamy, N., Shimojo, M., et al. 2003, *The Astrophysical Journal*, 586, 562

Gouttebroze, P. 2004, *Astronomy and Astrophysics*, 413, 733

Gouttebroze, P. 2005, *Astronomy and Astrophysics*, 434, 1165

Gouttebroze, P. 2006, *Astronomy and Astrophysics*, 448, 367

Gouttebroze, P. 2007, *Astronomy and Astrophysics*, 465, 1041

Gouttebroze, P. 2008, *Astronomy and Astrophysics*, 487, 805

Gouttebroze, P. & Heinzel, P. 2002, *Astronomy and Astrophysics*, 385, 273

Gouttebroze, P., Heinzel, P., et al. 1993, *Astronomy and Astrophysics Supplement Series*, 99, 513

Gouttebroze, P. & Labrosse, N. 2009, *Astronomy and Astrophysics*, 503, 663

Gouttebroze, P., Vial, J. C., et al. 1997, *Solar Physics*, 172, 125

Grant, I. P. 1958, *Monthly Notices of the Royal Astronomical Society*, 118, 241

Grebinskij, A., Bogod, V., et al. 2000, *Astronomy and Astrophysics Supplement Series*, 144, 169

Gunár, S., Heinzel, P., et al. 2018, *The Astrophysical Journal*, 853, 21

Gunár, S., Heinzel, P., et al. 2008, *Astronomy and Astrophysics*, 490, 307

Gunár, S., Heinzel, P., et al. 2016, *The Astrophysical Journal*, 833, 141

Gunár, S., Heinzel, P., et al. 2007, *Astronomy and Astrophysics*, 472, 929

Gunár, S., Schwartz, P., et al. 2010, *Astronomy and Astrophysics*, 514, A43

Harrison, R. A., Carter, M. K., et al. 1993, *Astronomy and Astrophysics*, 274, L9

Heasley, J. N. & Mihalas, D. 1976, *The Astrophysical Journal*, 205, 273

Heasley, J. N. & Milkey, R. W. 1978, *The Astrophysical Journal*, 221, 677

Heasley, J. N. & Milkey, R. W. 1983, *The Astrophysical Journal*, 268, 398

Heinzel, P. & Anzer, U. 2001, *Astronomy and Astrophysics*, 375, 1082

Heinzel, P. & Anzer, U. 2012, *Astronomy and Astrophysics*, 539, A49

Heinzel, P. & Avrett, E. H. 2012, *Solar Physics*, 277, 31

Heinzel, P., Berlicki, A., et al. 2015a, *Solar Physics*, 290, 1981

Heinzel, P., Gouttebroze, P., et al. 1987, *Astronomy and Astrophysics*, 183, 351

Heinzel, P., Gouttebroze, P., et al. 1994, *Astronomy and Astrophysics*, 292, 656

Heinzel, P., Gunár, S., et al. 2015b, *Astronomy and Astrophysics*, 579, A16

Heinzel, P., Schmieder, B., et al. 2008, *The Astrophysical Journal*, 686, 1383

Heinzel, P., Schmieder, B., et al. 2015c, *The Astrophysical Journal, Letters*, 800, L13

Heinzel, P., Schmieder, B., et al. 2001a, *The Astrophysical Journal*, 561, L223

Heinzel, P., Schmieder, B., et al. 2001b, *Astronomy and Astrophysics*, 370, 281

Heinzel, P. & Vial, J.-C. 1983, *Astronomy and Astrophysics*, 121, 155

Heinzel, P., Vial, J.-C., et al. 2014, *Astronomy and Astrophysics*, 564, A132

Hills, R. E., Kurz, R. J., et al. 2010, in Society of Photo-Optical Instrumentation Engineers (SPIE) Conference Series, Vol. 7733, Ground-based and Airborne Telescopes III, 773317

Hirayama, T. 1971, *Solar Physics*, 19, 384

Högbom, J. A. 1974, *Astronomy and Astrophysics, Supplement*, 15, 417

Iakovkin, N. A., Zeldina, M. I., et al. 1982, *Solar Physics*, 81, 339

Irimajiri, Y., Takano, T., et al. 1995, *Solar Physics*, 156, 363

Iwai, K., Loukitcheva, M., et al. 2017, *The Astrophysical Journal, Letters*, 841, L20

Jafarzadeh, S., Wedemeyer, S., et al. 2019, *Astronomy and Astrophysics*, 622, A150

Jejčič, S. & Heinzel, P. 2009, *Solar Physics*, 254, 89

John, T. L. 1988, *Astronomy and Astrophysics*, 193, 189

Karlický, M., Bárta, M., et al. 2011, *Solar Physics*, 268, 165

Karpen, J. T. 2015, in Astrophysics and Space Science Library, Vol. 415, Solar Prominences, ed. J.-C. Vial & O. Engvold, 237

Kippenhahn, R. & Schlüter, A. 1957, *Zeitschrift fur Astrophysik*, 43, 36

Koda, J., Sawada, T., et al. 2011, *The Astrophysical Journal, Supplement*, 193, 19

Kundu, M. R. 1972, *Solar Physics*, 25, 108

Kundu, M. R., Fuerst, E., et al. 1978, *Astronomy and Astrophysics*, 62, 431

Kundu, M. R. & McCullough, T. P. 1972, *Solar Physics*, 24, 133

Kundu, M. R., Melozzi, M., et al. 1986, *Astronomy and Astrophysics*, 167, 166

Labrosse, N. 2015, in Astrophysics and Space Science Library, Vol. 415, Solar Prominences, ed. J.-C. Vial & O. Engvold, 131

Labrosse, N. & Gouttebroze, P. 2001, *Astronomy and Astrophysics*, 380, 323

Labrosse, N. & Gouttebroze, P. 2004, *The Astrophysical Journal*, 617, 614

Labrosse, N., Heinzel, P., et al. 2010, *Space Science Reviews*, 151, 243

Labrosse, N., Rodger, A., et al. In Prep

Labrosse, N. & Rodger, A. S. 2016, *Astronomy and Astrophysics*, 587, A113

Lang, K. R. & Willson, R. F. 1989, *The Astrophysical Journal*, 344, L73

Leenaarts, J., Pereira, T. M. D., et al. 2013a, *The Astrophysical Journal*, 772, 89

Leenaarts, J., Pereira, T. M. D., et al. 2013b, *The Astrophysical Journal*, 772, 90

Lemen, J. R., Title, A. M., et al. 2012, *Solar Physics*, 275, 17

Levens, P. J. & Labrosse, N. 2019, *Astronomy and Astrophysics*, 625, A30

Levens, P. J., Schmieder, B., et al. 2016, *The Astrophysical Journal*, 826, 164

Lin, Y., Engvold, O., et al. 2007, *Solar Physics*, 246, 65

Lin, Y., Martin, S. F., et al. 2008, in Astronomical Society of the Pacific Conference Series, Vol. 383, Subsurface and Atmospheric Influences on Solar Activity, ed. R. Howe, R. W. Komm, K. S. Balasubramaniam, & G. J. D. Petrie, 235

Loukitcheva, M., Solanki, S. K., et al. 2004, *Astronomy and Astrophysics*, 419, 747

Loukitcheva, M., Solanki, S. K., et al. 2015, *Astronomy and Astrophysics*, 575, A15

Loukitcheva, M., White, S. M., et al. 2017a, *Astronomy and Astrophysics*, 601, A43

Loukitcheva, M. A., Iwai, K., et al. 2017b, *The Astrophysical Journal*, 850, 35

Loukitcheva, M. A., White, S. M., et al. 2019, *The Astrophysical Journal, Letters*, 877, L26

Mackay, D. H. 2015, in Astrophysics and Space Science Library, Vol. 415, Solar Prominences, ed. J.-C. Vial & O. Engvold, 355

Mackay, D. H., Gaizauskas, V., et al. 2008, *Solar Physics*, 248, 51

Mackay, D. H., Karpen, J. T., et al. 2010, *Space Science Reviews*, 151, 333

Marqué, C. 2004, *The Astrophysical Journal*, 602, 1037

Martin, S. F., Bilimoria, R., et al. 1994, in NATO Advanced Science Institutes (ASI) Series C, ed. R. J. Rutten & C. J. Schrijver, Vol. 433, 303

Martin, S. F., Marquette, W. H., et al. 1992, in Astronomical Society of the Pacific Conference Series, Vol. 27, The Solar Cycle, ed. K. L. Harvey, 53

Menzel, D. H. & Pekeris, C. L. 1935, *Monthly Notices of the Royal Astronomical Society*, 96, 77

Michelson, A. A. 1920, *The Astrophysical Journal*, 51, 257

Michelson, A. A. & Pease, F. G. 1921, *The Astrophysical Journal*, 53, 249

Mihalas, D., Auer, L. H., et al. 1978, *The Astrophysical Journal*, 220, 1001

Moreton, G. E. & Ramsey, H. E. 1960, *Publications of the ASP*, 72, 357

Munro, R. H., Gosling, J. T., et al. 1979, *Solar Physics*, 61, 201

Nindos, A., Alissandrakis, C. E., et al. 2018, *Astronomy and Astrophysics*, 619, L6

Noyes, R. W., Dupree, A. K., et al. 1972, *The Astrophysical Journal*, 178, 515

Ofman, L., Kucera, T. A., et al. 1998, *Solar Physics*, 183, 97

Oliver, R. & Ballester, J. L. 2002, *Solar Physics*, 206, 45

Orrall, F. Q. & Schmahl, E. J. 1980, *The Astrophysical Journal*, 240, 908

Oster, L. 1963, *The Astrophysical Journal*, 137, 332

Paletou, F., Vial, J. C., et al. 1993, *Astronomy and Astrophysics*, 274, 571

Parenti, S. 2014, *Living Reviews in Solar Physics*, 11, 1

Parenti, S., Lemaire, P., et al. 2005, *Astronomy and Astrophysics*, 443, 685

Parenti, S. & Vial, J. C. 2007, *Astronomy and Astrophysics*, 469, 1109

Patsourakos, S., Gouttebroze, P., et al. 2007, *The Astrophysical Journal*, 664, 1214

Patsourakos, S. & Vial, J.-C. 2002, *Solar Physics*, 208, 253

Pereira, T. M. D., Leenaarts, J., et al. 2013, *The Astrophysical Journal*, 778, 143

Pojoga, S. 1994, in IAU Colloq. 144: Solar Coronal Structures, ed. V. Rusin, P. Heinzel, & J.-C. Vial, 357–360

Poland, A. & Anzer, U. 1971, *Solar Physics*, 19, 401

Poland, A. I. & Mariska, J. T. 1986, *Solar Physics*, 104, 303

Rayet, M. 1869, *Astronomical register*, 7, 133

Rodger, A. & Labrosse, N. 2017, *Solar Physics*, 292, 130

Rodger, A. S. & Labrosse, N. 2018, *Astronomy and Astrophysics*, 617, L6

Rodger, A. S., Labrosse, N., et al. 2019, *The Astrophysical Journal*, 875, 163

Rust, D. M. & Kumar, A. 1994, *Solar Physics*, 155, 69

Rutten, R. J. 2003, Radiative Transfer in Stellar Atmospheres, https://ui.adsabs.harvard.edu/abs/2003rtsa.book.....R

Rutten, R. J. 2017, in IAU Symposium, Vol. 327, Fine Structure and Dynamics of the Solar Atmosphere, ed. S. Vargas Domínguez, A. G. Kosovichev, P. Antolin, & L. Harra, 1–15

Rybicki, G. B. & Hummer, D. G. 1991, *Astronomy and Astrophysics*, 245, 171

Rybicki, G. B. & Hummer, D. G. 1992, *Astronomy and Astrophysics*, 262, 209

Ryle, M. & Vonberg, D. D. 1946, *Nature*, 158, 339

Schmieder, B., Heinzel, P., et al. 1999, *Solar Physics*, 189, 109

Selhorst, C. L., Silva, A. V. R., et al. 2005, *Astronomy and Astrophysics*, 433, 365

Selhorst, C. L., Simões, P. J. A., et al. 2019, *The Astrophysical Journal*, 871, 45

Shimojo, M., Bastian, T. S., et al. 2017a, *Solar Physics*, 292, 87

Shimojo, M., Hudson, H. S., et al. 2017b, *The Astrophysical Journal*, 841, L5

Shimojo, M., Yokoyama, T., et al. 2006, *Publications of the ASJ*, 58, 85

Simões, P. J. A., Kerr, G. S., et al. 2017, *Astronomy and Astrophysics*, 605, A125

Sivia, D. & Skilling, J. 2006, Data Analysis: A Bayesian Tutorial (Oxford University Press)

Skokić, I., Brajša, R., et al. 2018, Tech. Rep. ALMA Memo 611, ALMA

Sommerfeld, A. 1951, Atombau und Specktrallinein II (Vieweg, Braunschweig)

SunPy Community, T., Mumford, S. J., et al. 2015, *Computational Science and Discovery*, 8, 014009

Thompson, A. R., Moran, J. M., et al. 2017, Interferometry and Synthesis in Radio Astronomy, 3rd Edition

Thompson, W. T. & Schmieder, B. 1991, *Astronomy and Astrophysics*, 243, 501

Tsuneta, S., Ichimoto, K., et al. 2008, *Solar Physics*, 249, 167

van Ballegooijen, A. A. & Martens, P. C. H. 1989, *The Astrophysical Journal*, 343, 971

van Hoof, P. A. M., Williams, R. J. R., et al. 2014, *Monthly Notices of the Royal Astronomical Society*, 444, 420

Vial, J. & Engvold, O. 2015, Astrophysics and Space Science Library, Vol. 415, Solar Prominences

Vial, J. C. 1982, *The Astrophysical Journal*, 253, 330

Vial, J. C., Zhang, P., et al. 2019, *Astronomy and Astrophysics*, 624, A56

Vrsnak, B., Pohjolainen, S., et al. 1992, *Solar Physics*, 137, 67

Wang, Y. M. 1999, *The Astrophysical Journal*, 520, L71

Warmels, R., Biggs, A., et al. 2018, ALMA Technical Handbook, ALMA

Wedemeyer, S., Bastian, T., et al. 2016, *Space Science Reviews*, 200, 1

Wedemeyer-Böhm, S., Ludwig, H. G., et al. 2007, *Astronomy and Astrophysics*, 471, 977

White, S. M., Iwai, K., et al. 2017, *Solar Physics*, 292, 88

Wilhelm, K., Curdt, W., et al. 1995, *Solar Physics*, 162, 189

Wootten, A. & Thompson, A. R. 2009, *IEEE Proceedings*, 97, 1463

Yagoubov, P. A. 2013, in 2013 38th International Conference on Infrared, 1

Yokoyama, T., Shimojo, M., et al. 2018, *The Astrophysical Journal*, 863, 96

Zhang, P., Buchlin, É., et al. 2019, *Astronomy and Astrophysics*, 624, A72

Zirker, J. B., Engvold, O., et al. 1994, *Solar Physics*, 150, 81